

# **FLOOD MODELING AND MAPPING IN THE UPPER AWASH RIVER BASIN, ETHIOPIA**

Thesis

Submitted in partial fulfillment of the requirements for the degree of

**DOCTOR OF PHILOSOPHY**

By

**SINTAYEHU YADETE TOLA**



**DEPARTMENT OF WATER RESOURCES AND OCEAN  
ENGINEERING**

**NATIONAL INSTITUTE OF TECHNOLOGY KARNATAKA,  
SURATHKAL, MANGALORE - 575 025**

**February, 2024**

# **FLOOD MODELING AND MAPPING IN THE UPPER AWASH RIVER BASIN, ETHIOPIA**

Thesis

Submitted in partial fulfillment of the requirements for the degree of

**DOCTOR OF PHILOSOPHY**

By

**SINTAYEHU YADETE TOLA**

**(Reg. No.: 197088AM006)**

Under the guidance of

**PROF. AMBA SHETTY**



**DEPARTMENT OF WATER RESOURCES AND OCEAN  
ENGINEERING**

**NATIONAL INSTITUTE OF TECHNOLOGY KARNATAKA,  
SURATHKAL, MANGALORE - 575 025**

**February, 2024**



## DECLARATION

*by the Ph.D. Research Scholar*

I hereby *declare* that the Research Thesis entitled “**FLOOD MODELING AND MAPPING IN THE UPPER AWASH RIVER BASIN, ETHIOPIA**”, which is being submitted to the **National Institute of Technology Karnataka, Surathkal** in partial fulfillment of the requirements for the award of the Degree of **Doctor of Philosophy** in the **Department of Water Resources and Ocean Engineering** is a *bonafide report of the research work carried out by me*. The material contained in this Research Thesis has not been submitted to any University or Institution for the award of any degree.



Reg. No.: 197088AM006, Sintayehu Yadete Tola

(Register Number, Name & Signature of the Research Scholar)

Department of Water Resources and Ocean Engineering

National Institute of Technology Karnataka, Surathkal

Place: NITK-Surathkal

Date: February, 2024

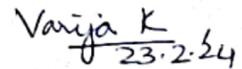
## CERTIFICATE

This is to *certify* that the Research Thesis entitled **FLOOD MODELING AND MAPPING IN THE UPPER AWASH RIVER BASIN, ETHIOPIA** submitted by **SINTAYEHU YADETE TOLA**, (Register Number: 197088 197AM006) as the record of the research work carried out by him, is *accepted as the Research Thesis submission* in partial fulfillment of the requirements for the award of degree of **Doctor of Philosophy**.



**Prof. Amba Shetty**

Research Guide



**Prof. K. Varija**

Chairman – DRPC

## ACKNOWLEDGMENT

First and foremost, I sincerely thank the late supervisor, **Prof. Paresh Chandra Deka**, Department of Water Resources and Ocean Engineering, for his initial impression and continued support during the early stage of my research journey at NITK, Surathkal. His guidance and expertise have been invaluable in shaping my ideas and pushing me to strive for excellence.

I am pleased to express my heartfelt gratitude to my supervisor, **Prof. Amba Shetty**, Department of Water Resources and Ocean Engineering, for unwavering encouragement, professional ideas, scientific guidance, and timely feedback. All your incredible motivation and inspiration helped me focus, accomplish my research on time, and publish many articles in renowned journals.

I thank my Research Progress Appraisal Committee (RPAC) members, **Dr. Subrahmanya Kundapura**, Department of Water Resources and Ocean Engineering, and **Prof. Basavaraju Manu**, Department of Civil Engineering, for examining and their time and dedication throughout the proposal, first progress, second progress, and pre-synopsis seminars. The comments and suggestions RPAC members made were valuable additions to the study effort and enhancements of the overall works of the research.

I am grateful to the Ethiopian Ministry of Education for sponsoring my study and providing financial support. I thank the Ministry of Water and Energy for hydrological data and the National Meteorology Agency for climate data.

I acknowledge the excellent support provided by Mr. Girma Tessema, manager of Kebele, a local lower administrative level, during the site visit in the Becho/Bello flood area, Ethiopia.

I thank the Academic Section for assisting with official work, the Hostel office, and the academic and non-academic staff of NITK, Surathkal, for their kind wishes throughout my stay and for helping me in any way possible in NITK, Surathkal.

The motivation and support of fellow research scholars, particularly, Mudesir Nesru Kebede, Abraham Aboneh Bekele, Biruk Tagesse Lambe, Esayas Lateno Shirko, and Fiseha Befikadu Deneke have been invaluable in my research journey. Their encouragement and guidance have played a significant role in keeping me motivated and focused. I am grateful for their willingness to share their expertise and knowledge.

I sincerely thank my family and my wife, **Aselefech Getu**, for their invaluable encouragement during my research, and I could not have accomplished my goals without their unwavering support. I am truly grateful for their presence in my life and the love and support they have shown me throughout this journey. Their contributions have been invaluable, and I am forever thankful to them.

Finally, I thank almighty God for blessing me with health, strength, and a guide in every stage of my life.

**Sintayehu Yadete Tola**

Place: NITK-Surathkal

Date: February, 2024

**Dedication**

*This thesis is dedicated to my parents, who assisted and encouraged me;*

*my wife Aselefech Getu, who was always there for me;*

*my daughter Heran Sintayehu Yadete:*

*and*

*my friends and colleagues.*

## **ABSTRACT**

Climate variability, land cover change, and catchment characteristics significantly impact hydrological extremes. However, their impact on flood response behavior varies spatiotemporally, and quantifying possible causes is essential for effectively mitigating floods. Identifying the potential flood areas, and flood hazard mapping, considering changing environmental factors and an alternative flood frequency model for developing flood hazard management and mitigation strategies are crucial in the flood-prone basin. This thesis comprehensively investigates the potential factors affecting and explaining floods, possible flood sites, and flood hazard maps over the Upper Awash River Basin (UARB), Ethiopia, during the study period from 1985 to 2015.

First, the study investigated the variability of extreme hydroclimatic conditions and the relationship between anomalies in extreme local precipitation, El Niño Southern Oscillation indicators (ENSO) (Southern Oscillation Index (SOI), Niño 3.4, and Multivariate ENSO Index (MEI)), and extreme flow indices. The analysis used standardized anomaly index and coefficient of variation statistics to examine variability, the modified Mann-Kendall and Pettitt tests for trend and change point analysis, and Spearman's correlation test to explore relationships. Results showed that the basin-wise extreme precipitation indices had less variability but higher variability spatially, while the extreme flow indices showed high variability. The maximum temperature increased significantly, while the minimum temperature decreased significantly (except at a few northwest stations), with a considerable shift in the 1990s and 2000s. Anomalies and a decrease in extreme precipitation were consistent with the extreme flow at the basin outlet, Hombole station. However, the extreme flow indices at Melka Kunture increased significantly and shifted upward (2003/2005), and the anomalies in extremely wet and very wet precipitation in the northwest were possibly responsible for this change. The annual wet and very wet days of precipitation strongly affected the extreme flow in the basin. The effect of annual wet day precipitation, maximum yearly precipitation, and ENSO anomalies on extreme flow at the Hombole were significant.

Secondly, the study quantitatively assessed the effects of individual and coupled changes in land cover and climate on peak and high flows at Melka Kunture and Hombole over the baseline (1988-2001) and evaluation (2002-2015) period. The impact of these changes was estimated using the Soil Water and Assessment Tool (SWAT). The model satisfactorily simulated daily and extreme flows. The SWAT model showed that the main factor which affected the changes in upstream flow was the land cover change, increasing peak and high flow by 38.69% and 11.95%, respectively, compared to the baseline period. However, combined changes resulted in downstream peak and high flow reductions of 19.55% and 50.33%, respectively.

In addition, the spatial flood characteristics based on morphometric parameters were performed in four subbasins to understand the hydrological behaviour better. The topographic wetness index (TWI) and topographic position index (TPI) were also used to determine the potential flood areas and inundation extent. The aggregated parameters revealed that subbasin SB-1 comprises Melka Kunture, is highly susceptible to flooding, SB-3 and SB-4 are moderately susceptible, and SB-2 is low. The degree of susceptibility was also determined by incorporating the TWI and TPI through overlay analysis. The UARB accounts for 22.8%, 41.7%, and 35.6% of the total basin classified as high, medium, and low flood-prone, respectively.

Furtherly the study developed a flood hazard map based on the nonstationary flood frequency using a generalized extreme value distribution model for the highly susceptible subbasin (SB-1), the identified flood spot area, Becho floodplain. The distributional location parameter was modeled as a function of rainfall amount of different durations, annual total precipitation from wet days, yearly mean maximum temperature, and time as covariates. The one-dimensional Hydrological Engineering Center River Analysis System (HEC-RAS) hydraulic model with steady flow analysis was used to generate flood hazard map input, depth and velocity, and inundation extent for different return periods. The result indicated that the model as a function of rainfall, such as monthly rainfall (August) and annual wet day precipitation, best fit the observed hydrological data. The developed hazard map based on depth alone and the combination of depth and velocity thresholds

resulted in more than 70% of the floodplain area being classified as a high hazard zone under 2, 25, 50, and 100 years return periods.

**Keywords:** ENSO, climate variability, land cover change, flood susceptibility, flood hazard, nonstationary flood frequency analysis

## CONTENTS

<b>ABSTRACT</b> .....	i
<b>LIST OF FIGURES</b> .....	vii
<b>LIST OF TABLES</b> .....	x
<b>ABBREVIATIONS</b> .....	xii
<b>CHAPTER 1 INTRODUCTION</b> .....	1
1.1 Introduction .....	1
1.3 Floods .....	1
1.3.1 Cause of floods .....	3
1.4 Types of models .....	5
1.5 Flood mapping .....	7
1.6 Statement of the problem .....	8
1.7 Objective of the study .....	9
1.8 Organization of the study .....	10
<b>CHAPTER 2 LITERATURE REVIEW</b> .....	12
2.1 Introduction .....	12
2.2 Extreme hydroclimatic variability .....	12
2.3 Effect of El Niño and the southern oscillation on flood .....	17
2.4 Impact of changes in land cover and climate on hydrology .....	22
2.5 Flood susceptibility modeling techniques .....	26
2.5.1 DEM based approach .....	26
2.6 Nonstationary flood frequency model .....	28
2.7 Flood hazard map modeling .....	31
<b>CHAPTER 3 MATERIALS AND METHODOLOGY</b> .....	33
3.1 Introduction .....	33
3.1.1 Study area description .....	33
3.2 Data sets .....	35
3.3 Methods and model/tool used .....	36
3.3.1 Methodology .....	36
3.3.2 Details of tools used .....	37
<b>CHAPTER 4 EXTREME HYDROCLIMATIC VARIABILITY AND IMPACT OF LOCAL AND GLOBAL CLIMATE SYSTEM ANOMALIES ON EXTREME FLOW</b> .....	39

4.1	Introduction .....	39
4.2	Extreme hydroclimatic variability and its cause .....	39
4.3	Data and methodology .....	40
4.3.1	Data .....	40
4.3.2	Methodology .....	41
4.3.3	Variability analysis .....	42
4.3.4	Trend analysis .....	44
4.3.5	Change-point analysis .....	45
4.3.6	Correlation analysis .....	45
4.4	Result and discussion .....	46
4.4.1	Hydroclimatic characteristics.....	46
4.4.2	Variability analysis .....	47
4.4.3	Spatiotemporal trend analysis .....	55
4.4.4	Spatiotemporal change point analysis.....	59
4.4.5	Effect of local rainfall variability on streamflow.....	64
4.4.6	Effect of climate indices anomalies on streamflow .....	66
4.5	Conclusions .....	70
<b>CHAPTER 5 QUANTIFYING THE CHANGES IN LAND COVER AND RAINFALL VARIABILITY IMPACT ON FLOOD .....</b>		<b>73</b>
5.1	Introduction .....	73
5.2	Changes in land cover and rainfall variability impact on flood .....	73
5.3	Data and methodology .....	74
5.3.1	General overview of the SWAT model .....	77
5.3.2	SWAT model setup.....	78
5.3.3	Calibration, validation, and uncertainty .....	79
5.3.4	Model performance criteria.....	80
5.3.5	Quantitative evaluation of the influence of land cover and rainfall variability on flood .....	81
5.4	Result and discussion .....	82
5.4.1	Changes in land cover evaluation .....	82
5.4.2	The areal precipitation events and amounts .....	87
5.4.3	Rainfall and peak flow relationship .....	88
5.4.4	SWAT parameters sensitivity analysis .....	89
5.4.5	SWAT calibration and validation for daily streamflow.....	90

5.4.6	SWAT model in daily flood simulation.....	93
5.4.7	Contribution of changes in land cover and rainfall variability on flood discharge.....	94
5.5	Conclusions.....	97
<b>CHAPTER 6 FLOOD SUSCEPTIBILITY MODELING USING MORPHOMETRIC AND FLOOD HAZARD MAPPING OF THE HIGHLY SUSCEPTIBLE FLOOD AREA .....</b>		<b>99</b>
6.1	Introduction .....	99
6.1.1	Morphometry .....	99
6.1.2	Flood hazard.....	100
6.2	Data and methodology .....	101
6.2.1	Flood susceptibility modeling.....	101
6.2.2	Flood hazard mapping.....	105
6.3	Result and discussion .....	115
6.3.1	Geo-morphometric analysis .....	115
6.3.2	Topographic position index .....	123
6.3.3	Topographic wetness index.....	124
6.3.4	Flood susceptibility modeling.....	125
6.3.5	Nonstationary analysis .....	130
6.3.6	Model fitting and flood quantile .....	132
6.3.7	Flood hazard map.....	139
6.4	Conclusions .....	147
<b>CHAPTER 7 CONCLUSIONS AND FUTURE SCOPE .....</b>		<b>149</b>
7.1	Summary .....	149
7.2	Conclusions .....	149
7.3	Limitations of the study.....	151
7.4	Future scope of the study .....	152
<b>REFERENCES.....</b>		<b>153</b>
<b>LIST OF PUBLICATIONS .....</b>		<b>184</b>

## LIST OF FIGURES

<b>Figure No.</b>	<b>Caption</b>	<b>Page No.</b>
2.1	Effect of rainfall, ENSO, and land cover on extreme streamflow	13
3.1	Study area, including its river networks, hydro-meteorological stations, watershed, river network, and elevation	34
3.2	Flowchart illustrating the overall methodology of the study	37
4.1	Flow chart of the study for evaluating extreme hydroclimatic variability and impact of local precipitation and ENSO on extreme flow	41
4.2	Monthly rainfall distribution for UARB	47
4.3	Basin-wise coefficient of variation a) PRCPTOT, b) Rmax1, c) R99p, and d) R95p	49
4.4	Standardized anomaly index (SAI) for basin extreme precipitation indices a) PRCPTOT, b) Rmax1, c) R99p, and d) R95p. The line represents the slope of linear regression.	50
4.5	Standard anomaly index (SAI) of extreme streamflow indices for MK a) Qmax1, b) Q99p, c) Q95p and d) Q90p and Hombole e) Qmax1, f) Q99p, g) Q95p, and h) Q90p. The line represents the slope of linear regression and 5-year moving average (black line)	54
4.6	Basin temperature distribution and trend a) Tmax1 and b) Tmin1.	56
4.7	Basin extreme rainfall distribution and trend a) PRCPTOT, b) Rmax1, c) R99p, and d) R95p	57
4.8	Trends and change points for extreme flow indices at MK station a) Qmax1, b) Q99p, c) Q95p, and d) Q90p. The dotted line represents the slope of linear regression and broken line represent change point (before and after)	59
4.9	Basin temperature trend and change point a) Tmax1 and b) Tmin1. The dotted line represents the slope of linear regression and broken line represent change point (before and after)	61

4.10	Standardized anomalies of extreme flow indices for MK a-c and Hombole d-f stations and ENSO anomalies. The red and blue represent the cold (+) and warm (-) phases for SOI, and the red and blue represent the warm (+) and cold (-) phases for Niño 3.4 and MEI	70
5.1	Flow chart of the study for quantifying the separate and combined impact on the extreme flow	75
5.2	Land cover map of a) 1987 and b) 2001	84
5.3	Rainfall (RF) events and amount comparison between baseline and evaluation period in the a) Melka Kunture and b) Hombole sub-basin	88
5.4	Observed and SWAT simulated daily discharge hydrograph during calibration and validation period at MK station a) base period and b) evaluation period	91
5.5	Observed and SWAT simulated daily discharge hydrograph during calibration and validation period at Hombole a) baseline period and b) evaluation period	92
5.6	FDC observed and simulated during the calibration and validation period at a-d MK and e-h Hombole. FDC for peak (< 2 % of the exceedance probability flow) and high flow (2 to 20% of the exceedance probability flow) at MK station during the a-b baseline and c-d evaluation period; FDC for peak (< 2 % of the exceedance probability flow) and high flow (2 to 20% of the exceedance probability flow) at Hombole station during the e-f baseline and g-h evaluation period	96
6.1	Flowchart for flood susceptibility modeling using geomorphometric parameters	102
6.2	Flowchart for flood hazard mapping using nonstationary flood frequency model	106
6.3	Subbasin drainage network map and stream order after Strahler (1964)	116
6.4	Topographic position index a) SB-1 b) SB-2, c) SB-3 and d) SB-4	124

6.5	Topographic wetness index a) SB-1 b) SB-2, c) SB-3 and d) SB-4	125
6.6	Flood susceptibility map of subbasins based on morphometric parameters	127
6.7	Flood susceptibility map based on the weighted overlay analysis of TWI and TPI and identified specific locations	129
6.8	The flood-susceptible areas under low, medium, and high of the SB-1, SB-2, SB-3, and SB-4	129
6.9	Modified Mann-Kendall trend test and Pettitt's test results for a) Berga, b) Holeta, and c) Ginchi stations at the 5% significance level	131
6.10	1D floodwater depth map for various return periods: a) 2-year flood b) 25-year flood c) 50-year flood d) 100-year flood	140
6.11	1D floodwater velocity map for various return periods: a) 2-year flood b) 25-year flood c) 50-year flood d) 100-year flood	141
6.12	Flood hazard map of the Becho floodplain for different flood return periods: a) 2-year flood b) 25-year flood c) 50-year flood d) 100-year flood	144
6.13	The corresponding area of each flood hazard class for different flood return periods	145
6.14	Floodwater depth map for a 25-year return period and observed flood depth in August 2020	147

## LIST OF TABLES

<b>Table No.</b>	<b>Caption</b>	<b>Page No.</b>
3.1	Data type used in this study, periods or resolutions, and source description	36
3.2	Tools/platform used in this study	37
4.1	Extreme climatic and streamflow indices and description	43
4.2	Basin-wise extreme climate indices: statistics, trend, and change point test results	48
4.3	Results of the Hombole and MK hydrological stations' statistics, trends, and change point tests	53
4.4	Station-wise temperature indices: change point test and Sen's slope results	60
4.5	Station-wise extreme precipitation indices: change point test and Sen's slope results	63
4.6	Results of Spearman's rank correlation coefficients between anomalies in extreme precipitation, ENSO, and extreme flow	65
5.1	Scenarios of land cover and climate used	82
5.2	Land cover change information (%)	86
5.3	Sensitive parameter rank and calibrated range (max and min) on a daily basis in the Melka Kunture and Hombole sub-basin using 1987 and 2001 land cover	90
5.4	Calibration and validation performance results for MK and Hombole stations during the baseline and evaluation periods	93
5.5	Contribution of land cover and climate changes on peak and high flow in the MK and Hombole sub-basin	97
6.1	Morphometric parameters, formula, unit, and references	104
6.2	Flood frequency models used in this study	110
6.3	Morphometric analysis of subbasins	117
6.4	Characteristics of subbasins morphometry	120

6.5	Rank and the total rank-sum of morphometric parameters for subbasins	126
6.6	Distribution parameters of stationary and nonstationary models using the MLE method for Berga station	133
6.7	Estimated flood quantiles ( $m^3/s$ ) for 2, 25, 50, and 100-year return periods for Berga, Holeta, and Ginchi stations	134
6.8	Distribution parameters of stationary and nonstationary models using the MLE method for Holeta station	136
6.9	Distribution parameters of stationary and nonstationary models using the MLE method for Ginchi station	137
6.10	Flood hazard class based on the flood depth and the corresponding inundation area of different return level	142
6.11	Thresholds for flood hazard classification	143
6.12	Comparative analysis between the current and earlier study in the area	146

## **ABBREVIATIONS**

<b>Symbol</b>	<b>Representation</b>
CRED	Centre for Research on the Epidemiology of Disasters
WMO	World Meteorological Organization
EM-DAT	Emergency Events Database
US	United State
IPCC	Intergovernmental Panel on Climate Change
ENSO	El Niño and the Southern Oscillation
SWAT	Soil and Water Assessment Tool
HEC-RAS	Hydrological Engineering Centre - River Analysis System
OCHA	Office for the Coordination of Humanitarian Affairs
ETCCDI	Expert Team on Climate Change Detection Indices
MEI	Multivariate El Niño/Southern Oscillation Index
SOI	Southern Oscillation Index
SST	Sea Surface Temperature
DEM	Digital Elevation Model
SRTM	Shuttle Radar Topography Mission
TWI	Topographic Wetness Index
TPI	Topographic Position Index
FFA	Flood frequency Analysis
UARB	Upper Awash River Basin
SWAT-CUP	Soil and Water Assessment Tool Calibration Uncertainty Program
GEE	Google Earth Engine
CV	Coefficient of Variation
SAI	Standard Anomaly Index
MMK	Modified Mann Kendall
R	Correlation coefficient

USGS	United State Geological Survey
FAO	Food and Agricultural Organization
HRU	Hydrological Response Unit
FDC	Flow Duration Curve
WGS	World Geodetic System
UTM	Universal Transverse Mercator
GEV	General Extreme value
AIC	Akaike Information Criterion
MLE	Maximum Likelihood Estimator
MK	Melka Kunture



# **CHAPTER 1**

## **INTRODUCTION**

### **1.1 Introduction**

The hydrological cycle system includes precipitation, evaporation, runoff, and other phases. Extreme streamflow is an essential component of hydrological cycles. Altering the dynamic equilibrium of hydrological cycle component, such as meteorological variables (intensity, duration, and radiation), drive unusual streamflow characteristics in terms of magnitude, frequency, and timing of extreme events. River floods are the most common natural disaster/hazard worldwide. Natural climate variability, anthropogenic climate change, catchment characteristics, antecedent soil moisture condition, and river systems are prime drivers of flood regime change. Historical flood incidents have far-reaching consequences in different parts of Ethiopia's river basin. Ethiopia's topographic and climatic characteristics have made the country vulnerable to extreme floods, resulting in destruction, casualties, and damage to the economy, livelihoods, infrastructure, services, and health systems. Flood damages are expected to increase as a result of continued human activities. Understanding the underlying mechanisms of flood formation and drivers is needed for flood management and mitigation strategies. Thus, flood modeling and hazard mapping are critical for mitigation strategies and flood hazard management.

### **1.3 Floods**

Environmental hazard creates threats to people, goods, and the environment. Natural hazards are described as naturally occurring damages that are truly natural and unaffected by human activities. However, natural hazard events are certainly affected by human action. Thus, natural hazards become quasi-natural hazards. Hydrological hazard-flood is the most frequent natural hazard that causes loss of life and property damage and disrupts socio-economic activities.

Floods commonly result from heavy monsoonal rainfall, i.e., higher than normal, storm surges. Large and extreme riverine floods occur when excessive water overflows or overtops natural or artificial boundaries (its bank) of the channel and inundates the adjacent floodplain areas. Earth's surface and atmosphere are subject to anthropogenic climate change. Changing climate leads to changes in frequency, intensity, spatial extent, duration, and timing of climate and weather extremes, which are likely to amplify the disaster impact. These, however, may be unprecedented. The severity of extreme rainfall at the regional scale will vary depending on the amount of regional warming, changes in air circulation, and storm dynamics. With no direct anthropogenic changes in climate, climate and weather extremes, for example, heavy rainfall would still occur.

Historical records reveal that flood events have increased significantly recently and caused huge disasters (CRED 2020). According to Emergency Events Database (EM-DAT) records from 1970 to 2019, weather, climate, and water hazards caused 50% of all disasters, 45% of all recorded deaths, and 74% of reported economic losses, resulting in 2.06 million deaths and US\$3.6 trillion in monetary damages. Flood-related disasters were the most prevalent in Africa, and storms and floods caused the most economic damage (WMO 2021). In South Asia (India, Bangladesh, and Pakistan), flooding during the monsoon season is the most recurring, widespread, and disastrous, causing US\$ 1 billion in total damage, on average, annually in the most flood-prone rivers. The flood damage in this century (1998, 2007, 2009, and 2010) in the region was the greatest and worst, with an increasing tendency for large flood events (Kale 2014).

In Africa, floods are becoming increasingly prevalent in the last twenty years (2002-2021), according to EM-DAT, compared to 1982-2001. Ethiopia is among the top flood-affected countries, with 3,458,324 people (CRED 2022). In most parts of the region, flood frequency and affected area extent increased, and 2001-2010 was the most flooding decade. A flood event in 2010 affected 29 locations, whereas a flood event in 1997 covered the greatest extent and affected 12 areas. Of 15 flood events from 1960 to 2018, the Awash Basin recorded 13 events, followed by Wabi Shebele (12), the Rift Valley Lake Basin (11), and Genale Dawa (11) (Mamo et al. 2019).

The hazards will remain problematic as the globe warms, resulting in extreme and frequent precipitation and possibly a flood risk (Tabari 2020; IPCC 2021a) and continuing to adversely affect the social, economic, and health systems.

### **1.3.1 Cause of floods**

Global warming is due to greenhouse gases in the atmosphere, which increase surface temperatures and enhance hydrological cycles. Consequently, atmospheric moisture holding capacity increases, resulting in extreme precipitation and likely increasing extreme hydrological events such as extreme river discharge (Svensson et al. 2005). Extreme precipitation is a rare event above a given threshold e.g., percentiles of the heaviest precipitation event. The increase in the frequency of extreme to heavy precipitation (amount of rainfall above normal) events and the increase in the contribution of extreme to total precipitation increase are plausible causes for the recent rise in extreme flood events (Kale 2014).

It is unequivocally that the human effect has caused a rise in the observed well-mixed greenhouse gas concentration since 1970. The overall human-induced global surface temperature increase from 1850-1900 to 2010-2019 is likely between 0.8°C and 1.3°C, with a best estimate of 1.07°C. Greenhouse gases have likely contributed to a warming of 1.0°C to 2.0°C and have increased faster since 1970 than in any other 50-year period over the last 2000 years (high confidence). It is likely that human inference contributed to the fact that average precipitation on land globally has increased in frequency and intensity since 1950 (medium confidence). There is high confidence that with every additional increment of global warming, e.g., 0.5°C, discernible increases in the incidence and strength of heavy precipitation and very likely to occur in most regions (IPCC 2021b). Hot temperature extremes, heavy precipitation, and agricultural and ecological droughts are expected to increase in frequency and intensity over land with each incremental degree of global warming, meaning that surface flow will become more unpredictable.

Natural climate variability results in weather and climate extremes that have a pronounced effect on temperature and precipitation. Modes of climate variability

arise through atmospheric circulation but also through ocean-atmospheric coupling. The El Niño-Southern Oscillation (ENSO), Atlantic Multi-decadal Oscillation (AMO), North Atlantic Oscillation (NAO), and Pacific Decadal Oscillation (PDO) are among the leading large-scale oceanic-atmospheric variability patterns. It affects both local and remote regions via teleconnections. In particular, ENSO refers to a large-scale oceanic-atmospheric circulation pattern that accounts for inter-annual climate anomalies over the tropical Pacific. ENSO is the main modulator of global surface temperature at an interannual time scale and a source of climate predictability on a seasonal to interannual time scale (IPCC 2021c). It triggers climate teleconnections in various places of the world (Chiew and McMahon 2002; Ward et al. 2014b), and the cold phase of ENSO, La Niña, causes heavy precipitation and is mostly associated with floods; the warm phase, El Niño, is linked with droughts.

Destructive flood events are not caused solely by climate variability but also by human-induced changes (Kale 2014) to the earth's surface, such as alterations to land cover and other types of development. Human activities, especially intensive farming, deforestation, and urbanization (including development on floodplain land), often contribute to increased floodwater. Deforestation and urbanization are often blamed for altering the flood process, increasing the quantity and speed of flood flow, and intensifying flood risk (Smith 1993; Parker 2000).

The watershed characteristics influence the hydrological response behaviour of the watershed system, i.e., flood event and magnitude, and profound role in downstream flooding (Meraj et al. 2015). The unique characteristics of the watershed system, such as land cover, soil, drainage size, basin shape, basin slope, drainage density, etc., intensify the hydrological phenomena. Morphometric analysis gives a numerical description of the linear, area, and relief aspects of a watershed. These aspects are important for the drainage pattern, hydrology, and geomorphology (soil and underlying control structure), and they help us figure out what controls the flow of water during a flood. The hydrological investigations, such as flash flood potential, flood susceptibility, groundwater potential, and watershed prioritization for water resources development (Nooka Ratnam et al.

2005; Angillieri 2012; Choudhari et al. 2018; Mahmood and Rahman 2019) as well as instantaneous unit hydrograph development from the geomorphological parameters for flood prediction (Bhaskar et al. 1997), are among the critical morphometric based applications. Understanding the flooding mechanism and identifying sensitive areas using morphometric analysis supports flood management and mitigation approaches.

#### **1.4 Types of models**

Models are a simplified representation of the real world, and the best model describes close to reality. Hydrological models replicate the watershed hydrologic system and hydrological process and are used to predict, understand, and support decision-making. Hydrological models are designed to understand the operation of a system and predict system behaviour in rivers or floodplains (Teng et al. 2017). Different models have been designed to offer flood information or delineate the flood extent. Model inputs, parameters, and the principles or approach used in the model define model characteristics and types. The three important categories of models are empirical, conceptual, and physical.

Empirical models (black box or data-driven models) consist of mathematical equations derived from input and output relationships or fit the observed data without explicit physical consideration. The models do not assist in the physical understanding of behaviors of hydrological systems. However, they predict without the need for detailed information (Daniel et al. 2011). Also, these models are not capable of predicting under changing conditions. Simple linear regression, multiple linear regression, FFA, artificial neural networks (ANNs), generic algorithms (GAs), fuzzy logic, machine learning, deep learning, and other data-driven models are examples of empirical models or data-driven models that are used to establish linear or nonlinear relationships between inputs and outputs.

Conceptual hydrological models (parametric or gray box models) are simplified representations of hydrologic systems. More modest parameters are utilized to explain the hydrological process or depend on simplified hydraulic concepts. The

model consists of interrelated reservoirs, which explain certain physical processes in the basin that are recharged by precipitation, percolation, infiltration, and emptied by evapotranspiration, runoff, and drainage (Devia et al. 2015). It also requires a large number of meteorological and hydrological data for model calibration. It has uncertainties related to conceptualizing rainfall-to-runoff generation processes. Conceptual models include Hydrologiska Byrans Vattenavdelning (HBV) model, the TOPMODEL, CLARK model, the Tank model, the Xinanjiang model, the Sacramento model, etc. Physical models have been developed to address the shortcomings of conceptual models.

Physically based models (white box models or theoretical models) are based on understanding the physics associated with hydrological processes. These models use physically based algorithms to describe the catchment processes, represented in detail by solving differential equations that describe the physical laws of mass, energy, and momentum conservation. In a physical-based model, scale or resolution is an important factor. In fully distributed physical-based models, the hydrological processes are simulated over a spatial domain, typically represented by a grid structure. Semi-distributed when the watersheds are divided into individual units based on the terrain features and drainage network, where the input, parameters, and outputs vary spatially. Semi-distributed and distributed considers the spatial hydrological process variability, inputs, watershed characteristics, and boundary conditions. The capacity to simulate the mechanisms that comprise a basin's hydrologic cycle is the major advantage of physically based models (Mudashiru et al. 2021) and is characterized by higher intrinsic accuracy for predicting the effect of land cover disturbances or climate change (Dwarakish and Ganasri 2015).

Examples of some physically based hydrological models include the Soil and Water Assessment Tool (SWAT), Hydrologic Engineering Center-Hydrologic Modeling System (HEC-HMS), Variable Infiltration Capacity (VIC), European Hydrologic System (SHE), and so on. The physically based hydrodynamic models include one (1D) and two-dimensional (2D) Hydrologic Engineering Center River Analysis System (HEC-RAS), 1D MIKE 11, 1D and 2D MIKE FLOOD, etc. (Mudashiru et al. 2021).

The semi-distributed hydrological model SWAT and the hydrodynamic HEC-RAS are two extensively used and open-source models available globally (Mudashiru et al. 2021). SWAT (Arnold et al. 1998) was designed to predict the impact of land management practices on water, sediment and agricultural chemical yields in large complex watersheds with varying soils, land use and management conditions over long periods of time. It is an indispensable tool in understanding the dynamic interaction of climate and land surface hydrology. There has been much interest in using the SWAT model to assess and quantify hydro-climatic extreme studies in recent years (Tan et al. 2020). Similarly, hydrodynamic models are the most commonly employed in simulating flood dynamics, flood mapping, flood modeling (forecasting), and scenario analysis.

### **1.5 Flood mapping**

Flood damage management strategies include structural and non-structural components that minimize the negative impact on human life, socio-economic conditions, and property. The structural component involves the construction of flood protection works, such as levees, dams (reservoirs), channel modification, diversion works (floodways), and flood walls. However, relying solely on a structural approach is not enough to protect against recurrent flood events, and it may not be economically feasible and may sometimes damage the environment and humans. A non-structural measure is an effective tool alongside the structural approach (Masood and Takeuchi 2012). Non-structural strategies fundamentally include flood hazard assessment and mapping (Farooq et al. 2019), flood forecasting, and early warning systems. Floodplain maps are classified into three distinct types (Di Baldassarre et al. 2010): flood hazard maps depicting the intensity of floods and its associated exceedance probability; flood vulnerability maps showing the effect floods have on the economy, society, and the natural environment; and flood risk maps illustrate the spatial distribution of risk, which can be defined as the probability that a given event will occur multiplied by its consequences for natural disasters.

Flood hazard mapping indicates areas at risk of flooding under extreme weather or climate conditions and is essential for effective land use planning in flood-prone areas. The map provides flood extent, depth, and velocity based on the simulated flood scenarios. The information improves flood risk management and emergency preparedness and raises community, stakeholder, and decision-maker awareness of the likelihood of flooding from potential future events. Flood hazard modeling is an important stage in mitigating flood risks because it identifies the potentially hazardous regions and allows communities to respond in an anticipatory rather than reactive manner.

## **1.6 Statement of the problem**

Ethiopia is known for its diverse topographic and climatic types, which range from humid tropical to arid, and vulnerable to droughts and floods due to its high interannual variability in rainfall (Edossa et al. 2010; Viste et al. 2013; Zhang et al. 2016). The economy is primarily based on rain-fed agriculture, which is highly sensitive to variations in rainfall over time and space (Seleshi and Zanke 2004). The topographic and climatic characteristics have made the country vulnerable to extreme floods, resulting in destruction, casualties, and damage to the economy, livelihoods, infrastructure, services, and health systems. Over the last few decades, Ethiopia has experienced frequent flood disasters in different regions (Getahun and Gebre 2015; Erena et al. 2018; Melkamu et al. 2022). Heavy summer rainfall in 2020 recently caused floods in many parts of the country, affecting half a million people and displacing 300,000 people (OCHA 2020). On the other hand, degradation of natural resources, agricultural activities, deforestation, and urbanization are trending, directly impacting hydrological regimes.

Identifying the effect of changing climate and land cover in developing countries, such as the Ethiopian river basins, is a growing concern for water resource management and planning due to its limited capacity to handle extreme conditions. The Awash River basin is the fourth of twelve river basins most developed in Ethiopia. The basin's suitable conditions and strategic geographic region made it a hotspot for urbanization and the development of industrial and agricultural

activities. The Awash River basin, in particular, is prone to extreme flooding caused by heavy rains in the highlands that mostly inundate the low-lying plains. In the upstream of Koka Dam (Becho floodplain), Middle (Wonji area and Metehara), and the Lower section (Amibara, Gewane, Logiya and Asaita) are the most common flood-prone areas. For instance, in August 2006, Dire Dawa town, Dechatu River, flashed in the night to neighbouring villages (Billi et al. 2015) and killed 260 people. In August 2020, the Awash River burst its embankment into the neighbouring town and extensive farmlands due to above-normal rainfall in the highland and escarpment. The flood surge in these regions has also killed animals and destroyed large agricultural areas.

In the Upper Awash river basin, according to a local source, flooding frequently occurs in the Becho floodplain at the head of the Awash River, with the most recent occurrences in 1996, 2006, 2016, and 2020. This resulted in the displacement of local communities, property loss, economic loss, and the inundation of extensive farmlands.

Against all this backdrop, the basin needs a comprehensive investigation concerning floods to minimize the adverse effects on the economy, property, and lives. Extreme hydroclimatic variability in the face of climate change and the potential drivers of extreme hydrological variability would be significant for management and mitigation strategies in the region. Therefore, understanding and quantifying the possible factors explaining the floods in the region, detecting areas susceptible to flood hazards, and flood hazard mapping for flood mitigation and management-related practice are needed.

### **1.7 Objective of the study**

The main objective of the study is to model flood and flood mapping in the upper Awash River basin of Ethiopia.

The specific objectives of the present study are:

1. To investigate extreme hydroclimatic variability and the impact of local and global climate system anomalies on extreme flow
2. To quantify change in land cover and rainfall variability impact on flood hydrology
3. To investigate the basin's spatial flood characteristics based on morphometric effect and prepare flood hazard maps of the highly susceptible flood area.

## **1.8 Organization of the study**

Following this introduction, the remaining chapters are organized as follows:

### **Chapter 2 Literature review**

Comprehensive literature reviews conducted on key topics are presented in this chapter, including hydroclimatic variability, the effect of large-scale coupled atmospheric ocean variability on streams, the impact of changes in land cover and climate variability on the flood, flood susceptibility modeling, nonstationary flood frequency modeling, and flood mapping.

### **Chapter 3 Study area and methods**

This chapter describes the study area, methods, tools/models, and platform.

### **Chapter 4 Extreme hydroclimatic variability and impact of local and global climate system anomalies on extreme flow**

The present chapter investigates the basin's extreme hydroclimatic variability basin-wide and spatially. Precipitation indices and annual maximum and minimum temperature and streamflow indices were used to explore variability and change in the hydroclimatic series. It also investigates the impact of local precipitation and large-scale climate variabilities indices such as El Niño and the Southern Oscillation indicators (Southern Oscillation index, Niño 3.4 Sea Surface Temperature, bi-monthly Multivariate El Niño/Southern Oscillation index) on extreme flow indices.

## **Chapter 5 Quantifying the change in land cover and rainfall variability impact on flood**

The fifth chapter deals with the quantification of possible factors explaining flood variability in the basin. It employs a hydrological model to quantify the impact of land cover change and rainfall variability on extreme flows (i.e., peak and high flows).

## **Chapter 6 Flood susceptibility modeling using morphometric and flood hazard mapping of the highly susceptible flood area**

This chapter presents flood susceptibility and flood spot areas in subbasins based on morphometric parameters and flood hazard mapping for highly susceptible flood spot areas using a hydrodynamic model with nonstationary flood frequency model-based flood estimates as input.

## **Chapter 7 Conclusions and future scope**

The final chapter, seven, includes the study's main summary, conclusion, limitations, and future scope.

## **CHAPTER 2**

### **LITERATURE REVIEW**

#### **2.1 Introduction**

This chapter explores the previous literature on extreme hydroclimatic variability, the cause for hydrological variability, land cover and climate variability impact on hydrology, spatial basin's flood characteristics based on physiographic characteristics, and flood hazard mapping.

#### **2.2 Extreme hydroclimatic variability**

Climate and hydrology are very complex and uneven, have been varying in different regions of the world, and are significant environmental and societal challenges. Anthropogenic climate change of the earth's climate (global warming) and/or natural climatic variability, i.e., large-scale air circulation, are the leading causes of changes in extreme precipitation, temperature, evapotranspiration, and hydrologic conditions. It is well accepted that the hydrological cycle components are affected by the chain reaction of local climate variability and land cover change, among the essential factors controlling the hydrological regime (Legesse et al. 2003, 2010). Nevertheless, catchment storage, management practices (flow regulation, water abstraction), and river engineering are the primary drivers of changes in extreme hydrological characteristics.

The change may be a deviation from the long-term mean and gradual or abrupt, which means trends in the form of increasing or decreasing and upward or downward shifts in hydroclimatic series. Extreme climate events, in general, are unpredictable and pose growing threats to environmental sustainability, water resources management, and agriculture. Hence, understanding and modeling extreme hydroclimatic variability is essential in flood management and planning strategies.

Numerous regions worldwide have experienced changes in the magnitude and frequency of extreme precipitation events, both increasing and decreasing. The researchers globally report evidence of an apparent pattern change (trend and change points) in the extreme hydroclimatic over the past decades.

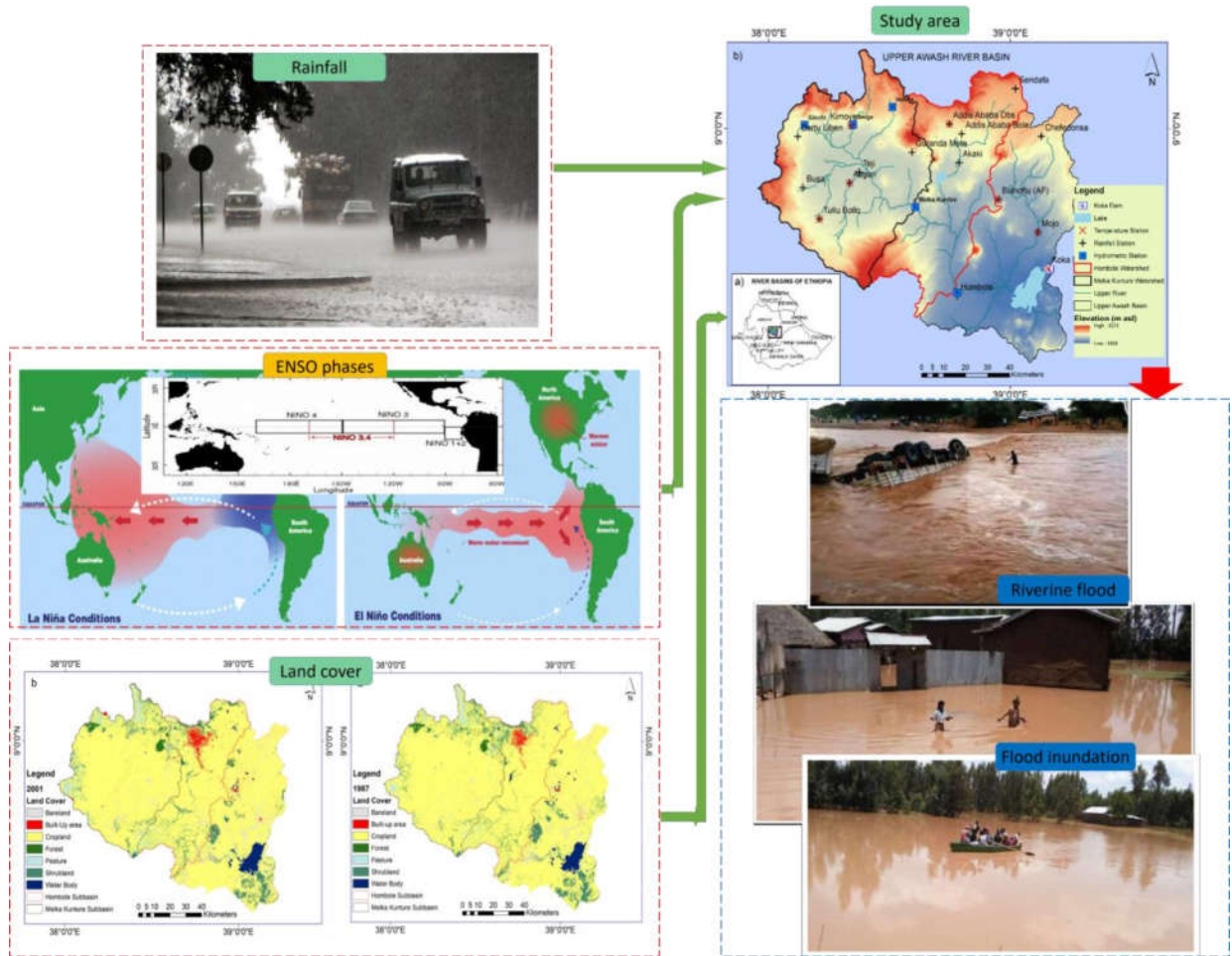


**Figure 2.1** Effect of rainfall, ENSO, and land cover on extreme streamflow

(Source: Rainfall: <https://commons.wikimedia.org/>, ENSO phase (El Niño and La Niña conditions): <https://scijinks.gov/el-nino/> and Niño regions: <https://www.ncei.noaa.gov/>)

An increase in the frequency of extreme rainfall with various dimensions extremes and an upward and downward trend over different regions of India were reported (Roy and Balling 2004). Spatially and temporally increasing or decreasing trends in extreme yearly precipitation were demonstrated in Texas (Mishra and Singh

2010). Jung et al. (2011) investigated spatiotemporal variability in Korean precipitation. They found an increase in annual and extreme rainfall (maximum daily precipitation) and noted that increased precipitation was associated with increased frequency and intensity of heavy rainfall.

The rate of change in daily extreme rainfall generally varies depending on the geographic location and duration of rainfall events (Westra et al. 2014). Keggenhoff et al. (2014) studied the trends in extreme precipitation indices recommended by the Expert Team on Climate Change Detection Indices (ETCCDI) over Georgia. From the eleven indices investigated, almost all indices showed an increasing number and more extreme precipitation events during 1971–2010; however, they were insignificant, and it was noted that heavy and extremely heavy precipitation contributed to the increase in total precipitation. A similar study by Chen et al. (2015) analyzed eleven extreme precipitation indices on the monthly, seasonal, and annual scales over Yunnan Province, China, resulting in a mixing trend and spatial difference.

A recent report on temperature and precipitation extreme indices has been done over the last few decades, providing compelling evidence that global warming is associated with large changes in temperature and precipitation extremes. Accordingly, heavy precipitation events have likely increased globally since 1950 and will become more frequent and intense with every additional increase in global warming over this century (IPCC 2021b). In numerous studies conducted around the world, the extreme precipitation and temperature indices showed a rising or falling trend and spatial variation (Dušek et al. 2017; Chang et al. 2018; Benzater et al. 2019; Bhatti et al. 2020; Zuo et al. 2021; Wu et al. 2021; Manzoor and Ahanger 2022; Mo et al. 2022; Zhang et al. 2023), including Ethiopia river basins (Shawul and Chakma 2020; Gebremichael et al. 2022; Wudineh et al. 2022; Lambe and Kundapura 2023). The change in climatic variables intensifies the hydrological cycles and results in extreme hydrological events (Asadieh and Krakauer 2017; Tabari 2020), and the existing risks and new risks could be amplified and created (Ansa Thasneem et al. 2019).

Streamflow is another essential feature of hydrology in water resources and hydrological studies. Extreme flow or floods are becoming more severe and frequent in different river basins worldwide, but a complex phenomenon caused by several factors associated with local, regional, and global climate processes. There have been studies on hydrological alteration using different quantiles or extreme flow indicators over different regions. Burn and Hag Elnur (2002) used annual maximum daily streamflow or flood data for trend analysis in Canada. They found a spatially rising tendency in the northern and a declining trend in the southern region. The spatial difference in temporal change in streamflow may result from the spatial difference in climate variability and the spatial difference in the transformation of climate variables into hydrological responses due to watershed characteristics.

According to Kundzewicz et al. (2005), the annual flood discharge trend over 195 gauging stations worldwide showed no ubiquitous increase in flood magnitude; however, no significant changes were detected for most stations. Birsan et al. (2005) analyzed streamflow in undisturbed river regimes in 48 watersheds in Switzerland for a temporal trend change over varying periods. The increase in yearly streamflow is noted due to increased winter, spring, and autumn runoff. Most of the basins (63%) saw a significant rise in the maximum stream flow in the winter. This led to an annual streamflow increase greater than the rise in spring and fall in moderate and low flow quantiles. The study suggested that a change in precipitation alone may not explain the temporal shift in streamflow and variability, and temperature and/or watershed factors influence the temporal change in streamflow.

Petrow and Merz (2009) used flood indices to track the trends and behavior of the Danube, Rihne, Elbe, and Weser catchments (145 record stations) in Germany. In the study, flood magnitude indicators on an annual basis and peak over the threshold, as well as the annual frequency of flood peak above the threshold, including the seasonal, were investigated. They found a significant upward flood trend and a rare downward flood trend over larger river basins. The annual maximum discharge at Rihne and peak over the threshold at Danube and Rihne were the most significant increases, while the Elbe was the least. Seasonally, during

winter, there are larger changes than in summer, and it was concluded that the observed flood discharge and magnitude are climate-driven.

Temporal variability (decadal) of extreme flows in one of the largest volumes of flow basin contribute to Nile River, Upper Blue Nile basin in Ethiopia was studied by Taye and Willems (2012). The study employed flow extremes (high and minimum flow) at various annual, monthly, and seasonal scales (rainy, small, and dry seasons). The 1980s had significant negative anomalies in extreme flow, while the 1990s-2000s had insignificant positive anomalies and no consistent increasing or decreasing trend. Tekleab et al. (2013) investigated the trends and changes in the hydrology of the Upper Abay/Blue Nile basin. The annual, seasonal, and extreme flows, 1-day and 7-day maximum, and lowest flows were employed in nine catchments. They found that Koga, Gumer, Gider, and Neshi catchments showed an increasing trend and upward shift (most in the 1990s) in the hydrological quantiles. The studies above blamed water management practices, local or global climate variability mainly from the Pacific and Atlantic Oceans, and land use/land cover change for the flow change or variability.

Extremes of the hydrological flow, including the annual maximum and low (7-day annual minimum flow) flows, were investigated in 252 basins for high flow and 230 basins for low flow in the United States. The significant change (an increase in the most and decreasing) and change points in the high flow were less than in the low flow. Also, the temporal variation in the 1990s and 2000s increased in high-flow quantiles (Ahn and Palmer 2016).

Flood on the basis of annual maximum daily discharge and peak-over-threshold for 15 hydrological stations was studied in Omo-Ghibe basin in Ethiopia by Degefu and Bewket (2017). The authors observed an increasing signal in flood magnitude 1982-2006 in annual maximum, 7-day annual maximum flow, and peak over the threshold of three events per year than a downward trend in flood indices. In a similar study, Degefu et al. (2019) inspected spatial trends of streamflow indices at 57 hydrological stations in Ethiopia's highlands (Abay, Awash, Baro Akobo, Genalle Dawa, Omo Ghibe, Rift Valley, and Wabi Shebele basins) using the Mann

Kendall test and Sen's slope estimator. They found a significant increase rather than a decrease in the extreme stream flow indices ( $Q_{\max 1\text{day}}$ ,  $Q_{\max 7\text{day}}$ , and  $Q_{\max 30\text{day}}$ ) at 5 and 10% significant levels. Besides, the annual maximum flood series, which covered the years 1981 to 2010, demonstrated an upward trend in the upper and middle portions and a downward trend in the eastern and lower portions of the Wabi Shebele basin (Wudineh et al. 2021).

Sharma et al. (2020) studied the hydrological extremes defined as the annual maximum, 5-day annual maximum, and percentile-based extreme flow indices exceeding 95th/99th percentile threshold in Tapi basin, India. They found a decreasing trend in high streamflow. The rise in high streamflow indices was associated with the warming Indian Ocean compared to other conditions such as ENSO and IOD. In recent, Lambe and Kundapura (2023) investigated the extreme flow indices in annual and seasonal scales, i.e., rainy, small rainy, and dry seasons (average, annual maximum, flow exceeding 90th/95th /99th percentile threshold), including minimum flow trend and shift upward/downward in Bilate river basin, Ethiopia. It was observed that most extreme flow indices showed an increasing trend and upward shift and indicated likely flooding in the basin during periods of heavy rainfall events. Local climate variability attributed to the change and variability in hydrology. Overall, there is no ubiquitous increase or decrease in flood magnitude worldwide, and the results vary widely in space and time.

### **2.3 Effect of El Niño and the southern oscillation on flood**

El Niño and the Southern Oscillation (ENSO) are defined as an episodic variation in ocean-atmospheric conditions (sea surface temperature (El Niño) and air pressure overlying the atmosphere (Southern Oscillation)) across the tropical Pacific Ocean every two to seven years time scales or so. The episodic are El Niño, La Niña and normal.

The sea surface temperature (SST) anomalies are one of the focuses of ENSO. The SST positive phase indicates the ENSO warm phase (El Niño), and the negative SST is linked with ENSO cold phase (La Niña). The five consecutive three-month

mean SST anomalies characterize El Niño (La Niña) in the Niño 3.4 region that is above (below), i.e., non-neutral conditions, the threshold of  $+0.5^{\circ}\text{C}$  ( $-0.5^{\circ}\text{C}$ ) across the equatorial Pacific Ocean ( $5^{\circ}\text{N}$ - $5^{\circ}\text{S}$ ,  $120^{\circ}\text{W}$ - $170^{\circ}\text{W}$ ).

The Southern Oscillation Index (SOI) is one of the ENSO indicators. It describes the standardized large-scale pressure difference between two barometric pressures in the western and eastern tropical Pacific during the El Niño and La Niña periods. The sea surface temperature and air pressure are strongly correlated. The negative (positive) SOI value coincides with El Niño (La Niña) phases, which are abnormally warm (cold) ocean water across the eastern Pacific. The bi-monthly Multivariate ENSO Index Version 2 (MEI.v2) is the recent large-scale fluctuation index with five oceanic and atmospheric variables: sea level pressure, sea surface temperature, zonal and meridional components of the surface wind, and outgoing longwave radiation over the tropical Pacific basin ( $30^{\circ}\text{S}$ - $30^{\circ}\text{N}$  and  $100^{\circ}\text{E}$ - $70^{\circ}\text{W}$ ). This has an advantage as it facilitates a single index assessment of ENSO. The MEI.v2 is calculated by overlapping the two-month seasons. A positive MEI event indicates a warm ( $\geq 0.5$ , El Niño), and a negative indicates a cold ( $\leq -0.5$ , La Niña) episode.

The abnormal state of ENSO modulates interannual climate anomalies worldwide, particularly precipitation and temperature variability. The streamflow-ENSO link was shown to be stronger than the rainfall-ENSO association because variability in precipitation is amplified in stream flow, and streamflow incorporates spatial information (precipitation, catchment storage, evapotranspiration losses, management practice, river engineering, etc.)(Cayan et al. 1999; Chiew and McMahon 2002). Heat waves, food security, water resources, health, and public safety are some of the regional effects of ENSO's warm and cold phases through teleconnections.

It is well understood that the two phases of ENSO have important implications for significant hydrological processes, such as floods (cold phase) and droughts (warm phase) events at many places around the globe (Jain and Lall 2001). It is the leading interannual signal of climate variability and is also known as a primary predictor of global climate disruptions on Earth (McPhaden et al. 2006). Several efforts have

been made to understand how global climate anomalies impact extreme hydrological events at regional and global scales. A detailed literature survey was performed and discussed in the following to understand the impact of ENSO on hydrological extremes.

Chiew and McMahon (2002) investigated the relationship between streamflow and two ENSO indicators, SOI and MEI, over 581 catchments worldwide. They found strong and regionally consistent ENSO-streamflow teleconnection in Australia, New Zealand, and South and Central America; weaker signals were identified in some parts of Africa and North America. The study indicated that strong ENSO-streamflow teleconnection is more critical in high interannual variability than in low variability in streamflow.

Abteu et al. (2009) investigated the relationship between ENSO indices (Niño 3.4 SST and SOI) and Blue Nile basin hydrology in the Ethiopian river basin. They found that high rainfall and flow are most sensitive to La Niña episodes, while dry years are most sensitive to El Niño episodes. Ward et al. (2010) studied the sensitivity of annual mean and high flows (annual 1-day and 7-day maximum discharge) to ENSO indicator-SOI signal of climate variability over 622 hydrological stations, particularly in North America and central Europe. High flows significantly correlated with SOI and were more sensitive than the annual mean discharge to SOI variations. The SOI significantly impacts the high annual flow events more than the mean annual flow at the studied gauging stations. The study suggested quantifying the impact of ENSO on extreme flow indices, which provides the possible influences of global climate variations on flooding and the basis for risk assessment.

The annual scale of flow extremes strongly correlates with SOI, indicating that changes in the Pacific Ocean impacted extreme hydrological events in the Upper Blue Basin (Taye and Willems 2012). Similarly, Zaroug et al. (2014) explored the drought (low flow) and flood (high flow) occurrences associated with Niño 3.4 SST events. In particular, extreme floods occur with about a 67% chance when La Niña follows El Niño in the Upper Blue Nile basin. Ward et al. (2014) investigated the

influence of the ENSO index on annual peak discharge (i.e., simulated gridded daily discharge) between 1958 and 2000 using a statistical relationship globally for the first time. They found that SOI significantly correlated with peak discharge for basins comprising one-third of the earth's land surface and greatly influenced peak discharge more than average discharge. The annual floods strengthen during the La Niña and weaken during the El Niño events.

Ouyang et al. (2014) investigated the impact of ENSO and PDO on rainfall and streamflow in China over the last century. The warm phase El Niño causes a decrease in precipitation/stream flow, while the cold phase La Niña causes an increase in precipitation/stream flow in China; however, the impact varies by river basin (e.g., ENSO episodes had a greater influence on stream flow changes in the Yellow, Yangtze, and Pearl River basin than in the Songhua River basin) and season.

Siam and Eltahir (2015) examined the relationship between the flow variability in African's longest Nile River, ENSO, and the Southern Indian Ocean (SIO) index. The sea surface temperature over the two oceans modulates the interannual variability in the Nile River flow. ENSO alone explains 25% of the interannual variability in the Nile flow, and when coupled with SOI SST, it increases the explained variability to 44%. The study confirmed flood predictability from the estimated relationship between the flow and two indices.

Degefu and Bewket (2017) studied the streamflow indices teleconnection with SSTs in the Omo-Ghibe River basin, Ethiopia. They found that the stream flow in summer and variability of high-flow events or flood magnitude can be traced to ENSO/Niño 3.4. The study concluded that warm and cold ENSO events are associated with deficit and excess in summer rainfall and discharge magnitude over Ethiopia. Similarly, according to Mamo et al. (2019), the historical flood events in Ethiopia are closely related to periods of significantly abundant precipitation during the La Niña events. Iqbal and Hassan (2018) examined the influence of the ENSO indicator (Niño 3.4) and IOD modes (SST Dipole index) on flood occurrence in Pakistan (1950-2011). They pointed out that a high percentage of floods occurred

in Pakistan after 1970 during El Niño, non-ENSO, and positive, negative, and non-Indian Ocean Dipole. Moreover, the influence of ENSO (El Niño and non-ENSO phases) with or individual IOD on floods in Pakistan was dominant.

Yan et al. (2020) demonstrated the impact of ENSO- Niño 3.4 on basin-scale floods across several large river basins worldwide (e.g., the Amazon River, Nile River, Murray-Darling basin, Mekong River, Yangtze and Pearl River basins, rivers in the Southwestern United States and northern Eurasia). They indicated that the simultaneous correlation between flood indices such as flood frequency and flood duration during peak flood months in many flood-prone basins was significant. Also, the ENSO-derived precipitation variation may cause floods in many river basins, and the ENSO effect on floods becomes weaker where other ocean-atmospheric systems significantly impact floods and precipitations.

Worako et al. (2021) studied the association between the magnitudes of streamflow and ENSO indicators, i.e., SOI, Niño 3.4, and MEI in the Rift Valley Lakes basin. The La Niña and El Niño phases caused positive and negative deviation, respectively, in streamflow, but they were insignificant. High flows in most catchments in the basin in response to La Niña were positive deviations and negative deviations during El Niño oscillations. Another study by Lambe and Kundapura (2023) indicated a weak association between ENSO indices (SOI and Niño 3.4) and extreme hydrometeorological indices in the Bilate River basin.

The literature generally shows a relationship between ENSO and streamflow in many river basins across the globe. The correlation analysis between the streamflow and ENSO indices provides information about the typical impact of ENSO on flood peak events (i.e., the potential driver of extreme hydrological variability or hydrological conditions). Overall, the ENSO indicators alter hydrological regimes in different river basins to varied degrees. Knowledge of local climate conditions and large-scale modes of climate variability and their impact on hydrological extremes is critical for flood mitigation. Few studies have been conducted on how combined local climate and ENSO indices (SOI, Niño 3.4, and MEI) affect the extreme flow. Therefore, a comprehensive study in the face of climate change is

essential for flood management. In addition to the effect of ENSO phases on streamflow variability, it is possibly related to human activities such as land cover change, water abstraction, and other local factors such as topography.

#### **2.4 Impact of changes in land cover and climate on hydrology**

The spatiotemporal pattern of the flood is related to the number of global change variables. Land cover and climate are the two major and often separate factors influencing hydrology. Land cover changes are among the most critical factors affecting the hydrological process, thus flood characteristics over time and space. Agriculture expansion, afforestation, deforestation, expansion of grazing land, and urbanization are some of the man-induced land cover changes that affect hydrology. The change in land cover often causes decreases in soil retention capacity, changes in evapotranspiration, reduced infiltration, surface roughness, and lower water concentration times, which control flow magnitude (e.g., flood events) and inundation.

In larger river basins, modification of long-term river discharge can be caused by interdecadal or multidecadal land cover change and climate variability. Anthropogenic activities are the leading cause of land cover change rather than natural events. Climate variability (primarily refers to the change in precipitation and temperature) in discharge is exacerbated by land cover changes. Quantifying the impact of land cover change and climate variability through scenarios has become important to understanding the prime cause of hydrological change.

Several studies indicated the impact of land use/land cover change on flood. De Roo et al. (2001) studied the effect of changes in land use on hydrological processes in the Meuse and Oder catchments. The study found that land cover change was noticed between 1975 and 1992 in the Meuse catchment, and as a result, hydrologic change was detected. A 0.2% increase in peak flood and a 4.06% increase in flood volume resulted from the modification in land cover. In the absence of significant alterations in precipitation, changes in land cover affect the seasonal and long-term time scales of river flow. Niehoff et al. (2002) showed that the influence of land

cover change on runoff and floods depends on precipitation characteristics and spatial scale. They concluded that the influence of land cover is stronger with high precipitation intensity than with long-time storm events with low precipitation intensity. The extent of high precipitation intensity events restricted to local occurrences is irrelevant for flood generation in the larger river basins. Upstream of the Tocantins River basin, agriculture land use increased dramatically to natural vegetation cover, resulting in an increase in long-term mean discharge by 24% and mean flow increase of high flow season by 28% in the intense land use period. The changes also affected the timing of peak flow which is earlier in the agriculture-dominated land use period (Costa et al. 2003).

Legesse et al. (2003) investigated the hydrological response sensitivity to rainfall, temperature change, and land use change in the scarce data of south-central Ethiopia. The climate input, precipitation, is the most sensitive, resulting in a difference of about 30% in simulated discharge for a 10% decrease in assumed change than the land use change. Changes in land cover/land use (loss of vegetation cover, agriculture expansion, overgrazing, and eucalyptus plantings), and rainfall decline contributed to the reduction in annual streamflow and no change in the extremely high flow during the rainy months in the Blue Nile basin's Chemoga watershed (Bewket and Sterk 2005). The change in flood frequency can be ascribed to the change in land cover scenarios. Brath et al. (2006) noted that an increment in peak flood is sensitive to changes in land use and greater incidence for lower return periods. The study concluded that streamflow sensitivity to land cover strongly depends on the climate and the geomorphological characteristics.

Hydrological effects also result from both land cover change and climate variability. However, the extent of the change that occurred and its influences vary on the hydrological process. In the agricultural-dominated catchment, the shift in shrubland and sparse woodland to medium or higher grassland and the decrease in precipitation and increase in temperature led to a reduction in the runoff, soil water, and evapotranspiration. However, climate variability had a more significant impact on surface hydrology than land cover change, possibly due to the relatively small extent of land cover change (Li et al. 2009). Similarly, individual and coupled

effects of land cover alteration and climate variability increased streamflow in the Johor River Basin, Malaysia. Climate change had a stronger influence on streamflow than land cover change, and these changes contributed to the frequent occurrence of flood events in the basin. In other words, the impact of the increasing precipitation trend on discharge is further exacerbated by changes in land cover. (Tan et al. 2015).

A land cover change alone impact study in the Tekeze dam catchment by Welde and Gebremariam (2017) showed a benefit in increased stream flow on a yearly and seasonal time scale due to the bare land and agricultural expansions. Similarly, an increase in streamflow and surface runoff in the Upper Blue Nile (Woldesenbet et al. 2017), Beressa watershed (Worku et al. 2017), Andassa watershed (Gashaw et al. 2018), were reported mainly to land cover change-agricultural intensifications. In all studies mentioned above, the wet season flow had increased, possibly increasing flooding in the watersheds. Fenta Mekonnen et al. (2018) found that the combined effect was higher on the streamflow (El Diem station, situated Ethiopia–Sudan border) than the individual effect; however, the impact of climate variability (an increase in the intensity and extreme events in precipitation) was significant in the upper Blue Nile basin. Land cover conversion, primarily the extension of cultivated land at the cost of vegetation cover, a nonsignificant increase in long-term precipitation, and a significant increase in temperature, resulted in increased runoff in three watersheds located in the upper Blue Nile basin.

Lee et al. (2018) explored the influence of land cover change on river discharge in South America's Paraná River basin and found that an increased discharge and change in peak flow timing can be explained by the land cover change in the basin over the past several decades, despite a nonsignificant increase in rainfall. Increased river discharge is primarily attributed to agricultural land expansion into the forest, and the combined effect contributed to the change in seasonal discharge. In the Upper Awash basin, Shawul et al. (2019) reported that forest, shrubland, and pasture land conversion predominantly to cultivation and urban significantly increased the surface flow, and the impact of land cover on the subbasin level is more pronounced than the basin level.

Setti et al. (2020) evaluated the relative influence of changes in land cover and climate variability in the Nagavalli river basin in India, which could explain the recent increase in floods. The basin was forest-dominated and under agricultural expansion. They found that precipitation and temperature variability over weighted land cover change was a leading factor contributing to hydrological changes in the basin. Nevertheless, in the land cover change scenario alone, agricultural intensification offsets the impact of rainfall variability, diminishing streamflow.

Mzava et al. (2021) quantified the impact of land cover and climate change on peak flow magnitude in a Dar es Salaam metropolitan Tanzania area across the past (1969-2017) and future (2018-2050) scenarios. In a distinct scenario, climate change has more significant effects on peak flow than changes in land cover, increasing the probability of occurrence by 1.5 times in the past and is expected to decrease by 1.1 times when compared to land cover change alone. Mean peak flow is expected to grow due to the combined effect of climate and land cover change, while peak flow is likely to decrease due to decreased volatility in land cover and climate changes in the future. They concluded that the collective effects of climate and land-cover changes have a far greater impact on peak flow change than any single scenario. A similar outcome by Ahmed et al. (2022) indicated that climate change significantly influenced stream flow in the Yangtze River Source Region, China. In the Dhidhessa River basin in Ethiopia, surface runoff and stream flow increased by land cover variations alone and by climate variability alone, respectively, as reported by Wedajo et al. (2022). Malede et al. (2023) demonstrated the influences of land cover and climate, both separately and together, enhanced surface runoff and peak flow in the Birr River watershed in Ethiopia. They also found that the minimum and maximum daily streamflow of 1-day, 3-day, 7-day, and 30-day increased.

Overall, land cover change and climate variability impact the hydrological components to vary among river basins and subbasin scales; however, individual and combined effects differ. When changes in land cover and climate variability simultaneously occur, the overall influence on hydrological components is amplified. It is observed that climate-driven change in streamflow is greater. Few

studies investigated the relative influence of climate variability and land cover change on extreme flows. However, no studies have evaluated the impact of both combined and separately on peak flow and high-flow derived in the basin.

## **2.5 Flood susceptibility modeling techniques**

Rapidly changing land cover and climate characteristics cause floods to increase, and topography is a key factor in intensifying the severity of the flood and categorizing flood-prone areas. Flooding concerns have recently become more prevalent, necessitating robust modeling to better comprehend the issue and minimize its devastating effects. Identifying the extent of the exposed area is important for proper flood management strategies and land use planning. There are different approaches to flood to determine the extent of flood inundation in the literature. The first, which is simple and can be applied in the data-scarce region, is the application of the DEM-based geomorphic (combination remote sensing and GIS) method and hydrologic and hydrodynamic (hydraulic) modeling. Hydrological models can compute past and forecast stream flow peaks at the watershed outlet or grid-grid flood forecasting, consequently producing the spatial flood. It also serves as observation to support the calibration, validation, and data assimilation for other models, such as hydrodynamic models. Hydrological models lack simulating flood extent, depth, duration, and flow velocity. Hydrodynamic models simulate details of flood dynamics and characteristics and can be directly linked to hydrological models to provide flood mapping, flood forecasting, and scenario analysis (Teng et al. 2017). The subsequent section discusses DEM-based flood susceptibility modeling (Section 2.5.1) and hydrodynamic-based flood hazard modeling (Section 2.7).

### **2.5.1 DEM based approach**

A geomorphic approach is quantitative for evaluating watershed characteristics and drainage networks. Horton (1932, 1945), Strahler (1952, 1964), and Schumm (1956) pioneered the development of numerous measurable descriptive parameters of watershed characteristics. The morphometric analysis can also be carried out by

measuring the basin's linear, areal, and relief parameters to obtain watershed characteristics (Strahler 1964). Also, a quantitative description of the basin geometry involves measuring the linear features (aspects), the gradient of the channel system, and contributing ground slope (Nautiyal 1994; Nag 1998). The parameters are generally derived from field observation and topographic maps, and with recent technological advancements using remote sensing and DEMs (Nag 1998; Moussa 2003; Sreedevi et al. 2005).

Basin drainage characteristics are critical to understanding hydrological processes and underlying factors controlling the hydrological response behaviour in the watershed (Ozdemir and Bird 2009; Altaf et al. 2013) and predicting hydrologic conditions. Drainage basin analysis in relation to the existing climate, tectonic process, lithology, and geomorphology reveals important information on the drainage development, hydro-geomorphic and denudation characteristics (Sreedevi et al. 2005; Das and Pardeshi 2018).

Evaluation of morphometric parameters includes analysis of various drainage parameters such as the ordering of multiple streams, area, drainage length, drainage density, frequency of stream, bifurcation ratio, texture ratio, basin relief, ruggedness number, and time of concentration (Kumar et al. 2000; Ozdemir and Bird 2009) and these parameters play a crucial role in controlling the surface/subsurface hydrology. A set of factors constituted flood conditioning factors such as Stream Power Index (SPI), Sediment Transport Index (STI), Topographic Wetness Index (TWI), Topographic Roughness Index (TRI), and Topographic Position Index (TPI) are attributes of flood and effective for flood susceptibility modeling. A set of network and basin parameters captures each characteristic. Remote sensing technology coupled with hydrological and geomorphological parameters and GIS tools provide a good platform for quickly manipulating and analyzing the data to determine potential flood areas more efficiently (Youssef et al. 2011).

In the earlier studies, geo-morphometric analysis was used for the prediction of peak floods, erosion rates, and sediment yield (Gardiner 1990), groundwater potential zone delineation (Nag 1998; Sreedevi et al. 2005), flash flood level at sub-

watershed within the watershed (Youssef et al. 2011), flash flood potential evaluation under the heavy rainfall and predict the behaviour of the basin, and potential flood hazard to downstream (Perucca and Angilieri 2011; Angillieri 2012; Esper Angillieri and Perucca 2014), hydrological behaviour of sub-watersheds (e.g., prone to flooding) (Altaf et al. 2013), basin characterization (Magesh and Chandrasekar 2014; Singh et al. 2019), flood vulnerability (Meraj et al. 2015), flood susceptibility mapping (Mahmood and Rahman 2019), flood hazard mapping, flood susceptibility assessment and mapping using flood potential index (Kanani-Sadat et al. 2019; Khosravi et al. 2019; Popa et al. 2019; Tehrany et al. 2019; Chowdhuri et al. 2020; Sarkar and Mondal 2020; Ullah and Zhang 2020), and watershed prioritizing with respect to flash flood (Obeidat et al. 2021) are among.

As a first step, previous studies in Ethiopia, Koriche and Rientjes (2016) used remote sensing products for early flood warning in the Awash River basin. A combination of the standard precipitation index, TWI, and a hydrological model was used to identify the possible spatial sources of runoff in the basin. They concluded that a remote sensing-based hydrological model in ungauged is effective for early flood warning systems. In the Blue Nile River basin, there was an attempt to employ morphometric approaches to identify soil erosion potential areas and delimit potential flood areas. For example, Debelo et al. (2017) prepared a soil erosion potential map for Jema and Dhidhessa sub-watersheds, Kabite and Gessesse (2018) performed the hydrogeomorphological characterization and soil erosion susceptibility in the Dhidhessa watershed using morphometric analysis, Asfaw and Workineh (2019) investigated the association between soil erosion and morphometric parameters for soil and water conservation practice in Ribb and Gumara watershed, and Jothimani et al. (2021) produced flood susceptibility mapping in Megech catchment using morphometric characteristics.

## **2.6 Nonstationary flood frequency model**

When developing hydraulic infrastructure or analyzing flood risk in a specific location, an accurate estimation of the projected peak flows of a river is critical. Such probable flood estimates are typically produced using extreme value statistical

models through peak flow frequency analysis. Flood frequency analysis (FFA) is conventionally based on the assumption of independent and stationary flood characteristics or observations. Climate change, climate variability, land cover change, and water management techniques (water withdrawal, reservoir construction), in particular, have called into doubt the hypothesis of stationary flow in extreme conditions. Changing flood characteristics caused by climate change necessitate more accurate assessments of the probabilities of rare flood events.

The presence of trends and changes in hydrological extremes renders the assumptions in flood frequency analysis (FFA) invalid, e.g., stationary in annual peak flood series (Milly et al. 2008), suggesting that traditional FFA methods for design quantile estimation need to be revisited by allowing parameter of the flood frequency distribution time-varying (time-dependent moment) (Strupczewski et al. 2001; Khaliq et al. 2006). The evidence of nonstationary hydrological observation significantly affects the result of flood estimation, future probabilities of occurrences of rare extreme events, and the usefulness of the concept of the return period becomes questionable (Khaliq et al. 2006).

In the nonstationary framework, the probability distribution parameters are modeled as a function of covariates. The covariates are external forces that represent the hydrological process and better explain the flood variability over time. Different covariates are used as functions: time, rainfall, temperature, and climate indices. However, climate and human activities are the fundamental drivers of hydrological variability. Covariates may be selected based on a clear link with a change in the flood regime or significant governance of the flood regime. The relationship between flood occurrence and external forces (covariates) provides a robust basis for using covariates (López and Francés 2013; Machado et al. 2015). Many researchers have studied flood frequency using the nonstationary approach incorporating external forces (covariates) to vary linearly or nonlinearly depending on the distributional parameters. The nonstationary frequency analysis method has recently become an alternative to stationary-based frequency analysis.

López and Francés (2013) applied a nonstationary model to annual maximum flood records in Spanish rivers, in which the selected distribution parameters were designed as time-dependent, climate indices and human activities (reservoir indices), and the covariates as explanatory. The flood quantile estimates under nonstationary to longer return periods were higher than flood estimates under stationary conditions. Machado et al. (2015) also employed the possibility of incorporating covariates such as climate indices and reservoir indices in statistical distribution parameters for the selected probability distribution. They reported a better description of temporal variability in historical flood regimes (annual maximum flood series).

Extreme precipitation indices such as the 99th rainfall percentile for each year in the parameter is advantageous in explaining floodwater variability, as demonstrated by Prosdocimi et al. (2014). In the nonstationary model, Šraj et al. (2016) considered the parameter as a function of time and annual precipitation. The inclusion of annual precipitation in the parameter enhanced the goodness of fit to the observed annual maximum discharge. They also proved that stationary-based flood quantile estimates are underestimated relative to nonstationary-based estimates, and they suggested that nonstationary is one alternative to consider when calculating design flood. In a similar study, Šraj and Bezak (2020) recently proved that the precipitation-informed model gave a better fit than the stationary and time-dependent model and showed a difference in flood design estimates.

Flood design estimates provide flood risk information through flood hazard maps, and flood quantiles of different return periods are input for flood hazard management. Few studies conducted nonstationary-based flood quantiles estimates for flood risk assessment, and the failure risk flood control is higher under nonstationary compared to stationary assumption (Gu et al. 2017). Binh et al. (2019) used nonstationary assumptions when developing a flood hazard map for Ho Chi Minh City, Vietnam, and the floodplain inundation area was more extensive when nonstationary assumptions were used. It was noted that different covariates would result in different flood quantile estimates. Therefore, to achieve greater accuracy in flood hazard assessment and consequent risk, the best-fit models and covariates

that explain the data are crucial for improving the estimates of the probability of rare floods.

## **2.7 Flood hazard map modeling**

Flood hazard maps are a prerequisite for flood management plans as the maps represent spatial distributions of flood hazards with significant potential for flooding river basins (Di Baldassarre et al. 2010; Bellos 2012). Flood hazard maps illustrate inundation extent with maximum depth and velocity maps of probable rare floods, and the hazard can be presented as a combination of or the product of depth and velocity (Smith et al. 2014). A hazard map can also be prepared using flood duration (Mani et al. 2014).

Due to the increased socioeconomic significance of flood studies, there has been a widespread interest in understanding, predicting, assessing, and quantifying floods and their impacts. This has led to the development of flood inundation modeling, for example, in flood risk mapping (Apel et al. 2006). The use of physically based models, such as the hydrodynamic modeling approach, has received considerable attention to map floodplains due to the development of robust numerical methods, computer processes, and topographic data. Hydrodynamic models are mathematical models designed to model fluid and typically require computational solving. These models simulate water flow by solving equations derived from physical laws. The models are classified as 1D, 2D, and 3D according to their spatial representation of floodplain flow. The numerical models 1D or 2D are based on numerical methods, i.e., finite difference, finite element, and finite volume methods (Teng et al. 2017).

1D is the simplest representation of floodplain flow through 1D equations. The model is computationally efficient, easy to run, and needs fewer input data. A 1D hydrodynamic model can simulate the averaged velocity of a floodplain cross section and floodwater depth. However, the model is not constrained to simulate lateral flood flow as floodplains are widespread in different directions, the topography is discretized through cross-sections rather than a continuous surface, and there are subjective cross-sectional and orientation values. The 2D

hydrodynamic models are the most widely applied in flood hazard mapping. The model accurately estimates depths and velocities across a surface area by a discretized grid (structured, unstructured, and flexible mesh) representing the topography. However, the model is computationally intensive. Recent developments in coupling 1D-2D hydrodynamic models maximize the advantages of 1D and 2D modeling methodologies (Teng et al. 2017).

Several well-known hydrodynamic models are used for flood hazard mapping, given that they are accessible to global users, commercial, open sources, and research (Teng et al. 2017; Mudashiru et al. 2021). According to a recent review of flood hazard mapping methods by Mudashiru et al. (2021), hydrodynamics models (open sources) are capable of river modeling, flood inundation modeling, urban drainage modeling, flood hazard modeling, water quality modeling, sediment transport modeling, flood forecasting, 1D and 2D steady and unsteady flow computations, overland tidal, tsunami, dam break analysis, complex flow simulation (3D), and others. The Hydrologic Engineering Centre-River Analysis System (HEC-RAS), developed by the US Army Corps of Engineers, is one of the most well-known, studied, and used flood mapping in scientific literature and practice. The model performs fully 1D, 2D, and integrated 1D and 2D simulations (Costabile et al. 2020). Several studies used the HEC-RAS model to assess flood hazards by developing a flood hazard map: for instance, Bangladesh (Masood and Takeuchi 2012), Slovakia (Vojtek and Vojteková 2016), India (Rangari et al. 2019; Pandya et al. 2021) and in different river basins of Ethiopia (Getahun and Gebre 2015; Robi et al. 2019; Melkamu et al. 2022; Namara et al. 2022; Tamiru and Wagari 2022).

Overall, in the literature, a combination of flood susceptibility modeling using morphometrics to identify the susceptible subbasin and locating flood hotspots using topographic factors is rare. Few studies (Binh et al. 2019) in the literature showed a nonstationary-based flood frequency and analysis and used it as input to the hydrodynamic model for flood hazard assessment. No studies have been conducted in the Ethiopia River basin based on nonstationary flood modeling and flood hazard assessment.

## **CHAPTER 3**

### **MATERIALS AND METHODOLOGY**

#### **3.1 Introduction**

This chapter describes the study area, including the basin characteristics, climate, physiography, soil, data sets, model or tools, and overall methodology.

##### **3.1.1 Study area description**

###### **3.1.1.1 Upper Awash river basin**

The Awash basin is Ethiopia's fourth largest river basin, covering 110,000 km<sup>2</sup>. The basin is bounded between 7°53'47" to 12°07'20" N latitude and 37°56'23" to 42°57'21" E longitude, and the river extends from central to eastern Ethiopia to Lake Abbe on the Djibouti border. The Awash River Basin has been divided into the Upper Basin, Middle Basin, and Lower Basin based on several interrelated factors such as location, altitude, climate, topography, agricultural development, inhabitants, administrative boundaries, etc.

The Awash River originates in the highlands of Ethiopia near Ginchi town at an elevation of around 3000 m above sea level (m asl) in the west. It flows through high plateaux to the northeastward. The main tributaries are Berga, Holeta, Teji, Akaki, and Mojo Rivers. Climate variability characterizes the basin, resulting in periodic floods and droughts. The basin's suitable conditions for water supply, hydropower, irrigation, and strategic geographic region made it a hotspot for urbanization and the development of industrial and agricultural activities.

Along with the region's urbanization, water supply, large irrigation projects, and hydroelectric dams are dominant developmental activities in the basin. Rapid population growth and urbanization have significantly impacted the land use system. The upper regions are under significant pressure compared to other lowlands due to climate conditions, soil fertility, and agricultural suitability.

The Upper Awash River basin (UARB) is located between 8°1' to 9°4' latitude and 37°58' to 39°4' longitude. The basin was defined using the Koka Dam discharge outlet, with a drainage area of 11,450 km<sup>2</sup> and an elevation between 1569 and 3576 m asl. Awash River is named after the confluence of the Holeta, Berga, and Ginchi Rivers. The UARB basin plays a crucial role in water supply, hydropower generation, and irrigation.

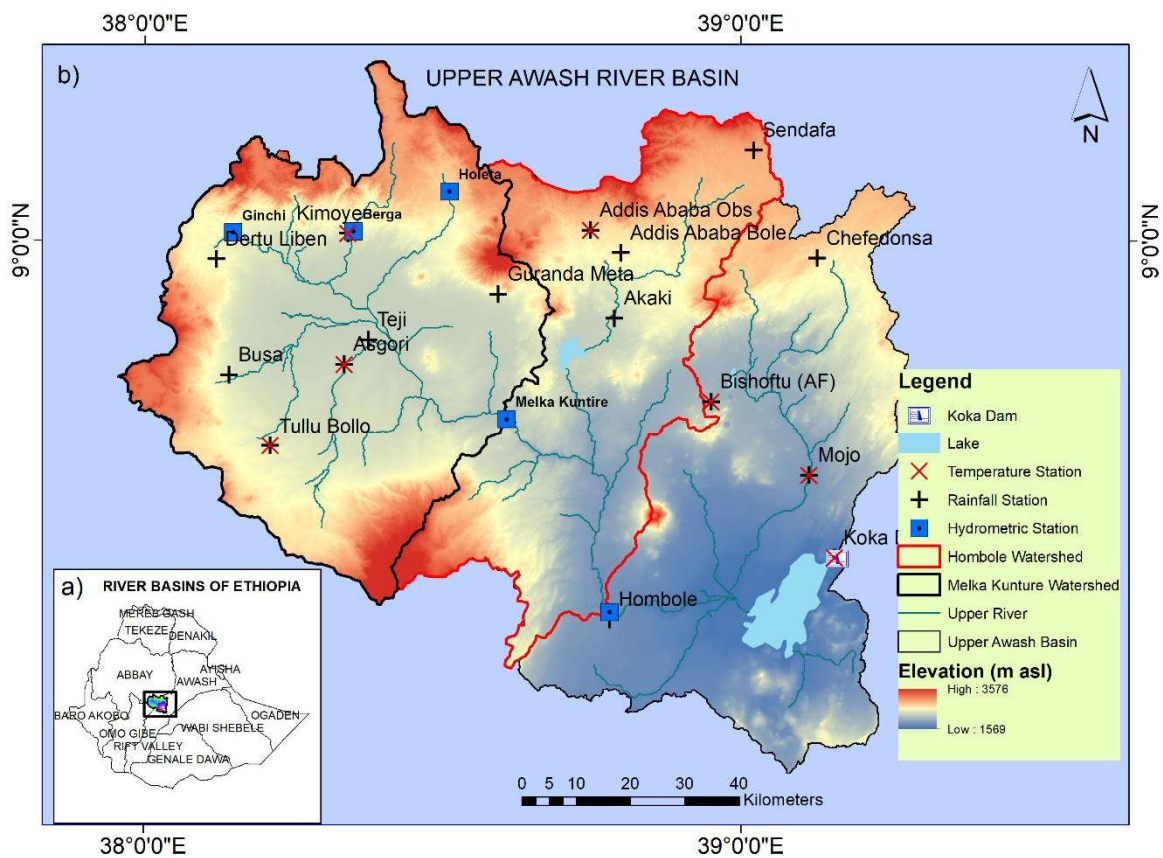


**Figure 3.1** Study area, including its river networks, hydro-meteorological stations, watershed, river network, and elevation

The climate condition in the UARB is a humid subtropical highland. Three seasonal periods are known in Ethiopia: summer or *Kiremt* (June, July, August, and September), wet season; winter or *Bega* (October, November, December, and January), dry season; and spring or *Belg* (February, March, April, and May), short rainy season. During the wet seasons, rainfall is higher in the Upper basin, making the low-lying (plain) area more prone to flooding. The mean annual area precipitation is about 974 mm from 1985 to 2015. The upper part of the basin

receives an average of more than 1000mm. Precipitation from June to September accounts for 74% of total annual rainfall, and the distribution is changing in highland areas. The average maximum and minimum temperatures over the basin are 26°C and 11°C, respectively.

UARB covers eight primary land cover classes: cropland, grassland, shrubland, forest, built-up area, degraded land, wetland, and water bodies. The urban development stretches along the main roads leading from Addis Ababa, the capital city of Ethiopia. However, cropland predominantly covered the basin, with urban and forest areas in the upper and lower portions, including large water reservoirs.

The highland area includes high plateaux, high to mountainous relief hills, dissected plateaux, and hills plain. The peripheral section comprises a series of moderate to high-relief hills and severely dissected side slopes and plateaus. The central and northeastern of the basin contain moderate to low relief hills with patches of sand and silt deposit zones. The geomorphology of the basin is favorable for flood genesis upland and peripheral section and accumulation in the center and lowland areas.

The Eutric vertisols is the dominant soil type in the upland of UARB, followed by Vertic cambisols, Humic nitosols, and Chromic luvisols. The physical properties of individual soil vary in terms of hydraulic conductivity, Texture, and soil moisture content. According to the geological survey of Ethiopia, the geological features are characterized by quaternary and tertiary volcanic (upper highland). The main geological structure or lithology consists of lineament, fault, rift, and major fault.

### **3.2 Data sets**

In this study, several spatial and temporal data such as observed hydroclimatic data, remote sensing data such as DEM, multitemporal Landsat images, and soil data are essential to achieve objectives. The daily temperature (maximum and minimum) of eight stations, daily precipitation recorded at 16 gauging stations, solar radiation, wind speed, and relative humidity are used, as shown in Figure 3.1, and are essential for modeling the basin hydrology. Representative daily streamflow data at two

hydrometric stations, mainly along the main Awash River, Melka Kunture at the upper and Hombole lower reach station, and three tributary stations, Holeta, Berga and Ginchi stations, were selected (Figure 3.1).

Melka Kunture and Hombole are the two main stations on the main Awash River. The Hombole station controls 7432 km<sup>2</sup> of the basin's total area, accounting for 65 % of the total area, and the Melka Kunture station owns more than 38% of the entire basin. The average annual discharge at the Hombole and Melka Kunture outlets is 43 m<sup>3</sup>/s and 29 m<sup>3</sup>/s during 1985-2015, respectively. Table 3.1 presents the types of data sets, data period, resolution, and sources of the data used for the study.

**Table 3.1** Data type used in this study, periods or resolutions, and source description

Data	Period/Resolution	Sources
Climate	1985-2015 (Daily)	Ethiopian Meteorology Agency
Discharge	1985-2015 (Daily)	Ethiopian Ministry of Water and Energy
DEM	30m (2000)	<a href="https://earthexplorer.usgs.gov/">https://earthexplorer.usgs.gov/</a>
Soil map	1:5,000,000 (2007)	Food and Agricultural Organization
Landsat 5 TM	1987 (30m)	Google Earth Engine
Landsat 7 ETM+	2001 (30m)	Google Earth Engine
ENSO indicators		
SOI	1985-2015	
Niño 3.4	(Annually and	<a href="https://ncei.noaa.gov/access/monitoring/enso/">https://ncei.noaa.gov/access/monitoring/enso/</a>
MEI	Monthly)	<a href="https://psl.noaa.gov/enso/mei/">https://psl.noaa.gov/enso/mei/</a>

### 3.3 Methods and model/tool used

#### 3.3.1 Methodology

The overall methodology of the study is shown in Figure. 3.2

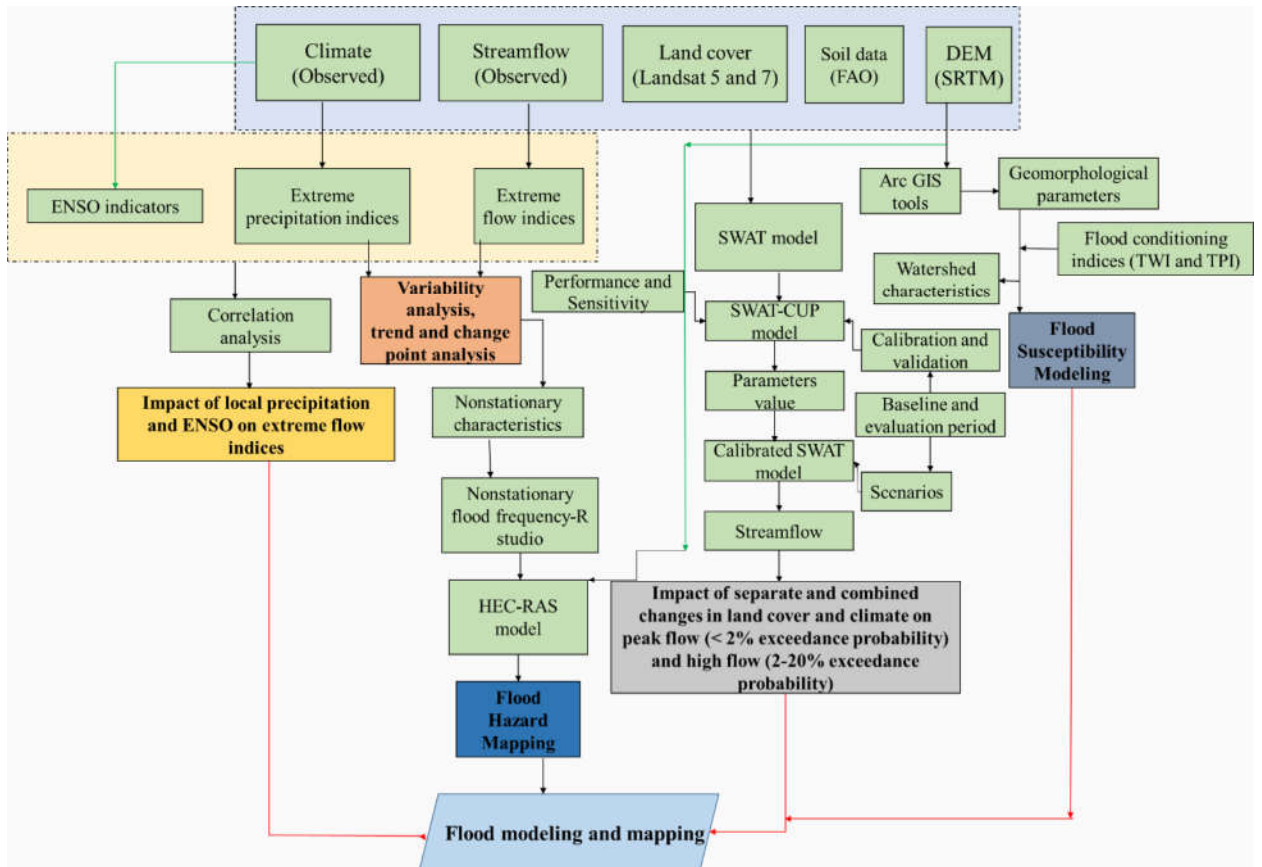


**Figure 3.2** Flowchart illustrating the overall methodology of the study

### 3.3.2 Details of tools used

The study used tools, platforms, software, and packages for image analysis, land cover classifications, hydroclimatic variability detection, and flood modeling. Table 3.2 presents a detailed list of tools used in this study.

**Table 3.2** Tools/platform used in this study

Tools/Platform	Purpose
Google Earth Engine (GEE)	Land cover classification (1987 and 2001 using the random forest algorithm)
Arc GIS 10.3	Visualize and analyze geospatial data

**Table 3.2** (Cont...)

Tools/Platform	Purpose
Soil and Water Assessment Tool (SWAT 2012)	Simulating stream flow and quantification of the contribution of land cover change and climate variability on peak (< 2% exceedance probability) and high flows (2-20% exceedance probability)
SWAT Calibration Uncertainty Program (SWAT-CUP 2012)	Sensitivity, calibration, validation, and uncertainty analysis
R studio (version 4.2.1)	Statistical analysis, for example, RClimDex for climate data analysis, “modifiedmk” and “trend” for trend test and change point detection, “cor.test” for Pearson’s and Spearman’s correlation test, “extRemes” for estimating distributional parameters and performance criteria, etc.
Hydrological Engineering Centre - River Analysis System (HEC-RAS 6.2)	River flow modeling and flood mapping

The study begins with the first objective investigating extreme hydroclimatic variability and the impact of local and global climate system anomalies on extreme flow.

## **CHAPTER 4**

### **EXTREME HYDROCLIMATIC VARIABILITY AND IMPACT OF LOCAL AND GLOBAL CLIMATE SYSTEM ANOMALIES ON EXTREME FLOW**

#### **4.1 Introduction**

Extreme hydroclimatic variability is the primary concern for flood management in the river basins. Chapter four investigates the spatiotemporal variation in extreme hydroclimatic variability and identifies the cause for extreme flow variability, mainly at two hydrological stations, Melka Kunture and Hombole. This study focuses on extreme climate indices from ETCCDI, extreme flow indices, and large-scale ocean-atmospheric indices to identify the variability (anomalies, trend, and change point) and underlying cause of a change in extreme hydrological indices.

#### **4.2 Extreme hydroclimatic variability and its cause**

Climate variability causes extreme climate events such as high-temperature events, extreme precipitation, floods, and droughts (van der Wiel and Bintanja 2021). It is also understood that the hydrological cycle components are influenced by climate variability and land cover change (Legesse et al. 2003, 2010; Bao et al. 2019; Liu et al. 2020). In a warmer environment, the effects of climate change on hydrology are increasingly severe and extensive (Donnelly et al. 2017), which drives natural and societal concerns.

Hydroclimatic variability is the primary concern for water resources management in the Awash River basin (Bekele et al. 2017; Taye et al. 2018, 2021; Daba and You 2020). Several studies have been carried out in the different river and lake basins of Ethiopia, focusing on hydroclimatic trends and variability (Tekleab et al. 2013; Asfaw et al. 2018; Belihu et al. 2018; Jaweso et al. 2019; Mekonen and Berlie 2020; Anose et al. 2021; Orke and Li 2021; Lambe and Kundapura 2023), resulting in a decreasing or no trend in rainfall and an increasing trend in temperature. Recent

trend studies (Gedefaw et al. 2018; Tadese et al. 2019; Daba et al. 2020) concluded a change in hydroclimatic variables (annual, seasonal, and monthly). The spatiotemporal variability of extreme precipitation in the Upper Awash River basin was modest, but the maximum temperature increased significantly (Shawul and Chakma 2020).

Large-scale oceanic-atmospheric circulation patterns such as El Niño and the Southern Oscillation (ENSO) account for interannual climate anomalies worldwide (Ward et al. 2014b) and strongly influence flood occurrence in many parts of the world (Dilley and Heyman 1995; Chiew and McMahon 2002; Ward et al. 2014b; Emerton et al. 2017; Guan et al. 2022). ENSO indices influenced hydrological regimes in various river basins of Ethiopia with varying degrees of impact (Abteu et al. 2009; Degefu and Bewket 2017; Worako et al. 2021; Lambe and Kundapura 2023).

Knowledge of local climate conditions and large-scale modes of climate variability and their impact on hydrological extremes is critical for flood mitigation. The underlying causes of the significant change in the hydrological index are crucial in comprehending the growing concern about the cumulative effect of climate change and human activity. Therefore, understanding extreme hydroclimatic variability in the face of climate change and its potential driver on extreme hydrological variability is essential for water resources management, including flood management.

### **4.3 Data and methodology**

#### **4.3.1 Data**

The study used selected daily rainfall data from sixteen and eight maximum/minimum air temperature stations. Daily streamflow data from 1985 to 2015 of two representative hydrological stations, Melka Kunture and Hombole, were chosen at the head and lower reach of the Awash River. Furthermore, coupled ocean-atmospheric ENSO indicators, such as Southern Oscillation Index (SOI),

Niño 3.4 Sea Surface Temperature (SST), bi-monthly Multivariate El Niño/Southern Oscillation Index (MEI) anomalies were used.

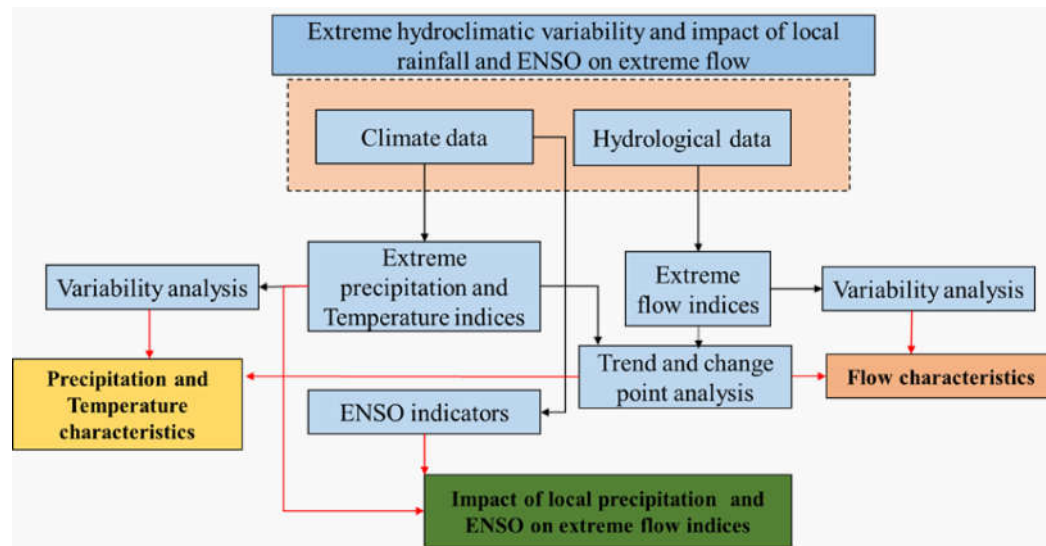


**Figure 4.1** Flow chart of the study for evaluating extreme hydroclimatic variability and impact of local precipitation and ENSO on extreme flow

### 4.3.2 Methodology

The general schematic flowchart of the study is depicted in Figure 4.1. This study uses extreme climate indices from standard indices provided by the Expert Team on Climate Change Detection and Indices (ETCCDI), which cover a broad spectrum of rainfall and temperature extremes. Extreme hydrological indices, such as annual maximum flow (Qmax1) and daily stream flow greater than or equal to the 99th (Q99p), 95th (Q95p), and 90th (Q90p) percentile, are used in this study to provide a clear understanding of basin response for water resource management. The chosen indices explain the persistence, change in total precipitation, strength or intensity of extreme rainfall, and floodwater variability. ENSO indicators, such as the Southern Oscillation Index (SOI), Niño 3.4 Sea Surface Temperatures (SST), and the bi-monthly Multivariate El Niño /Southern Oscillation Index (MEI), are used to identify potential physical drivers of hydrological variability. Table 4.1 summarizes extreme climate indices extracted from daily climate and hydrological data analyzed in this study.

The RClimDex package in R software, which can be downloaded for free from the ETCCDI website (<http://etccdi.pacificclimate.org/software.shtml>), is used to calculate the extreme indices. The basin precipitation was estimated based on the areal average across the basin weighted using Thiessen polygons created based on gauging stations. The maximum and minimum temperatures for the basin were calculated using the average of the eight stations. The inverse distance weighted (IDW) method was used in ArcGIS software, version 10.3, to spatially interpolate climate indicators for the basin.

### 4.3.3 Variability analysis

This study used the coefficient of variation (CV) and standardized anomaly index (SAI) to investigate variability in extreme hydroclimatic conditions. The CV statistics is the ratio of the standard deviation to the mean. CV has been applied in long-term hydroclimatic variability studies (Chen et al. 2014; Kisaka et al. 2015). The statistics CV values were defined as less ( $< 0.2$ ), moderate ( $0.2 - 0.3$ ), and high variability ( $> 0.3$ ) (Asfaw et al. 2018; Tadesse et al. 2019). SAI detects positive and negative anomalies in hydroclimatic data, where positive and negative are associated with wet and dry conditions, respectively (Orke and Li 2021). It is defined as the difference between the annual and long-term averages of hydroclimatic data divided by the data's long-term standard deviation and computed as:

$$SAI = \left( \frac{x - \mu}{\sigma} \right) \quad (4.1)$$

where  $x$  = annual hydroclimatic data,  $\mu$  = long-term average of observed data, and  $\sigma$  = standard deviation of data. The anomaly based on SAI is extreme wet ( $> 2$ ), very wet ( $1.5 - 2$ ), moderate wet ( $1.0 - 1.5$ ), near normal ( $-1.0$  to  $1.0$ ), moderate dry ( $-1.5$  to  $-1.0$ ), severe dry ( $-2.0$  to  $-1.5$ ) and extremely dry ( $-2.0$  and less).

**Table 4.1** Extreme climatic and streamflow indices and description

Indices	ID (Unit)	Description
Maximum daily temperature	Tmax1 (°C)	Annual maximum 1-day temperature
Minimum daily temperature	Tmin1 (°C)	Annual minimum 1-day temperature
Annual total precipitation	PRCPTOT (mm)	Annual total precipitation from wet days $\geq 1$ mm
Annual maximum precipitation	Rmax1 (mm)	Annual maximum 1-day precipitation depth
Extremely wet days	R99p (mm)	Annual total precipitation from wet days $\geq 99$ percentile
Very wet days	R95p (mm)	Annual total precipitation from wet days $\geq 95$ percentile
Maximum daily flow	Qmax1 ( $\text{m}^3 \text{s}^{-1}$ )	Annual maximum 1-day flow
Extremely high flow days	Q99p ( $\text{m}^3 \text{s}^{-1}$ )	Annual total flow from days $\geq 99$ percentile
Very high flow days	Q95p ( $\text{m}^3 \text{s}^{-1}$ )	Annual total flow from days $\geq 95$ percentile
High flow days	Q90p ( $\text{m}^3 \text{s}^{-1}$ )	Annual total flow from days $\geq 90$ percentile

The variability analysis of extreme precipitation and extreme flow is the main emphasis of this study.

#### 4.3.4 Trend analysis

##### 4.3.4.1 Modified Mann-Kendall trend test (MMK)

The robust non-parametric Mann-Kendall trend test (Mann 1945; Kendall 1975) method detects trends in the hydroclimatic time series. This test, however, requires the serial independence of data time series, which is rare in hydroclimatic data. The presence of serial correlation leads to rejecting the null hypothesis (no trend) and accepting the significant trend (Von Storch and Navarra 1995). Hamed and Rao (1998) modified the original Mann-Kendall test method to avoid the effect of serial correlation in the data series. Thus, for this study, the robust modified Mann-Kendall (MMK) trend test was used to capture the trend in hydroclimatic variables at a 5% significant level. The methods were most commonly applied to hydrological and climatological data (Kundzewicz and Robson 2004).

##### 4.3.4.2 Sen's slope estimator (SSE)

If a trend exists, the magnitude of the linear trend slope in time series is estimated using Sen's slope, a non-parametric method (Theil 1950; Sen 1968). The monotonic trend slope was calculated using:

$$\alpha_i = \text{Median} \frac{X_i - X_j}{i - j}, \forall i \geq j \quad (4.2)$$

$X_i$  and  $X_j$  are the data observation corresponding to time  $i$  and  $j$ . The median of  $N = n(n - 1)/2$  for  $\alpha_i$  is Sen's estimator of the slope where  $n$  is the number of periods. The  $\alpha_i$  is tested against the two-sided test at a 5% significant level, and the actual slope is estimated by a non-parametric test. The sign of the  $\alpha_i$  obtains increasing if  $\alpha_i$  is positive and decreasing if  $\alpha_i$  is negative.

### 4.3.5 Change-point analysis

The Pettitt test (Pettitt 1979) is a non-parametric and rank-based test used to detect an abrupt change in the time series. This test is assumed to be distribution-free and not sensitive to outliers and skewed distribution. This method was used to determine when an abrupt shift occurred in the hydrological and climatological series (Kundzewicz and Robson 2004). If the observed sequence  $X_1, X_2, X_3 \dots X_n$  has a change point at time  $t$  such that  $X_1, X_2, X_3 \dots X_t$  has distribution function  $f_1(x)$ , which is different from the distribution function  $f_2(x)$  of the series  $X_{t+1}, X_{t+2}, X_{t+3} \dots, X_{t+n}$ . Then the non-parametric test statistics,

$$K_T = \text{Max} |U_{t,T}|, 1 \leq t \leq T \quad (4.3)$$

Where  $U_{t,T} = \sum_{i=1}^t \sum_{j=i+1}^T \text{sgn}(X_i - X_j)$ ,  $\text{sgn}(x) = 1$  if  $X > 0$ ,  $0$  if  $X = 0$ , and  $-1$  if  $X$

$< 0$ . The confidence level,  $\rho$ , of the sample  $n$  length and its associated  $K$  statistics,

$$\rho = \exp\left(\frac{-K}{n^2 + n^3}\right) \quad (4.4)$$

This study considered the 5 % significance level for conducting the tests. When the  $\rho$ -value is less than the chosen significance level ( $\alpha = 0.05$ ), the null hypothesis is rejected, and there is a change between two parts of the data series. The trend analysis, Sen's slope calculation, and change point identification were all carried out in R software using the “modifiedmk” and “trend” packages.

### 4.3.6 Correlation analysis

Correlation analysis can assist in determining the potential impact of climate indices on hydrology and improve flood forecasts. Extreme local rainfall anomalies and ESNO indicator anomalies were compared with extreme hydrological indices anomalies to determine statistical significance. ESNO indicators, such as the SOI,

Niño 3.4 SST, and MEI, were averaged from June to September between 1985 and 2015. The study area's summer rainy season made these months ideal for selection. The Spearman rank correlation test is a non-parametric correlation test that measures the strength of monotonic associations. The test was employed at a 5% significance level, giving a value between -1.0 and 1.0, with 0 indicating no correlation. This helps to determine whether the altered flood characteristics in the basin are the effect of a large-scale climate anomaly. The Spearman's rank correlation test was used between the streamflow and ENSO indices (Worako et al. 2021).

## **4.4 Result and discussion**

### **4.4.1 Hydroclimatic characteristics**

Figure 4.2 shows the monthly mean areal rainfall over the basin from 1985 to 2015 of 16 rainfall stations and indicates that the basin experienced substantial rainfall during the summer months. July and August receive extreme rainfall, followed by spring's small rainy season. The lowest intensities were observed in November and December during the winter season. Summer, spring, and winter rainfall account for 73.58%, 21.58%, and 4.43% of total annual rainfall. July and August each contributed approximately 34% of total summer rainfall. During the summer, the highland areas in the west, north, and east receive more rainfall (736, 787, and 792 mm, respectively) than the rainfall (658 mm) in the south.

During the study period, the average maximum and minimum temperatures over the basin are 26°C and 11°C, respectively. The mean maximum temperature during the warmest months of spring is around 30°C. The maximum temperatures during the summer and winter were 26.3 and 27.2°C, respectively. Seasonally, the minimum temperature ranges from 6°C in the winter (coldest) to 10 to 11°C in the spring and summer seasons, respectively. The maximum and minimum temperatures are greater on the basin's southern and western sides. The northern side had a lower maximum temperature than the south and western parts.

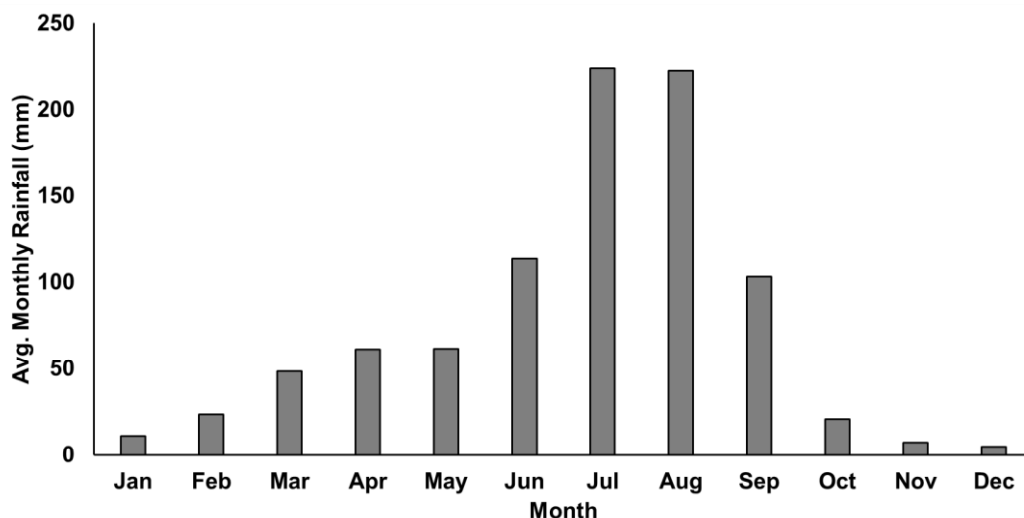


**Figure 4.2** Monthly rainfall distribution for UARB

The lower reach of Hombole had the highest mean annual discharge value in the basin ( $43.66 \text{ m}^3/\text{s}$ ). River discharges are persistently high throughout the summer season. The lower reach of Hombole ( $803.10 \text{ m}^3/\text{s}$ ) and Melka Kunture ( $399 \text{ m}^3/\text{s}$ ) recorded the greatest daily annual peak flow measurements in August. The daily discharge of Awash River at the Hombole and Melka Kunture stations had above zero minimum values. The discharge accumulation significantly increases from Melka Kunture (MK) to Hombole station. Spatially, the lower reach has the most extended duration and highest flow availability range. The temporal flow distribution designates that Hombole stations receive the highest flow annually. More increased average monthly flow was observed in August, while July and September were moderate, and June and October were the lowest mean values.

#### **4.4.2 Variability analysis**

##### **4.4.2.1 Extreme precipitation**

The summarized results of the extreme climate variability analysis are provided in Table 4.2 for different indices (Tmax1, Tmin1, PRCPTOT, Rmax1, R99p, and R95p). The CVs of extreme rainfall indices for the entire basin resulted in less than 20%, thus less variability. Rmax1 and R99p, and PRCPTOT and R95p CVs were comparable. The variability analysis revealed spatial variations in the rainfall

indices (Figure 4.3). Results of high CV were observed in PRCPTOT and R95p, with 12.5% and 37% of stations, respectively.

**Table 4.2** Basin-wise extreme climate indices: statistics, trend, and change point test results

Indices	Statistics		MMK trend test		Pettitt's test		
	Mean (°C, mm)	CV (%)	Z	<i>p</i> value	Sen's Slope (°C/year, mm/year)	<i>p</i> value	Year
Tmax1	30.24	3.28	<b>4.27</b>	0.00	0.08	<b>0.00</b>	1999
Tmin1	5.02	18.03	-1.19	0.23	-0.02	0.07	-
PRCPTOT	947.5	13.03	-0.20	0.83	-0.56	0.99	-
Rmax1	20.23	16.1	-0.14	0.88	-0.02	0.99	-
R99p	116.29	17.67	0.71	0.48	0.26	0.9	-
R95p	308.22	12.25	0.92	0.36	0.86	0.57	-

CV Coefficient of Variation *Bold face* Significant at 0.05 level

The Rmax1 and R99p rainfall indices had the highest proportion of stations with high variability (56%). Rmax1 and R99p had moderate variability in 44% of the stations, while PRCPTOT and R95p had moderate variability in 37.5% and 31.3%, respectively. PRCPTOT had the highest percentage of sites with the least variability (about 50%). Regarding spatial CVs, the southern (Koka station, CV up to 68%) and western (Busa station, CV up to 59%) parts of the basin showed high variability of all rainfall indices analyzed. However, as far as the flood is concerned, the southwest regions of the basin, which experience high annual rainfall, exhibited the greatest variability in extreme indices. A recent study in the Awash River basin found that the variability analysis (CV) of PRCPTOT agrees with previous findings on an annual and summer season scale in a few upstream stations (AA Bole, Bishoftu, Kimoye, Tullu Bollo, and Koka Dam) (Tadese et al. 2019).

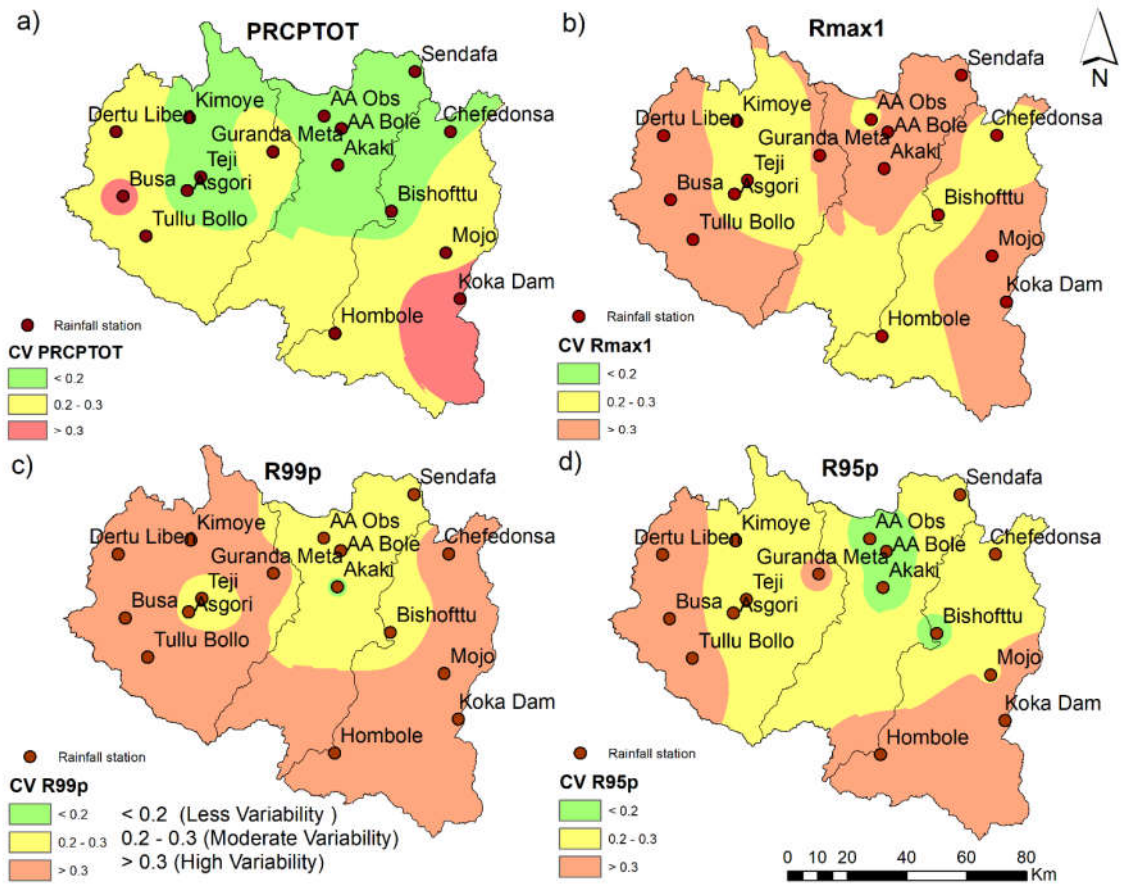


**Figure 4.3** Basin-wise coefficient of variation a) PRCPTOT, b) Rmax1, c) R99p, and d) R95p

It is critical to examine the rainfall anomaly compared to the long-term mean on an annual basis, as this aids in identifying wet years, particularly floods in the region. The 1990s and 2000s were investigated for anomalies that could explain the floods of 1996 and 2006. The anomalies of the extreme rainfall indices are calculated for each, and the results are shown in Figure 4.4. The analyses resulted in weak negative slope anomalies (insignificant) in PRCPTOT and Rmax1, while R99p and R95p showed positive slope anomalies (insignificant) for the entire basin.

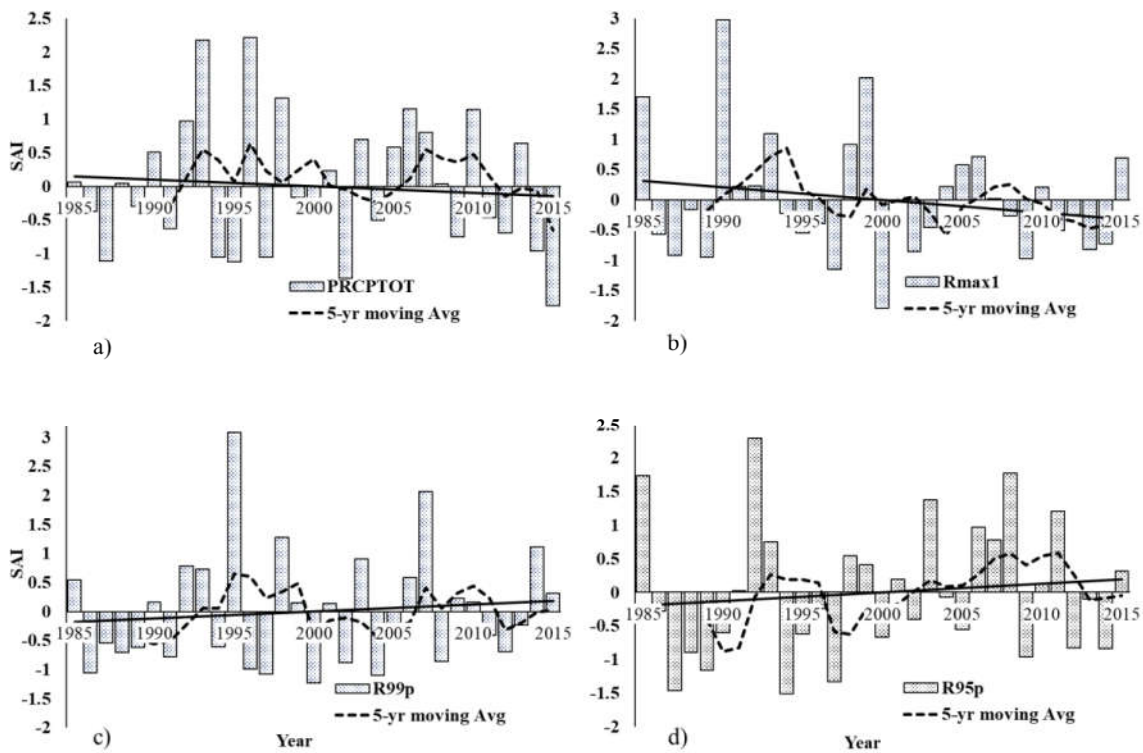


**Figure 4.4** Standardized anomaly index (SAI) for basin extreme precipitation indices a) PRCPTOT, b) Rmax1, c) R99p, and d) R95p. The line represents the slope of linear regression.

In addition, the smoothed anomalies with a five-year moving average revealed a definite trend, and the basin experienced several negative and positive anomalies that were short and continuous. For instance, several positive anomalies (wet conditions) were observed from 1992 to 2000 and 2007 to 2014 in PRCPTOT, 1999 to 2003 and 2005 to 2008 in Rmax1, 1993 to 1999 and 2007 to 2011 in R99p, and 2002 to 2012 in R95p. The early 1990s witnessed the largest positive anomalies of greater than 2.2 in extreme rainfall indices. This suggests that rainfall in the basin increased significantly during this period, indicating extremely wet conditions. In 1986, 1987, 1994, 2002, and 2009, all rainfall indices showed a negative anomaly, a sign of a lack of precipitation or drought. This finding is consistent with the drought that occurred in Ethiopia (Anose et al. 2021). After 2001, the magnitude anomalies with values of less than 1 became noticeable, especially in Rmax1, followed by R99p, R95p, and PRCPTOT, which indicate near normal. The Rmax1

and R95p anomalies revealed that 58% and 55% of the study period were below the long-term mean of Rmax1 and R95p, respectively. PRCPTOT and R99p had negative SAI values for almost half of the duration. The 1996 flow event coincides with a higher regional PRCPTOT anomaly ( $SAI > 2$ ), whereas the 2006 event has positive precipitation indices ( $SAI < 1.0$ ), indicating extremely wet and close to normal conditions, respectively. According to research by Edossa et al. (2010), interannual rainfall variability in the basin led to frequent floods and droughts.

### **PRCPTOT**

About 75% of the rainfall stations with PRCPTOT displayed a declining slope. The 1990s had the highest positive anomalies recorded, with 1996 showing a value greater than two and the early 2010s showing a value of around -1.6. Dertu Liben and Guranda Meta stations had longer positive anomaly years with steep slopes, but negative and positive anomaly levels remained consistent after 2007 and 2005, respectively. This indicates that excess and deficit rainfall occurred persistently during the rainy seasons. Spatially, the western, Akaki, Hombole, and Bishoftu stations experienced high positive anomaly periods in the 1990s, while some of these stations experienced negative anomaly periods in the 2000s. In the 1990s, high negative anomaly periods were also observed at northern, southern, and eastern stations. The total number of negative anomaly periods increased by 10% in the 2000s, up from the 1990s (47%). During the flood events of 1996 and 2006, the majority of the stations experienced moderate to extreme wetness, particularly in the northwest.

### **Rmax1**

Except for a few stations in the southwest (Teji, Tullu Bollo, and Mojo), most stations in the basin showed a negative anomaly in Rmax1. Rmax1 anomalies with values beyond 2 were more prevalent in the 1990s and late 1980s. In the 1990s, the northwestern regions experienced more pronounced positive anomalies. During the 2006 flood event, most stations showed normal to moderate wet conditions. Dertu Liben station had the most extended year above the long-term mean. In 1985-1986

and 2012-2014-2015, the highest negative anomaly exhibited ranged from -1.0 to -1.8. In the 2000s, the negative anomalies nearly increased by 22% from the 1990s. Only a few stations had recently encountered the largest negative anomalies. Notably, most of the station's anomalies had values less than 1.

### **R99p and R95p**

Results showed that ten of sixteen stations' R99p and R95p anomaly values exhibited a negative slope, while six stations showed a positive slope. The slopes in the R95p and R99p indices for the Dertu Liben and Guranda Meta stations were higher than the slopes (steeply declining and rising, respectively) in the other rainfall stations. The 1990s had the highest positive anomalies (up to 3.32). However, the maximum levels of negative anomalies (less than or equal to 2) were generally observed in the years 1985–1986 and 2012–2014–2015, which is a similar anomaly pattern to PRCPTOT and Rmax1. In the 1990s, some western parts (Busa, Kimoye, and Dertu Liben), Bishoftu, and Hombole stations generally experienced more frequent positive anomalous periods. The negative anomalous periods in the 2000s were remarkably high for some western, southern, and northern stations. During the floods of 1996 and 2006, more than 75% of the stations showed positive anomalies ranging from near normal to extreme wet conditions. The northwest region (Busa, Teji, and AA Bole) experienced heavy rains. Overall, there was no discernible shift (a 3% increase in R99p and a 3% decrease in R95p) in the extreme rainfall indices during the anomalous times between the two decades. The R99p underwent long-term positive variation for 16–18 years, while the R95p experienced long-term negative variation for 16–20 years, especially in the southern stations.

#### **4.4.2.2 Extreme Flow**

The results of the variability analysis are presented in Table 4.3, with indices at the scale of Qmax1, Q99p, Q95p, and Q90p for two selected stations. The extreme flow indices variability between the two stations was mostly similar. It is apparent that,

except for the MK station's Q95p, the extreme flows of the selected two main Awash River stations showed high variability. The variability observed in the two stations followed the same pattern of variability as some western parts of extreme rainfall indices. The MK extreme flow indices CVs results are consistent with previous findings on an annual and summer season scale (Tadese et al. 2019). The above discussions were consistent with Billi et al. (2014) report that the annual runoff shows a broader range of variation among rivers in Ethiopia.

**Table 4.3** Results of the Hombole and MK hydrological stations' statistics, trends, and change point tests

Indices	CV (%)	MMK trend test		Pettitt's test		Year
		Z	p value	Sen's slope (m <sup>3</sup> s-1 year-1)	p value	
Hombole station						
Qmax1	35.15	-1.3	0.2	-2.66	0.65	-
Q99p	33.36	-1.2	0.22	-18.94	0.57	-
Q95p	31.33	-1.1	0.26	-41.7	0.68	-
Q90p	30.22	-1	0.34	-59	0.94	-
Melka Kunture station						
Qmax1	38.6	2.84	<b>0.00</b>	6.62	<b>0.01</b>	2005
Q99p	38	4.74	<b>0.00</b>	39.43	<b>0.00</b>	2003
Q95p	32.36	4.1	<b>0.00</b>	77.45	<b>0.01</b>	2003
Q90p	29.05	4	0.09	112.1	<b>0.01</b>	2003

CV Coefficient of Variation *Bold face* Significant at 0.05 level

The basin's main characteristics are the interannual variability in extreme hydrological events. Figure 4.5 shows the extreme flow anomalies of two stations on the main Awash River using SAI. The general anomaly slope for MK station was positive (significant), while it was negative (insignificant) for Hombole downstream station. Each station had high and low inter-annual and decadal flow anomalies. The five-year moving average of extreme flow anomalies shows that

both stations experienced continuous positive anomalies between 2006 and 2015 at MK and 1990 to 2003 at Hombole.

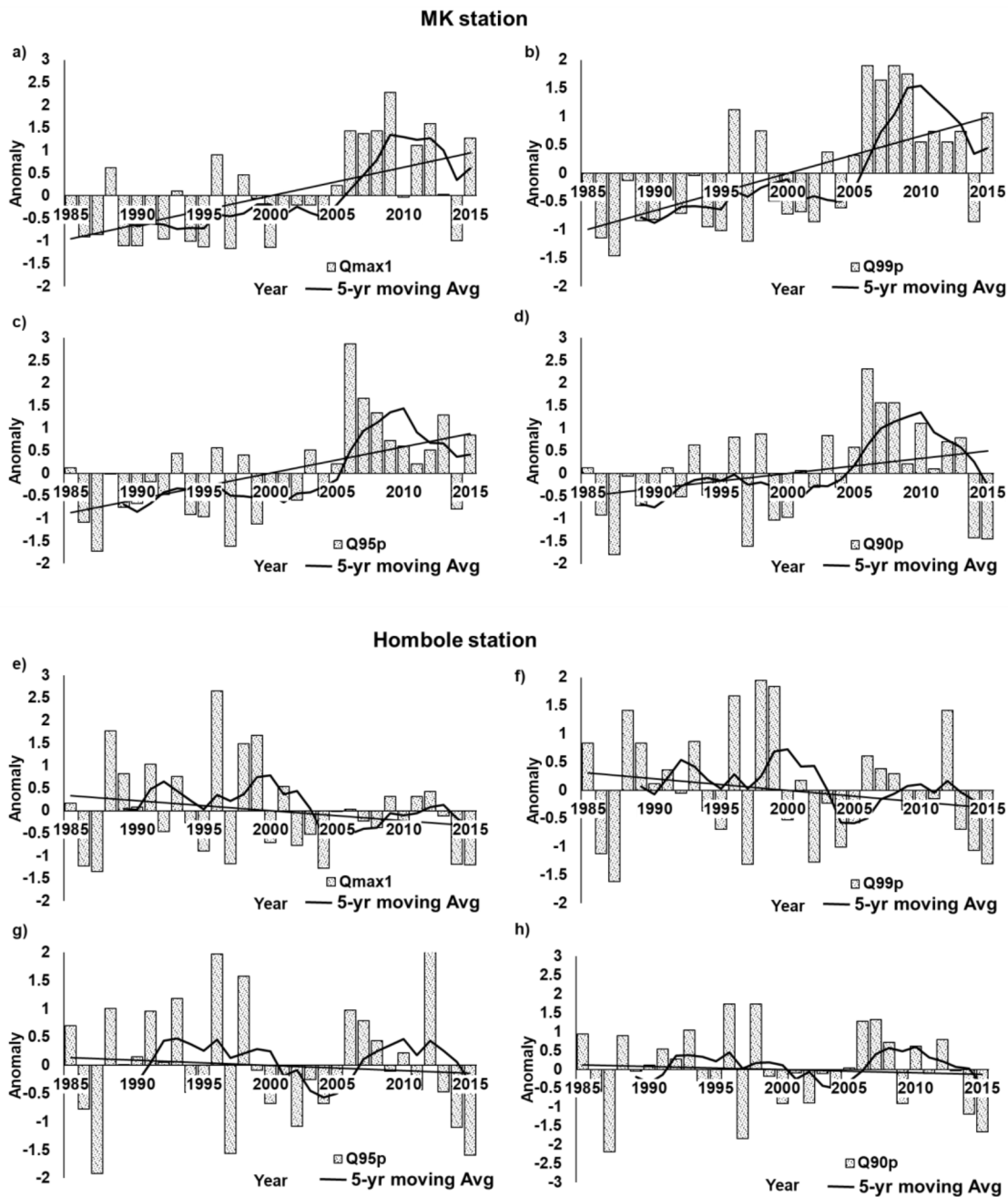


**Figure 4.5** Table 4.4 Standard anomaly index (SAI) of extreme streamflow indices for MK a) Qmax1, b) Q99p, c) Q95p and d) Q90p and Hombole e) Qmax1, f) Q99p, g) Q95p, and h) Q90p. The line represents the slope of linear regression and 5-year moving average (black line)

The most notable anomalies in the MK and Hombole were in 2006 and 1996, respectively, which were above the long-term mean flow indices. The period 1987 was found to have the highest proportion of negative anomalies in these stations. At upper station MK, one of the noteworthy characteristics of hydrological variability is the inter-decadal variability observed in extreme flow. Negative anomalies were persistent from 1985 to 2005, followed by high positive anomalies beginning in 2006. Hombole station experienced high positivity in the 1990s and negative in the 2000s and early 2010s. This pattern is very similar to the anomaly pattern of extreme rainfall indices in the basin (Figure 4.4). The 1996 and 2006 witnessed the greatest flooding in the basin. As previously mentioned, these years are among those with a high positive anomaly in extreme precipitation and flow, suggesting that the excess rainfall experienced in these years may have contributed to flooding in the area. Similarly, the 1990s (1996 and 1998) and 2000s (2006) experienced the most extreme floods in Ethiopia, primarily in the Awash River basin (Mamo et al. 2019).

#### **4.4.3 Spatiotemporal trend analysis**

##### **4.4.3.1 Temperature**

Figure 4.6 shows the basin's spatial pattern and trend of Tmax1 and Tmin1. The Tmax1 and Tmin1 in the basin appear to rise and fall at 0.08 and 0.02°C/year, respectively. Except for the north-south stations (AA Bole and Mojo), most of the stations witnessed a significant increase in maximum temperature ( $p$  value < 0.05). The rate of increase varies between stations and ranges from 0.04 to 0.08°C/year (Table 4.4). The most noticeable increase was 0.1°C per year at the southern Koka dam station, indicating a rapid rate of warming. Most of the stations in the southwest region showed a decreasing trend in Tmin1. The Tmin1 has increased significantly at the northern AA Bole stations at 0.2°C/year. The southern Koka site, Tmin1, indicated a significant decline of 0.14°C/year. Spatially, the magnitudes of Tmax1 and Tmin1 increased by about 0.02 to 0.15°C/year. The increase reflects an increase in evapotranspiration, soil moisture deficit, and frequency of extreme precipitation, all of which affect the hydrological process. Similarly, Shawul and Chakma (2020)

found an upward temperature trend in the basin from 1980 to 2015. A relative change of up to  $0.08^{\circ}\text{C}/\text{year}$  in maximum and minimum temperatures (1982-2014) in the Gidabo catchment, Rift Valley basin, was reported by Belihu et al. (2018).

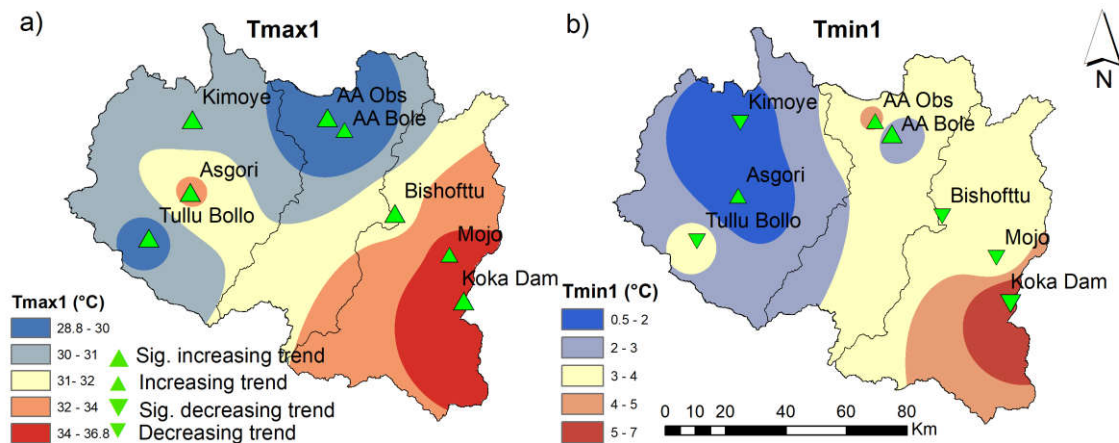


**Figure 4.6** Basin temperature distribution and trend a) Tmax1 and b) Tmin1.

#### 4.4.3.2 Extreme precipitation

The trend analysis results of the R99p and R95p revealed insignificant increasing trends of 0.26 and 0.86 mm/year, respectively, while Rmax1 and PRCPTOT showed weak decreasing trends of less than 1mm (Table 4.2). Figure 4.7 depicts the trend direction, increasing and decreasing, and average extreme rainfall indices distribution using the IDW method. However, regarding spatial distribution, most stations' extreme rainfall in the basin showed a decreasing trend (Figure 4.7) and a similar inter-indices anomaly pattern. The very wet and extremely rainy-day precipitation at northwest stations showed an upward trend. However, significant increases in PRCPTOT, R99p, and R95p were observed in the northern part of the Guranda Meta station by 22, 13, and 18mm/year, respectively, resulting from a shift towards more frequent excess rainfall years after 2000. In the southern station (Mojo, p-value < 0.05, and Koka dam station, p-value > 0.05), extreme indices increased between 6 and 10 mm/year. The increasing trends in Mojo rainfall indices can be attributed to a rainfall deficit in the 1990s and a long wet period in the 2000s and early 2010s. This could suggest a greater risk of flooding in the upper and lower plains of the UARB. On the other hand, the extreme rainfall indices appear to be

decreasing significantly in the western part (Dertu Liben station) with a range of 13 to 16mm/year, followed by Hombole station in the south with a range of 4 to 10mm/year. The late 1980s, excess rainfall, and a shift toward long dry years from 2007(2000) to 2015 are responsible for a significant downward trend. Additionally, trends of up to 3.4 mm/year of increase and 7.5 mm/year of decline were observed (Table 4.5). Shawul and Chakma (2020) and Gebremichael et al. (2022) found an increase in annual extreme 1-day, 5-day, and R99p and R95p indices, primarily in the basin's lower reaches, which complements the trend pattern in this study.

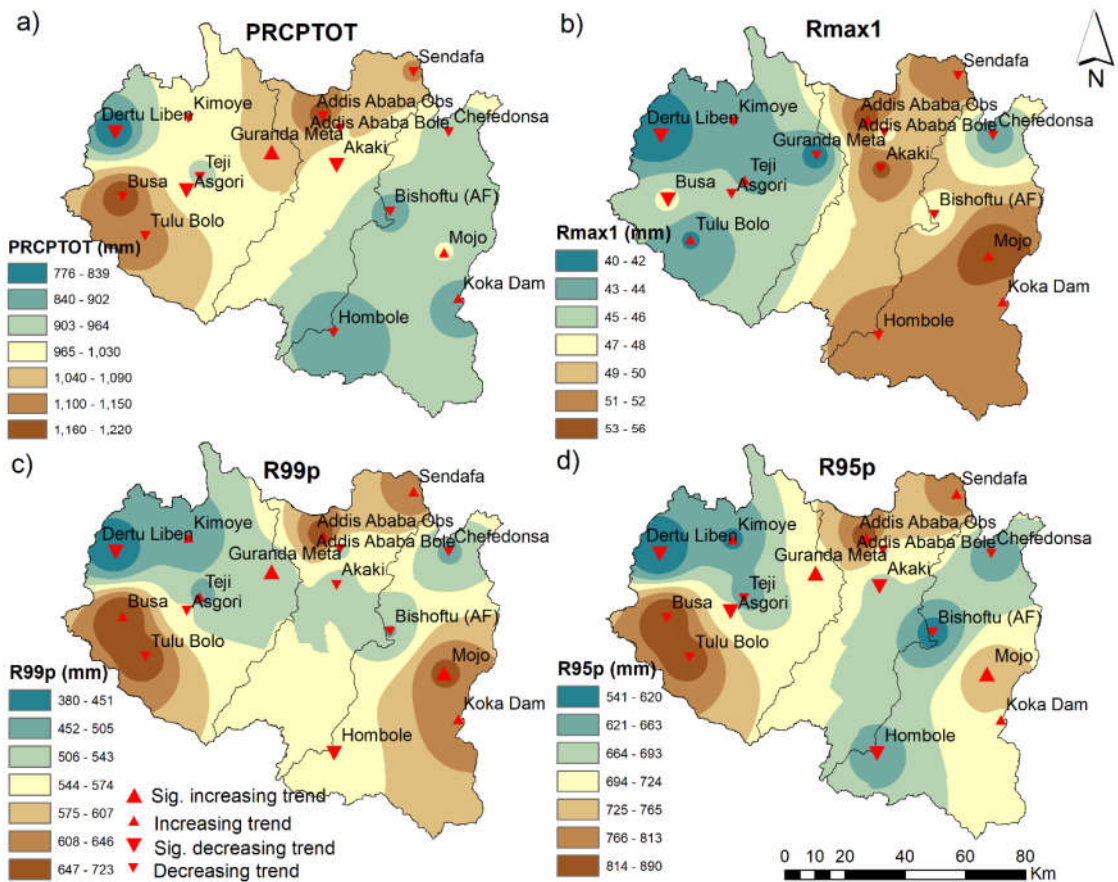


**Figure 4.7** Basin extreme rainfall distribution and trend a) PRCPTOT, b) Rmax1, c) R99p, and d) R95p

Similarly, Lambe and Kundapura (2023) indicated an increase in extreme rainfall in the southwest Bilate River basin, Ethiopia. In addition, Duguma et al. (2021) showed a decreasing trend in the annual precipitation in most stations found in the

UARB during the study period (1991-2015). In line with the current study, Mekonen and Berlie (2020) found a decreasing trend in rainfall over Ethiopia's highlands. In the neighboring Omo Ghibe basin, Ethiopia, Jaweso et al. (2019) indicated a decrease in rainfall.

#### **4.4.3.3 Extreme Flow**

Figure 4.8 depicts the temporal trends of  $Q_{max1}$ ,  $Q_{99p}$ ,  $Q_{95p}$ , and  $Q_{90p}$  for MK stations from 1985 to 2015. The results revealed that the upper MK station had a significantly increasing trend of  $Q_{max1}$ ,  $Q_{99p}$ , and  $Q_{95p}$  by 6.6, 39.4, and 77.5  $m^3/s/year$ , respectively.  $Q_{90p}$  showed an increase of 112.1  $m^3/s/year$  (Table 4.3). Even though PRCPTOT is declining,  $R_{99p}$  is increasing, and a few in  $R_{max1}$  and  $R_{95p}$  are rising in the MK subbasin. All indices at the downstream Hombole station revealed a declining trend that ranged from 2.6 to 59  $m^3/s/year$ . In particular, the decrease in flow at Hombole station may be significantly associated with a reduction in rainfall across the basin and tributary river flow, and a similar finding was observed in annual discharge (Gedefaw et al. 2018). Stream flow trend analysis in the UARB by Duguma et al. (2021) on an annual and wet season scale from 1991 to 2015 was consistent with extreme flow trend analyses. In a similar study, Degefu et al. (2019) inspected spatial trends of streamflow indices at 57 hydrological stations in Ethiopia's highlands (Abay, Awash, Baro Akobo, Genalle Dawa, Omo Ghibe, Rift Valley, and Wabi Shebele basins) using the MK test and Sen's slope estimator. They found a significant increase rather than a decrease in the extreme stream flow indices ( $Q_{max1day}$ ,  $Q_{max7day}$ , and  $Q_{max30day}$ ) at 5 and 10% significant levels. Besides, the annual maximum flood series, which covered the years 1981 to 2010, demonstrated an upward trend in the upper and middle portions and a downward trend in the eastern and lower portions of the Wabi Shebele basin (Wudineh et al. 2021).

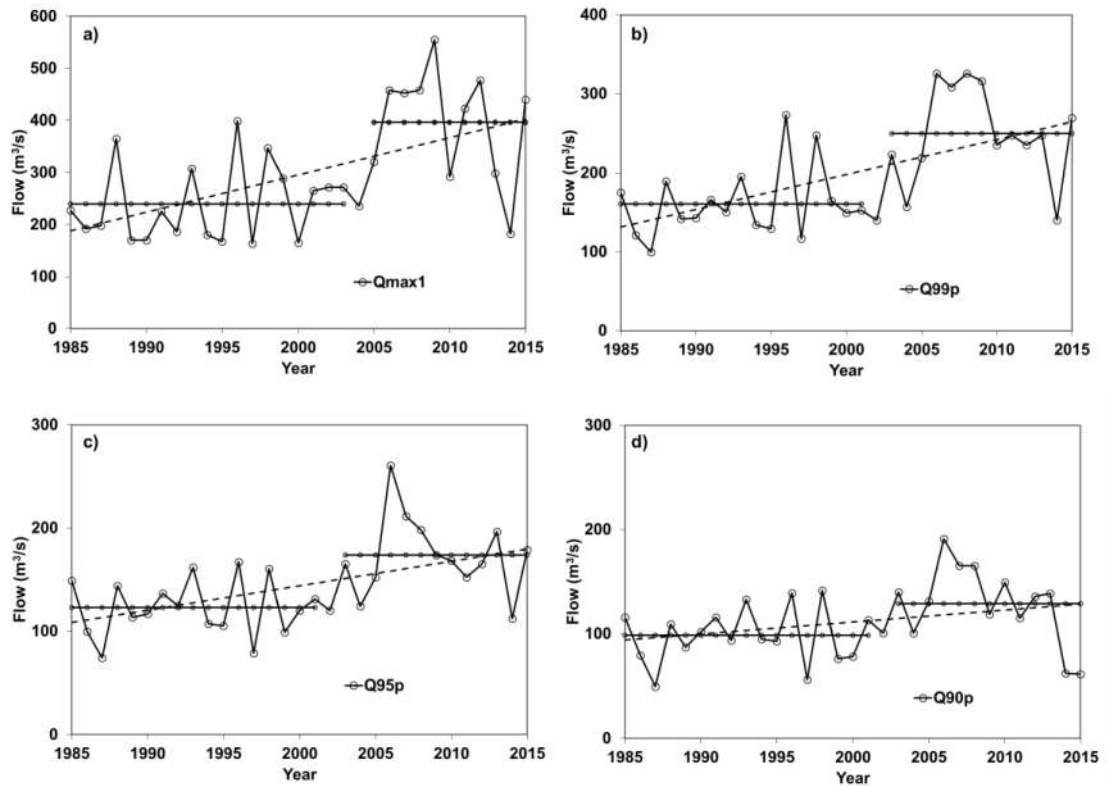


**Figure 4.8** Trends and change points for extreme flow indices at MK station a) Qmax1, b) Q99p, c) Q95p, and d) Q90p. The dotted line represents the slope of linear regression, and the broken line represents the change point (before and after)

#### 4.4.4 Spatiotemporal change point analysis

##### 4.4.4.1 Temperature

The change point analysis identified a significant upward shift in the Tmax1 in 1999 but a negligible downward shift in the Tmin1, as shown in Figure 4.9. The Tmax1 mean before and after the change point was 29.37 °C and 30.96 °C, respectively (an upward change of 1.6°C). The Tmin1 mean before and after the transition point was 5.3°C and 4.4°C, respectively (downshift of 0.88 °C). The change of points is widely different between stations. However, the late 1990s and early 2000s exhibited significant abrupt shifts (Table 4.4).

**Table 4.4** Station-wise temperature indices: change point test and Sen's slope results

Station	Tmax1			Tmin1		
	Pettitt (k)	<i>p</i> value	Sen's Slope (°C/year)	Pettitt (k)	<i>p</i> value	Sen's Slope (°C/year)
AA Obs	1998	<b>0.01</b>	0.05	-	0.12	0.02
AA Bole	1996	<b>0.05</b>	0.04	2001	<b>0.00</b>	0.15
Asgori	2002	<b>0.00</b>	0.08	-	0.57	0.02
Kimoye	1997	<b>0.02</b>	0.07	-	0.24	-0.05
Tullu Bollo	2001	<b>0.00</b>	0.06	-	0.94	0.00
Bishoftu	1998	<b>0.01</b>	0.05	2004	<b>0.02</b>	-0.06
Mojo	-	0.09	0.05	2008	<b>0.03</b>	-0.02
Koka dam	1999	<b>0.02</b>	0.1	2005	0.06	-0.14

*Bold face* Significant at 0.05 level

At the majority of the stations, Tmax1 has increased significantly after change points (except Mojo) ( $p$ -value < 0.05). During the study period, an increase in temperature ranging from 1.0 to 1.4°C was observed on average. However, the Koka and Asgori climate stations exhibited a higher average temperature rise of 2.95°C and 1.9°C, respectively. The downward shifts in Tmin1 were noticed recently, in the early 2000s. However, only a few stations (Bishoftu, AA Bole, and Mojo) experienced significant upward shifts in the 2000s. Similarly, the Koka dam station measured 2.88°C on average downward shift, nearly equal to the Tmax1. In other stations, an average downward shift of 1.6 to 3.1°C and an upward shift of 0.85 to 2.5°C, mainly in the northern parts noted. The significant change in these series may be attributed to the combined impact of climate change, urbanization, growing industries, and commercial activities. It can be inferred from the analysis that the basin is becoming warmer. Similarly, Tekleab et al. (2013) observed a

significant shift in mean Tmax1 and Tmin1 in the Abay/Blue Nile basin, Ethiopia, during the 1980s and 1990s.

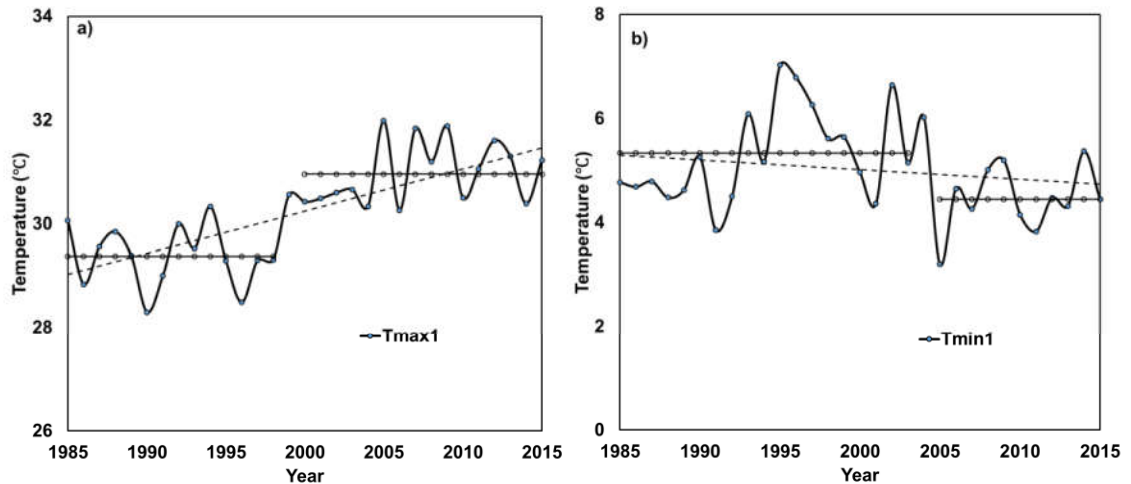


**Figure 4.9** Basin temperature trend and change point **a)** Tmax1 and **b)** Tmin. The dotted line represents the slope of linear regression, and the broken line represents the change point (before and after)

#### 4.4.4.2 Extreme precipitation

The results in Table 4.2 show that the extreme rainfall indices detected an insignificant change in the basin. Change points were seen spatially, with significant abrupt upward and downward shifts most visible in the 1990s and 2000s (Table 4.5). In the highland area, following the change points, R99p (2001), R95p (2001), and PRCPTOT (2003) increased vastly in Guranda Meta station from 400 to 621mm, 549 to 873mm, and 913 to 1288mm, respectively. This could be related to an increase in the frequency of heavy rainfall after 2001. After 2008, there was a significant decrease in PRCPTOT at Busa station, from 1345 to 841 mm. After change points, the average reduction in R99p (2004) and R95p (2001) at Dertu Liben station was 465 to 245 and 654 to 420, respectively. Other stations, including Chedonsa (in R99p, 1992) and Mojo (in R99p and PRCPTOT, 2003), also detected a significant rainfall increase following the abrupt shift. The abrupt downward or upward shift could be attributed mainly to changes in the frequency and intensity of extreme rainfall over time. The increased frequency of heavy

rainfall intensities may lead to a higher likelihood of flood conditions (Mamo et al. 2019; Shawul and Chakma 2020).

**Table 4.5** Station-wise extreme precipitation indices: change point test and Sen's slope results

Station	PRCPTOT			Rmax1			R99p			R95p		
	Pettitt (k)	<i>p</i> value	Sen's Slope (mm/year)	Pettitt (k)	<i>p</i> value	Sen's Slope (mm/year)	Pettitt (k)	<i>p</i> value	Sen's Slope (mm/year)	Pettitt (k)	<i>p</i> value	Sen's Slope (mm/year)
AA Obs	-	0.81	-2.53	-	0.99	0.06	-	0.99	0.95	-	0.99	1.81
AA Bole	-	0.38	-4.17	-	0.99	-0.07	-	0.38	-2.35	-	0.31	-1.79
Akaki	-	0.11	-6.20	-	0.28	-0.18	-	0.31	-2.65	1992	<b>0.04</b>	-5.62
Asgori	1997	<b>0.02</b>	-7.63	-	0.65	-0.03	-	0.21	-5.49	1999	<b>0.02</b>	-7.56
Busa	2008	<b>0.03</b>	-4.37	-	0.06	-0.68	-	0.11	0.61	1999	<b>0.02</b>	-0.51
Guranda												
Meta	2003	<b>0.00</b>	22.45	-	0.47	-0.29	2001	<b>0.00</b>	13.03	2001	<b>0.00</b>	17.97
Kimoye	-	0.85	-0.24	-	0.99	-0.06	-	0.54	3.39	-	0.90	0.37
Teji	-	0.81	-1.57	-	0.57	0.26	-	0.99	0.21	-	0.99	-0.33
Tullu Bollo	-	0.65	-0.28	-	0.83	0.11	-	0.61	-3.19	-	0.65	-2.91
Dertu												
Liben	2008	<b>0.01</b>	-16.16	2008	<b>0.02</b>	-0.86	2004	<b>0.02</b>	-12.74	2001	<b>0.01</b>	-15.16
Sendafa	-	0.99	-0.88	-	0.99	-0.29	-	-0.17	-0.57	-	0.99	0.65
Chefedonsa	-	0.21	-5.78	-	0.44	-0.38	1992	<b>0.04</b>	-4.87	-	0.06	-3.68
Bishofttu	-	0.73	-2.53	-	0.54	-0.01	-	0.50	-1.60	-	0.57	-2.10
Hombole	-	0.57	-3.84	-	0.61	-0.13	1999	<b>0.02</b>	-10.43	-	0.07	-7.88
Mojo	2003	<b>0.01</b>	9.16	-	0.63	0.37	2003	<b>0.00</b>	10.87	2003	<b>0.01</b>	10.19
Koka Dam	-	0.50	10.18	-	0.73	0.18	-	0.41	6.73	-	0.41	7.75

*Bold face* Significant at 0.05 level

#### **4.4.4.3 Extreme flow**

Abrupt changes may be attributed to natural or anthropogenic climatic, hydrological, or landscape changes (Ryberg et al. 2020). The extreme flow indices of Hombole and MK stations were analyzed using Pettitt's test, and the results are presented in Table 4.3 and Figure 4.8. The Hombole station change points test resulted in an insignificant downward abrupt shift in the flow indices, which mostly corresponds with high negative anomaly periods in the extreme rainfall indices, e.g., 2012/2014/2015. However, the MK station in the upstream showed a significant upward shift after change points in the flow indices, mostly in 2003 for Q99p, Q95p, and Q90p and 2005 for Qmax1. Qmax1, Q99p, Q95p, and Q90p increased by 156, 90, 51, and 31 m<sup>3</sup>/s, respectively. The extreme flow has an abrupt shift in spite of decreased rainfall over the MK subbasin. The change may be associated with diverting small streams to the main river, the rainfall intensity in the northwest region, and agricultural land intensification.

In addition to variability in rainfall extremes in high-land areas, the land cover change could drive increased extreme flow in the basin. In support of the present study, the possibility of a shift or trend change in the record data is mainly associated with the remarkably changing environment, global and local climate variability, land-use dynamics (Wagesho et al. 2012), and nature (Arrieta-Castro et al. 2020).

#### **4.4.5 Effect of local rainfall variability on streamflow**

Climate variability, land cover, and physical factors are the primary drivers of changes in extreme hydrological events. As a result, it is reasonable to identify the possible cause of extreme discharge variability in the upper and downstream river sections because rainfall is the primary factor influencing hydrological processes, apart from land cover and geomorphology. Spearman's rank correlation coefficients (R) were calculated between the anomalies of Rmax1 and Qmax1, R99p and Q99p, R95p and Q95p, PRCPTOT and Q90p, and PRCPTOT and extreme flow indices anomalies. The results of correlation tests between the anomalies of extreme areal rainfall and extreme flow indices at the two stations are given in Table 4.6. The

findings revealed a positive relationship between extreme rainfall and flow anomalies. For the Hombole, there is a correlation of 0.33 between Rmax1 and Qmax1 and a significant correlation ( $p$  value  $< 0.05$ ) between PRCPTOT/ Rmax1 and extreme flow indices anomaly. The MK subbasin PRCPTOT/R95p and the extreme flow indices (Q99p, Q95p, and Q90p) were significantly correlated. This suggests that an area-wide PRCPTOT and R95p anomaly was the primary cause of the extreme flow anomalies at Hombole and MK outlet stations. Besides, R99p and Rmax1 have no discernible impact on flood indices at the basin and MK subbasin scales, respectively.

**Table 4.6** Results of Spearman’s rank correlation coefficients between anomalies in extreme precipitation, ENSO, and extreme flow

Indices	Hombole				Melka Kunture			
	Qmax1	Q99p	Q95p	Q90p	Qmax1	Q99p	Q95p	Q90p
PRCPTOT	<b>0.49</b>	<b>0.60</b>	<b>0.65</b>	<b>0.68</b>	0.29	<b>0.37</b>	<b>0.44</b>	<b>0.47</b>
Rmax1	0.33	<b>0.37</b>	<b>0.38</b>	<b>0.37</b>	0.21	0.23	0.20	0.20
R99p	0.07	0.20	0.18	0.20	0.16	0.21	0.22	0.18
R95p	0.14	0.29	0.35	<b>0.38</b>	0.39	<b>0.48</b>	<b>0.53</b>	<b>0.43</b>
SOI	<b>0.45</b>	<b>0.42</b>	<b>0.43</b>	<b>0.44</b>	0.25	0.32	0.29	0.31
Niño 3.4	<b>-0.48</b>	<b>-0.53</b>	<b>-0.51</b>	<b>-0.51</b>	-0.02	-0.11	-0.11	-0.06
MEI	<b>-0.50</b>	<b>-0.55</b>	<b>-0.55</b>	<b>-0.55</b>	-0.29	<b>-0.38</b>	-0.35	-0.35

*Bold face* Correlation is significant at the 0.05 level

Individual rainfall stations with a positive trend in extreme precipitation indices and anomalies under the MK subbasin, mostly in the western part, were investigated as part of the correlation analysis. Positive correlations exist between the variables. Guranda Meta rainfall station showed a significant correlation of 0.83 (between PRCPTOT and Q90p), 0.64 (between R99p and Q99p), and 0.66 (between R95p and Q95p). Other stations, Addis Ababa (AA) Obs. and Kimoye, had a correlation value 0.24. (R99p and Q99p), 0.35 (R95p and Q95p), 0.14 (R99p and Q99p), and 0.02 (R95p and Q95p), respectively. The correlation between R95p and Q95p

showed a value of 0.2 at Teji station. The correlation analysis indicates that extreme rainfall anomalies in northwestern stations may result in extreme flow anomalies. Also, extremely wet and very wet precipitation indices may be the primary controlling factor for extreme hydrological events in the MK subbasin.

Similarly, Wang et al. (2019) investigated the correlation between extreme water levels and extreme rainfall anomalies in Taihu Basin, China. They found positive (significant) correlations between the two variables for different seasons, concluding that rainfall anomalies heavily influenced extreme flow anomalies. According to Woldegebrael et al. (2020), extreme precipitation events are directly related to flooding in the Awash and Omo Ghibe basins during the flood years. Likewise, the nonlinear catchment response in the upper highland areas (mainly in the northwest) related to geomorphological characteristics may lead to frequent floods in the floodplain (e.g., Becho floodplain).

#### **4.4.6 Effect of climate indices anomalies on streamflow**

The correlation between ENSO indicators: Southern Oscillation Index (SOI), Niño 3.4 Sea Surface Temperature (SST), bi-monthly Multivariate El Niño/Southern Oscillation (ENSO) Index (MEI), and extreme flow indices anomalies are also presented in Table 4.6. The anomaly in extreme flow and ENSO indicators is shown in Figure 4.11. The anomaly SOI with Hombole extreme indices showed a significant correlation, with  $R$  ranging from 0.42 to 0.45 ( $p$  value  $< 0.05$ ), while the MK has only demonstrated a positive correlation. This indicates that anomalies of extreme flow indices at Hombole follow the pattern of positive and negative phases of SOI, except from 2008 to 2011, which showed incomparable anomalies leading to a decreasing trend. The positive correlation result at MK station and the prolonged positive phase of the SOI (2003/2005 to 2013) coincides with the increasing trend and upward shift in extreme flows. Floods in 1996 coincided with positive SOI values (Figure 4.11).

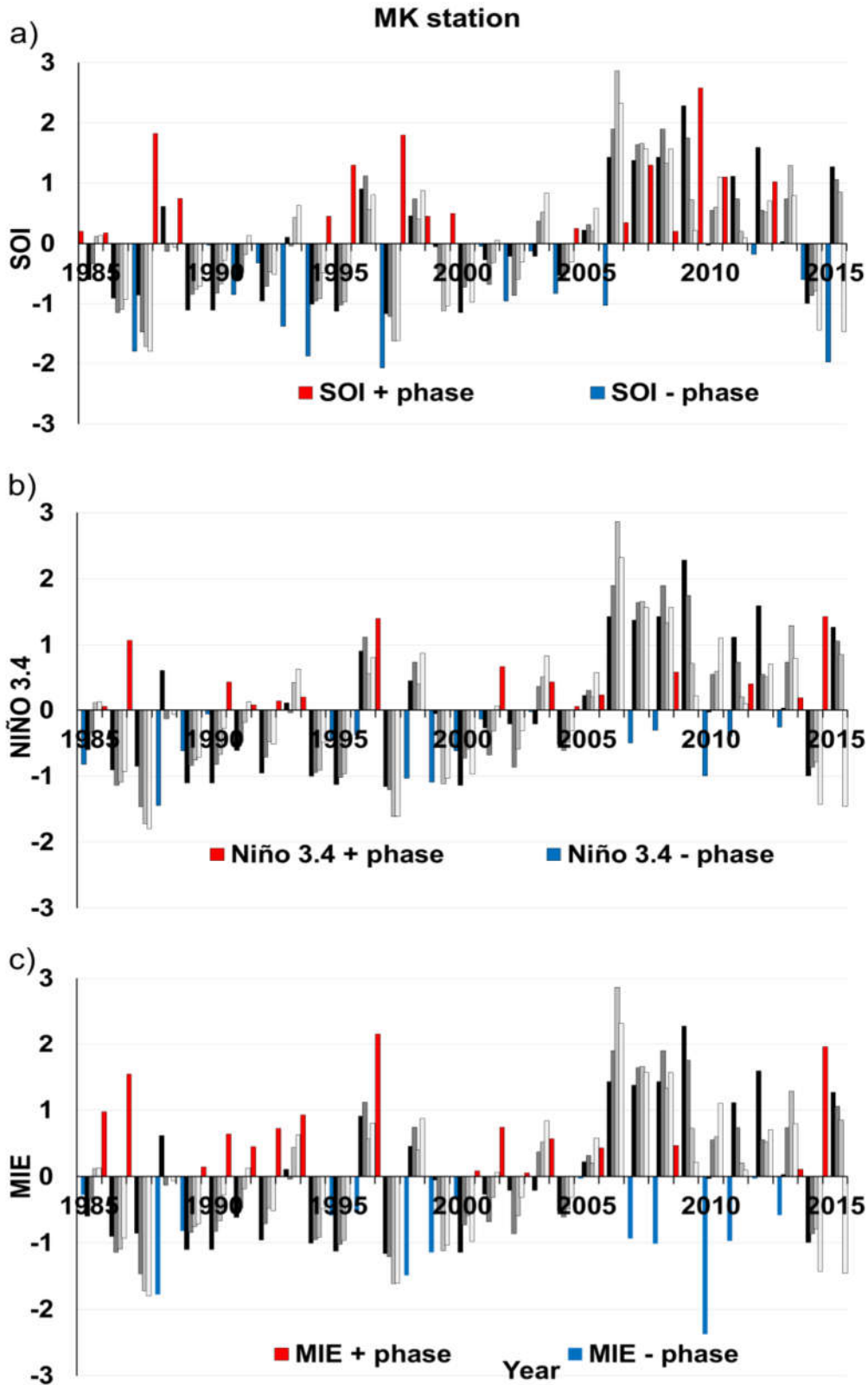
Niño 3.4 SST showed significant negative correlations with Hombole extreme flow anomalies ( $R$  from -0.48 to -0.53,  $p$  value  $< 0.05$ ), implying that positive (negative)

SST is related to below (above) long-term average extreme flow events, i.e., negative (positive), and may be related to a decreasing trend in Hombole flow extremes. The Niño 3.4 index had a weak negative correlation with MK extreme flows, indicating that El Niño (positive phase) did not affect extreme flow anomalies. For instance, El Niño episodes 2005/2006/2009/2012/2015 did not affect flow anomalies, implying that other mechanisms play a significant role in extreme flow occurrence (Figure 4.11). It is well known that 2015 was the worst El Niño year while the MK flow indices were not influenced, but the downstream station showed negative anomalies during the El Niño phase. The peak event in 1996, in particular, agrees with the La Niña episode at both stations.

The two basin stations were negatively correlated with the Multivariate ENSO index, more significant than Niño 3.4. All extreme flow indices at Hombole were negatively correlated with the MEI index,  $R$  ranging from -0.50 to -0.55 ( $p$  value < 0.05). MK extreme flow indices Q99p ( $R = -0.38$ ) also significantly correlated with the MEI index. This indicates that extreme flow is below average (deficit) and above average (wet or excess) during the MEI positive (warm) and negative (cold) episodes, respectively. The Hombole station demonstrated a strong relationship with negative anomalies during the positive MEI phase (warm) and a consistent downward trend with MEI.

Thus, MEI phases are regarded as essential indices related to extreme flow variability and as prediction indexes for the basin. Like Niño 3.4 SST, flow indices at MK station displayed positive anomalies during MEI warm (positive) phases, demonstrating an inconsistent correlation between the anomalies. For example, the peak flood event in 1996, in particular, also agrees with the negative MEI event at both stations. The 2006 extreme flood event at Hombole and MK occurred during the MEI's positive year (Figure 4.11). It was also noted that the extreme flow, representing the greatest amount at MK, had no significant relationship with extreme rainfall or ENSO indicators. Regarding the flood events in 1996, they occurred at the same time as ENSO anomalies at both stations. However, the peak flood in 2006 appeared opposite to the ENSO (warm phase of SOI, Niño 3.4 and

MEI), suggesting that other factors, besides positive anomalies of extreme local rainfall, might have driven the extreme occurrences.



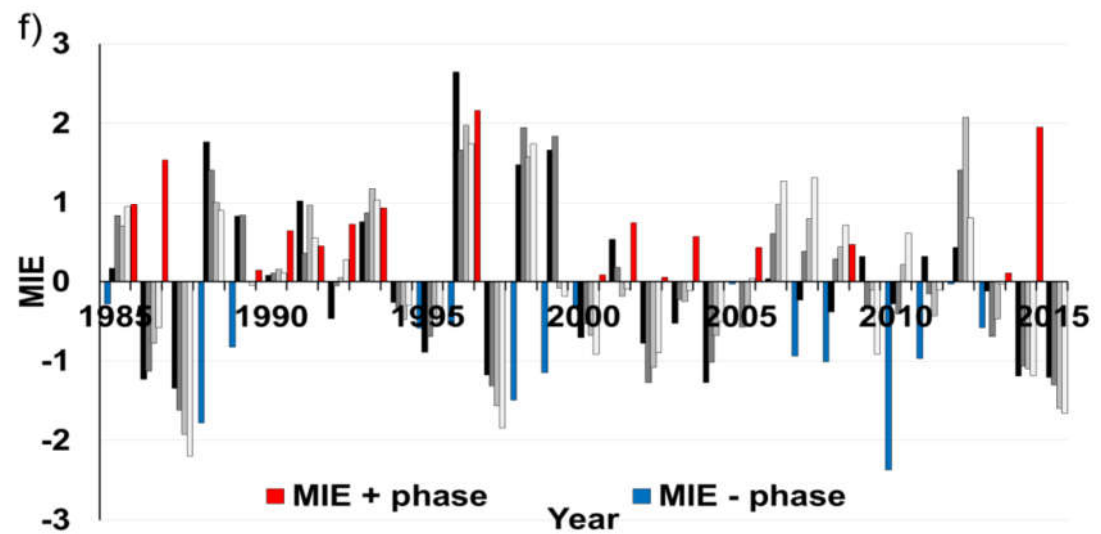
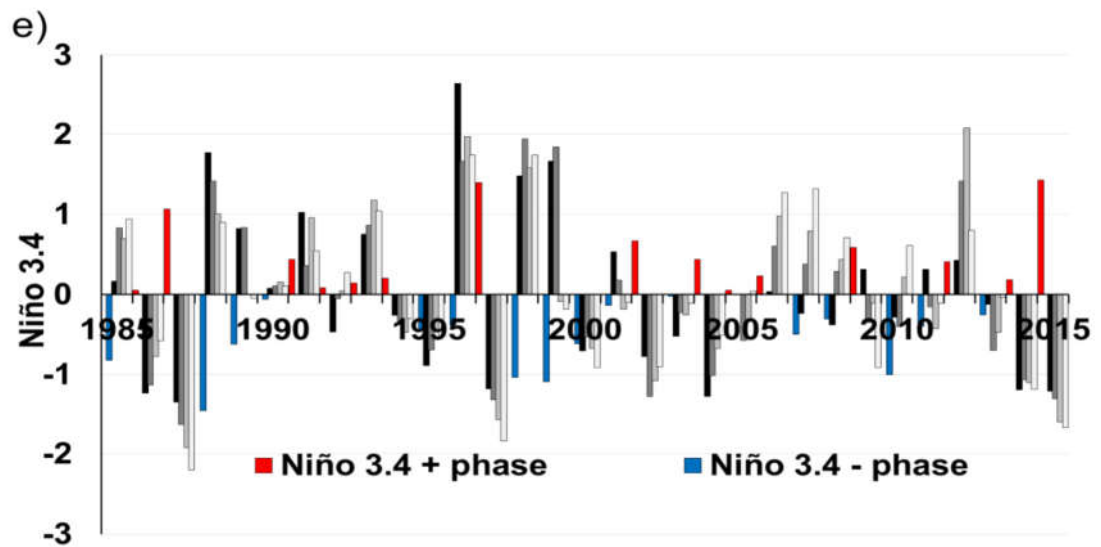
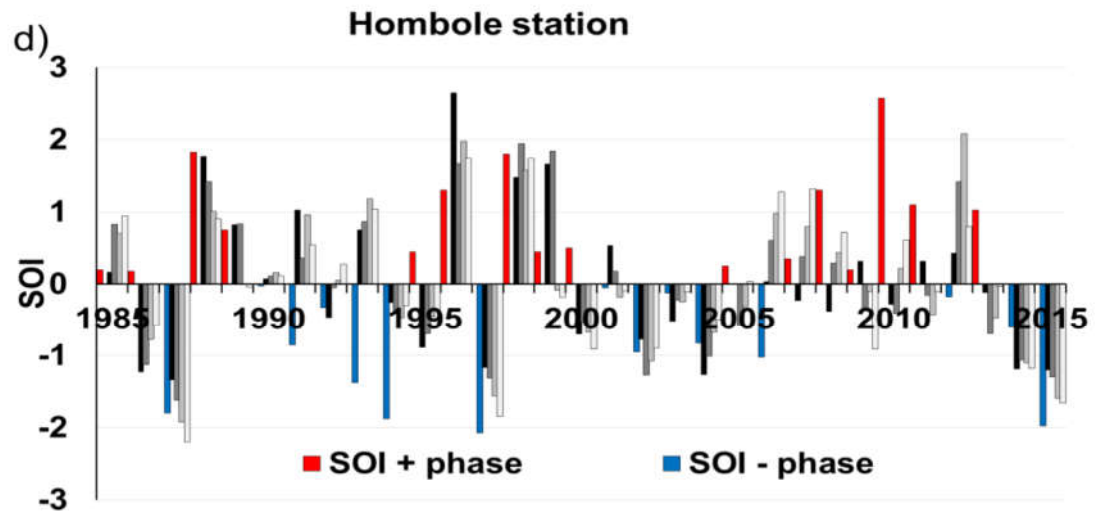


**Figure 4.10** Standardized anomalies of extreme flow indices for MK **a-c**) and Hombole **d-f**) stations and ENSO anomalies. The red and blue represent the cold (+) and warm (-) phases for SOI, and the red and blue represent the warm (+) and cold (-) phases for Niño 3.4 and MEI

As a result, ENSO is regarded as a climate index that influences extreme flow variability in the Hombole subbasin. Similarly, Degefu and Bewket (2017) observed a negative relationship between high flow variability and Niño 3.4 SST in the Omo-Ghibe River basin, Ethiopia. A study by Worako et al. (2021) in the Ethiopian Rift Valley lake basin reported an ENSO effect on high flow variability, indicating that most catchments in the basin experienced a deficit (excess) during the El Niño (La Niña) period. They also demonstrated that every negative (positive) anomaly was unrelated to El Niño (La Niña) periods, consistent with MK station anomalies. Further, Taye et al. (2021) noted the equatorial Pacific Ocean SST influence on Ethiopia's summer rainfall (July, August, and September), mainly upper Awash and summer rainfall predictability, consistent with the current study.

The study successfully identified significant hydroclimatic variations in the basin, shedding light on the extreme flow variability induced by intense local rainfall and global-scale atmospheric-ocean changes. The study pinpointed the likely hotspots for heavy rain and the indices responsible for the basin's extreme flow changes. Additionally, it emphasized that stream flow exhibits nonstationary qualities. The observed alterations in flood discharge in the basin's upper MK and lower portions could have noticeable consequences in the future. Changes in precipitation and temperature negatively affect rainfed agriculture, ecosystem services, and water supply for various sectors in the basin. These findings align with earlier research conducted in Ethiopia and elsewhere.

#### **4.5 Conclusions**

The conclusions of the study can be summarized as follows.

The overall variability of extreme rainfall indices across the entire basin was less than 20%, suggesting less variability. However, a high degree of spatial variability

(with  $CV > 30\%$ ) was observed in the rainfall indices (specifically  $R_{max1}$ ,  $R_{99p}$ , and  $R_{95p}$ ) and extreme flow indices at the Hombole and MK stations. Decadal anomaly analysis of the rainfall indices indicated a higher frequency of positive anomalies in the 1990s compared to the 2000s. Similar findings were also observed in the anomaly patterns of extreme flow indices at the Hombole station, which serves as the basin outlet.

The magnitude of temperature increased by approximately  $0.08\text{ }^{\circ}\text{C}$  per year (in  $T_{max1}$ ) and  $0.15\text{ }^{\circ}\text{C}$  per year (in  $T_{min1}$ ) spatially, indicating a warming trend in the basin. The result also showed a significant upward shift in  $T_{max1}$  and a downward shift in  $T_{min1}$  in the late 1990s and early 2000s. The MMK and Sen's slope estimator revealed a statistically non-significant upward trend in  $R_{99p}$  and  $R_{95p}$  and a weak decreasing trend in  $PRCPTOT$  and  $R_{max1}$ . The point change analysis in rainfall indices showed significant abrupt upward and downward shifts in the 2000s. Furthermore, the hydrological extremes in the upstream MK station exhibited a significant increasing trend, with the MK subbasin showing an increase in strong precipitation events,  $R_{max1}$ ,  $R_{99p}$ , and  $R_{95p}$ . The change point analysis revealed an upward shift in the upstream MK station in 2003 and 2005, whereas the downstream Hombole station exhibited a trend toward decline. Overall, the changes in extreme flow indices aligned with changes in climate variability across the subbasins and basins.

Extreme flow anomalies significantly correlate ( $R$  ranging from 0.4 to 0.68) with the extreme rainfall anomalies. This suggests widespread  $PRCPTOT$  and  $R_{95p}$  anomalies triggered the extreme water flow anomalies at the MK and Hombole outlet stations. Notably, the intense precipitation events in northwestern rainfall stations displayed a relationship with MK's extreme flow indices, which could explain the extreme occurrences. The Hombole outlet station's extreme water flow anomalies also exhibited a more robust relationship with ENSO indicators than the MK. Thus, ENSO is a crucial climate index that influences extreme flow variability, and its impact, in conjunction with wet-day precipitation anomalies, is complementary at a basin level. Therefore, positive extreme flow anomalies may be expected in the basin during the positive SOI, negative Niño 3.4, and MEI

phases. Further, climate variability can explain flood discharge variability in the studied basin in complement to catchment characteristics.

## **CHAPTER 5**

### **QUANTIFYING THE CHANGES IN LAND COVER AND RAINFALL VARIABILITY IMPACT ON FLOOD**

#### **5.1 Introduction**

Changes in land cover and climate variability can influence the basin hydrology. Individual or combined changes influence watershed hydrology and amplify the extreme flow. The present chapter comprehensively explains the impact of separate and combined land cover and climate at two hydrological stations, namely, Melka Kunture and Hombole stations. Scenarios were developed, and a semi-distributed hydrological model was used to quantify the relative impact. It identifies the relative impact and contribution to flood hydrology (here referred to as peak and high flows) at the main hydrological stations.

#### **5.2 Changes in land cover and rainfall variability impact on flood**

Climate variability and intensive human activities significantly impact the natural environment and human societies. Several studies reported extreme rainfall events in different world regions (Sheikh et al. 2015; Bhatti et al. 2020; Comin et al. 2021; Wudineh et al. 2022), which appear to have a significant role in frequent floods (Kunkel et al. 2020; Comin et al. 2021). Changes in land cover, such as urbanization, deforestation/afforestation, and agriculture expansion, can alter the hydrological regime, particularly the magnitude of streamflow (Gashaw et al. 2018; Khorn et al. 2022).

Quantitative evaluations of the past and future based on climate change, land cover change, and the combined effects on stream flow variation investigated using hydrological models have shown that these changes significantly impact hydrological regimes (Akter et al. 2018; Saddique et al. 2020; Torabi Haghghi et al. 2020; Woltemade et al. 2020; Mitiku et al. 2023). However, climate change has been reported to impact floods significantly (Akter et al. 2018; Torabi Haghghi et

al. 2020; Woltemade et al. 2020). Changes in land cover have also been noted to affect the magnitude of streamflow (Berihun et al. 2019). Fewer studies have addressed separate and combined changes in surface runoff and other variables in the river basins of Ethiopia (Berihun et al. 2019; Wedajo et al. 2022; Mitiku et al. 2023). In recent years, there has been much interest in using the SWAT model to assess extreme flow (Pfannerstill et al. 2014; Maghsood et al. 2019; Tan et al. 2020). Identifying the flood-influencing mechanism in the basin is, therefore, necessary for flood management and mitigation strategies. Therefore, a comprehensive study is required to quantify the effects of changing environmental conditions on extreme streamflows, i.e., peak and high discharge.

### **5.3 Data and methodology**

Figure 5.1 shows the overall steps used to quantify the impact of land cover change and climate variability. Quantitative analysis requires several spatial and temporal data inputs to replicate the basin's hydrology. A 30-m resolution Shuttle Radar Topography Mission (SRTM) digital elevation model (DEM) was downloaded from USGS Earth Explorer (<https://earthexplorer.usgs.gov/>), and used to delineate the basin and subbasins. Melka Kunture and Hombole hydrological stations were used as outlet points, and the basin was divided into upstream and downstream subbasins. The Hombole station controls 7432 km<sup>2</sup> of the basin's total area, accounting for 65 % of the total area, and the Melka Kunture station owns about 38 % of the entire basin.

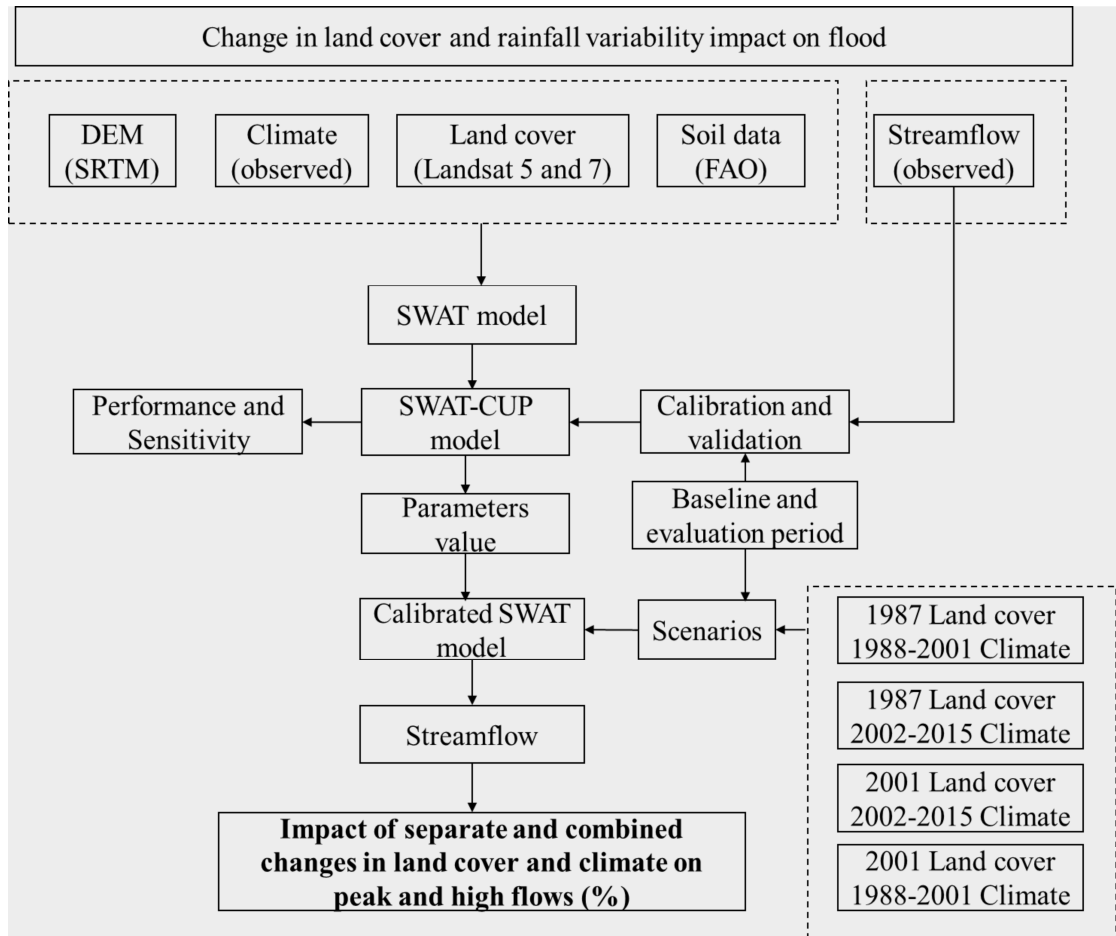


**Figure 5.1** Flow chart of the study for quantifying the separate and combined impact on the extreme flow

Soil data were obtained from the world digital soil map of the Food and Agricultural Organization (FAO 2007) (<https://storage.googleapis.com/fao-maps-catalog-data/uuid/446ed430-8383-11db-b9b2-000d939bc5d8/resources/DSMW.zip>) at 1:5,000,000 scale in ESRI shapefile format. Pellic Vertisols (43%) and Eutric Nitisols (33%), followed by Haplic Xerosols (7%) and Eutric Cambisols (6%), are the dominant soil types in the basin.

The land cover maps of 1987 and 2001 were prepared using a random forest (RF) classifier algorithm in the Google Earth Engine (GEE) platform. The RF is a supervised learning model and ensemble learning composed of multiple decision trees to perform classification. It comprises nodes with branches that lead to another node and, finally, a leaf without any branches. A node consists of a set of rules to

classify data, branches show the possibility the node could lead, and a leaf is the end of the decision tree. The algorithm uses the leaves to make its final decision, meaning that it merges the decision of multiple decision trees to determine the end classification by averaging all the decision trees. The RF has several parameters that directly impact and aren't learned from data in the RF algorithm, influencing the LC classification accuracy. The hyper-parameters through adjusting and finding the optimal value parameters such as the number of decision trees, variable per split, minimum leaf population, bag fraction, maximum node, and seed) and determined iteratively until the model accuracy is high. For land cover classifications, four main steps were used: 1) image collection/selection, 2) training land cover classes, 3) classification/prediction, and 4) accuracy assessment. A 30m resolution of images was used for supervised land cover classification. Atmospherically corrected surface reflectance from the Landsat 5 Thematic Mapper (TM) and Landsat 7 Enhanced Thematic Mapper Plus (ETM+) available in the GEE platform were utilized for the years 1987 (filter date of '1987-01-01', '1987-12-31') and 2001 (filter date of '2000-01-01', '2001-12-31'), respectively. Tier 1 data images with a cloud cover of less than 1% were chosen, and the temporal aggregation method, i.e., the mean calculation, was applied. It is worth noting that LC classification is inherently affected by the uncertainty of the selection of training sample and validation data set (reference sample) and size. Generally, the larger training sample size reduces the model's uncertainty and ensures a precise visual depiction. Several input features, image tiles, spatial resolution, and ground truth data also affect the accuracy of LC classification.

The land cover classes were chosen using previous knowledge of the study basin. Bare land refers to a rock, barely exposed soil, and degraded land. The built-up area includes urban and rural settlements, airports, roadways, and industrial zones. Cropland refers to both farmland and harvested land. Forest consists of thick forest. The pasture land is land covered with grass. Shrubland consists of small and well-spaced trees. Water bodies are Lakes and reservoirs. Then, a prediction was made using Band 1 through Band 7. The samples were divided into training and validation groups, with 70% used for training and 30% used for validation. The key parameters

in the random forest, the number of decision trees = 300, and the variable per split = 5 are considered. The bare land, built-up area, cropland, forest, shrubland, water body, and pasture land were all identified. Finally, the accuracy assessment between the classified and reference samples was evaluated using the overall accuracy and Kappa coefficient. These typical accuracy assessments are the most commonly used to assess land cover classification accuracy (Rientjes et al. 2011). Overall accuracy (in percentage) is the number of correctly classified pixels divided by the total number of pixels used for validation, and the Kappa coefficient measures the improvement in classification accuracy over random unsupervised classification. The coefficient value ranges from 0 to 1. A score close to 1 indicates a significant improvement, while 0 shows no improvement over random classification.

This study used sixteen daily observed rainfall stations and eight maximum and minimum air temperature stations. User-defined Weather Generator parameters were created using daily precipitation, maximum/minimum temperature, solar radiation, wind speed, and relative humidity. From 1985 to 2015, daily observed discharge data from two stations, Melka Kunture and Hombole, was used. The Thiessen polygon method was used to calculate the areal rainfall for the subbasins and UARB.

### **5.3.1 General overview of the SWAT model**

Soil and Water Assessment Tool (SWAT) (Arnold et al. 1998) is a continuous-time, semi-distributed, and process based used to simulate hydrology at a different scale. SWAT version 2012 is available as an ArcSWAT extension in the ArcGIS tool. The model can perform the impact of alternate land management practices on water resources, sediment transport, and pollutant loads that work on daily or sub-daily time steps (Neitsch et al. 2011). The physical process simulated in the watershed can be separated into the land and water or routing phases governing the amount to the main channel in each subbasin and movement through the channel network to the watershed outlet, respectively. The water balance equation calculates the land phase of the hydrological cycle amount, as given in Equation 5.1. SWAT model

computes surface runoff using the Soil Conservation Service Curve number (SCS-CN) method at daily time steps (Neitsch et al. 2011; Arnold et al. 2012).

$$SW_t = SW_0 + \sum_{i=1}^t (R_{day} - Q_{surf} - E_a - w_{seep} - Q_{gw}) \quad (5.1)$$

where  $SW_t$  = the final soil water content (mm)

$SW_0$  = initial soil water content (mm)

$t$  = time (in days)

$R_{day}$  = precipitation (mm)

$Q_{surf}$  = surface runoff (mm)

$E_a$  = evapotranspiration (mm)

$w_{seep}$  = water entering the vadose zone from the soil profile (mm)

$Q_{gw}$  = return flow (mm)

### 5.3.2 SWAT model setup

The SWAT model project was created based on the standard procedure, from watershed delineation to homogenous HRUs and simulation. The grid-based spatial input DEM is the primary input to the SWAT hydrological model to divide the watershed into subbasins. Each subbasin is then divided into hydrological response units (HRUs). Each HRU's possesses unique land cover, soil, and management practices. The hydrological cycle components are predicted for each HRU and routed through the subbasins to obtain the total runoff of the basin (Neitsch et al. 2011). The slope was classified into four classes (< 3%, 3-5%, 5-10%, and > 10%). HRUs of the subbasins were set to a threshold of 10%, 15%, and 15% for land use, soil class, and slope class, respectively. The Penman-Monteith method was utilized

to calculate evapotranspiration. SWAT model was run with climate input data (daily precipitation, maximum and minimum temperature, solar radiation, wind speed, and relative humidity) from 1985 to 2015, with 1985-1987 being a warm-up period.

### **5.3.3 Calibration, validation, and uncertainty**

Semi-automatic calibration, validation, and uncertainty and sensitivity analysis of the stream flow were carried out using the semi-automated Sequential Uncertainty Fitting version 2 (SUFI-2) algorithm in SWAT Calibration Uncertainty Program (SWAT-CUP) (Abbaspour et al. 2004, 2007). Eighteen parameters that affect surface runoff were set for calibration based on previous studies in the basin (Shawul et al. 2019) and other literature. In uncertainty analysis, input uncertainty propagates to model output uncertainty and is expressed as 95% prediction uncertainty (95PPU). The p-factor ( $> 0.7$ ) and r-factor ( $< 1.5$ ) statistics were used to determine whether the simulations were well modeled and whether the measurements were within the simulation uncertainty. The p-factor is the percentage of measured data bracketed by the 95PPU, and the r-factor is the thickness of the 95PPU. A Nash-Sutcliffe was used as the objective function to calibrate the daily discharges. A global sensitivity analysis was used to identify the dominant parameters related to changes in hydrological response (Abbaspour et al. 2017).

According to the local community in the UARB, the following years witnessed flood inundation: 1996, 2006, 2016, and 2020. Pettitt test detected that the year 2002 was found to be an insignificant change point for Hombole ( $p$ -value = 0.65), while 2005 was a significant change point for Melka Kunture station ( $p$ -value = 0.008), an upward shift. Therefore, the change point in 2002 is reason enough to divide the entire study period into before and after 2002. Hence, the baseline period from 1988 to 2001 (assuming 1987 land cover) and change (evaluation) period from 2002 to 2015 (assuming 2001 land cover) were chosen to include historical flood events of 1996 and 2006, respectively. Calibration and validation were performed at two reaches of the main Awash River. In the baseline period, data from 1993 to 2001 and 1988 to 1992 were used for calibration and validation, respectively. In the

evaluation period, data from 2007 to 2015 and 2002 to 2006 were used for calibration and validation, respectively.

### 5.3.4 Model performance criteria

Three performance metrics, coefficient of determination ( $R^2$ ), Nash-Sutcliffe efficiency (NSE), and percent bias (PBIAS), suggested by Moriasi et al. (2007), were used to compare the variance between observed and simulated data.  $R^2$  calculates the degree of agreement between measured and simulated data.  $R^2$  value ranges from 0 to 1, and a closer to 1 indicates less error variance. NSE measures the model's ability to accurately simulate hydrological processes, with a value closer to 1 representing the best performance and a negative value representing the worst. PBIAS measures the average tendency of simulated data. If the percent bias is positive, the simulated data from the model is understated. If the percent bias is negative, the simulated data from the model is overestimated. The optimal percent bias value is 0%, and  $\pm 25\%$  indicates satisfactory model performance. Validation was carried out using the optimized calibrated parameter ranges, and performance was assessed using the  $R^2$ , NSE, and PBIAS (Eq. 5.1 to 5.3)

$$R^2 = \left( \frac{\sum_{i=1}^n (Y_i^{Obs} - Y^{Mean}) * (Y_i^{Simu} - Y^{Simu.Mean})}{\left[ \sum_{i=1}^n (Y_i^{Obs} - Y^{Mean})^2 \sum_{i=1}^n (Y_i^{Simu} - Y^{Simu.Mean})^2 \right]^{0.5}} \right)^2 \quad (5.1)$$

$$NSE = 1 - \left[ \frac{\sum_{i=1}^n (Y_i^{Obs} - Y_i^{Sim})^2}{\sum_{i=1}^n (Y_i^{Obs} - Y^{Mean})^2} \right] \quad (5.2)$$

$$PBIAS = \left[ \frac{\sum_{i=1}^n (Y_i^{Obs} - Y_i^{Sim}) * 100}{\sum_{i=1}^n (Y_i^{Obs})} \right] \quad (5.3)$$

Where  $Y_i^{Obs}$  is the  $i$ th observed data,  $Y_i^{Simu}$  is  $i$ th simulated data,  $Y_i^{Mean}$  is the mean observed data and  $n$  is the number of observed data.

Another performance metric used in this study was the flow duration curve (FDC), which summarizes the essential metrics in the data series and can be used to assess model bias visually. The percent exceedance probability curves demonstrate how well the model replicates observed extremes over the calibration and validation period (Moriasi et al. 2007; Pfannerstill et al. 2014). Each FDC segment represents a particular physical process and peak (0-2%), high (2-20%), medium (20-70%), and low flow (70-100%) segments (Chilkoti et al. 2018). The percent error in peak discharge (PEP) evaluation statistics (Moriasi et al. 2007) was applied to the peak and high flow events throughout calibration and validation. PEP is the difference between the simulated and observed peak (or high) flow divided by the observed peak (or high) flow. Therefore, the model can replicate the hydrological process if the model simulation produces values within the acceptable range, i.e.,  $\leq \pm 25\%$ .

### 5.3.5 Quantitative evaluation of the influence of land cover and rainfall variability on flood

The concepts of scenarios were designed to assess the contribution of climate (primarily refers to rainfall variability) and changes in land cover. First, the base and evaluation periods were calibrated and validated using corresponding climate and land cover data. Then, with the land cover held constant, meteorological data for the evaluation were entered into the model to simulate flow under climate variability and vice versa. Detail scenarios-based simulations are provided in Table 5.1. Finally, the contribution of land cover change and climate to flood events were evaluated separately using Equations 5.4 to 5.6.

$$g_c = \frac{(R_{SC} - R_{SB})}{R_{SB}} \times 100\% \quad (5.4)$$

$$g_l = \frac{(R_{SL} - R_{SB})}{R_{SB}} \times 100\% \quad (5.5)$$

$$\Delta R_{lc} = R_{SE} - R_{SB} \quad (5.6)$$

$\mathcal{G}_c$  and  $\mathcal{G}_l$  express the contribution of climate and change in land cover on discharge variation.  $\Delta R_{lc}$  is the simulated discharge as a result of land cover and climate. The contribution rate in percentage is finally expressed for comparative purposes for peak and high flow ranges in upper and downstream reaches and the flood-influencing mechanisms identified.

**Table 5.1** Scenarios of land cover and climate used during the simulation

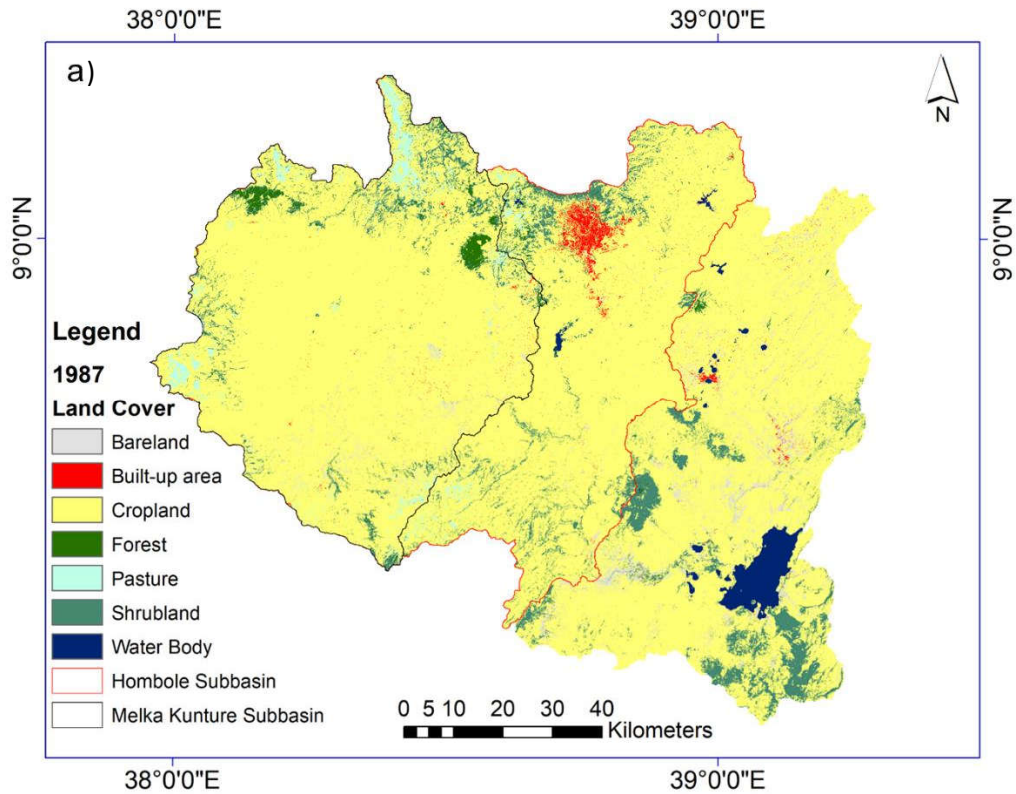
Simulation	Scenarios	LC	Climate	Conditions
R <sub>SB</sub>	Scen. 1	1987	1988-2001	Simulates 1987 LC and 1988-2001 climate
R <sub>SC</sub>	Scen. 2	1987	2002-2015	Simulates under 1987 LC and 2002-2015 climate
R <sub>SE</sub>	Scen. 3	2001	2002-2015	Simulates under 2001 LC and 2002-2015 climate
R <sub>SL</sub>	Scen. 4	2001	1988-2001	Simulates under 2001 LC and 1988-2001

## 5.4 Result and discussion

### 5.4.1 Changes in land cover evaluation

The land cover (LC) change state of the UARB in 1987 and 2001 is shown in Figure 5.2, and Table 5.2 presents the percentage change. The classification accuracy assessment, i.e., cumulative overall accuracy, was 94.55% and 94.31% for the 1987 and 2001 LC years, respectively, and validation Kappa was 0.89. It is worth mentioning that uncertainties

The basin experienced a drastic change in LC in terms of built-up area, bare land, pastured land, and water body, while forest and cropland decreased. It was observed that cropland constitutes around 86.31% of the UARB, with a change of -2.7% in 2001. Cropland continued to be the dominant land cover type in the basin. The bare land and pasture land areas expanded by 42% and 35.8%, respectively.



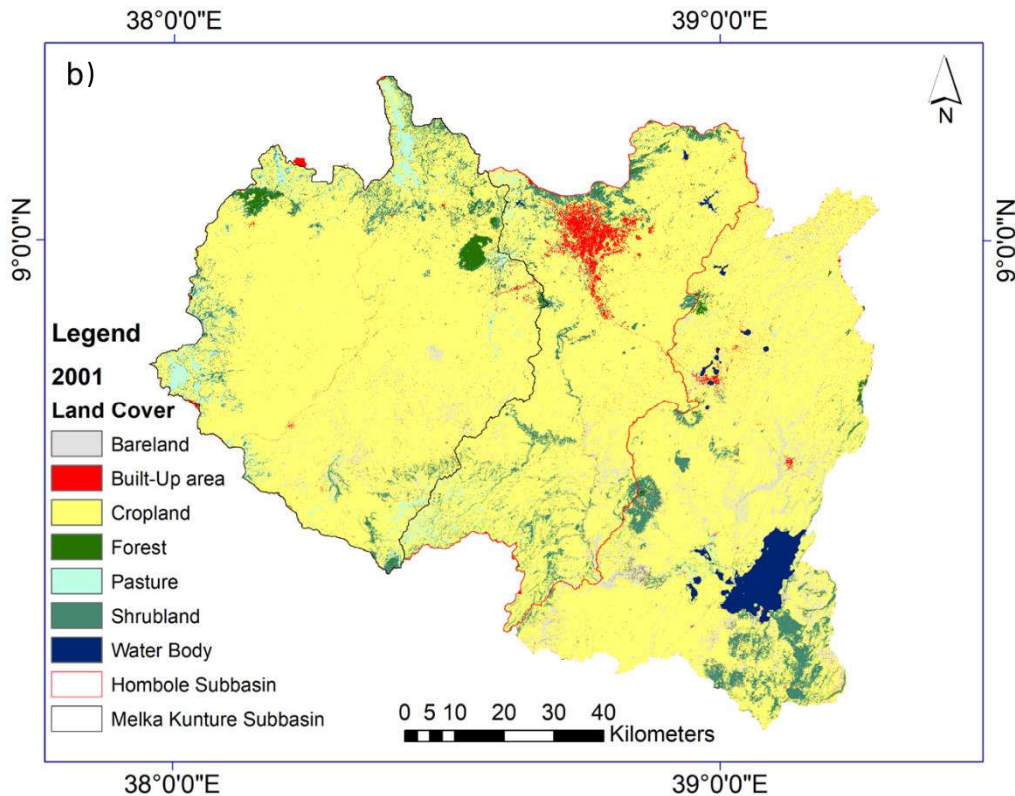


**Figure 5.2** Land cover map of a) 1987 and b) 2001

The Melka Kunture and Hombole watershed analysis also demonstrated a similar tendency. Built-up areas expanded rapidly in both subbasins at the expense of croplands and vegetation. The Hombole sub-basin mainly consists of the urbanized region, including the capital city of Ethiopia, Addis Ababa. Cropland was the dominant type of land cover in the sub-basins in 1987, making up around 89 % of the total area, but by 2001, it had decreased by 3.4% in Hombole and 2.3% in the Melka Kunture subbasin. In the Hombole sub-basin, other land types, including shrublands (5.56%) and pasture lands (2.47%), expanded by 12.8% and 29.3% between 1987 and 2001, whereas bodies of water shrank by 40.3 %.

Thus, cropland is the most noticeable landform in the base and evaluation periods, followed by shrubland, pasture land, built-up area, and forest. As a result, it plays a significant role in runoff hydrology compared to bare land, pasture land, or shrub land due to minimal change and area coverage, especially in the upstream section. In contrast to the previous study (Shawul and Chakma 2019), cropland had the

slightest range of variability (-2.7 %). The difference could be attributed to the image series and classification methodology used. The accuracy obtained from the cloud-based GEE platform was higher than that obtained from previous studies in the basin (Shawul and Chakma 2019; Tadese et al. 2020). Previous land cover modeling studies in GEE have shown that the RF algorithms in the supervised classification can carry out high-accuracy land cover modeling (Ghorbanian et al. 2020; Phan et al. 2020).

**Table 5.2** Land cover change information (%)

Sno.	Land cover	Hombole (7432 km <sup>2</sup> )			Melka Kunture (4390 km <sup>2</sup> )			UARB (11450 km <sup>2</sup> )		
		1987	2001	Change (%)	1987	2001	Change (%)	1987	2001	Change (%)
<b>Built-up</b>										
1	area	74.32	129.54	74.3	8.78	19.45	121.5	91.06	162.17	78.1
2	Forest	67.71	61.31	-9.4	58.91	52.50	-10.9	74.99	72.02	-4.0
3	Shrubland	413.52	466.36	12.8	206.81	231.70	12.0	745.46	747.66	0.3
4	Bare land	68.37	141.73	107.3	46.67	66.68	42.9	282.90	401.57	41.9
5	Cropland	6614.78	6389.81	-3.4	3923.69	3832.95	-2.3	9877.30	9610.13	-2.7
<b>Pasture</b>										
6	land	183.79	237.60	29.3	145.18	185.92	28.1	201.02	272.92	35.8
7	Waterbody	9.59	5.72	-40.3	-	-	-	170.93	176.61	3.3

According to Tolessa et al. (2017), forest cover declined in the western highlands while shrubland, barren land, and settlement increased. In several studies, the land cover change varies by location, but cropland is the dominant land cover in most river basins of Ethiopia (Desalegn et al. 2014; Gashaw et al. 2018; Belihu et al. 2018; Bekele et al. 2019; Tessema et al. 2020).

#### **5.4.2 The areal precipitation events and amounts**

Figure 5.3 shows the analysis of precipitation event class from 1988 to 2001 and 2002 to 2015 based on the daily precipitation amount set by the World Meteorological Organization (WMO) standard (WMO 2008). The later period (2002-2015) generally had less rainfall than the earlier period (1988 to 2001). The occurrence and amount of heavy precipitation decreased in the subbasins during the later period. In contrast, the high moderate rainfall and events increased in subbasins during the later period. The earlier period experienced greater violent downpours, raising the possibility of an intense runoff response. During both periods, the Melka Kunture subbasin received greater rainfall (except for violent rainfall) than the Hombole subbasin. Although the Hombole subbasin is larger than the Melka Kunture subbasin, the Melka Kunture subbasin rainfall amount was greater by 4.6% (667mm) and 4.5% (624mm) during the baseline and later periods, respectively. However, heavy rainfall dropped by 7.1% and 6.1% in the Melka Kunture and Hombole subbasins. Violent precipitation also dropped in the Melka Kunture and Hombole subbasins by 39.5% and 17.8%, respectively.

Based on the criteria, the Busa and Addis Ababa Obs stations were identified as the highest receiving heavy and violent rainfall in the previous period, and Addis Ababa Obs and Tullu Bollo in the later period. Busa is one of the stations that experienced a significant decrease in violent rainfall (940mm to 53mm) and events (15 to 1). Guranda Meta and Chefedonsa showed an increase in heavy rainfall in the later period compared to the earlier period. Addis Ababa Obs, Teji, Tullu Bollo, Akaki, Addis Ababa Bole, Sendafa, and Chefedonsa increased in violent rainfall. Furthermore, only Chefedonsa station experienced increased violent rainfall events and amounts. The peak discharge events at Melka Kunture (MK) (on August 22)

and Hombole (on August 20) in 1996 are significantly linked to heavy rainfall events in the preceding and on event days.

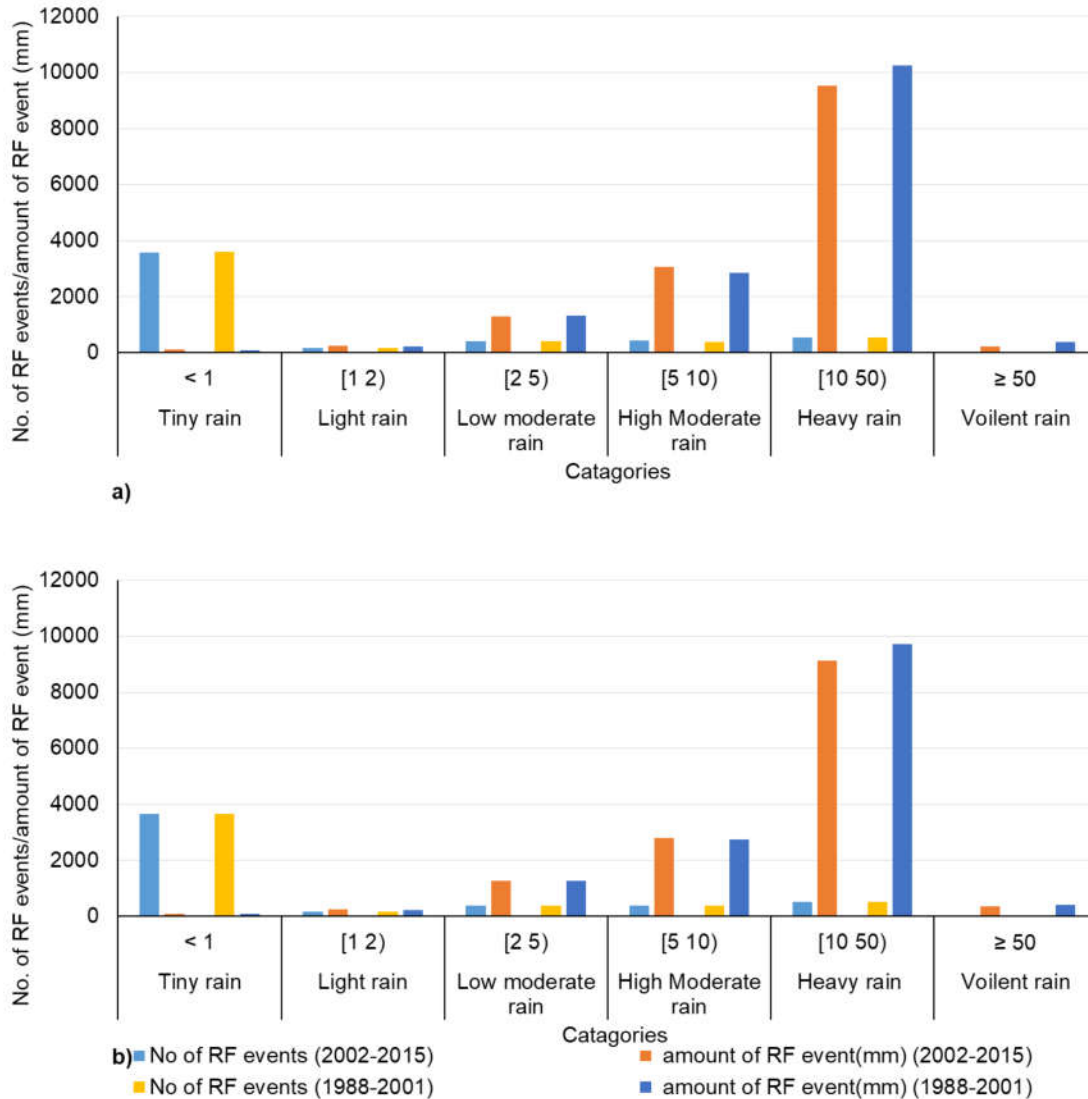


**Figure 5.3** Rainfall (RF) events and amount comparison between baseline and evaluation period in the **a)** Melka Kunture and **b)** Hombole sub-basin

### 5.4.3 Rainfall and peak flow relationship

The correlation analysis using the Pearson's product-moment correlation *cor.test* in the R package was set to observe the degree of strength between peak discharge and PRCPTOT over the total periods at the  $\alpha = 0.05$  significance level. The correlation statistic between the Hombole peak flow and the PRCPTOT over the Hombole

subbasin was 0.53, statistically significant ( $p$  value = 0.0021), and the correlation statistic between the MK peak and the PRCPTOT over the MK sub-basin was 0.2, insignificant ( $p$  value = 0.284). During the study periods (1988-2001 and 2002-2015), MK peak discharge and PRCPTOT correlation statistics showed 0.75 ( $p$  value = 0.0084) in the earlier period and 0.04 ( $p$ -value = 0.8917) in the later period. The Hombole discharge station and precipitation correlation was 0.69 ( $p$  value = 0.0172) from 1988 to 2001 and 0.1 ( $p$  value = 0.7571) from 2002 to 2015. Generally, the correlation coefficients between AM discharge and PRCPTOT in both sub-basins were significant from 1988 to 2001 and insignificant from 2002 to 2015 at  $p = 0.05$ . The analysis shows a change in the relationship between precipitation and streamflow in the latter period. This could be due to a change in land cover and the frequency of extreme precipitation (violent and heavy rainfall) in most stations in the highlands of the basin. As a result, it is reasonable to include other factors influencing hydrological processes, mainly land cover, to determine the cause of extreme discharge variability in the upper and downstream river sections.

#### **5.4.4 SWAT parameters sensitivity analysis**

The hydrology of two sub-basins was simulated in the SWAT model using the corresponding climate and land cover data from 1988 to 2001 and 2002 to 2015. The sensitive parameters that replicate the hydrology of the basin were identified. The list of the initial parameter range (maximum and minimum) and final rank of sensitive parameters from the last iteration during calibration is provided in Table 5.3. These sensitive parameters related to surface runoff generation, base flow, ground flow, and others have changed between the two periods, indicating that land surface characteristics have changed. This study considers a  $p$  value of less than 0.05 as a higher parameter sensitivity. The sensitive parameters ESCO, CH\_K2, GWQMN, and SOL\_K in the MK subbasin have been changed to not sensitive in the later period, while CN2 remains unchanged. There was also a shift in the sensitive parameter, GWQMN, in the Hombole subbasin, and the most important parameter, CN2, ALPHA\_BF, and LAT\_TTIME, later became the sensitive parameter. The significant shift in these sensitive parameters and other data such as

soil, land cover, climate, management practice, and measured data for calibration outlines the basin hydrology.

**Table 5.3** Sensitive parameter rank and calibrated range (max and min) on a daily basis in the Melka Kunture and Hombole sub-basin using 1987 and 2001 land cover

Sno.	Parameter name	Initial value		Melka Kunture		Hombole	
		Min	Max	1988-2001 using 1987 LC	2002-2015 Using 2001 LC	1988-2001 using 1987 LC	2002-2015 Using 2001 LC
1	CN2.mgt	-0.2	0.2	1*	1*	14	2*
2	ALPHA_BF.gw	0	1	17	4*	8	3*
3	GW_DELAY.gw	0	500	15	8	6	14
4	GWQMN.gw	0	5000	4*	7	2*	10
5	SOL_AWC().sol	0	1	12	13	5	6
6	SOL_K().sol	0	2000	5*	15	15	13
7	SOL_BD().sol	0.9	2.5	11	3*	10	9
8	REVAPMN.gw	0	500	16	14	18	15
9	GW_REVAP.gw	0.02	0.2	9	5*	17	17
10	ESCO.hru	0	1	2*	9	9	8
11	EPCO.hru	0	1	14	6*	16	11
12	HRU_SLP.hru	0	1	18	17	13	16
13	OV_N.hru	0.01	30	13	12	7	5
14	SURLAG.bsn	0.05	25	8	11	12	18
15	CH_K2.rte	-0.01	200	3*	10	11	12
16	RCHRG_DP.gw	0	1	7	18	1*	1*
17	LAT_TTIME.hru	0	180	6*	2*	4	4*
18	SLSUBBSN.hru	10	150	10	16	3	7

\*Sensitive parameter ( $p$  value < 0.05)

#### 5.4.5 SWAT calibration and validation for daily streamflow

Figures 5.4 and 5.5 visually compare the daily observed and simulated stream discharges at MK and Hombole stations during the calibration and validation periods in the baseline (1988-2001) and evaluation period (2002-2015), respectively. The model underestimated peak flows (during the base and evaluation periods) and slightly overestimated low flows (base period) at MK. The model also underestimated peak flows (during the base and evaluation period) at Hombole. For instance, the PRCPTOT was higher in 1996 and 2006 than in previous years, and

the observed hydrograph was much higher than the simulated. It could be due to sensitive parameter adjustments to capture the underlying changing system in the watershed. For instance, the governing peak flows CN2, ESCO, GW REVAP, and GWQMN values vary across periods for the MK subbasin. The lower the GWQMN, the higher the base flow, indicating an overestimated low flow in the base period. Compared to the base period, the lower GW\_REVAP value in the evaluation period reduced the gap between the observed and simulated low flow. The higher ESCO value indicates that peak flow was underestimated in the base period compared to the evaluation period. The results agreed with Almeida et al. (2018), who reported that the SWAT model underestimated some peaks. It is worth noting that the single peak value, in this case, affects the model's performance.

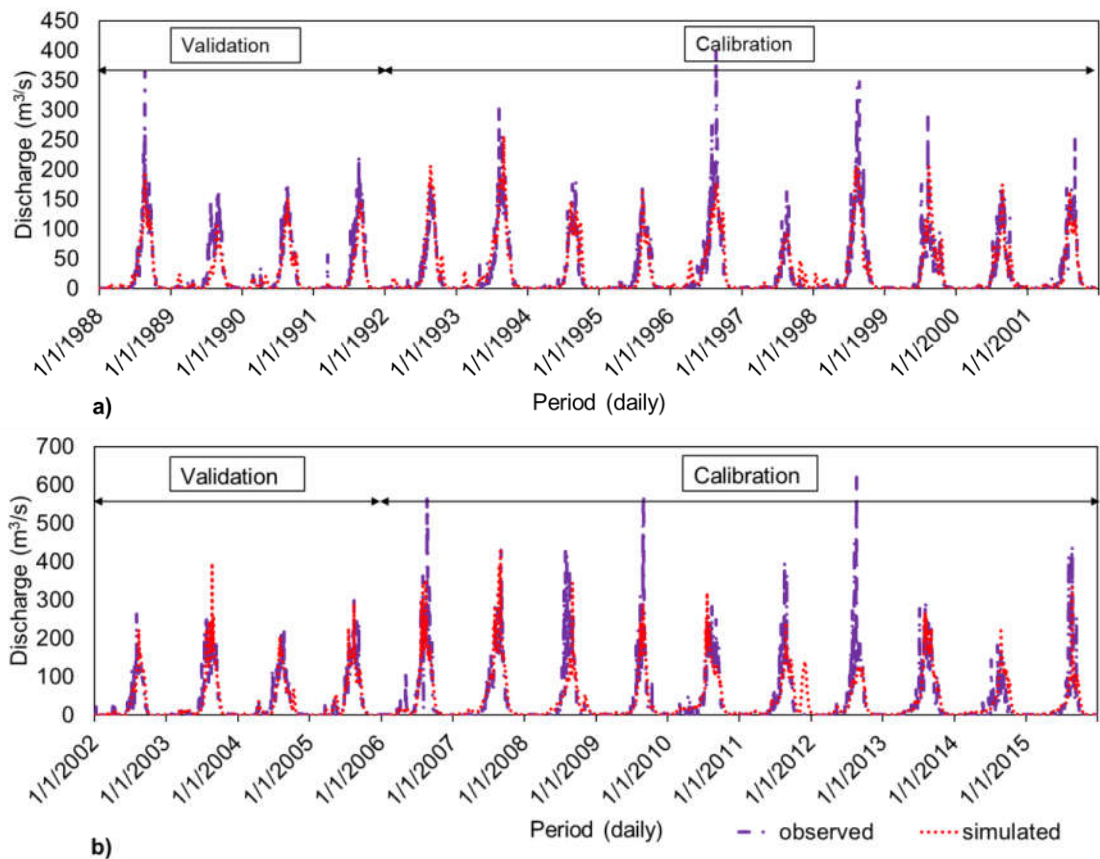


**Figure 5.4** Observed and SWAT simulated daily discharge hydrograph during calibration and validation period at MK station **a)** base period and **b)** evaluation period

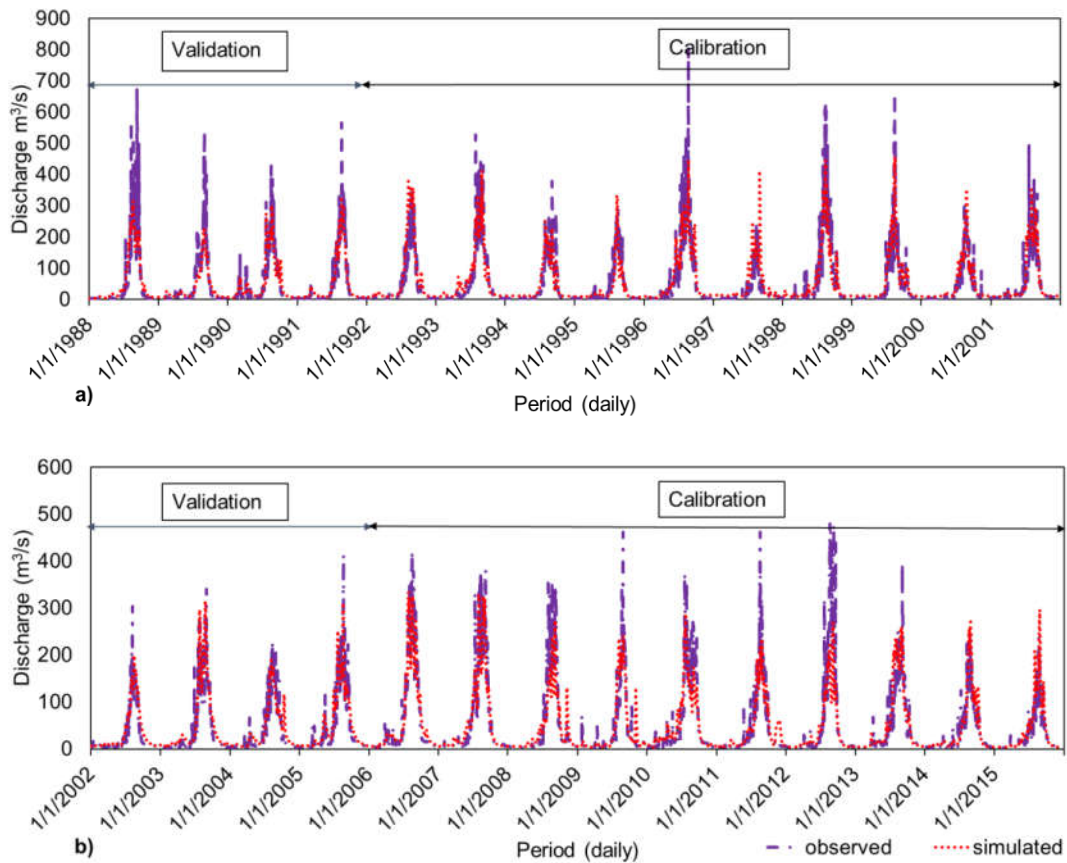


**Figure 5.5** Observed and SWAT simulated daily discharge hydrograph during calibration and validation period at Hombole **a)** baseline period and **b)** evaluation period

The NSE,  $R^2$ , and PBIAS model performance evaluation statistics and the uncertainty p-factor and r-factor values during the calibration and validation periods are provided in Table 5.4. According to the criteria set by Moriasi et al. (2007), the model performance at the gauging stations was rated as satisfactory. The performance metrics at MK and Hombole stations in the later period showed a higher negative deviation in peak flow during calibration. The SWAT model can effectively simulate daily stream discharge in the basin and represent the watershed's overall response to the climate.

**Table 5.4** Calibration and validation performance results for MK and Hombole stations during the baseline and evaluation periods

Baseline period				
Statistic s	MK station		Hombole station	
	Calibration (1993-2001)	Validation (1988-1992)	Calibration (1993-2001)	Validation (1988-1992)
NSE	0.82	0.82	0.78	0.76
PBIAS	0.6	9	-14.7	-9.2
R <sup>2</sup>	0.82	0.82	0.79	0.76
p-factor	0.75	0.67	0.78	0.81
r-factor	0.26	0.31	0.65	0.31
PEP peak	-8.7%	-7.4%	-24.5%	-19.9%
PEP high	-0.8%	-17.5%	6.6%	0.3%
Evaluation period				
Statistic s	MK station		Hombole station	
	Calibration (2007-2015)	Validation (2002-2006)	Calibration (2007-2015)	Validation (2002-2006)
NSE	0.65	0.72	0.75	0.86
PBIAS	-2.5	4.9	-2.7	-14.2
R <sup>2</sup>	0.65	0.72	0.75	0.87
p-factor	0.68	0.75	0.83	0.8
r-factor	0.47	0.8	0.51	0.52
PEP peak	-22.5%	-19.9%	-22.1%	-4.0%
PEP high	-3.0%	-0.9%	2.1%	3.1%

#### 5.4.6 SWAT model in daily flood simulation

The results of FDC segments (peak and high flow) performance evaluation metrics are summarized in Table 5.4. A negative value of the average percent error in the peak discharge (PEP) indicates that the simulated flow was underestimated, while a positive value indicates that the simulated flow was overestimated. The extreme flows at MK during the baseline and evaluation periods were underestimated during the simulation periods. The PEP for the peak flow in the evaluation period was -22.5% and -19.9% during the calibration and validation period, respectively. The

Hombole station had the highest peak flow deviation during calibration and validation. PEP for peak and high flow was -24.5% and 6.6%, respectively, in the base period and showed improvements in the latter. PEP less than  $\pm 10\%$  predominates in the calibration and validation period for peak and high flow in the base and evaluation periods, respectively.

In addition, Figure 5.6 (a-h) presents FDC for illustration purposes. The SWAT model underestimated peak flow,  $< 2\%$  of the exceedance probability flow, but flow  $< 1\%$  exceedance probability was vastly underestimated, resulting in a high negative value. However, the high flow was calibrated successfully. Except for Figure 5.6b, the high flow was almost perfectly predicted during the validation period. The SWAT model fairly captured the observed discharges but performed poorly on  $< 1\%$  of the exceedance probability flow. It is worth noting that the single peak value, in this case, negatively affected the model performance. However, it is accepted that measured data are inherently uncertain and affect model evaluation (Moriassi et al. 2007). Rainfall measurements during extreme events, the spatial resolution used to represent rainfall, and the soil scale used to describe soil type may cause the difference between the simulated and observed extreme discharges. In addition, other meteorological variables, classified land cover, input parameters that control hydrological processes, adjustment of sensitive parameters that govern peak flow elevation model, model structures simplifications, and assumptions of the natural system within the model possibly impact streamflow simulation outcomes. In general, the SWAT model can capture high and peak flow occurrence, which can then be used to evaluate the impacts of change in land cover and precipitation variability between the baseline and evaluation periods.

#### **5.4.7 Contribution of changes in land cover and rainfall variability on flood discharge**

The peak and high discharge simulations for different scenarios are shown in Table 5.5. The quantity of flow that increased and decreased based on the designed scenario varied widely at the sub-basin level. In the MK sub-basin, the peak and high flows increased under scenario 3. In Scenario 4, both the peak and high flow

significantly increased. As observed, a change in land cover increased extreme flow, while a change in rainfall decreased peak flow. The land cover change (Scenarios 1 and 4) accounts for about 38.69% of the peak flow increment and about 11.95% of the high flow increment compared to the combined climate and land cover change (14.34% for peak and 12.25% for high flow) (Scenarios 1 and 3). In the Hombole sub-basin, in comparison between scenarios 1 and 3, peak and high flow discharge decreased. Peak and high discharge decreased slightly in Scenario 2, when only the change in rainfall was taken into account.

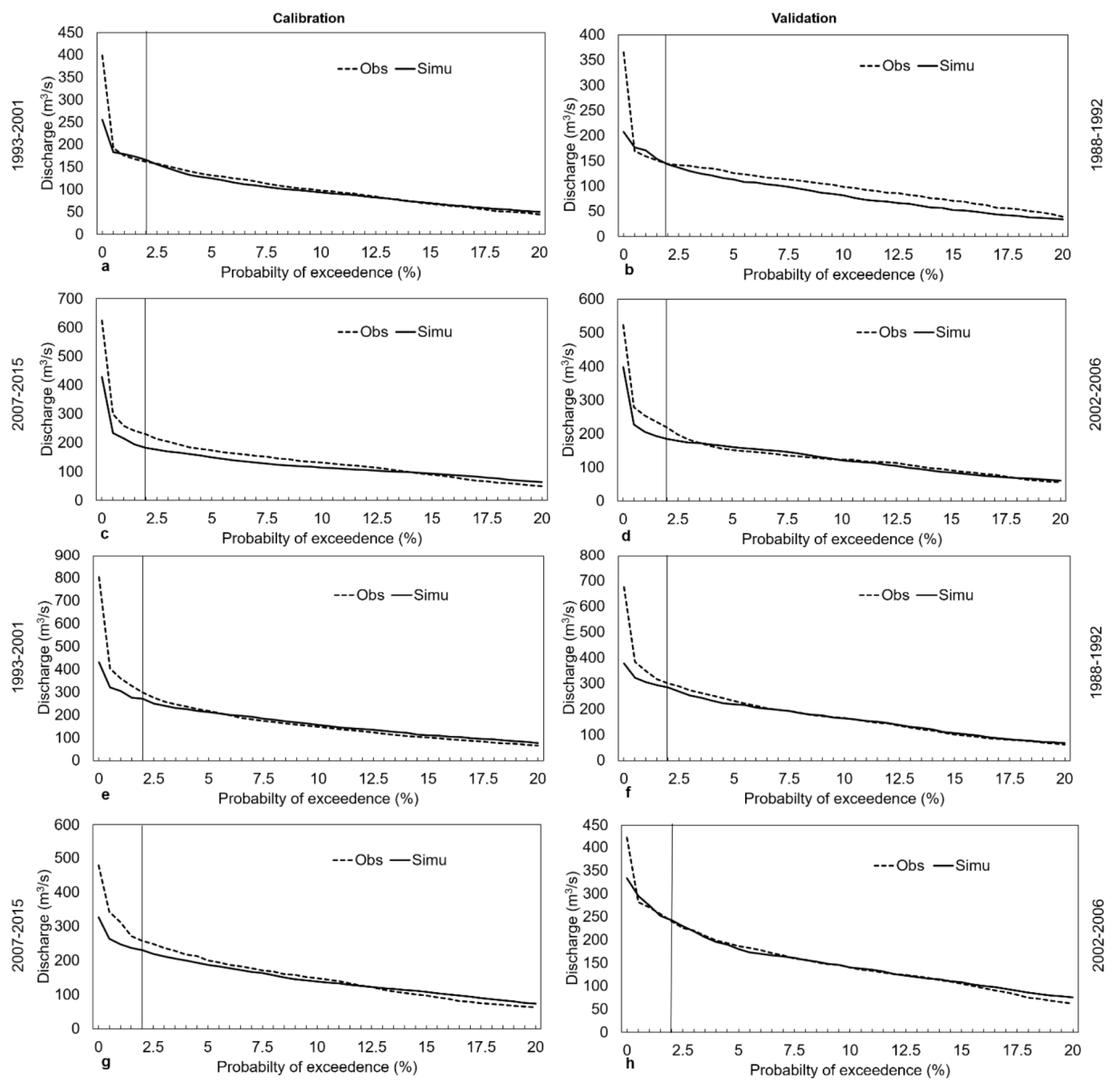


**Figure 5.6** FDC observed and simulated during the calibration and validation period at **a-d)** MK and **e-h)** Hombole. FDC for peak (< 2 % of the exceedance probability flow) and high flow (2 to 20% of the exceedance probability flow) at MK station during the **a-b)** baseline and **c-d)** evaluation period; FDC for peak (< 2 % of the exceedance probability flow) and high flow (2 to 20% of the exceedance probability flow) at Hombole station during the **e-f)** baseline and **g-h)** evaluation period

Under scenario 4, peak discharge increased, and high discharge reduced. Based on this analysis, climate variability decreased extreme flows while the change in land cover increased/amplified peak flow. The peak and high flow were reduced due to combined climate and land cover change, making up approximately 19.55% and 50.33%, respectively, similar to the decrease in the PRCPTOT trend over the subbasin/basin. The combined effect of climate and land cover changes (Scenario 3) contributed more to high flow decrease than land cover changes alone (Scenario 4). The change in land cover (Scenarios 1 and 4) alone increased peak flow by 9.93%. It is noticeable that even though the land cover and climate variability influenced peak and high flows in both sub-basins, land cover vastly outweighed climate variability as a factor in the change of river discharges, especially in the flooding MK subbasin. However, it is apparent that heavy rainfall dropped by 7.1% and 6.1% in MK and Hombole subbasins, respectively, during the later period (2002–2015). Additionally, violent precipitation dropped in the sub-basins (by 39.5% and 17.8%). Thus, results showed that although land cover and climate variability decreased extreme flow in the downstream reach, land cover change alone increased the upstream flow.

The result agrees with the basin's previous study in terms of surface runoff response to land cover change (Shawul et al. 2019). Similarly, Mitiku et al. (2023) noted that the combined effects of change in land use and climate variability under future scenarios would likely intensify the flooding in the basin. However, climate variability would be higher than the land cover change, impacting streamflow in the UARB during the rainy season. A similar report has been issued, stating that cropland areas contribute more to surface runoff (Gashaw et al. 2018; Belihu et al.

2020). This is consistent with the results obtained elsewhere by Panahi et al. (2010) and Hounkpè et al. (2019), that peak flow is sensitive to the cropland/agricultural land. Thus, the combination of intense precipitation in the highlands with land cover (mainly cropland), Vertisols soil, and the basin's geomorphological features are possibly responsible for the greater magnitude of flood response. As a result, the volume and speed of water in the river system increase, heightening the risk of flooding. The study confirms that land cover change is to blame for the variation in the flood, mostly upstream of the basin.

**Table 5.5** Contribution of land cover and climate variability on peak and high flow in the MK and Hombole sub-basin

Scenarios	MK sub-basin		Hombole sub-basin	
	Avg. Peak flow	Avg. High flow	Avg. Peak flow	Avg. High flow
	(m <sup>3</sup> /s)	(m <sup>3</sup> /s)	(m <sup>3</sup> /s)	(m <sup>3</sup> /s)
Scen. 1	240.75	89.36	335.25	166.28
Scen. 2	213.45	98.76	318.38	152.74
Scen. 3	275.28	100.3	269.73	82.59
Scen. 4	333.9	100.03	368.55	92.1
$\vartheta_c$ (%)	-11.34	10.52	-5.03	-8.14
$R_{lc}$ (%)	14.34	12.25	-19.55	-50.33
$\vartheta_1$ (%)	38.69	11.95	9.93	-44.62

## 5.5 Conclusions

The individual and combined impacts of land cover change and climate variability were investigated in this chapter by separating the entire period into two sections: 1988-2001 and 2002-2015. Different scenarios were designed to identify potential variables that affected peak and high flows at the two main hydrological stations, and the SWAT hydrological model was used to simulate the designed scenarios. The conclusions are summarized as follows:

At MK and downstream Hombole stations, the significant correlation coefficient between the annual peak flow and annual wet day precipitation was 0.69 ( $p$  value =

0.0172) and 0.75 ( $p$  value = 0.0084) for the base period (from 1988 to 2001), respectively, and the later (from 2002 to 2015) had none, indicating a change in rainfall streamflow relationship.

Daily simulation of the SWAT results at two sub-basins during the base and evaluation period was satisfactory. In general, the model gave well-estimated peak and high flood discharges. Simulation in the upstream sub-basin indicated that the land cover change alone scenario with cropland dominating land cover was the prime contributor to peak and high flow increases of 38.69 % and 11.95%, respectively, in the later period. For high flow, the combined scenarios also contributed similarly to LC changes. The MK sub-basin experienced more heavy rainfall in the later period than the Hombole sub-basin, which could be attributed to higher rainfall in the western and northern highlands. This implies that heavy and violent rainfall coupled with land cover-cropland is the mechanism for increased surface runoff and eventually causes flooding in this region. The combined scenario was the leading cause, accounting for 19.55 % and 50.33 % of the decrease in peak and high flow in the downstream Hombole sub-basin over the later period. Cropland-dominated land cover produced a pronounced peak flow in the subbasins under stable climatic conditions. It is recommended that uncertainty analysis of land cover classification and its effect on change detection needs further analysis. The SWAT model input and related uncertainty analysis are critical for a better decision-making process.

## **CHAPTER 6**

### **FLOOD SUSCEPTIBILITY MODELING USING MORPHOMETRIC AND FLOOD HAZARD MAPPING OF THE HIGHLY SUSCEPTIBLE FLOOD AREA**

#### **6.1 Introduction**

In addition to climate and land cover change's impact on floods, watershed characteristics also affect flood movement and accumulation. Reasonable rare flood quantile estimates are the basis for better flood hazard assessment and management. In this case, nonstationary flood frequency is significantly important in flood hazard assessment. The chapter investigates the spatial flood characteristics using the watershed features and identifies the flood-susceptible subbasins and flood-potential areas. It also provides a flood hazard map of the very susceptible area.

##### **6.1.1 Morphometry**

Flood management requires various quantitative and qualitative flood conditioning factors. Horton (1932,1945), Strahler (1952,1964), and Schumm (1956) pioneered the development of several quantitative descriptive parameters of watershed characteristics to infer the behaviour of hydrological response and interaction between rainfall and earth that is a rapid or delayed. Floods are linked to the watershed system's unique characteristics and rising human activity, such as urbanization, ecosystem degradation, and climate change (Berz et al. 2001). Systematic evaluation based on strong relationships between hydrological and physiographic characteristics is thought to be computationally simple (Bhat et al. 2019).

Several researchers have used morphometric indices as a practical tool for describing the watershed, identifying flash flood hazard zones, quantifying soil erosion, evaluating the watershed, water recharge area, rainwater harvesting, and

other purposes in recent years (Angillieri 2012; Patel et al. 2012; Esper Angillieri and Perucca 2014; Rais and Javed 2014; Pande and Moharir 2017; Choudhari et al. 2018). The expanded role has implications for watershed management and mitigation measures such as water and soil conservation (Asfaw and Workineh 2019) and improving flood predictions with parameters (Patton and Baker 1976).

Flood susceptibility, for example, was determined using morphometric criteria that agreed with their flood capacity (Altaf et al. 2013; Meraj et al. 2015; Singh and Kumar 2019; Bhat et al. 2019; Mahala 2020). The linear parameters, such as drainage pattern, stream order, stream length, bifurcation ratio, and length of overland flow; areal parameters, such as drainage density, circularity ratio, elongation ratio, stream frequency, form factor and relief parameters such as basin relief, relative relief, relief ratio, dissection and ruggedness index, among others, are directly or inversely linked to hydrological response (Meraj et al. 2015; Taha et al. 2017; Elsadek et al. 2019; Singh and Kumar 2019). The morphometric analysis reflects the physiographic, soil, underlay control structure, and flow features. It is still necessary to better understand basin hydrological response behaviour and the hazard level for flood management and mitigation planning.

### **6.1.2 Flood hazard**

Flood hazard analysis in the changing environment is critical for management plans and future flood risk reduction. It is well accepted that there has been a significant shift in the magnitude and frequency of extreme flood and precipitation events in recent decades due to climate variability, rainfall intensities, temperature change, and land cover changes (Panahi et al. 2010; Kundzewicz et al. 2014; Salas and Obeysekera 2014). Flood hazard mapping often employs flood frequency models that rely on the stationary assumption of the data, meaning that the data is devoid of trends and shifts. Changes in flow characteristics could indeed intensify the frequency and magnitude of flooding and inundation in unforeseen ways.

As an alternative to stationary-based frequency analysis, the nonstationary frequency method has recently gained popularity (Šraj et al. 2016; Šraj and Bezak

2020). Nonstationary frequency analysis adjusts the probability distribution parameters based on physical covariates that are thought to be associated with and responsible for changes in extreme hydrological events (Salas and Obeysekera 2014; Šraj and Bezak 2020). Therefore, reported timely changing of flood characteristics owing to climate change requires enhanced estimates of the probabilities of rare flood events. In general, in practical flood hazard management, stationary-based models may underpredict floods and fail to account for covariates that may influence floodwater. Therefore, to achieve greater accuracy in flood hazard assessment and consequent risk, the best-fit models and covariates that explain the flood are crucial for improving the estimates of the probability of rare floods. In this regard, reasonable flood estimates are a significant advantage in flood-prone areas for flood hazard management of recurring rare extreme events (low probability).

## **6.2 Data and methodology**

### **6.2.1 Flood susceptibility modeling**

Figure 6.1 shows the flowchart for flood susceptibility modeling using geomorphometric parameters. The morphometric analysis was performed in ArcMap 10.3 software using the Spatial Analyst Tool with DEM input and the projected coordinate system WGS 1984 UTM Zone 37N. Subtools were utilized in the Hydrology tool, such as fill-to-fill sinks in DEM, flow direction, flow accumulation, watershed, stream link, stream order, surface tools to derive slope, map algebra for the raster calculator, and density tools to form line density, among others.

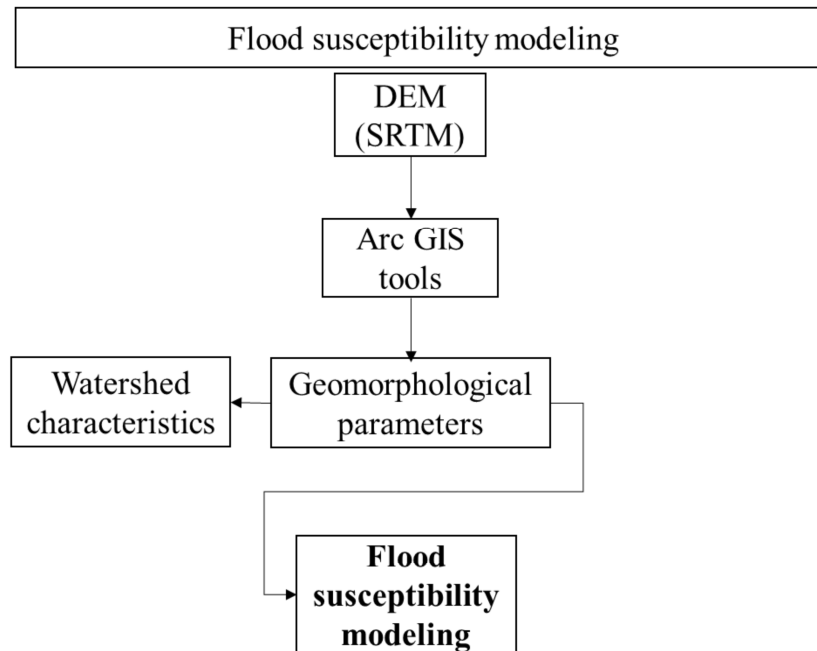


**Figure 6.1** Flowchart for flood susceptibility modeling using geomorphometric parameters

For the present study, the stream network was created by applying a threshold value of 100 DEM cells ( $0.835 \text{ km}^2$ ). The UARB was divided into four subbasins, subbasin 1 (SB-1), subbasin 2 (SB-2), subbasin 3 (SB-3), and subbasin 4 (SB-4) based on stream order, with the junction point of stream order six being utilized to distinguish the subbasins. The subbasin area ranges from  $1630 \text{ km}^2$  to  $4848.5 \text{ km}^2$ . The areas of SB-1, SB-2, SB-3, and SB-4 are  $4848.5$ ,  $1630$ ,  $2112.21$ , and  $2838.52 \text{ km}^2$  respectively.

The literature has demonstrated that hydrological parameters correlate with the physical characteristics of a drainage basin. Altaf et al. (2013) used 21 physical parameters of drainage basins (drainage density, bifurcation ratio, elongation ratio, circularity ratio, length, etc.) to characterize the hydrologic response of 17 sub-watersheds. They commonly used aspects directly proportional, such as stream order, total stream number, total stream length, drainage density, bifurcation ratio, stream frequency, circularity ratio, texture ratio, infiltration number, basin relief, relief ratio, and slope. Indirectly proportional, such as basin length, length of overland flow, compactness coefficient, and elongation ratio, are partly related to

hydrological response and sediment. Based on the derived drainage network of the basin, twenty-three morphometric parameters were calculated based on their corresponding formula (Horton 1932, 1945; Strahler 1952, 1964; Schumm 1956) and are presented in Table 6.1. The stream order of the basin was attained by using Strahler (1964). Basin area and perimeter were also computed using calculate geometry in the attribute table. The basin length was calculated according to Nooka Ratnam et al. (2005).

The flood conditioning indexes, including the Topographic Wetness Index (TWI) and Topographic Position Index (TPI), were used in this study to identify the specific location and inundated areas. TWI generally shows the flow accumulation due to the topography effect at a specific position in the basin (Moore et al. 1991). TPI shows the elevation difference effect on flow generation and accumulation. Higher elevation is an attribute of minor inundation, and lower elevation is an attribute of flood accumulation (Kanani-Sadat et al. 2019). TWI and TPI have been used for flood vulnerability mapping (Kanani-Sadat et al. 2019; Popa et al. 2019).

The ranking score approach was used to determine each subbasin's degree of flood susceptibility (Singh and Kumar 2019). Three standardized classes were determined for each parameter using a simple statistical approach: the difference of maximum and minimum parameter values divided by three. Depending on the degree of relationship with flood vulnerability, rank was assigned to individual parameters; for instance, rank 1 was given to a low degree and 3 was given to a high degree. Morphometric parameters directly related to flooding such that higher parameter values ranked higher, and parameters indirectly proportion were ranked such that higher values ranked lower. A total summation of the assigned value was ranged to prioritize the subbasin potentially susceptible to a flood as low, moderate, and high. In addition to the flood-susceptible information provided by these variables, coupling the flood conditioning indices (TWI and TPI) through overlay tool in Arc GIS-weighted overlay analysis was carried out to identify the specific flood-susceptible areas within the subbasins. Weighted overlay analysis is one approach to modeling suitability; in this regard, a flood-prone location. Raster layers are used as input (TWI and TPI), and each layer is assigned a weight for flood-prone location

analysis. The raster layers are overlaid, multiplying each raster cell's by its layer weight. Giving importance to each raster in the overlay process allows the control of the influence of different criteria in identifying the flood-prone location. In this study, the two raster cells were allocated 55% weight for TWI and 45% weight for TPI. TWI is given higher weightage as this flood condition factor is more sensitive and has a higher influence than the TPI in locating flood-prone areas. Weighted values are totaled for each overlaying cell and then written to an output layer and values in the rasters are reclassified to a scale of low, medium, and high flood-prone areas. Each area under this scale is calculated and used to identify the subbasin's high susceptibility to flood.

**Table 6.1** Morphometric parameters, formula, unit, and references

Sr no.	Aspects	Morphometric parameters and Symbol	Formula and Unit	References
1	linear	Stream order ( $S_u$ )	Hierarchical ranking	Strahler (1952)
2		Stream number ( $N_u$ )	$N_u = N_1 + N_2 + N_3 \dots N_u$	Horton (1945)
3		Stream length ( $L_u$ )	$L_u = L_1 + L_2 + L_3 \dots L_u$ (Km)	Strahler (1964) Nooka Ratnam et al. (2005)
4		Basin length ( $L_b$ )	$L_b = 1.312 A^{0.568}$ $L_b =$ Length of basin(km), $A =$ Area of the basin ( $km^2$ )	
5		Stream length ratio ( $R_l$ )	$R_l = L_u / L_{u-1}$ $L_{um} =$ Total stream length of order u $L_{u-1} =$ Total stream length of its next lower order	Horton (1945)
6		Mean stream length ( $L_{um}$ )	$L_u = L_u / N_u$ (Km)	Strahler (1964)
7		Bifurcation ratio ( $R_b$ )	$R_b = N_u / N_{u+1}$	Schumm (1956)
8		RHO	$RHO = R_l / R_b$	Horton (1945)
9	Areal	Basin area ( $A$ )	Area of the basin ( $Km^2$ )	Horton (1945)
10		Basin perimeter ( $P$ )	Perimeter of the basin (Km)	Horton (1945)

**Table 6.1 (Cont...)**

11		Drainage density (D <sub>d</sub> )	$D_d = L_u/A(\text{km}/\text{km}^2)$	Horton (1932)
12		Stream frequency (F <sub>s</sub> )	$F_s = N_u/A (N_u / \text{km}^2)$	Horton (1932)
13		Texture ratio (R <sub>t</sub> )	$R_t = N_u/P (N_u / \text{km})$	Horton (1945)
14		Elongation ratio (R <sub>e</sub> )	$R_e = (2/L_b) \times \sqrt{A/\pi}$	Schumm (1956)
15		Circularity ratio (R <sub>c</sub> )	$R_c = 4 \times \pi \times A/P^2$	Strahler (1964)
16		length of overland flow (l <sub>o</sub> )	$l_o = 0.5/D_d (\text{km}/\text{km}^2)$	Horton (1945)
17		Compactness ratio (C <sub>c</sub> )	$C_c = 0.2821P/\sqrt{A}$	Horton (1945)
18	Relief	Basin relief (H)	H(m) H = highest H – Lowest	Strahler (1952)
19		Relief ratio (R <sub>r</sub> )	$R_r = H/L_b (\text{m}/\text{Km})$	Schumm (1956)
20		Slope (S)	Slope (degree)	Kabenge et al. (2017)
21		Infiltration number (I <sub>f</sub> )	$I_f = D_d * F_s$	Alqahtani and Qaddah (2019)
22		Topographic Wetness index (TWI)	$TWI = \ln(A_s/\tan(\beta))$ A <sub>s</sub> = Specific catchment area, β = slope in radians	Beven and Kirkby (1979)
23		Topographic Position Index (TPI)	$TPI = Z_0 - \sum_{i=1}^n Z_i/n$ Z <sub>0</sub> = Elevation of the model input Z <sub>i</sub> = Elevation of cell n = Elevation neighbouring cells	Weiss (2001)

### 6.2.2 Flood hazard mapping

Figure 6.2 shows the overall methodology for flood hazard mapping using nonstationary flood frequency model. Holeta (1981–2009), Berga (1981–2010),

and Ginchi (1993–2010) rivers are located upstream of the floodplain and serve as important monitoring stations (Figure 3.1). These river tributaries combine to form the main Awash River. Furthermore, no hydrological station exists below the floodplain that could be used for calibration. Annual daily peak flood data were extracted to characterize the flow and flood modeling. It was chosen because the annual maximum flood sequence is simple to extract, can be considered independent, and can be fitted to a probability distribution function such as generalized extreme value (GEV) (Coles 2001). An alternative is a peak over threshold, which is more complicated and less common because selecting the appropriate threshold is not straightforward, possibly subjective, and may not be fully independent events.

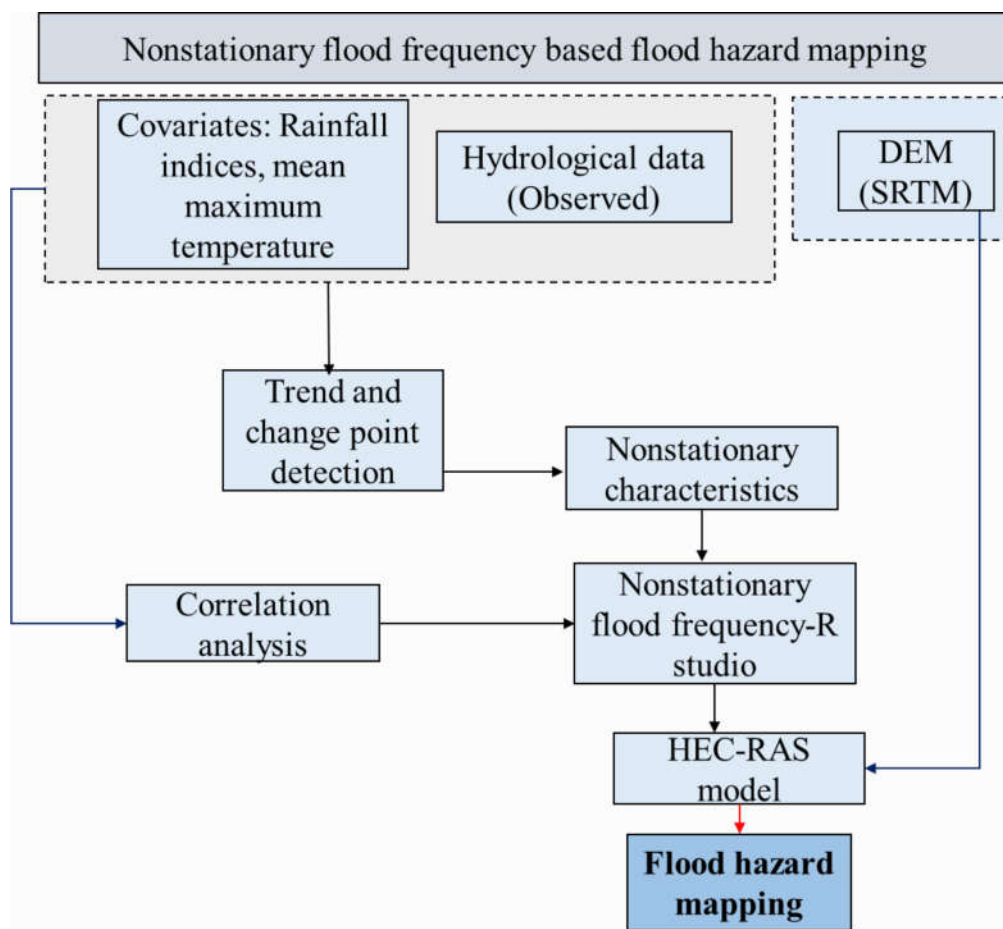


**Figure 6.2** Flowchart for flood hazard mapping using nonstationary flood frequency model

The flood record length is another concern in flood frequency analysis (FFA), and it is the most common challenge in developing countries like Ethiopia, where it is typically limited to not exceeding 30 years. This is true for Upper Awash. However, FFA is performed using 10 or more years and is often limited to 30 years, with only a few exceptions reaching 90 years (Opere et al. 2006; Kobierska et al. 2018). The lack of data affects longer return period flood estimation, resulting in larger uncertainty (Bobée et al. 1993). This study assumes that the period is satisfactory to estimate the 25 and 50-year floods but that the 100-year flood is uncertain. The 100-year flood is considered in this study because flood protection works, like levees, are designed using an estimate of the 100-year flood quantile.

#### **6.2.2.1 Covariates**

In the nonstationary FFA, the distributional frequency parameters are modeled as a function of covariates. In this study, climatic variables such as monthly rainfall in August (R1), monthly rainfall in July and August (R2), monthly rainfall from June to August (R3), monthly rainfall from July to September (R4), annual rainfall (R12), annual total rainfall from wet days (R12e), annual mean maximum temperature, and time were examined (sequence of hydroclimatic years) as a covariate in the location parameter. The R1, R2, R3, R4, R12, and R12e values are computed from the areal precipitation using the Thiessen polygon for corresponding years of discharge data length. Besides, the variables were established based on the date of maximum flow events; for example, about 17.2%, 58.3%, and 24.5% of peak floods occurred in July, August, and September at Ginchi and Holeta stations, respectively. In addition, Berga hydro station experienced 33.3% in July, 53.3% in August, and 13.3% in September. Most rainfall occurs during these months, with a peak in August. The annual total rainfall from wet days (PRCPTOT) (i.e.,  $\geq 1\text{mm}$ ) from extreme precipitation indices was used to reflect the aspect of extreme. Hereafter, the R12e and PRCPTOT are used interchangeably.

#### **6.2.2.2 Statistical tests**

In nonstationary flood frequency, linear combinations of covariates and flood events are considered, and the significance of the association and the relevant

covariate variables (high correlation) must be determined. Pearson’s product-moment correlation test, “cor. Test”, was run using the R software to examine the relationships between the covariates and annual maximum peak flow at 5% significance level. It has the advantage of considering the linear associations between two variables. The correlation coefficient levels range from -1 to 1, with close to 0 indicating a weak correlation, close to 1 indicating a strong correlation, > 0 indicating a positive correlation, and < 0 showing a negative correlation.

Moreover, it is also critical for nonstationary flood frequency analysis to assess nonstationary behaviour in the form of long-term trends and change points in the hydroclimatic series. Preliminary detection of trend and change point analysis of the climatic variables and annual peak flood was performed to demonstrate empirically that changes in the extreme series occur. A robust non-parametric modified Mann-Kendall (MMK) trend test was used for this study. A non-parametric Pettitt’s test (Pettitt 1979) was also used to detect the abrupt change in the mean/variance of the data series. This test does not require that the data follow a specific distribution and can detect the year in which the change occurred. Furthermore, the “modifiedmk” and “trend” packages in R were used to identify trends and changes in the data. When the alpha value is less than 0.05, significance is detected.

### 6.2.2.3 Nonstationary frequency analysis

The three-parametric GEV distribution is one of the most widely used in the nonstationary extreme analysis because of its flexibility in covariate inclusions and expressing the cumulative distribution and quantile function (Salas and Obeysekera 2014; Šraj et al. 2016; Šraj and Bezak 2020). Equations 6.1 and 6.2 give the cumulative density function and quantile function of the GEV distribution, respectively.

$$F(x) = \exp \left\{ - \left[ 1 + \xi \left( \frac{x - \mu}{\sigma} \right) \right]^{-1/\xi} \right\} \quad (6.1)$$

$$x_T = \mu + \frac{\sigma}{\xi} \left[ 1 - \left( \ln \frac{T}{T-1} \right)^\xi \right] \quad (6.2)$$

Where  $\mu$ ,  $\sigma$ ,  $\xi$  and T denote location, scale, shape parameters and return period (years), respectively. Under the nonstationary framework, using the package “extRemes” – Weather and Climate Applications of Extreme Value Analysis (EVA) (Gilleland and Katz 2016), the GEV distribution location parameter is allowed to vary linearly with climate variables and time. Furthermore, a multivariate model that includes both climate and time was incorporated to improve flood estimates and fit the model. The rainfall amounts of different duration data, annual mean maximum temperature, and time are combined with the corresponding discharge data length. Parameters estimation through a maximum likelihood estimator (MLE) has been widely used in literature (Salas and Obeysekera 2014). In this study, the scale and shape parameters are assumed to be trend-independent, with the shape parameter being notably difficult to estimate (Coles 2001; Salas and Obeysekera 2014). In the nonstationary framework, the relationship between the location parameter and covariates is presented in Table 6.2. The best fit of the proposed GEV models is chosen using the Akaike Information Criterion (AIC) (Akaike 1974). AIC measures the predicted relative distance between two models and is commonly used in hydrology to identify the best model among competing models. The preference for an optimal frequency model from competing models that account for covariates and time-independent distributions entails identifying explanatory variables and the link function between the parameter and covariates, i.e., linear or multiple linear regression. These tests are performed when the parameter estimation is based on the MLE. The smaller the AIC value, the best the fit for a given model. The “extRemes” R package was also used to compute the parameters estimation and performance criteria.

#### 6.2.2.4 Flood hazard classification and mapping

Flood potential depth and velocity or combinations are principal parameters in the flood hazard assessment. HEC-RAS (Hydrological Engineering Centre – River Analysis System) 6.2 is a hydraulic model developed by the US Army Corps of Engineers to model river flow. It is the most commonly used flood mapping model (Roy et al. 2021; Vasconcellos et al. 2021). The model can simulate one-dimensional (1D), two-dimensional (2D) hydrodynamics, steady simulations, unsteady simulations, sediment transport, and water quality. As a preliminary study, 1D steady flow calculation was employed.

The steady flow 1D energy equation, known as Bernoulli’s equation, is used to compute 1D steady flow (Equation 6.3). The energy equation is solved iteratively from one cross-section to the next and downstream water surface elevation is required for each profile to be computed. The known water surface, the critical depth, the normal depth (Manning’s equation), and the rating curve can all be used as boundary conditions at the downstream water surface elevation.

**Table 6.2** Flood frequency models used in this study

Model	Covariates	Equations
1 GEV	all parameters are constant location parameter as a function of monthly precipitation of Aug.	$\mu, \sigma,$ and $\xi = \text{constant}$ $\mu(R1) = \mu_0 + \mu_1 R1, \sigma$ and $\xi$ $= \text{constant}$
2 GEV(R1)	location parameter as a function of monthly precipitation of JA	$\mu(R2) = \mu_0 + \mu_1 R2, \sigma$ and $\xi$ $= \text{constant}$
3 GEV(R2)		

**Table 6.2 (Cont...)**

		location parameter as a	
		function of monthly	$\mu(R3) = \mu_0 + \mu_1 R3, \sigma$ and $\xi$
4	GEV(R3)	precipitation of JJA	= constant
		location parameter as a	
		function of monthly	$\mu(R4) = \mu_0 + \mu_1 R4, \sigma,$ and $\xi$
5	GEV(R4)	precipitation of JAS	= constant
		location parameter as a	
		function of annual	$\mu(R12) = \mu_0 + \mu_1 R12, \sigma$
6	GEV(R12)	precipitation	and $\xi =$ constant
		location parameter as a	
		function of annual wet-day	$\mu(R12e) = \mu_0 + \mu_1 R12e,$
7	GEV(R12e)	precipitation	$\sigma$ and $\xi =$ constant
		location parameter as a	
		function of annual	$\mu(R12+T12) = \mu_0 +$
		precipitation and	$\mu_1 R12 + \mu_2 T12, \sigma$ and $\xi =$
8	GEV(R12+T12)	temperature	constant
		location parameter as a	$\mu(R12+t) = \mu_0 +$
		function of annual	$\mu_1 R12 + \mu_2 t, \sigma$ and $\xi =$
9	GEV(R12+ t)	precipitation and time	constant
			$\mu(R12e+T12) = \mu_0 +$
		location parameter as a	$\mu_1 R12e + \mu_2 T12, \sigma$ and $\xi =$
10	GEV(R12e+T12)	function of annual wet-day	constant

		precipitation and temperature	
		location parameter as a function of annual wet-day precipitation and time	$\mu(R12+t) = \mu_0 + \mu_1 R12e+\mu_2 t$ , $\sigma$ and $\xi =$ constant
11	GEV(R12e+ t)		

The simple method for determining downstream boundary conditions is calculating the normal depth using the downstream slope, measured at the river's downstream reach. The flow conditions represent upstream boundary conditions.

$$Z_2 + Y_2 + \frac{a_2 V_2^2}{2g} = Z_1 + Y_1 + \frac{a_1 V_1^2}{2g} + h_e \quad (6.3)$$

where

$Z$  = Elevation of the main channel inverts at cross sections 1 and 2

$Y$  = Depth of water at cross sections 1 and 2

$V$  = Average velocity of water (Q/A)

$\alpha$  = Velocity weighting coefficients

$g$  = Gravitational acceleration

$h_e$  = Energy losses from cross section 2 to 1. (Friction losses ( $h_f$ ) and contraction/expansion losses ( $h_{ce}$ ))

$h_f$  = Friction losses  $h_f = LS_f$

$L$  = weighted average distance between cross sections

$$h_{ce} = \text{Contraction and expansion losses } h_{ce} = C \left( \frac{a_1 V_1^2}{2g} - \frac{a_2 V_2^2}{2g} \right)$$

$C$  = Contraction or expansion loss coefficient

Remote sensing data, such as terrain information, are the primary input for hydrological models used in flood hazard mapping. Multiple free sources of topographic data with varying acquisition techniques and resolutions are available. However, open-source elevation models are sensitive to vertical accuracy, which affects modeling accuracy and simulation outputs, for instance, flood depth, velocity, and extent overestimation or underestimation. A 30m resolution SRTM digital elevation model from the US geological survey for the specific floodplain area was imported and projected in the HEC-RAS model using the RAS-Mapper interface. The built-in RAS mapper offers hydraulic modeling tools with geospatial capabilities. The tool assists the user in creating geometries (river networks, cross-sections, cross-section parameters, 2D flow area, structures, etc.) over DEM and visualizing simulation results (water surface depths, velocity, inundation boundary, etc.). Furthermore, the Map layer tool displays background web imagery, such as Google satellite or a reference layer related to the project. It can be used to display inundation map boundary maps. Geometric data such as river networks, bank lines, flow paths, cross sections, and flood paths representing the river system were plotted. Based on visual inspection of both channel and floodplain characteristics, Manning's  $n$  (Chow 1959) value for both banks and the main channel was set to 0.035 and 0.033, respectively. These values are specified based on land cover, cropland land, and the earth channel, which is clean and irregular due to erosion.

The combined Berga and Ginchi flows were pooled as a single tributary on the right side as an upstream boundary because the two rivers meet before the main Awash River, and the Holeta River flows as a single upstream boundary. The combination of three rivers forms the main Awash river flow. Estimates of flood quantiles over various return periods (probability of extreme events) are essential in hazard evaluation. The best fit nonstationary condition was used to predict each station's flood quantiles of different return periods. The T-year flood estimate using the

stationary model is related to probability  $p$  ( $T = 1/p$ ) that exceeds the design flood quantile  $X_T$  each year and remains constant. However, the exceedance probability  $p$  is associated with flood changes yearly for nonstationary conditions (Salas and Obeysekera 2014). The estimated flood quantiles of return periods, 2, 25, 50, and 100 years flood, and downstream boundary condition, i.e., normal depth slope of 0.002 (the downstream slope measured at the downstream portion of the river for normal depth calculation), were then entered into the river cross-sections. After successfully entering geometry and flow data, the simulation of steady flow water surface profiles was performed.

Floodwater depths are computed by subtracting terrain elevation from spatially interpolated water surface elevation at each cross-section. The 1D model simulation generates horizontally and vertically averaged velocities for each cross-sectional area (main channel, left and right overbank area). The velocity can be further discretized based on cross-section conveyance (shape and roughness value) and the assumption that flow is perpendicular to the cross-section. The floodwater depth map is derived from water and terrain elevation differences. The computed velocities at each cross-section are used to generate 1D spatially interpolated velocity results. The inundation boundary map type generates a polygon boundary at the zero-depth contour when comparing the water surface elevation to the associated Terrain layer. The depth, velocity, and inundation boundary of individual quantile profiles are then visualized in the RAS Mapper. All simulation results were exported to Arc GIS through the export layer options for further analysis and development of a flood hazard map.

The flood hazard level developed for the Becho floodplain area is based on flood depth and combinations of flood depth and velocity (product of depth and velocity). Smith et al. (2014) developed a flood hazard classification method based on the product of floodwater depth and velocity used in this study. The method applied flood depth and velocity thresholds related to the stability of people, vehicles, and buildings to develop flood hazard classification based on the particular vulnerability thresholds. The combined-based flood hazard classification offers more details on different flood hazard levels to people, vehicles, and structures than a single

parameter (depth alone). A combination of flood depth and velocity-based flood hazard assessment in flood-prone areas is advantageous in determining the relative degree of flood hazard in a floodplain without the need to understand what is at risk specifically. This improves the area's flood hazard management practice, emergency management, and land use planning in the future. Several studies have used this method to classify flood hazards (Binh et al. 2019; Rangari et al. 2021). During the August 2020 floods in the study area, a floodwater mark of 0.6 m was estimated at the head of the river overflow point, affecting the stability of mud houses and the movement of people. As a result, any depth above 1m was designated as a high-level flood hazard.

## **6.3 Result and discussion**

### **6.3.1 Geo-morphometric analysis**

#### **Linear Aspects**

The hierarchical ranking of streams using Strahler (1952) drainage ordering system scheme is referred to as stream order. The first order is an overland flow with no branches. Stream order numbers are proportional to basin size, channel size, and discharge (Strahler 1957). The subbasins (SB-1 to SB-4) have the highest order of stream six (Figure 6.3), implying that the accumulated discharge and sediment loads flow through these stream segments. Stream segments of order one are the most common and vary according to drainage basin size. The total count of stream numbers of each hierarchical ranking is higher in SB-1(2853) and lower in SB-2(956). The variation in the number of streams reflects the physical characteristics of drainage subbasins and impacts peak discharge and sediment properties. Increased stream numbers are a result of higher relief and slope, which increases flash floods. According to the literature, higher-order stream segments have a higher potential for flooding and velocity (Singh and Kumar 2019). As a result, each of the six order subbasins has the potential for peak discharges, velocity, and flooding. According to ground observations, the Becho or Bello area in the sixth-order SB-1 is still flooding almost every rainy season.

SB-1 has the longest calculated basin length (162.68 km), while SB-2 has the shortest (87.6 km) (Table 6.3). The total length of the stream is greatest in SB-1 and shortest in SB-2. The longer the stream, the longer the travel time, and vice versa. The length of the stream decreases as the order of the stream segments increases, which agrees with Horton (1945) second law.

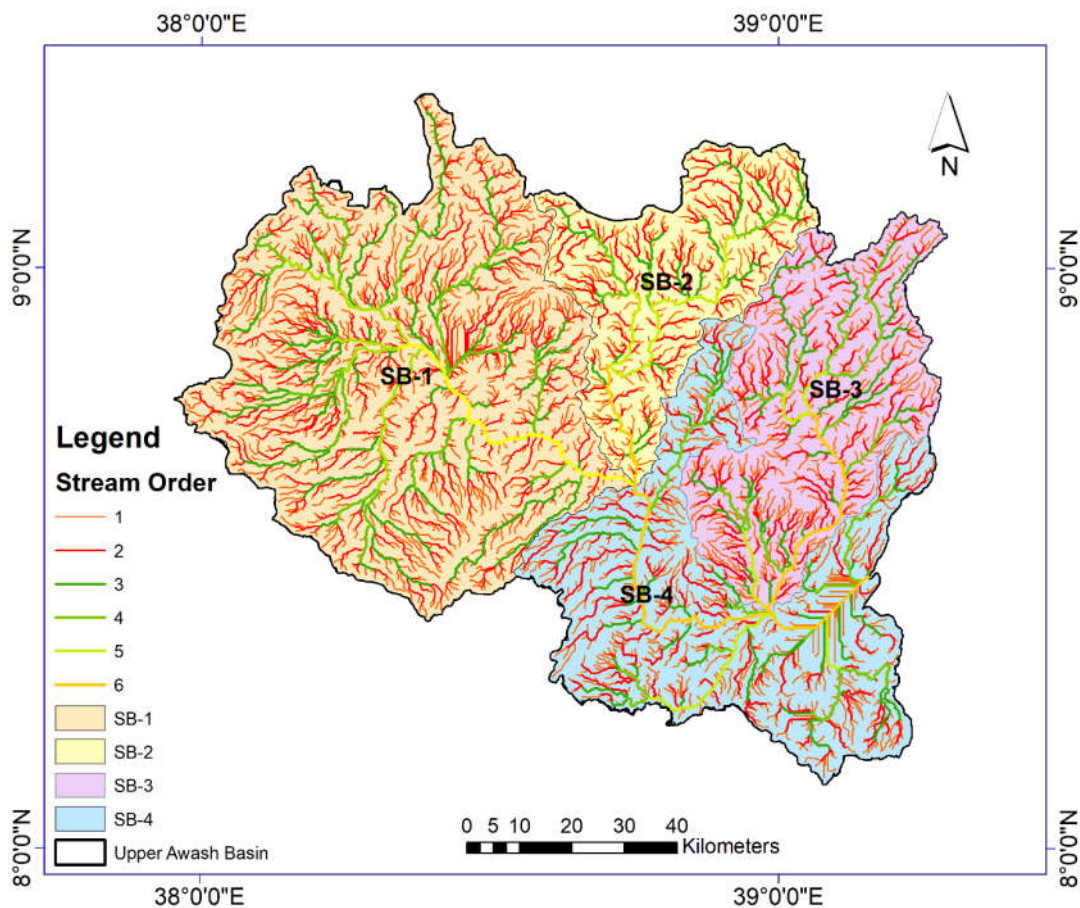


**Figure 6.3** Subbasin drainage network map and stream order after Strahler (1964)

The first-order stream length is about 51.4% of the total stream length. The mean stream length ranges from 1.41 in SB-2 to 1.55 in SB-4. There is a variance in stream length in the sequential stream ordering, indicating relief and slope attributes to variation (Asfaw and Workineh 2019). From an active hydrological point of view, in this study, SB-1 is a more active basin than SB-2. SB-1 and SB-4 have steeper slopes, resulting in fewer long streams and lower infiltration capacity, but SB-2 has a higher infiltration capacity. The bifurcation ratio ( $R_b$ ) expresses the

drainage system, which is referred to as the ratio of a specific segment order to the next higher segment order (Schumm 1956).

**Table 6.3** Morphometric analysis of subbasins

Sno.	Morphometric Parameters	Subbasins			
		SB-1	SB-2	SB-3	SB-4
1	Area (Km <sup>2</sup> )	4848.5	1630	2112.21	2838.52
2	Perimeter (Km)	383.64	251.61	280.12	459.17
3	Stream Order	6	6	6	6
4	Basin length (Km)	162.689	87.590	101.481	120.030
5	Mean stream length (Km)	1.49	1.41	1.45	1.55
6	Stream length (Km)	4258.87	1352.26	1804.51	2514.21
7	Mean bifurcation	1.90	1.65	1.88	2.12
8	RHO coefficient	1.57	4.45	2.74	3.59
9	Drainage density (Km/Km <sup>2</sup> )	0.88	0.83	0.85	0.89
10	Stream frequency	0.59	0.59	0.59	0.57
11	Texture ratio	7.44	3.80	4.45	3.54
12	Elongation ratio	0.48	0.52	0.51	0.50
13	Circularity ratio	0.41	0.32	0.34	0.17
14	length of overland flow (Km/Km <sup>2</sup> )	0.57	0.60	0.59	0.56
15	Compactness coefficient	1.55	1.76	1.72	2.43
16	Infiltration number	0.52	0.49	0.50	0.51
17	Basin relief (m)	1755	1566	1472	1490
18	Relief ratio (m/Km)	0.011	0.018	0.015	0.012
19	Average slope (Degree)	3.88	4.52	3.31	3.32

The bifurcation ratio value ranges from 2 for a flat or rolling drainage basin to 3 or 4 in the mountainous or heavily dissected river basin (Horton 1945; Giusti and Schneider 1965). The value of the bifurcation ratio ranges 3 to 5, where the geologic structure control does not distort the runoff pattern (Strahler 1957). On the other hand, the high value of Rb indicates a higher degree of runoff hydrograph and low permeability. The mean Rb determines the degree to which drainage networks will form. In Table 6.3, the bifurcation value is found to be 2.12 in SB-4, 1.9 in SB-1, 1.88 in SB-3, and 1.65 in SB-2. In the current study, Rb denotes that the subbasin stream network is built on a nearly flat drainage surface. It also implies that stream network branching is unaffected by geological structure or lithology. Thus, higher runoff rates are achieved after a long time but with a significant flood danger thereafter. The RHO ratio is a measurement of the drainage channel's storage capacity. It can be obtained by dividing the stream length ratio by the bifurcation ratio. The ratio values above 0.5 suggest high storage capacity during the flood period. The subbasin's RHO was more than 0.5, indicating that the drainage system has a large storage capacity during floods (Table 6.3).

### **Areal Aspects**

Drainage density is a fundamental morphometric quantity that determines the hydrological complexity of the surface and subsurface. It is a measure of drainage channel spacing that is computed by dividing the total length of all drainage channels (km) by the basin's area (km<sup>2</sup>) (Horton 1932). It denotes dissection texture, i.e., the smaller, very coarser (2), and the higher (> 8), very finer (Smith, 1950), which affects the amount of runoff and soil from the basin. The higher stream density is related to the fast hydrological response to rainfall, raising floods and impervious surfaces and vice versa. Drainage density is controlled by land use, land cover, rock type, catchment features (slope, infiltration rate, relief), and precipitation (Ignacio and Walling 1968). However, as cited by Ignacio and Walling (1968), the recent change in drainage density contributes to increasing flood discharges (Howe et al. 1966). In addition, low vegetation cover and land use/cover reduce erosion resistance and alter the drainage density channel. An insignificant difference in drainage density exists between subbasins, with 0.88 for SB-1, 0.83

for SB-2, 0.85 for SB-3, and 0.89 for SB-4. SB-1 and SB-4 have the highest and lowest density in SB-2 and SB-3, respectively. It suggests coarse basin texture ( $< 2$ ), slow runoff response, moderate slope and relief, low dissected topography, erosional resistance, and permeable terrain. Higher drainage densities in SB-1 and SB-4 and lower basin relief were found to cause peak flooding in the basin's lowest flat channel.

Stream frequency is another important parameter that plays a role in flood modeling. It is defined as the total sum of the order of each stream segment per unit area of the basin (Horton 1932). It depicts the basin runoff response and aids peak flow prediction (Patton and Baker 1976). The low stream frequency indicates low runoff production. Furthermore, lower stream frequency is strongly related to permeability, infiltration rate, and low basin relief (Mahala 2020). The stream frequency of the current study basin is 0.59 and 0.57 for SB-1 to SB-3 and SB-4, respectively, indicating that runoff is slowly concentrating and that peak discharge takes longer (Table 6.3). Hence, the lower stream frequency of study subbasin was found to have permeable sub-surface and low relief. Thus there is a modest risk of flash flooding and erosion, but runoff from the upper subbasins may augment the flood in SB-4.

Drainage texture refers to the spacing of stream channels in a specific basin and is impacted by infiltration capacity (Mahala 2020). According to Horton (1945) the drainage texture ratio is the total number of channel segments divided by the basin perimeter. A texture ratio, a very coarse ( $< 2$ ), course (2-4), moderate (4-6) and very fine (6-8) were defined by Smith (1950). Accordingly, SB-1 has a texture ratio of 7.44, SB-2 of 3.79, SB-3 of 4.45 and SB-4 of 3.54. SB-1 texture class is very fine, SB-2 and SB-4 texture classes are courser, and SB-3 texture class is moderate (Table 6.3). The texture of the subbasin drainage system ranges from coarse to very fine. SB-1 has an extremely fine texture, which indicates a low infiltration rate, making it a potential flood location.

**Table 6.4** Characteristics of subbasins Morphometry

Parameters	Subbasin	Stream Order					
		I	II	III	IV	V	VI
Stream Number	SB1	1434	696	385	191	73	74
	SB2	481	245	105	35	64	26
	SB3	632	289	158	91	30	47
	SB4	823	378	183	159	36	46
Stream Length		I	II	III	IV	V	VI
	SB1	2206.16	1075.55	557.1	250	103	67.22
	SB2	649.37	398.68	143.36	50.02	80.7	30.122
	SB3	930.77	434.65	228.22	120	42	48.87
Average Area		I	II	III	IV	V	VI
	SB1	5.25	19.06	61.5	186.65	626	4848.5
	SB2	4.04	11.88	25.5	150	690	1630
	SB3	5	12.5	38.64	123.67	430	2112.2
Stream length ratio		II/I	III/II	IV/III	V/IV	VI/V	Mean
	SB1	2.05	1.93	2.23	2.43	1.53	2.03
	SB2	1.63	2.78	2.87	0.62	2.68	2.12
	SB3	2.14	1.9	1.9	2.86	0.86	1.93
Bifurcation ratio		I/II	II/III	III/IV	IV/V	V/VI	Mean
	SB1	2.06	1.81	2.02	2.62	0.99	1.9
	SB2	1.96	2.33	3	0.55	0.41	1.65
	SB3	2.19	1.83	1.74	3.03	0.64	1.88
	SB4	2.18	2.07	1.15	4.42	0.78	2.12

**Table 6.4** (Cont...)

Parameter	Subbasin	Stream length ratio /Bifurcation ratio					Mean
RHO	SB1	1	1.07	1.11	0.93	1.55	1.13
	SB2	0.83	1.19	0.96	1.13	6.6	2.14
	SB3	0.98	1.04	1.1	0.94	1.35	1.08
	SB4	1.06	0.93	1.5	0.79	2.72	1.4

The basin shape, such as elongation and circularity, controls the degree of the hydrological responses. Elongation is the ratio of the diameter of a circle having the same area to the maximum basin length (Schumm 1956). It is a non-dimensional component that reveals information about the geometry and hydrology of the basin. Re near 1 is almost circular (Schumm 1956) and characterized by high relief, steep ground, and early peak flood response (Memon et al. 2020). The subbasins' elongation ratios range from 0.48 to 0.52 (Table 6.3). SB-2 has the highest proportion of elongated basin form, followed by SB-3, SB-4, and SB-1, with  $Re < 0.7$  (Schumm 1956). Concerning Re value, the basin is a nearly moderate relief and slope. Thus, an elongated basin proceeds a longer time of concentration and peak runoff at the outlet of the basin (Schumm 1956; Mahmood and Rahman 2019).

Another shape measure, the circularity ratio, illustrates the involvement of watershed characteristics in flood response. The circularity ratio (Rc), according to Strahler (1964) is the ratio of the basin area to the area of a circle with the same perimeter. The ratio approaches one value, which means a circular basin shape, and the lower shows an elongated basin shape. Peak discharges occur over a shorter period due to the circular form and vice versa. The significant Rc is influenced by the length and frequency of the stream, geological structure, land use land cover, climate, relief, and slope of the basin. Rc denotes a stage in geomorphology (young, matured, and old) (Mahala 2020). It's also a deciding element in the dendritic set. SB-4 has the basin's lowest Rc value of 0.17, indicating that it has a more elongated shape and creates less peak flow in the subbasins. SB-1 has a greater 0.41, which results in faster flood discharges. It's also a sign of matured geomorphological stage and dendritic drainage patterns.

The length of overland flow is the independent parameter affecting both the hydrologic and physiographic development of drainage systems (Horton 1945). It is valued at around half of the drainage density and is inversely related to flood susceptibility. SB-1, SB-3, and SB-4 have a calculated value of 0.56, whereas SB-2 has a calculated value of 0.60 (Table 6.3), indicating that the lower value has a higher flood proneness and steeper slope, and vice versa. The compactness coefficient (Cc) depicts the relationship between the basin and a circular basin of the same size. The parameter inversely donates morphometric parameters to hazardous hydrological responses, such as flood susceptibility. The basin Cc value varies from 1.55 for SB-1 to 2.43 for SB-4 (Table 6.3), showing a total divergence from the circular shape; thus, a higher value indicates a longer duration of concentration before peak flow, and vice versa (Memon et al. 2020).

The amount of infiltration is proportional to the catchment's hydrological response. It is inversely proportional to the basin's infiltration capacity and is a product of drainage density (Dd) and stream frequency (Fs) (Alqahtani and Qaddah 2019). The lower the infiltration number (Ni) is, the higher the infiltration capacity. The maximum Ni number in SB-1(0.52) and minimum in SB-2 (0.49) was observed in the study subbasins (Table 6.3), indicating that SB-1 has a lower infiltration rate and SB-2 has a high infiltration rate (i.e., high potential groundwater). Thus the larger the infiltration capacity, the lower the Ni.

### **Relief Aspects**

The hydrological and geomorphological processes of the basin are explained by the basin relief parameter (Alqahtani and Qaddah 2019). It expresses the difference between the subbasin's maximum and minimum altitude. SB-1 and SB-2 have larger discharge-producing capacities with denudational features, with a maximum basin height of 1755 masl in SB-1 and a minimum of 1472 masl in SB-3. Furthermore, the lower area receives the accumulated rapid runoff from the top, resulting in a high risk of flooding. The dimensionless basin relief to basin length ratio indicates the overall steepness of the watershed surface and sediment yield (Schumm 1956). A larger relief ratio favors faster runoff, resulting in flash floods

and higher sediment production, whereas a lower value indicates erosion resistance and a low degree slope (Alqahtani and Qaddah 2019).

SB-1 had a relative ratio of 0.011, SB-2 had a ratio of 0.018, SB-3 had a ratio of 0.015, and SB-4 had a ratio of 0.012 (Table 6.3). The slope is one determinant factor influencing flood occurrences (Kabenge et al. 2017), drainage network formation, runoff velocity, recharge rate, and erosion (Magesh and Chandrasekar 2014). The high degree of slope directs quick runoff and flash floods, and vice versa. The slope of the subbasins was sectioned into five classes. The mean gradient varies from 3.88 ° in SB-1, 4.52 ° in SB-2, 3.31 ° in SB-3, and 3.32° in SB-4 (Table 6.3). SB-1 has a slope of 52.57 percent less than 2.5°, indicating a high plateau surface dominance, whereas SB-2 has the maximum degree slope, indicating a high discharge genesis. A plateau-dominated topology dominates the majority of subbasins. Flood concentration is concentrated mostly in SB-1 and SB-4 due to the surrounding high-relief hills, high mountainous terrain, and somewhat dissected plateau. Above the average slope, moderate and steep slopes are primary sources and faster surface runoff and soil transport to flatter areas, increasing soil accumulation to the main trunk, thus increasing flood vulnerability.

### **6.3.2 Topographic position index**

Hydrological responses are considerably correlated with the topographic position. TPI represents the elevation difference of each cell in DEM with a mean elevation of its neighbouring cells (Weiss 2001). TPI positive indicates cells are higher than the average of their surroundings (ridges), while TPI negative suggests that cells are lower than the average (valley). A TPI approaching zero represents a level terrain or a constant slope. The topography of a specified location relative to the neighbouring may be a ridge, valley, flat plain, middle, upper or lower slope (Weiss 2001). The TPI was calculated for each subbasin considering a radius of 3 cell size and predicted the topographic positions.

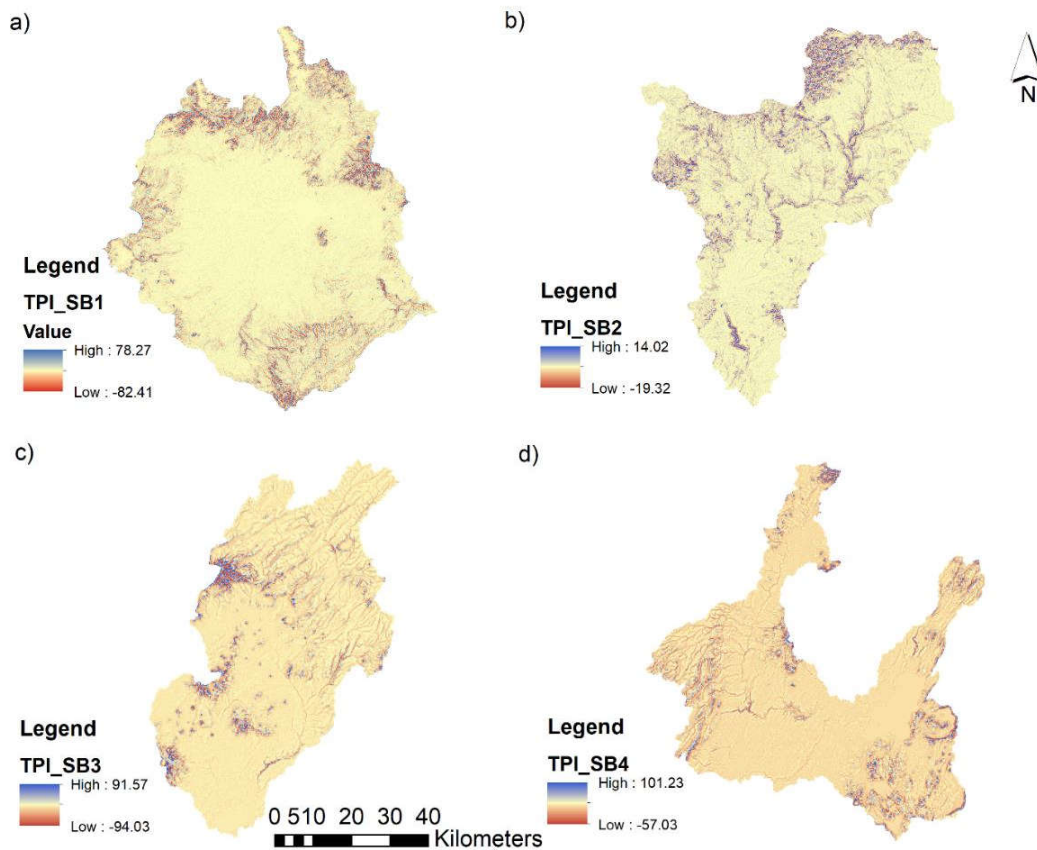


**Figure 6.4** Topographic position index a) SB-1 b) SB-2, c) SB-3 and d) SB-4

Lower locations (flat areas) are prone to flooding relative to higher TPI. Therefore each subbasin (SB-1, SB-2, SB-3, and SB-4) low topographic positions (near zero) were identified as water inundation area and susceptible to flood event. The TPI for individual subbasins is shown in Figure 6.4. The spatial pattern of extended lower topographic position in SB-1 has been identified in the middle and lower sections in SB-2, SB-3, and SB-4.

### 6.3.3 Topographic wetness index

TWI describes and quantifies the impact of local relief on flood generation. It provides topographic wetness through the use of the specific catchment areas of the upstream drainage and slope. A higher TWI indicates more moisture in a particular area and a tendency for water to move downward, which, in turn, makes it more

prone to flood events (Tehrany et al. 2019). In this study, the TWI ranged from 4.44 (lowest) to 24.58 (highest) (Figure 6.5).

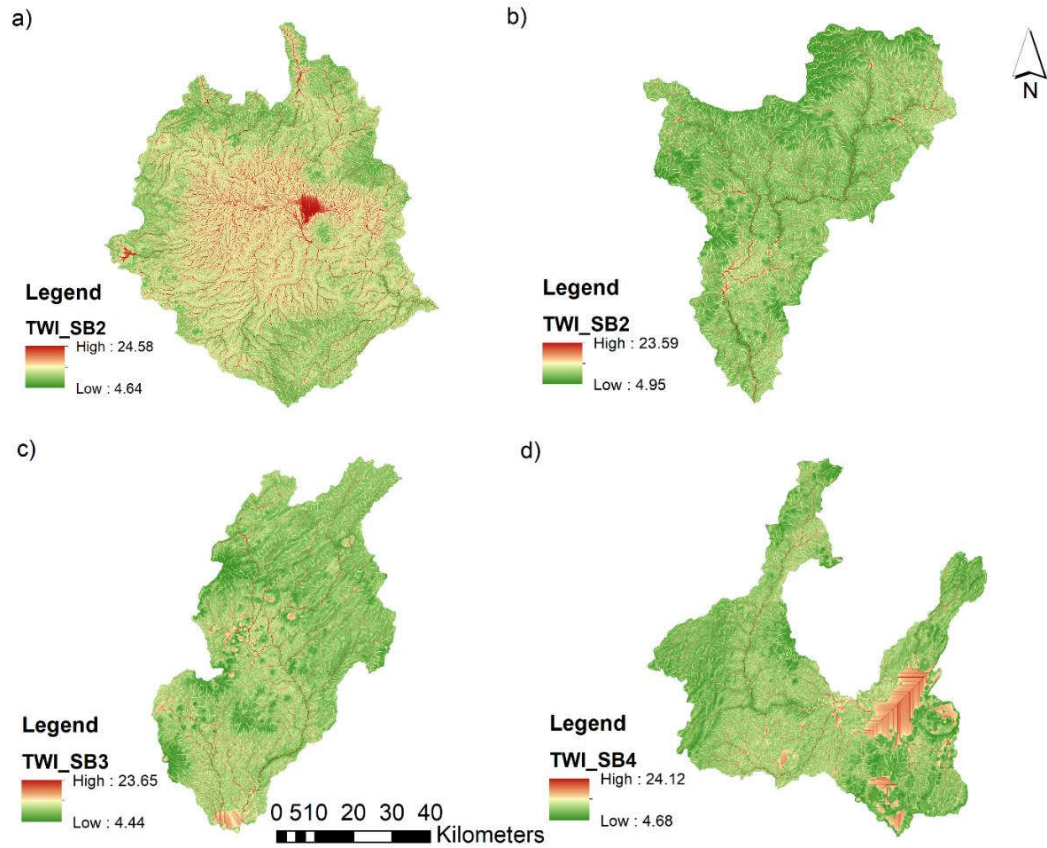


**Figure 6.5** Topographic wetness index a) SB-1 b) SB-2, c) SB-3 and d) SB-4

The lowest TWI value indicates a lesser tendency for water accumulation and a higher direction of water movement. All subbasins resulted in relatively close high TWI; however, different extents of high TWI (Figure 6.5).

### 6.3.4 Flood susceptibility modeling

In this study, the linear, areal, and relief morphometric parameters directly and inversely proportional to hydrological response were evaluated for the flood susceptibility modeling. A total of 15 parameters were chosen to identify the susceptible subbasin for flood management, including stream number, stream length, drainage density, bifurcation ratio, stream frequency, circularity ratio, texture ratio, infiltration number, basin relief, relief ratio, slope, as well as indirectly

proportional parameters like length of overland flow, compactness coefficient, Rho coefficient, and elongation ratio (Singh and Kumar 2019; Obeidat et al. 2021). Each parameter in each subbasin was given a rank (1, 2, 3) based on its value and its relationship (directly and indirectly) to floods. For directly proportional parameters, rank 1 represented a low level of susceptibility, 2 moderate, and 3 highest level of susceptibility. In contrast, rank 3 designated a low level of susceptibility for indirectly proportional parameters, and so on. The greatest cumulative rank value is referred to as a high level/degree of flood susceptibility, while the lowest value is referred to as low, and the medium range value is referred to as moderate. Subbasins with the same rank sum were assigned the same susceptibility level.

**Table 6.5** Rank and the total rank-sum of morphometric parameters for subbasins

Sno.	Morphometric Parameters	Subbasins			
		SB-1	SB-2	SB-3	SB-4
1	Stream number	3	1	1	2
2	Basin length	3	1	1	2
3	Stream length	3	1	1	2
4	Mean bifurcation	2	1	2	3
5	RHO coefficient	3	1	2	1
6	Drainage density	3	1	2	3
7	Stream frequency	3	3	3	1
8	Texture ratio	3	1	1	1
9	Elongation ratio	3	1	1	2
10	Circularity ratio	3	2	3	1
11	length of overland flow	3	1	2	3
12	Compactness coefficient	3	3	3	1
13	Infiltration number	3	1	2	3

**Table 6.5 (Cont..)**

Sno.	Morphometric Parameters	Subbasins			
		SB-1	SB-2	SB-3	SB-4
14	Relief ratio	1	3	2	1
15	Average slope	2	3	1	1
	Total Sum	41	24	27	27

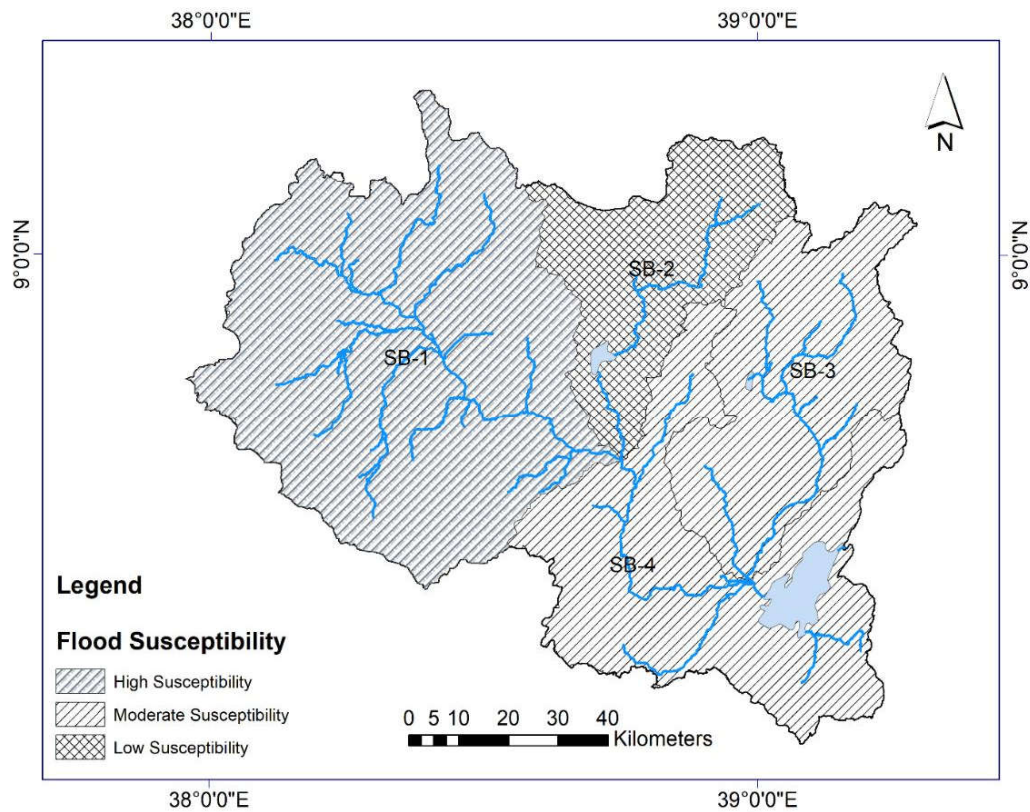


**Figure 6.6** Flood susceptibility map of subbasins based on morphometric parameters

Thus, based on the sum score ranking, the subbasin has been categorized into high ( $\geq 41$ ), moderate (ranging from 27 to 41), and low ( $< 27$ ) susceptibility (Table 6.5). In the current study, SB-1 exhibited the highest rank-sum then high (41) and SB-3 and SB-4 moderate (27), and SB-2 low (24), susceptible to flood (Figure 6.6).

The highly susceptible SB-1 is the primary origin of Awash River and covers a large area. It is characterized by higher stream frequency, circularity ratio, stream length and lower compactness coefficient, overland flow, and RHO, which are directly or indirectly proportional to massive runoff generation. The direct proportional parameter has an average value of 2.6, whereas the indirect proportional parameter has an average value of 3, showing that the direct proportional characteristics compose the majority of SB-1 flood susceptibility. In addition, the basin periphery is high relief hills, the high mountainous, and the moderately dissected plateau that instantly enlarges flood in the plain area of the basin. SB-2 has an average value of 1.7 and 1.4 for direct and indirect proportional parameters, respectively. The direct and indirect proportional parameters in SB-3 have the same average value of 1.8. SB-4 has direct and indirect proportional parameters of 1.9 and 1.6, respectively. Compared to SB-3, the indirect proportional parameters in SB-2 and SB-4 have the highest rank of a higher number, and the direct proportional parameters in these subbasins have a modest influence on flood susceptibility.

Further, the flood conditioning factors were able to predict the susceptibility of specific areas. The higher the topographic wetness index (TWI) shows, the higher wetness indicates more potential for flood events. In addition, the topographic positioning index (TPI) contributes to flooding events, accumulating water in the flat topography. The combinations of this spatial information through the weighted overlay technique in GIS identified the potential areas susceptible to flooding (high, moderate, and low) (Figure 6.7). The categorization is then composed of three clusters using Jenks natural breaks optimization: high, moderate, and low susceptibility. Subbasin SB-1 exhibited the highest flood susceptible area containing high weighted (highest TWI and lower TPI), and subbasin SB-2 had the lowest flood susceptibility. The subbasins SB-3 and SB-4 higher susceptible to flood than SB-2. The area under individual subbasins, which are high, medium, and low flood-sensitive areas, is shown in Figure 6.8.

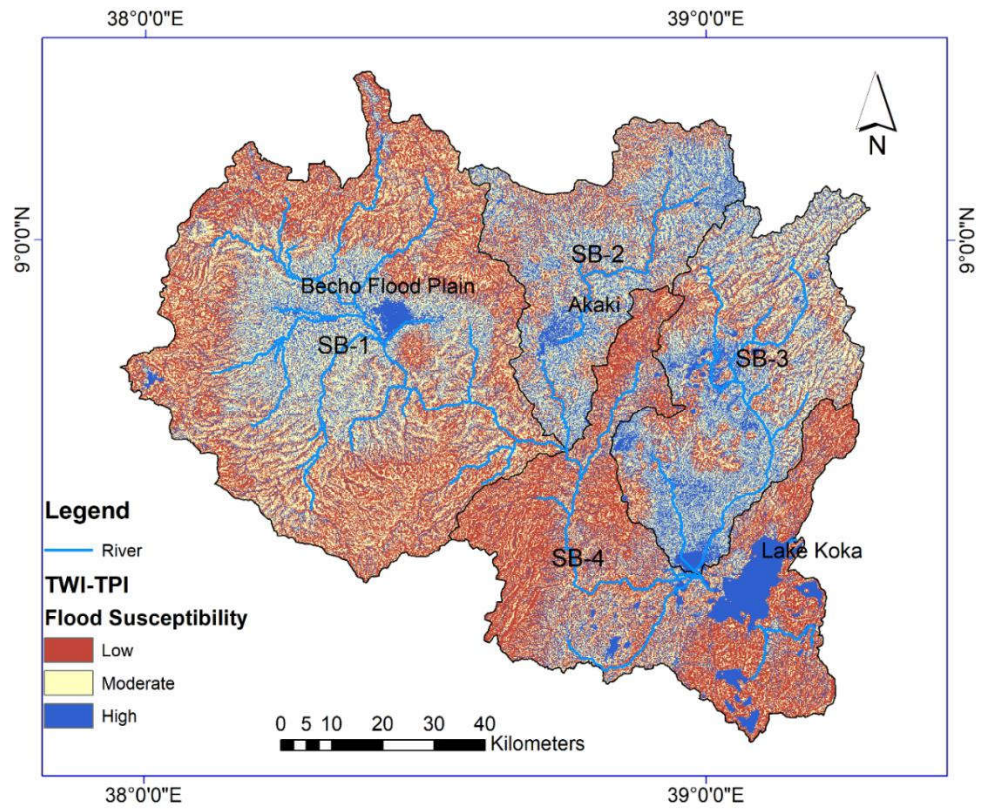


**Figure 6.7** Flood susceptibility map based on the weighted overlay analysis of TWI and TPI and identified specific locations

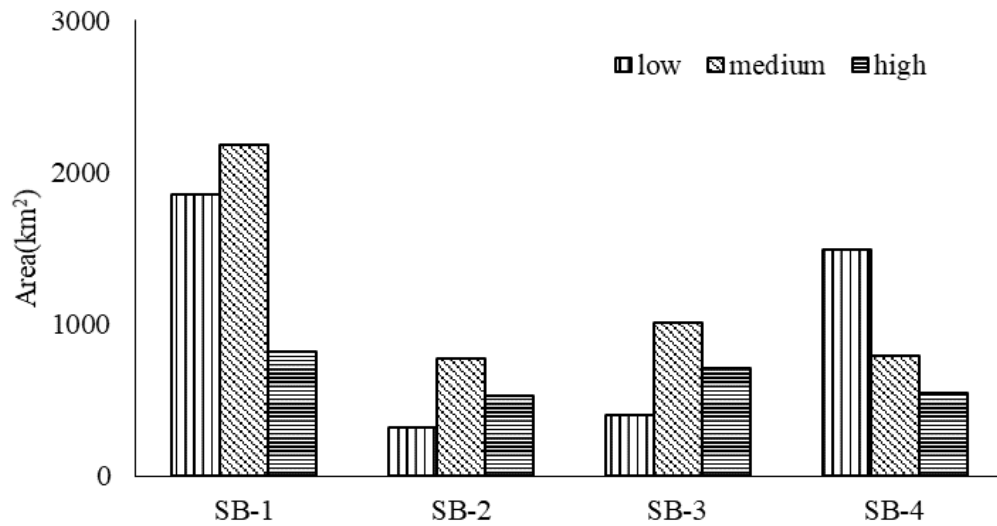


**Figure 6.8** The flood-susceptible areas under low, medium, and high of the SB-1, SB-2 , SB-3, and SB-4

The Upper Awash River basin, which constitutes 22.8%, 41.7% and 35.6% of the total basin, is high, medium, and lowly susceptible to flooding, respectively. Based on the combination of two indices, high flood potential sites were identified, for instance, SB-1(Becho flood plain), SB-2 (Akaki and Andode area), and SB-4 (Koka area). In subbasin SB-3, Lakes, and ponds were identified in the middle and western side of the basin; however, the lower section is prone to flood events (Figure 6.7). Therefore the results obtained through these indices agree with the rank-based flood susceptibility evaluation; moreover, the specific flood susceptible areas were able to predict. The Becho flood plain is consistent with Koriche and Rientjes (2016), who used TWI along with the standard precipitation index.

During a site inspection at the Becho flood plain, which lies in the center of the SB-1, it was observed that runoff water remains stagnant for a long time after the rainy season (June to September). Local informants believe that 24 tiny streams (eight large streams in total) converge at the spot. Some have lately been added, bringing the other three upland Ginchi, Berga, and Holeta Rivers closer together. The simultaneous discharge flow renders the main channel incapable of containing the massive flow, resulting in overflow. The flat topography (lower slope) is attributed to the slow runoff removal from the channel. Over 4000 villagers are forced to displace the place every flood and lose their agricultural lands, properties, houses, and animals. Therefore, based on aggregate morphometric analysis of subbasins, sites susceptible to flood are identified for further integrated flood management and planning. Flood hazard mapping is now the next step for the identified subbasin SB-1, in this case, the Becho flood plain.

### **6.3.5 Nonstationary analysis**

The preliminary hydro-climatic nonstationary identifications using trend and change-point tests were performed at a 0.05 significance level. Through a trend test, increasing and decreasing, and change point, the breakpoint at which year the variables increased upward or downward was identified. Figure 6.9 shows the MMK test result for the annual maximum flow sequence at three tributary stations characterized as a statistically insignificant trend. MMK detected one station,

Berga, with a statistically positive trend. However, Holeta and Ginchi stations resulted in a negative trend. Pettitt's test detected nonsignificant change points in the discharge series at tributaries. The trend in the R1, R2, R3, R4, R12, R12e, and mean annual temperature was also investigated. The trend test detected a significant positive trend in the R1, R2, R3, and mean annual temperature ( $p$  value  $< 0.05$ ), while a nonsignificant trend was demonstrated in the R4, R12, and R12e ( $p$  value  $> 0.05$ ). The same time series for which MMK discovered a significant trend also showed a significant abrupt change. The same time series that revealed a significant trend also showed a significant abrupt change, demonstrating the validity of the nonstationary (Milly et al. 2008; Li et al. 2015; Liu et al. 2017).

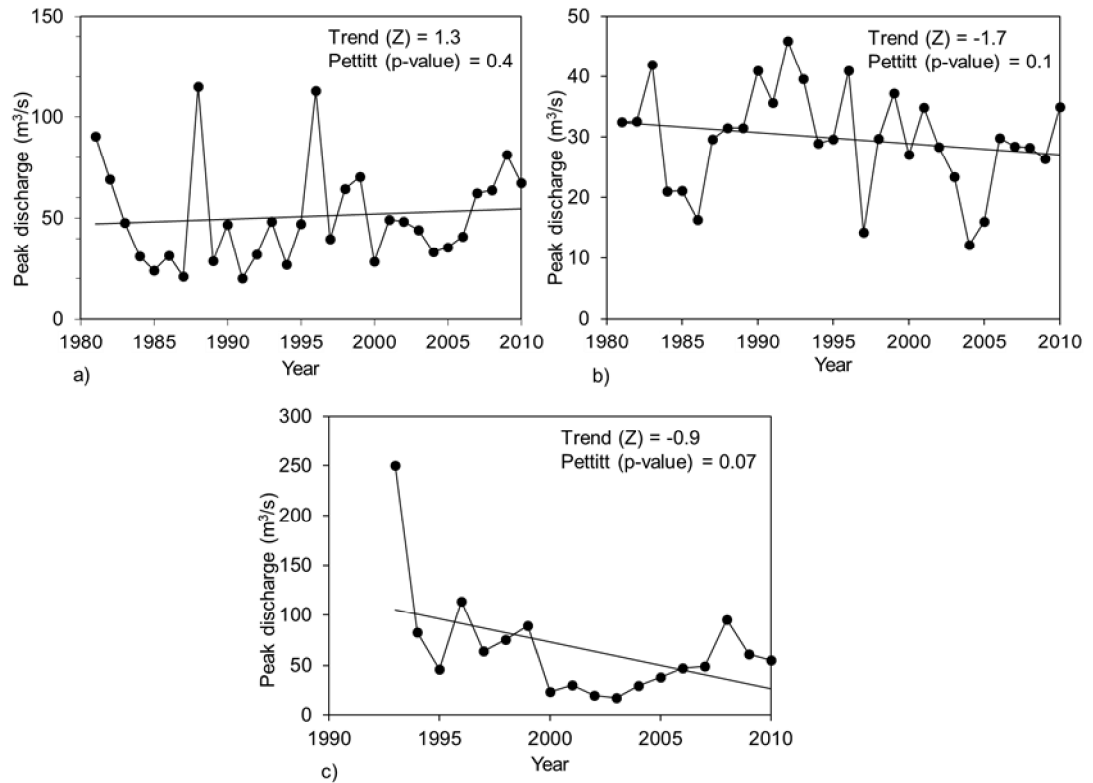


**Figure 6.9** Modified Mann-Kendall trend test and Pettitt's test results for **a)** Berga, **b)** Holeta, and **c)** Ginchi stations at the 5% significance level

Additionally, linear correlation tests were performed between the flood discharge series and climatic covariates. For Berga hydrological station, the correlation between the peak flow series and rainfall (R4, R12, and R12e) was statistically

significant ( $p$  value  $< 0.05$ ). The strongest correlation was detected between the peak and R12e (0.5,  $p$  value = 0.01). The correlation coefficient between peak flow and mean temperature showed no association (0.07,  $p$  value = 0.73). For Holeta peak discharge, the relationship showed a significant correlation with all rainfall durations. The peak flow and R1 relationship was higher (0.55,  $p$  value = 0.001). Peak flow was negatively correlated to temperature (-0.21,  $p$  value = 0.28). Since the trend and change point are detected in the time series, it is sufficient to conclude that the hydro-climatic series is a nonstationary type. Also, a higher correlation indicates that rainfall is a possible factor, apart from non-climatic factors like land cover change, catchment management practices, river control structures, water withdrawal, etc., that may be responsible for the nonstationary flood characteristics. Šraj et al. (2016) also showed that peak flood series strongly correlate with annual precipitation. The same was reported by Šraj and Bezak (2020), who found that monthly rainfall of varying durations correlates with annual peak flow series. Furthermore, these rainfall indices explain the temporal variability of flood records and modulate the flood frequency and magnitude.

### **6.3.6 Model fitting and flood quantile**

The fitted model parameters using MLE and the performance for the Berga station are presented in Table 6.6. According to the goodness-of-fit performance metric, AIC rank, the location parameter as a linear function of annual total rainfall in wet days (Model 7) gave the best fitting model, followed by Model 10 and Model 11. Models 6, 8, and 9 (for example) fit better than the stationary model when annual rainfall alone, annual rainfall and temperature, and annual rainfall and time were added as covariates. This suggests that annual total rainfall in wet days alone and with temperature and time are the variables that can best explain the variability of flood discharges apart from other factors, such as climate indices and human activities. For example, during the 1996 flood year, the peak discharge was 113 m<sup>3</sup>/s, and the corresponding PRCPTOT and annual rainfall amounts were 1395 and 1562 mm, respectively. This surge results from the substantial annual total rainfall in wet days that occurred in 1996, which was explained by the strong correlation between PRCPTOT and annual peak discharge.

**Table 6.6** Distribution parameters of stationary and nonstationary models using the MLE method for Berga station

Berga Station							
Model	$\mu$			$\sigma$	$\xi$	AIC	Rank
	$\mu_0$	$\mu_1$	$\mu_2$				
Model 1-GEV	38.08			15.87	0.2	273.64	8
Model 5-GEV(R4)	9.53	0.04		15.25	0.18	272.47	7
Model 6-GEV(R12)	-12.78	0.04		12.86	0.38	268.52	4
Model 7-GEV(R12e)	-25.03	0.06		12.07	0.41	265.48	1
Model 8-GEV(R12+T12)	38.32	0.05	-2.31	12.70	0.40	270.25	5
Model 9-GEV(R12+ t)	38.38	0.04	-0.03	12.99	0.37	270.72	6
Model 10-GEV(R12e+T12)	38.53	0.07	-3.02	11.46	0.48	266.67	2
Model 11-GEV(R12e+ t)	38.34	0.06	-0.03	12.07	0.41	267.69	3

The flood quantile of the  $T$  return period can then be calculated once the model parameters have been estimated. In nonstationary conditions, the exceedance probability corresponding to the flood quantile varies with time (time-varying probabilities) because the frequency distributional parameters are a function of time. In this case, the best nonstationary model estimates flood quantiles based on annual total rainfall in wet days events. According to the suggested models, Table 6.7 provides the estimated flood quantiles for return periods of 2, 25, 50, and 100 years. The station flood quantiles estimate using the stationary and nonstationary frequency analysis differ significantly. For instance, the 25-year return flood would have 138 m<sup>3</sup>/s and 149 m<sup>3</sup>/s using the annual total rainfall on wet days alone and annual total rainfall on wet days with temperature as a covariate, respectively.

**Table 6.7** Estimated flood quantiles ( $m^3/s$ ) for 2, 25, 50, and 100-year return periods for Berga, Holeta, and Ginchi stations

Return Period	Model 1	Model 2	Model 3	Model 4	Model 5	Model 6	Model 7	Model 8	Model 9	Model 10	Model 11
Berga											
2	44.12	51.19	51.47	52.32	54.10	60.47	62.9238	61.239	60.68	67.3229	63.4689
25	109.72	114.11	114.23	116.24	114.26	135.56	137.99	137.94	134.61	149.29	138.72
50	132.80	135.62	136.19	139.28	134.60	170.44	174.54	174.39	168.28	193.416	175.409
100	159.24	159.96	161.28	165.95	157.50	215.60	222.91	222.25	211.47	254.62	223.99
Holeta											
2	29.93	41.11	36.24	33.51	36.74	37.81	38.86	40.341	38.24	40.4665	39.1825
25	43.14	54.28	50.45	46.64	50.57	49.99	50.56	52.18	50.39	52.33	50.77
50	44.76	56.50	52.78	48.37	52.75	51.48	51.95	53.655	51.84	53.8147	52.1619
100	45.98	58.41	54.75	49.72	54.57	52.60	53.00	54.79	52.95	54.95	53.22
Ginchi											
2	50.50	53.85	51.16	53.01	55.23	54.28	54.06	79.199	79.69	74.9294	71.776
25	185.04	181.86	183.21	182.72	181.18	185.25	183.70	192.46	193.94	191.18	189.12
50	246.49	237.48	242.65	240.11	235.82	243.64	241.298	237.67	239.91	238.02	236.80
100	325.45	307.37	318.51	312.81	304.43	317.85	314.39	292.37	295.73	294.91	294.92

In this case, in Models 7 and 10, the addition of covariates increased by 26% and 35% more than the stationary model predicted. The quantile flood estimates for the lower return period of 25 years are comparable under nonstationary models (Model 2-5). Flood estimates at longer return periods by stationary and nonstationary (Model 1-5 and Model 6-11) models differ significantly. This implies that the stationary model underestimates flood quantiles. The best fit nonstationary model (Model 7) for a 100-year flood ( $223 \text{ m}^3/\text{s}$ ) corresponds to a flood associated with a PRCPTOT of 1395 mm in the year 1996. The flood year 1996 recorded  $113 \text{ m}^3/\text{s}$ , and the flood return period become 29 under the stationary model and 17 under the nonstationary model (Model 7). The 100-year flood of  $159 \text{ m}^3/\text{s}$  under the stationary model corresponds to a 39-year return under the nonstationary condition. This suggests the exceedance probability of an extreme event increases (i.e.,  $> 0.01$ ) under covariate-dependent models. It is also worth mentioning that the flood quantile estimate for the 100-year return period with short record lengths is uncertain; for example, the short record lengths at Berga showed a wider range of variability compared to the 30-year record length. The flood quantile relative difference associated with 20 and 25 record length scenarios randomly sampled from the entire record length is approximately 74% and 61%, respectively. This suggests that the flood quantile is sensitive to the record length.

Holeta is the second most important tributary station. Table 6.8 shows the estimated parameters using MLE and the AIC ranking of all models. The best fit for the Holeta station was found to be Model 2, less AIC value, where the single monthly (August) rainfall was used as a covariate. Models 7 and 8 showed that annual total rainfall on wet days alone and annual rainfall with temperature as covariates gave the station the second and third best fits, respectively. The first best-fit model gave higher flood quantile estimation than other rainfall-informed and stationary models, given the significant linear correlation between the August total rainfall and annual maximum flood. According to Model 2, the estimated flood quantile increased to  $54 \text{ m}^3/\text{s}$  ( $58 \text{ m}^3/\text{s}$ ) from the 25-year (100-year) flood of  $43 \text{ m}^3/\text{s}$  ( $46 \text{ m}^3/\text{s}$ ) under stationary conditions. The addition of covariates increased the flood estimate by 8 (e.g., Model 4) to 27% (e.g., Model 2), more than the value estimated by the stationary model.

**Table 6.8** Distribution parameters of stationary and nonstationary models using the MLE method for Holeta station

Holeta							
Model	$\mu$			$\sigma$	$\xi$	AIC	Rank
	$\mu_0$	$\mu_1$	$\mu_2$				
Model 1-GEV	26.95	-	-	8.71	-0.38	210.69	11
Model 2-GEV(R1)	-0.60	0.10	-	6.66	-0.21	202.58	1
Model 3-GEV(R2)	2.25	0.04	-	7.38	-0.23	207.75	6
Model 4-GEV(R3)	14.33	0.02	-	8.16	-0.34	210.06	10
Model 5-GEV(R4)	3.39	0.03	-	7.44	-0.25	207.62	5
Model 6-GEV(R12)	4.82	0.02	-	8.07	-0.38	208.09	7
Model 7-GEV(R12e)	-0.61	0.03	-	7.88	-0.39	206.93	2
Model 8-GEV(R12+T12)	84.99	0.02	-3.47	7.69	-0.37	207.31	3
Model 9-GEV(R12+ t)	55.06	0.02	-0.03	8.13	-0.39	209.46	9
Model 10-GEV(R12e+T12)	53.37	0.03	-2.26	7.69	-0.37	207.57	4
Model 11-GEV(R12e+ t)	32.95	0.03	-0.02	7.73	-0.38	208.59	8

The average flood quantile increase from a 25 to 100-year return period in each covariate-informed model is about 3.1 m<sup>3</sup>/s, indicating no significant difference in flood quantiles and possibly related to the decreasing trend shown in the flood series. In rainfall-incorporated models, flood quantile estimates would have a shorter return period or increased exceedance probability under stationary conditions. For instance, the R2 inclusion in the model leads the current 100 years of the flood (46 m<sup>3</sup>/s) event under stationary conditions to become 11 year return period. According to Model 2, a flood of 54 m<sup>3</sup>/s (25-year) and 58 m<sup>3</sup>/s (100-year) corresponds to a maximum August monthly rainfall of 409 mm from 1981 to 2009.

However, due to the short data series, the 100-year flood estimate is uncertain, and the estimated range of variability was less than 11%.

Table 6.9 presents the MLE-based parameters and fitting performance (AIC rank) for the Ginchi station. According to AIC performance criterion, the third tributary Ginchi station best fit the stationary model (Model 1) from 1993 to 2010. The inclusion of a covariate in the model resulted in no further improvements. However, the JAS rainfall integration into the location parameter (Model 5) gave the second-best fit. Models 5 and 6 were the last two best fits to the discharge sequences.

**Table 6.9** Distribution parameters of stationary and nonstationary models using the MLE method for Ginchi station

Ginchi							
Model	$\mu$			$\sigma$	$\xi$	AIC	Rank
	$\mu_0$	$\mu_1$	$\mu_2$				
Model 1-GEV	41.26	-	-	23.55	0.37	183.99	1
Model 2-GEV(R1)	34.67	0.03	-	23.91	0.34	185.88	6
Model 3-GEV(R2)	40.01	0.00	-	23.56	0.36	185.96	7
Model 4-GEV(R3)	32.87	0.01	-	23.66	0.35	185.82	5
Model 5-GEV(R4)	26.96	0.02	-	23.57	0.34	185.59	2
Model 6-GEV(R12)	32.15	0.01	-	23.66	0.35	185.67	3
Model 7-GEV(R12e)	31.54	0.01	-	23.52	0.35	185.73	4
Model 8-GEV(R12+T12)	40.65	0.07	-3.61	23.54	0.28	186.36	10
Model 9-GEV(R12+ t)	40.81	0.07	-0.04	23.51	0.29	186.42	11
Model 10-GEV(R12e+T12)	40.70	0.07	-2.72	23.89	0.29	186.99	12
Model 11-GEV(R12e+ t)	40.79	0.06	-0.03	23.86	0.29	187.07	13

In terms of flood quantile estimation, the stationary model gave a higher than the covariate-dependent model. The stationary model predicted 325.5 m<sup>3</sup>/s for a 100-year return period, while the nonstationary model predicted less. However, both models' predictions become more noticeable in high flood quantile estimations at 100-year return periods. In 1996, flood discharge was the greatest, measuring around 113 m<sup>3</sup>/s, the same as Berga station, which would have a return period of 13 under the stationary model. It is worth noting that the integration of covariates will turn the time-invariant-based estimated flood quantile to happen earlier.

It is worth noting that covariates-dependent models where rainfall allowed in the location parameter outperformed stationary models for stations with statistically significant correlations, such as between Berga peak flood and annual total rainfall in wet days series and between Holeta peak discharge series and August month rainfall. Šraj and Bezak (2020) also demonstrated these relationships with model performance in Slovenia catchments. In addition, the rainfall-informed model outperformed the stationary model in stations with insignificant trends in annual peak discharge. In this case, Bertola et al. (2019) discussed that through rainfall-dependent models, long-term flood fluctuations are related to the covariates even in cases where no monotonic trend in time is detected. This study confirms that location parameters varying linearly with annual rainfall alone, monthly rainfall, and both annual rainfall and temperature are preferred as covariate and best-fit models over a stationary model, as suggested previously (Šraj et al. 2016; Šraj and Bezak 2020; Hesarkazzazi et al. 2021). Furthermore, the inclusion of annual total rainfall in wet days (R12e) alone and with temperature and time as a covariate in location parameters outperformed. This is consistent with previous studies that indicated extreme precipitation explains flood variability (Prosdocimi et al. 2014; Bertola et al. 2019).

There was also a difference in the return period between the covariate-informed and time-invariant models (increased probability exceedance). These changes in flood quantile and return period are similar to those that Salas and Obeysekera (2014) reported. The uncertainty increases as the data length decreases and vice versa. Similarly, Dysarz et al. (2019) demonstrated that the shorter the record length, the

greater the uncertainty for longer return period flood estimation. Based on this, decision-makers or hydrologic engineers further consider long data series or sampling techniques to reduce uncertainty when estimating the design flood.

The tributary stations and preferred models show that rainfall with varying durations, such as monthly, annual, and annual wet day rainfall, significantly describes the flood characteristics in the Upper Awash river basin, particularly rivers from the highland areas. Therefore, nonstationary characteristics are the dominant process in these gauging stations, indicating stationary does not exist and leads to unreasonable estimates. Thus, nonstationary should be considered when describing flood estimation and hazard mapping in frequent flooding areas like the Becho floodplain for flood management and mitigation works.

### **6.3.7 Flood hazard map**

The flood hazard map is then produced using combinations of annual wet day rainfall (for Berga), monthly flow (for Holeta), and stationary circumstances (for Ginchi) based on the best-fit proposed models. The discharge from three tributaries to the main Awash River is provided under nonstationary and stationary conditions to calculate the Becho floodplain depth, velocity and extent using the steady-state HEC-RAS model. Concurrent flows to the main channel were used in this study as the worst-case flood scenario. The simulated inundation depth and floodwater velocity at 2, 25, 50, and 100-year return period maps are shown in Figures 6.10 and 6.11. The average depth at 2, 25, 50, and 100-year return periods was 1.1 m, 1.4 m, 1.6 m, and 1.85 m, respectively. The high flood velocity approaches upstream and exiting downstream boundaries, indicating that floods steadily inundate the areas. The increase in inundation depth and extent correspond to the probable flood quantiles.

**Figure 6.10** 1D floodwater depth map for various return periods: **a)** 2-year flood **b)** 25-year flood **c)** 50-year flood **d)** 100-year flood

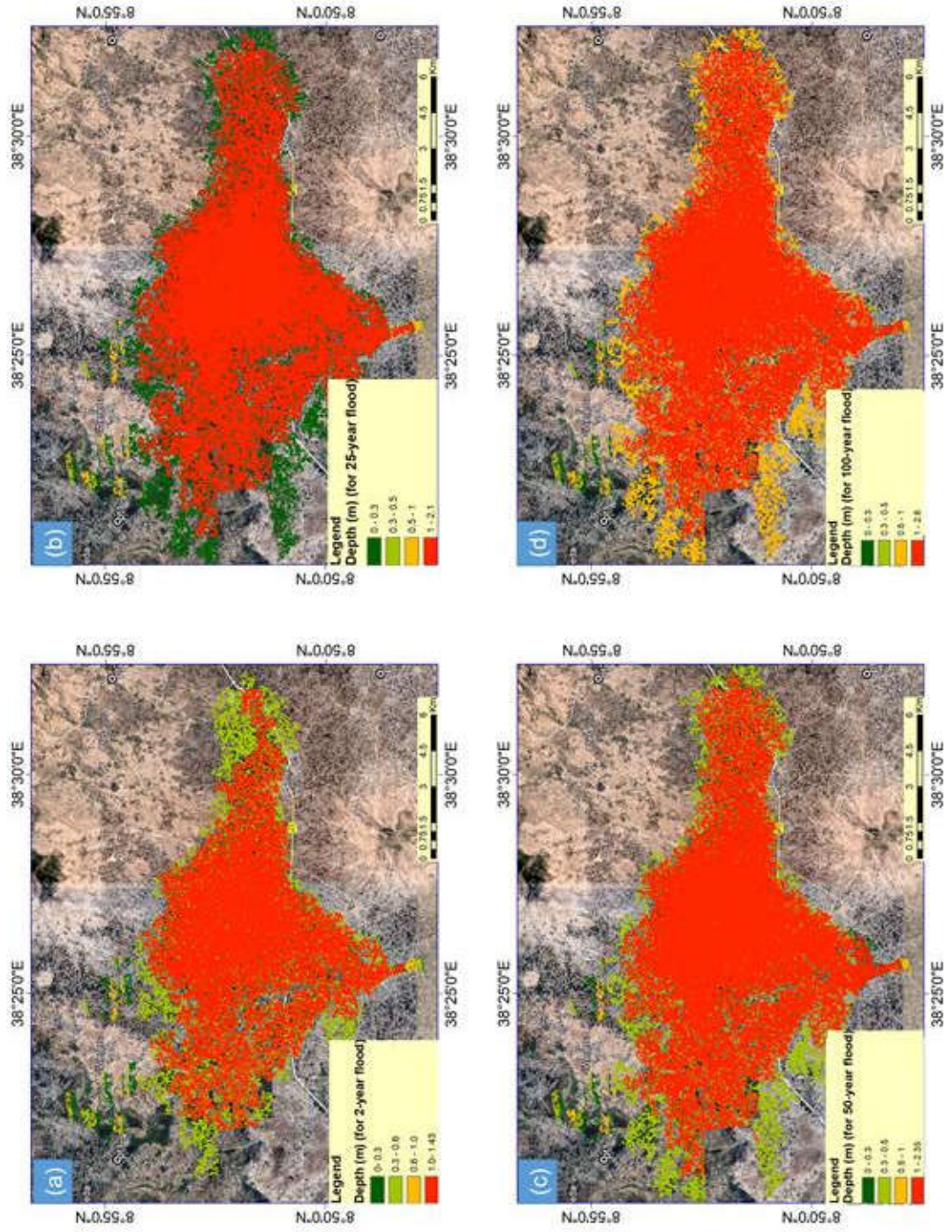
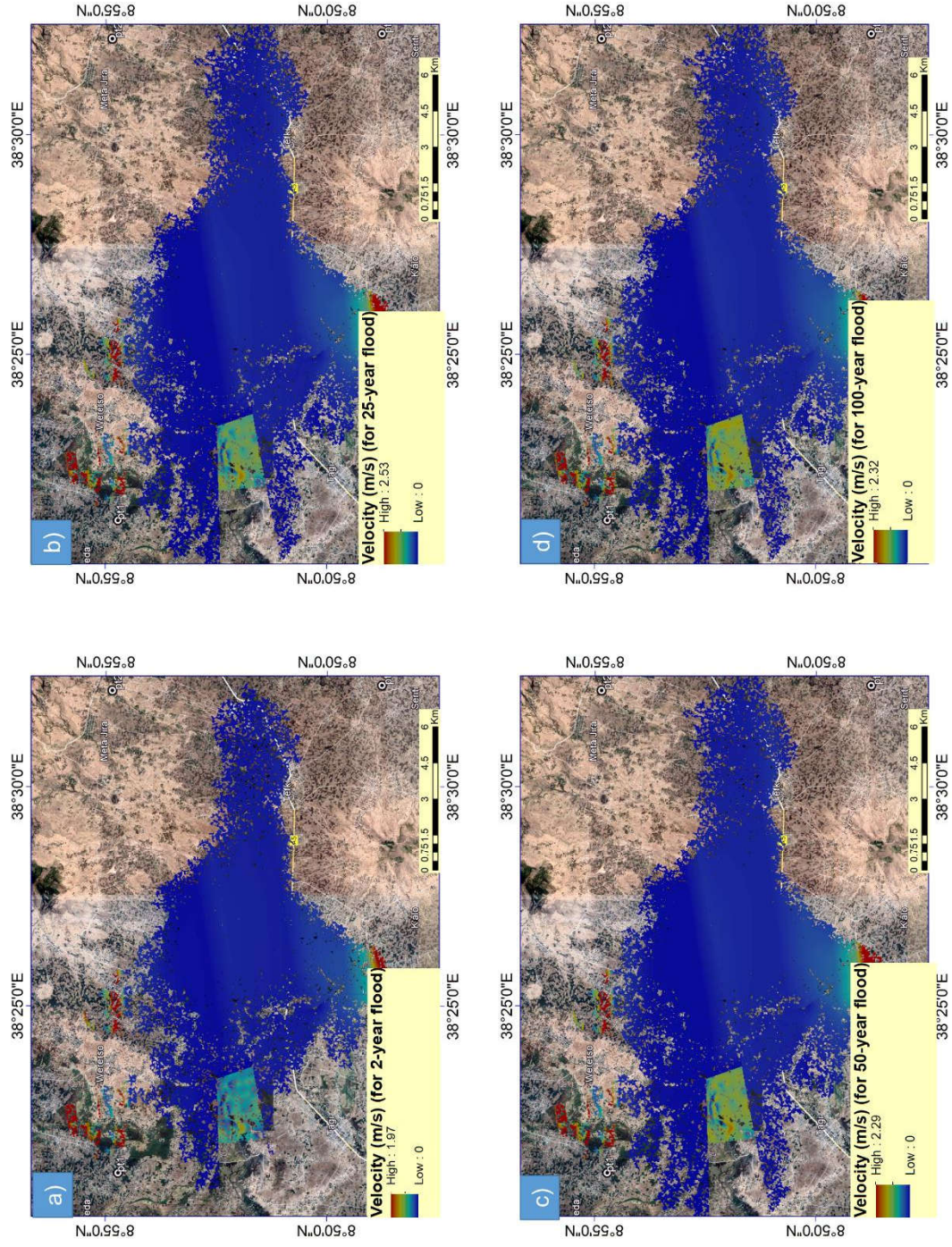


**Figure 6.11** 1D floodwater velocity map for various return periods: **a)** 2-year flood **b)** 25-year flood **c)** 50-year flood **d)** 100-year flood



Inundation depth, velocity, and the combination of depth and velocity are the parameters considered for evaluating flood hazards within the floodplain. The flood hazard can be classified as high ( $> 1\text{m}$ ), medium ( $0.5\text{-}1\text{m}$ ), low ( $0.3\text{-}0.5\text{m}$ ), and very low ( $\leq 0.3\text{m}$ ). The flood hazard was calculated based on the depth at 25 and 100 years of the return period. For a 25-year flood, the estimated areal percentage distribution of flooded areas for high, medium, low, and very low hazard levels is 75%, 1%, 1%, and 23%, respectively. For a 100-year return period, the area for high, medium, low, and very low hazard levels is 76%, 22%, 1%, and 1%, respectively (Table 6.10).

**Table 6.10** Flood hazard class based on the flood depth and the corresponding inundation area of different return level

Depth (m)	Class	Area (km <sup>2</sup> )			
		2-year	25-year	50-year	100-year
$0 \leq D \leq 0.3$	Very low	1.98	26	1.45	1.2
$0.3 \leq D \leq 0.5$	Low	24.1	1.5	25.5	1.1
$0.5 \leq D \leq 1$	Medium	0.69	0.77	0.75	25.6
$> 1$	High	62.4	85.5	86.2	86.2
Total		88.48	113.77	113.9	114.1

Smith et al. (2014) prepared a flood hazard curve and its categorization based on the combinations of flood depth and flow velocity thresholds to assess a community's relative vulnerability and assets. For instance, high depth, high velocity, high depth and flow (product of depth and velocity) can all pose a high level of risk. Combinations are used to categorize and quantify the hazard level. Flood hazard categorization was done using a threshold of 1 m depth and 2 m/s velocity for flood events with various return durations in the Becho floodplain. It was noted before that floodwater depths of 1 meter or more cause massive damage to this region's communities, properties, and agricultural farms. Table 6.11 presents the flood hazard classifications, which are divided into four categories: H-1, H-2, H-3, and H-4, as well as the depth threshold, velocity threshold, and hazardous conditions. It should be noted that the majority of the floodplain area velocity is less

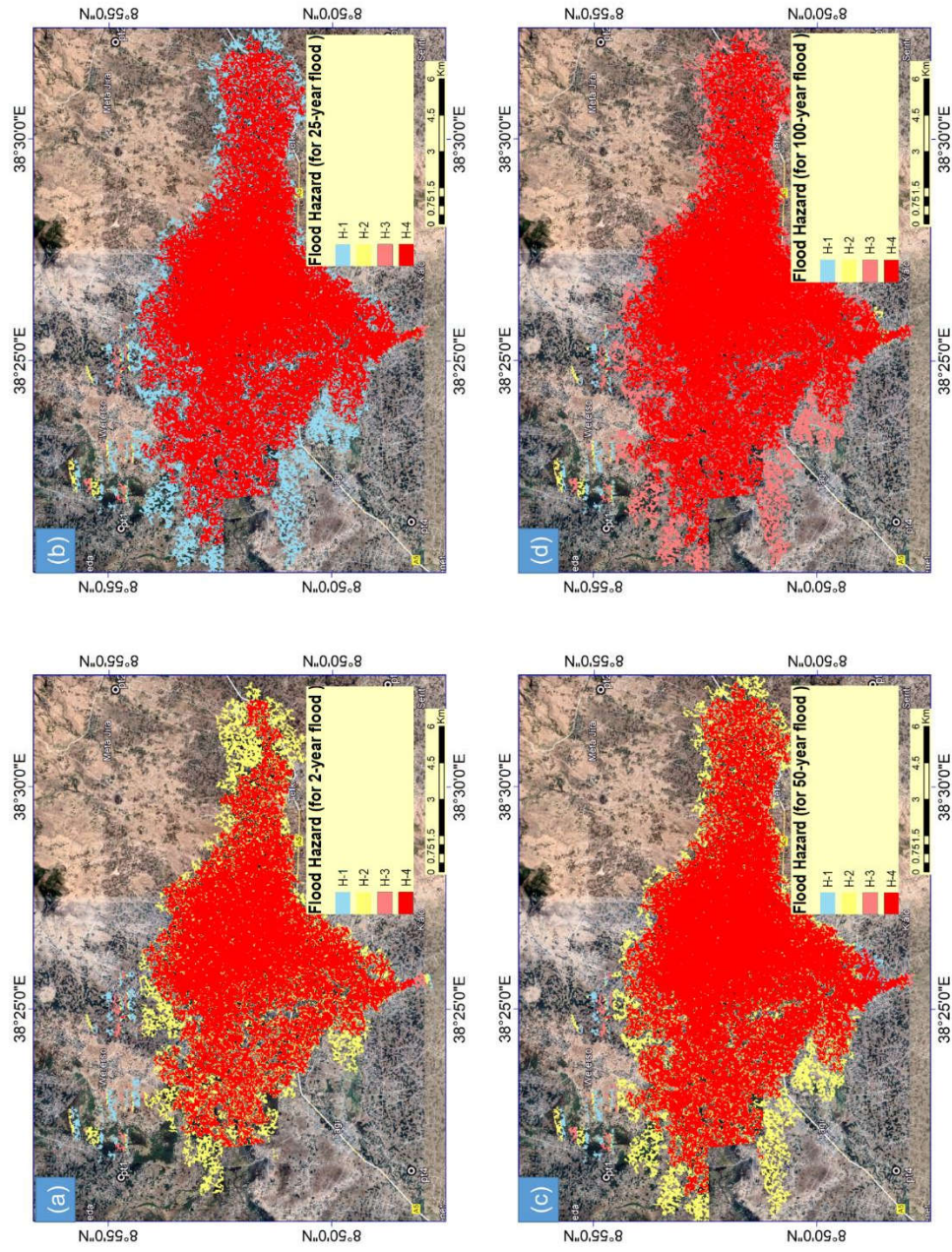
than 0.05 m/s, suggesting that flood depth may be the determining factor. Figures 6.12 and 6.13 depict the spatial variations of hazard class and its corresponding areas. The hazard class H-4 covers a broader area, about 70% of the flood extent of different flood events (2, 25, 50, and 100-years of return), which is generally unsafe for all.

**Table 6.11** Thresholds for flood hazard classification

Hazard Index	Depth (m)	Velocity (m/s)	Hazard class ( $D \cdot V$ , $m^2/s$ )	Description
H-1	$0 \leq D \leq 0.3$	$\leq 2$	$\leq 0.3$	safe for vehicles, people, and buildings
H-2	$0.3 \leq D \leq 0.5$	$\leq 2$	$\leq 0.6$	unsafe for small vehicles, children, and elderly
H-3	$0.5 \leq D \leq 1$	$\leq 2$	$\leq 1.0$	unsafe for vehicles and people
H-4	$> 1$	$\leq 2$	$> 1.0$	unsafe for all

It can be seen that the total area expands as the return period lengthens/longer, e.g., increased from 2 to 25 return years by about 28.7%, but after 25 years of return, the area becomes constant (114 km<sup>2</sup>). The area of the H-3 flood hazard class, where the floodwater depth is between 0.5 and 1m, is less than 0.74 km<sup>2</sup> for 2, 25, and 50-year floods, while the area for the 100-year flood is 25.6 km<sup>2</sup>. The hazardous condition of the class of H-2 covers an area of 24.5 and 25.26 km<sup>2</sup> for 25 and 50 years flood, respectively, is unsafe for the vehicle, children, and older people. There are very few safe zones ( $\leq 1.7$  km<sup>2</sup>) in the floodplain, but there are about 26 km<sup>2</sup> in the H-1 class for a 25-year flood event. In this case, the hazard areas are consistent with the hazard identified using depth-based hazard classification. The projected view in Google Earth Pro clearly shows that the area surrounding the communities is flooded, while high-elevated settlements are less flood-prone (Figure 6.14). However, the inundation increases as the flood discharge increases. The results showed that the left bank of the river has a significant flood extent and depth and

**Figure 6.12** Flood hazard map of the Becho floodplain for different flood return periods: **a)** 2-year flood **b)** 25-year flood **c)** 50-year flood **d)** 100-year flood



has a high probability of flooding in the future as long as no protection work along the river bank is available.

It can be concluded that most of the floodplain falls under the H-4 during flood events, which pose a significant risk to the community, properties, and agriculture. Flood occurring in plain areas where the flow steadily inundates, the role of floodwater velocity diminishes significantly in hazard assessment; the flood depth can be used instead.

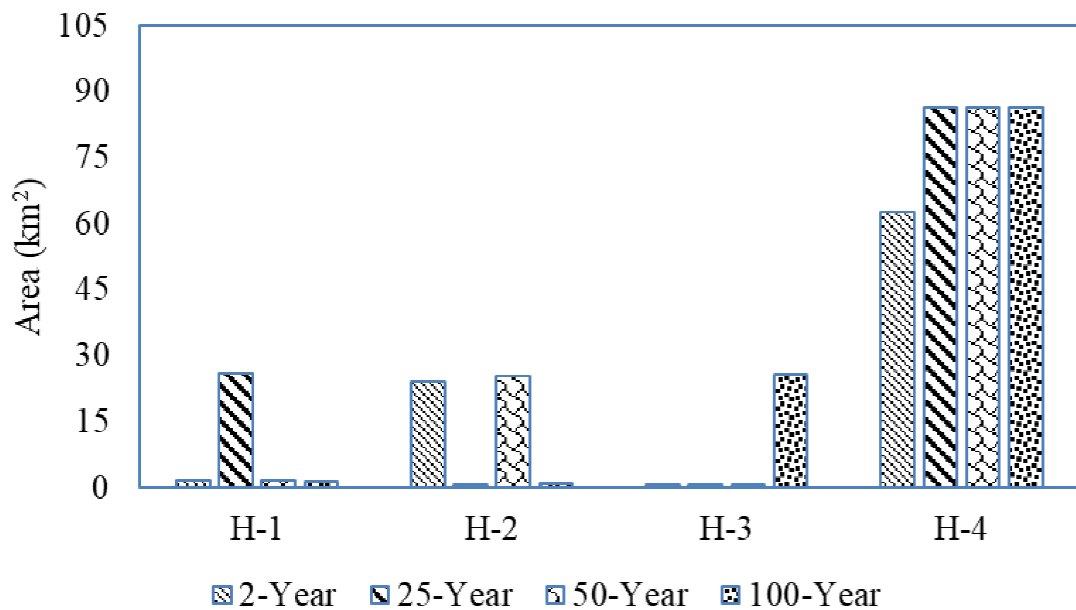


**Figure 6.13** The corresponding area of each flood hazard class for different flood return periods

The observed flood marks for August 2020, as shown in Figure 6.14, were compared to the simulated floodwater depth for the 25-year return period, and the simulated inundation depth was found to be 1.1m, except for point 1 (0.1m), which could be due to the flood amount being less than the estimated 25-year return and the assumptions in 1D steady simulations. Namara et al. (2022) produced stationary-based flood inundation area maps for 2, 25, 50, and 100 years of flood events, revealing statistical differences of 22%, 12.5%, 7.9%, and 4.3%, and obtained a flood depth of 0.5m, which is incomparable with current research and observed ground data (Table 6.12). The difference in both flood variables would

arise from the hydrological model-based flood quantile estimation, e.g., HEC HMS model) and flood frequency approach utilized (e.g., Log Pearson type III distribution). The flood water depth observed in 2020 and the simulated by Namara et al. (2022) may be similar at some points; however, most of the floodplains are not. The map showed similarities in the extent of inundation on both banks, with a greater extent on the river's left bank.

The significant difference observed could be attributed to the method used and the fact that nonstationary-based flood map modeling is more accurate than stationary-based flood map modeling (Binh et al. 2019). However, compared to the previous study, the current simulated flood depth of a 25-year return period is near the observed flood. Moreover, the previous study was less informative in aspects of hazard level. The present study focused solely on the floodplain area, accounting for depth, velocity, and combinations of both in a nonstationary framework. This work's outcome more practically applies to flood management and control planning.

**Table 6.12** Comparative analysis between the current and earlier study in the area

Return Period (year)	Current analysis		Namara et al. (2022)		Statistical Difference	
	Flood depth (m)	Flood extent (km <sup>2</sup> )	Flood extent (km <sup>2</sup> )	Flood depth (m)	Flood extent (%)	Flood depth (%)
2	1.43	89.23	71.5	0.45	22.06	104.26
25	2.1	113.71	100.3	0.467	12.53	127.23
50	2.35	113.88	105.2	0.477	7.92	132.51
100	2.6	114.2	109.5	0.489	4.20	136.68

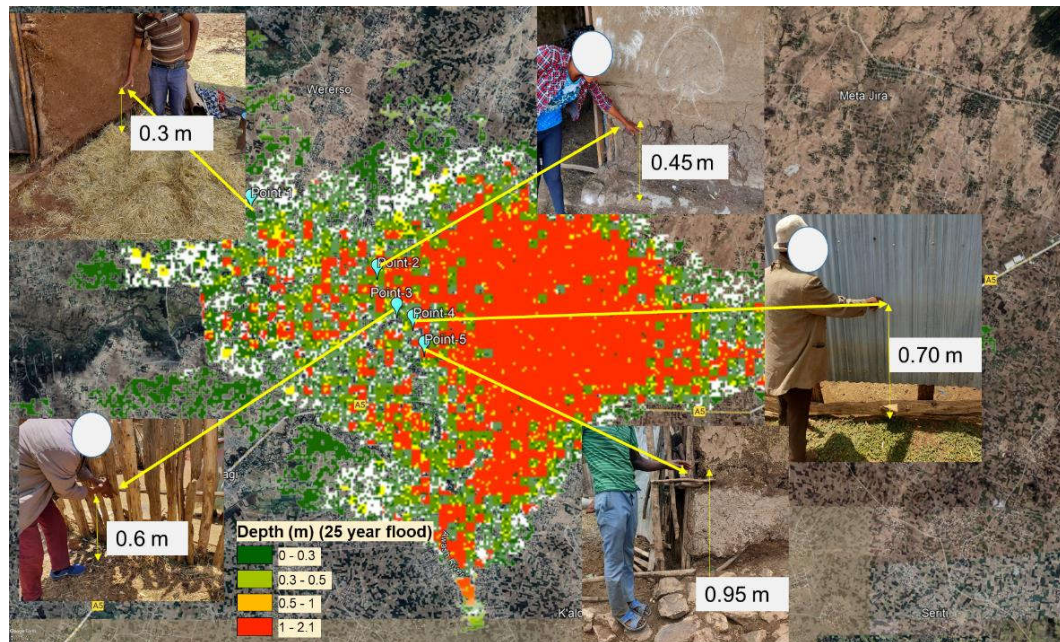


**Figure 6.14** Floodwater depth map for a 25-year return period and observed flood depth in August 2020

#### 6.4 Conclusions

This chapter proposed a morphometric approach to characterize the spatial flood characteristics and identify the subbasin’s flood susceptibility and flood spot areas. In addition, a nonstationary flood frequency technique was used for the flood hazard map of the specific flood-prone area. The following is a summary of the conclusion:

The drainage pattern of the basin is dendritic, and the sixth stream order drainage pattern revealed higher discharge volumes, velocity, and soil erosion from the subbasin. Very high stream segments indicate active hydrological response during rainfall and are exhibited in SB-1. There is a minimal difference in drainage density (0.83 – 0.89) and stream frequency (0.57 – 0.59) across subbasins, and the potential of flood effect is more significant in the upper SB-1 and lower SB-4. The fine drainage texture and circularity ratio of SB-1 suggest that it is more prone to floods. The elongated nature of the subbasins (SB-2, the most elongated) takes longer to respond to rainfall, more extended concentration, and peak flow. Higher relief aspects (basin relief, relief ratio, and slope) values indicate a substantial discharge

flow from upstream reach with denudational characteristics and contribute to an increased danger of flooding in the plateau-dominated area.

Cumulative evaluation of 15 parameters of the total 23 morphometric parameters based on score ranking revealed that each subbasin has comparative hydrologic response behaviour, but SB-1 is the highest, SB-3 and SB-4 moderate, and SB-2 low susceptible to flood. The direct proportional watershed characteristics to floods compose the majority of SB-1 flood susceptibility and modest influence in other subbasins. Subsequently, the specific regions susceptible to flood events and inundations were determined based on the combined topographic influence of the TWI and TPI. The Upper Awash River basin, which accounts for 22.8%, 41.7% and 35.6% of the entire basin, has been classified as high, medium, and low flood-prone, respectively. In this study, the topographic position index and topographic wetness index, in addition to morphometric factors, outperformed in locating flood-prone locations in agreement with the ground truth.

Nonstationary model outperformed the stationary flood frequency model. In this study, the covariates, August month and PRCPTOT rainfall indices, corresponding to the best models, had a stronger correlation with peak flow, indicating the stronger covariate relationship with peak, the best-fit model. These covariates explain the changing flood characteristics in the region. Flood hazard mapping based on the depth alone and the combination of depth and velocity thresholds resulted in about 70% of areas of the Becho floodplain being classified as a high hazard of various flood events (2, 25, 50, and 100 years). The hazardous condition is unsafe for people, properties, and assets.

## CHAPTER 7

### CONCLUSIONS AND FUTURE SCOPE

#### 7.1 Summary

A comprehensive investigation concerning floods to minimize the adverse effects on the economy, property, and lives is significant and proposed in this study. The study first aims to investigate the variability of extreme hydroclimatic conditions and the relationship between anomalies in extreme local precipitation, ENSO indicators (Southern Oscillation Index (SOI), Niño 3.4, and Multivariate ENSO Index (MEI)), and extreme flow indices. Then, quantitatively assessed the effects of individual and coupled changes in land cover and climate on peak and high flows. Further, spatial flood characteristics include the degree of susceptibility, potential flood areas, extent assessed, and developed flood hazard map for the specific flood area.

Conclusions are drawn based on current findings, and the study's limitations and future scope are put forward.

#### 7.2 Conclusions

The study's conclusions can be summarized in line with specific objectives.

**Objective 1:** To investigate the variability of extreme hydroclimatic and the relationship between anomalies in extreme local precipitation, ENSO indicators, and extreme hydrological indices

- The overall variability of extreme rainfall indices across the entire basin was found to be less than 20%, suggesting less variability. However, a high degree of spatial variability (with CV > 30%) was observed in the rainfall indices (specifically, Rmax1, R99p, and R95p) and extreme flow indices at the Hombole and Melka Kunture stations. Decadal anomaly analysis of the

rainfall indices indicated a higher frequency of positive anomalies in the 1990s compared to the 2000s. Overall, the changes in extreme flow indices aligned with changes in climate across the subbasins and basins.

- The basin-wise temperature increased significantly, and the maximum and minimum temperatures showed a significant upward shift, and the minimum temperature showed a downward shift in the late 1990s and early 2000s. Rainfall indices showed weak increasing and decreasing trend trends, and the change point was noted in 2000s. Spatially extreme flow in the basin decreased at Hombole and significantly increased at Melka Kunture station, and change points were observed in the 2000s. The hydroclimatic characteristics, in general, are nonstationary, i.e., variable over time.
- The widespread PRCPTOT and R95p anomalies triggered the extreme water flow anomalies of Melka Kunture and Hombole outlet stations. Notably, the intense precipitation events in northwestern rainfall stations displayed a relationship with Melka Kunture's extreme flow indices, which could explain the extreme occurrences. The Hombole outlet station's extreme water flow anomalies also exhibited a more robust relationship with ENSO indicators than the Melka Kunture. Therefore, positive extreme flow anomalies may be expected in the basin during the positive SOI, negative Niño 3.4, and MEI phases.

**Objective 2:** To quantify the change in land cover and rainfall variability impact on flood

- The SWAT model gave well-estimated peak and high flood discharges at Melka Kunture and Hombole hydrologic stations. The upstream Melka Kunture sub-basin indicated that the land cover change alone scenario with cropland dominating land cover was the major contributor to peak and high flow increases of 38.69 % and 11.95%, respectively, in the later period. The combined scenario was the leading cause, accounting for 19.55 % and 50.33 % of the decrease in peak and high flow in the Hombole sub-basin over the later period.

**Objective 3:** To investigate the basins spatial flood characteristics based on the morphometric effect and flood hazard map of the highly susceptible flood area using the nonstationary flood frequency model

- Cumulative evaluation of 15 parameters of the total 23 morphometric parameters based on score ranking revealed that each subbasin has comparative hydrologic response behaviour, but SB-1 is the highest, SB-3 and SB-4 moderate, and SB-2 low susceptible to flood. The Upper Awash River basin, which accounts for 22.8%, 41.7% and 35.6% of the entire basin, has been classified as high, moderate, and low flood-prone, respectively. In addition to morphometric factors, the topographic position index and topographic wetness index outperformed in locating flood-prone areas in agreement with the ground truth.
- The nonstationary model outperformed the stationary flood frequency model. In this study, the covariates, August month and PRCPTOT rainfall indices, corresponding to the best models, had a stronger correlation with peak flow. This indicates a stronger covariate relationship with peak, the best-fit model. These covariates have explanatory power for changing flood characteristics in the region. Flood hazard mapping based on depth alone and the combination of depth and velocity thresholds resulted in more significant areas of the Becho floodplain being classified as high-hazard areas for various flood events (2, 25, 50, and 100 years). The hazardous condition is unsafe for people, properties, and assets.
- The flood effect can be reduced through soil and water conservation practices above the Becho flood plain, providing more outlets in the plain areas, frequently removing sediment from the River, widening the channel, and building high river embankments. Non-structural measures such as early warning and early evacuation would minimize the effects.

### **7.3 Limitations of the study**

The study used limited climate indices and climate variables to assess the relationship with flood indices in the regions. Long-term hydrological and high-

resolution elevation data for flood hazard mapping are the study's major limitations for flood hazard assessment in the area. Uncertainty analysis related to land cover classification, simulated stream flow using the SWAT model, flood estimation, and parameter estimation during flood frequency analysis are also other limitations of the current study.

#### **7.4 Future scope of the study**

Human activities in the basin, water withdrawal for small-scale irrigation, land cover dynamics, basin soil moisture condition, topography, and other modes of climate variability like the Indian Ocean Dipole (IOD) and the Pacific Decadal Oscillation (PDO) all affect hydrological variability and need to be studied to learn more about how flood change in the basin. In the future, studies are essential to improve the current research with additional data such as high-resolution elevation data, covariates that directly reflect the changing flood events, and long hydrological data. A combination of hydrological and hydraulic models with unsteady flow 1D-2D could be used for detailed flood hazard evaluation in the area. Most importantly, determining the overall uncertainty of the nonstationary flood frequency approach is critical. The use of multiple models is feasible to investigate the uncertainty sources.

## REFERENCES

- Abbaspour KC, Johnson CA, van Genuchten MT (2004) Estimating Uncertain Flow and Transport Parameters Using a Sequential Uncertainty Fitting Procedure. *Vadose Zo J* 3:1340–1352. <https://doi.org/10.2136/vzj2004.1340>
- Abbaspour KC, Vaghefi SA, Srinivasan R (2017) A guideline for successful calibration and uncertainty analysis for soil and water assessment: A review of papers from the 2016 international SWAT conference. *Water (Switzerland)* 10:. <https://doi.org/10.3390/w10010006>
- Abbaspour KC, Yang J, Maximov I, et al (2007) Modelling hydrology and water quality in the pre-alpine/alpine Thur watershed using SWAT. *J Hydrol* 333:413–430. <https://doi.org/10.1016/j.jhydrol.2006.09.014>
- Abteu W, Melesse AM, Dessalegne T (2009) El Niño Southern Oscillation link to the Blue Nile River Basin hydrology. *Hydrol Process* 23:3653–3660. <https://doi.org/10.1002/hyp.7367>
- Ahmed N, Wang G, Lü H, et al (2022) Attribution of Changes in Streamflow to Climate Change and Land Cover Change in Yangtze River Source Region, China. *Water* 14:259. <https://doi.org/10.3390/w14020259>
- Ahn K-H, Palmer RN (2016) Trend and Variability in Observed Hydrological Extremes in the United States. *J Hydrol Eng* 21:1–10. [https://doi.org/10.1061/\(asce\)he.1943-5584.0001286](https://doi.org/10.1061/(asce)he.1943-5584.0001286)
- Akaike AH (1974) new look at the statistical model identification. In: *Automatic Control IEEE Transactions on*. pp 19(6):716-723
- Akter T, Quevauviller P, Eisenreich SJ, Vaes G (2018) Impacts of climate and land use changes on flood risk management for the Schijn River, Belgium. *Environ Sci Policy* 89:163–175. <https://doi.org/10.1016/j.envsci.2018.07.002>
- Alam A, Ahmed B, Sammonds P (2021) Flash flood susceptibility assessment using the parameters of drainage basin morphometry in SE Bangladesh. *Quat Int* 575–

576:295–307. <https://doi.org/10.1016/j.quaint.2020.04.047>

Almeida RA, Pereira SB, Pinto DBF (2018) CALIBRATION AND VALIDATION OF THE SWAT HYDROLOGICAL MODEL FOR THE MUCURI RIVER BASIN. *Eng Agrícola* 38:55–63

Alqahtani F, Qaddah AA (2019) GIS digital mapping of flood hazard in Jeddah–Makkah region from morphometric analysis. *Arab J Geosci* 12:.  
<https://doi.org/10.1007/s12517-019-4338-8>

Altaf F, Meraj G, Romshoo SA (2013) Morphometric Analysis to Infer Hydrological Behaviour of Lidder Watershed, Western Himalaya, India. *Geogr J* 2013:1–14.  
<https://doi.org/10.1155/2013/178021>

Angillieri MYE (2012) Morphometric characterization of the Carrizal basin applied to the evaluation of flash floods hazard, San Juan, Argentina. *Quat Int* 253:74–79.  
<https://doi.org/10.1016/j.quaint.2011.05.011>

Anose FA, Beketie KT, Terefe Zeleke T, et al (2021) Spatio-temporal hydro-climate variability in Omo-Gibe river Basin, Ethiopia. *Clim Serv* 24:100277.  
<https://doi.org/10.1016/j.cliser.2021.100277>

Ansa Thasneem S, Chithra NR, Thampi SG (2019) Analysis of extreme precipitation and its variability under climate change in a river basin. *Nat Hazards* 98:1169–1190. <https://doi.org/10.1007/s11069-019-03664-7>

Apel H, Thielen AH, Merz B, Blöschl G (2006) A probabilistic modelling system for assessing flood risks. *Nat Hazards* 38:79–100. <https://doi.org/10.1007/s11069-005-8603-7>

Arnold JG, Kiniry JR, Srinivasan R, et al (2012) Soil & Water Assessment Tool. Version 2012. 654

Arnold JG, Srinivasan R, Muttiah RS, Williams JR (1998) Large area hydrologic modeling and assessment Part I: model development. *J Am Water Resour Assoc* 34:73–89. <https://doi.org/10.1111/j.1752-1688.1998.tb05961.x>

- Arrieta-Castro M, Donado-Rodríguez A, Acuña GJ, et al (2020) Analysis of streamflow variability and trends in the meta river, Colombia. *Water (Switzerland)* 12:.. <https://doi.org/10.3390/w12051451>
- Asadieh B, Krakauer NY (2017) Global change in streamflow extremes under climate change over the 21st century. *Hydrol Earth Syst Sci* 21:5863–5874. <https://doi.org/10.5194/hess-21-5863-2017>
- Asfaw A, Simane B, Hassen A, Bantider A (2018) Variability and time series trend analysis of rainfall and temperature in northcentral Ethiopia: A case study in Woleka sub-basin. *Weather Clim Extrem* 19:29–41. <https://doi.org/10.1016/j.wace.2017.12.002>
- Asfaw D, Workineh G (2019) Quantitative analysis of morphometry on Ribb and Gumara watersheds: Implications for soil and water conservation. *Int Soil Water Conserv Res* 7:150–157. <https://doi.org/10.1016/j.iswcr.2019.02.003>
- Bao Z, Zhang J, Wang G, et al (2019) The impact of climate variability and land use/cover change on the water balance in the Middle Yellow River Basin, China. *J Hydrol* 577:123942. <https://doi.org/10.1016/j.jhydrol.2019.123942>
- Bekele D, Alamirew T, Kebede A, et al (2017) Analysis of rainfall trend and variability for agricultural water management in awash river Basin, Ethiopia. *J Water Clim Chang* 8:127–141. <https://doi.org/10.2166/wcc.2016.044>
- Bekele D, Alamirew T, Kebede A, et al (2019) Land use and land cover dynamics in the Keleta watershed, Awash River basin, Ethiopia. *Environ Hazards* 18:246–265. <https://doi.org/10.1080/17477891.2018.1561407>
- Belihu M, Abate B, Tekleab S, Bewket W (2018) Hydro-meteorological trends in the Gidabo catchment of the Rift Valley Lakes Basin of Ethiopia. *Phys Chem Earth, Parts A/B/C* 104:84–101. <https://doi.org/10.1016/j.pce.2017.10.002>
- Belihu M, Tekleab S, Abate B, Bewket W (2020) Hydrologic response to land use land cover change in the Upper Gidabo Watershed, Rift Valley Lakes Basin,

- Ethiopia. *HydroResearch* 3:85–94. <https://doi.org/10.1016/j.hydres.2020.07.001>
- Bellos V (2012) Ways for flood hazard mapping in urbanised environments : A short literature review. *Water Util J* 4:25–31
- Benzater B, Elouissi A, Benaricha B, Habi M (2019) Spatio-temporal trends in daily maximum rainfall in northwestern Algeria (Macta watershed case, Algeria). *Arab J Geosci* 12:. <https://doi.org/10.1007/s12517-019-4488-8>
- Berihun ML, Tsunekawa A, Haregeweyn N, et al (2019) Hydrological responses to land use/land cover change and climate variability in contrasting agro-ecological environments of the Upper Blue Nile basin, Ethiopia. *Sci Total Environ* 689:347–365. <https://doi.org/10.1016/j.scitotenv.2019.06.338>
- Bertola M, Viglione A, Blöschl G (2019) Informed attribution of flood changes to decadal variation of atmospheric, catchment and river drivers in Upper Austria. *J Hydrol* 577:123919. <https://doi.org/10.1016/j.jhydrol.2019.123919>
- Berz G, Kron W, Loster T, et al (2001) World map of natural hazards - a global view of the distribution and intensity of significant exposures. *Nat Hazards* 23:443–465. <https://doi.org/10.1023/A:1011193724026>
- Beven KJ, Kirkby MJ (1979) A physically based, variable contributing area model of basin hydrology / Un modèle à base physique de zone d'appel variable de l'hydrologie du bassin versant. *Hydrol Sci Bull* 24:43–69. <https://doi.org/10.1080/02626667909491834>
- Bewket W, Sterk G (2005) Dynamics in land cover and its effect on stream flow in the Chemoga watershed, Blue Nile basin, Ethiopia. *Hydrol Process* 19:445–458. <https://doi.org/10.1002/hyp.5542>
- Bhaskar NR, Parida BP, Nayak AK (1997) Flood Estimation for Ungauged Catchments Using the GIUH. *J Water Resour Plan Manag* 123:228–238. [https://doi.org/10.1061/\(asce\)0733-9496\(1997\)123:4\(228\)](https://doi.org/10.1061/(asce)0733-9496(1997)123:4(228))
- Bhat MS, Alam A, Ahmad S, et al (2019) Flood hazard assessment of upper Jhelum

- basin using morphometric parameters. *Environ Earth Sci* 78:54.  
<https://doi.org/10.1007/s12665-019-8046-1>
- Bhatti AS, Wang G, Ullah W, et al (2020) Trend in extreme precipitation indices based on long term in situ precipitation records over Pakistan. *Water* (Switzerland) 12:1–19. <https://doi.org/10.3390/w12030797>
- Billi P, Alemu YT, Ciampalini R (2015) Increased frequency of flash floods in Dire Dawa, Ethiopia: Change in rainfall intensity or human impact? *Nat Hazards* 76:1373–1394. <https://doi.org/10.1007/s11069-014-1554-0>
- Billi P, Fazzini M, Alemu YT, Ciampalini R (2014) Rainfall and runoff variability in Ethiopia. 16:7397
- Binh LTH, Umamahesh N V., Rathnam EV (2019) High-resolution flood hazard mapping based on nonstationary frequency analysis: case study of Ho Chi Minh City, Vietnam. *Hydrol Sci J* 64:318–335.  
<https://doi.org/10.1080/02626667.2019.1581363>
- Birsan MV, Molnar P, Burlando P, Pfandner M (2005) Streamflow trends in Switzerland. *J Hydrol* 314:312–329.  
<https://doi.org/10.1016/j.jhydrol.2005.06.008>
- Bobée B, Cavadias G, Ashkar F, et al (1993) Towards a systematic approach to comparing distributions used in flood frequency analysis. *J Hydrol* 142:121–136.  
[https://doi.org/10.1016/0022-1694\(93\)90008-W](https://doi.org/10.1016/0022-1694(93)90008-W)
- Brath A, Montanari A, Moretti G (2006) Assessing the effect on flood frequency of land use change via hydrological simulation (with uncertainty). *J Hydrol* 324:141–153. <https://doi.org/10.1016/j.jhydrol.2005.10.001>
- Burn DH, Hag Elnur MA (2002) Detection of hydrologic trends and variability. *J Hydrol* 255:107–122. [https://doi.org/10.1016/S0022-1694\(01\)00514-5](https://doi.org/10.1016/S0022-1694(01)00514-5)
- Cayan DR, Redmond KT, Riddle LG (1999) ENSO and hydrologic extremes in the western United States. *J Clim* 12:2881–2893. <https://doi.org/10.1175/1520->

0442(1999)012<2881:EAHEIT>2.0.CO;2

Chang X, Xu Z, Zhao G, et al (2018) Spatial and temporal variations of precipitation during 1979–2015 in Jinan City, China. *J Water Clim Chang* 9:540–554.

<https://doi.org/10.2166/wcc.2017.029>

Chen F, Chen H, Yang Y (2015) Annual and seasonal changes in means and extreme events of precipitation and their connection to elevation over Yunnan Province, China. *Quat Int* 374:46–61. <https://doi.org/10.1016/j.quaint.2015.02.016>

Chen J, Wu X, Finlayson BL, et al (2014) Variability and trend in the hydrology of the Yangtze River, China: Annual precipitation and runoff. *J Hydrol* 513:403–412. <https://doi.org/10.1016/j.jhydrol.2014.03.044>

Chiew FHS, McMahon TA (2002) Téléconnexion entre le phénomène ENSO et l'écoulement, les prévisions d'écoulement et la variabilité interannuelle. *Hydrol Sci J* 47:505–522. <https://doi.org/10.1080/02626660209492950>

Chilkoti V, Bolisetti T, Balachandar R (2018) Multi-objective autocalibration of SWAT model for improved low flow performance for a small snowfed catchment. *Hydrol Sci J* 63:1482–1501.

<https://doi.org/10.1080/02626667.2018.1505047>

Choudhari PP, Nigam GK, Singh SK, Thakur S (2018) Morphometric based prioritization of watershed for groundwater potential of Mula river basin, Maharashtra, India. *Geol Ecol Landscapes* 2:256–267.

<https://doi.org/10.1080/24749508.2018.1452482>

Chow V Te (1959) *Open-channel hydraulics*. McGraw-Hill, New York

Chowdhuri I, Pal SC, Chakraborty R (2020) Flood susceptibility mapping by ensemble evidential belief function and binomial logistic regression model on river basin of eastern India. *Adv Sp Res* 65:1466–1489.

<https://doi.org/10.1016/j.asr.2019.12.003>

Coles S (2001) *An Introduction to Statistical Modeling of Extreme Values*. Springer

London, London

Comin AN, Justino F, Pezzi L, et al (2021) Extreme rainfall event in the Northeast coast of Brazil: a numerical sensitivity study. *Meteorol Atmos Phys* 133:141–162. <https://doi.org/10.1007/s00703-020-00747-0>

Costa MH, Botta A, Cardille JA (2003) Effects of large-scale changes in land cover on the discharge of the Tocantins River, Southeastern Amazonia. *J Hydrol* 283:206–217. [https://doi.org/10.1016/S0022-1694\(03\)00267-1](https://doi.org/10.1016/S0022-1694(03)00267-1)

Costabile P, Costanzo C, Ferraro D, et al (2020) Performances of the New HEC-RAS Version 5 for 2-D Hydrodynamic-Based Rainfall-Runoff Simulations at Basin Scale: Comparison with a State-of-the Art Model. *Water* 12:2326. <https://doi.org/10.3390/w12092326>

CRED (2020) The human cost of disasters: an overview of the last 20 years (2000–2019). Centre for Research on the Epidemiology of Disasters

CRED (2022) The interplay of drought-flood extreme events in Africa over the last twenty years (2002-2021)

Daba MH, Ayele GT, You S (2020) Long-Term Homogeneity and Trends of Hydroclimatic Variables in Upper Awash River Basin, Ethiopia. *Adv Meteorol* 2020:1–21. <https://doi.org/10.1155/2020/8861959>

Daba MH, You S (2020) Assessment of climate change impacts on river flow regimes in the upstream of awash basin, ethiopia: Based on ipcc fifth assessment report (ar5) climate change scenarios. *Hydrology* 7:1–22. <https://doi.org/10.3390/hydrology7040098>

Daniel EB, Camp J V., LeBoeuf EJ, et al (2011) Watershed Modeling and its Applications: A State-of-the-Art Review. *Open Hydrol J* 26–50

Das S, Pardeshi SD (2018) Morphometric analysis of Vaitarna and Ulhas river basins, Maharashtra, India: using geospatial techniques. *Appl Water Sci* 8:1–11. <https://doi.org/10.1007/s13201-018-0801-z>

- De Roo A, Odijk M, Schmuck G, et al (2001) Assessing the effects of land use changes on floods in the meuse and oder catchment. *Phys Chem Earth, Part B Hydrol Ocean Atmos* 26:593–599. [https://doi.org/10.1016/S1464-1909\(01\)00054-5](https://doi.org/10.1016/S1464-1909(01)00054-5)
- Debelo G, Tadele K, Koriche SA (2017) Morphometric Analysis To Identify Erosion Prone Areas on the Upper Blue Nile Using Gis (Case Study of Didessa and Jema Sub-Basin, Ethiopia). *Int Res J Eng Technol* 4:1773–1784
- Degefu MA, Alamirew T, Zeleke G, Bewket W (2019) Detection of trends in hydrological extremes for Ethiopian watersheds, 1975–2010. *Reg Environ Chang* 19:1923–1933. <https://doi.org/10.1007/s10113-019-01510-x>
- Degefu MA, Bewket W (2017) Variability, trends, and teleconnections of stream flows with large-scale climate signals in the Omo-Ghibe River Basin, Ethiopia. *Environ Monit Assess* 189:. <https://doi.org/10.1007/s10661-017-5862-1>
- Desalegn T, Cruz F, Kindu M, et al (2014) Land-use/land-cover (LULC) change and socioeconomic conditions of local community in the central highlands of Ethiopia. *Int J Sustain Dev World Ecol* 21:406–413. <https://doi.org/10.1080/13504509.2014.961181>
- Devia GK, Ganasri BP, Dwarakish GS (2015) A Review on Hydrological Models. *Aquat Procedia* 4:1001–1007. <https://doi.org/10.1016/j.aqpro.2015.02.126>
- Di Baldassarre G, Schumann G, Bates PD, et al (2010) Cartographie de zone inondable: Un examen critique d’approches déterministe et probabiliste. *Hydrol Sci J* 55:364–376. <https://doi.org/10.1080/02626661003683389>
- Dilley M, Heyman BN (1995) ENSO and Disaster: Droughts, Floods and El Niño/Southern Oscillation Warm Events. *Disasters* 19:181–193. <https://doi.org/10.1111/j.1467-7717.1995.tb00338.x>
- Donnelly C, Greuell W, Andersson J, et al (2017) Impacts of climate change on European hydrology at 1.5, 2 and 3 degrees mean global warming above

preindustrial level. *Clim Change* 143:13–26. <https://doi.org/10.1007/s10584-017-1971-7>

Duguma FA, Feyessa FF, Demissie TA, Januszkiewicz K (2021) Hydroclimate Trend Analysis of Upper Awash Basin, Ethiopia. *Water* 13:1680. <https://doi.org/10.3390/w13121680>

Dušek J, Hudecová Š, Stellner S (2017) Extreme precipitation and long-term precipitation changes in a Central European sedge-grass marsh in the context of flood occurrence. *Hydrol Sci J* 62:1796–1808. <https://doi.org/10.1080/02626667.2017.1353217>

Dwarakish GS, Ganasri BP (2015) Impact of land use change on hydrological systems: A review of current modeling approaches. *Cogent Geosci* 1:1115691. <https://doi.org/10.1080/23312041.2015.1115691>

Dysarz T, Wicher J, Mariusz D, Joanna S (2019) Analysis of extreme flow uncertainty impact on size of flood hazard zones for the Wronki gauge station in the Warta river. *Acta Geophys* 67:661–676. <https://doi.org/10.1007/s11600-019-00264-8>

Edossa DC, Babel MS, Gupta A Das (2010) Drought analysis in the Awash River Basin, Ethiopia. *Water Resour Manag* 24:1441–1460. <https://doi.org/10.1007/s11269-009-9508-0>

Elsadek WM, Ibrahim MG, Mahmud WE (2019) Runoff hazard analysis of Wadi Qena Watershed, Egypt based on GIS and remote sensing approach. *Alexandria Eng J* 58:377–385. <https://doi.org/10.1016/j.aej.2019.02.001>

Emerton R, Cloke HL, Stephens EM, et al (2017) Complex picture for likelihood of ENSO-driven flood hazard. *Nat Commun* 8:1–9. <https://doi.org/10.1038/ncomms14796>

Erena SH, Worku H, De Paola F (2018) Flood hazard mapping using FLO-2D and local management strategies of Dire Dawa city, Ethiopia. *J Hydrol Reg Stud*

19:224–239. <https://doi.org/10.1016/j.ejrh.2018.09.005>

Esper Angillieri MY, Perucca LP (2014) Geomorphology and morphometry of the de La Flecha river basin, San Juan, Argentina. *Environ Earth Sci* 72:3227–3237. <https://doi.org/10.1007/s12665-014-3227-4>

FAO (2007) Digital soil map of the world.

<https://data.apps.fao.org/map/catalog/srv/eng/catalog.search#/home>

Farooq M, Shafique M, Khattak MS (2019) Flood hazard assessment and mapping of River Swat using HEC-RAS 2D model and high-resolution 12-m TanDEM-X DEM (WorldDEM). *Nat Hazards* 97:477–492. <https://doi.org/10.1007/s11069-019-03638-9>

Fenta Mekonnen D, Duan Z, Rientjes T, Disse M (2018) Analysis of combined and isolated effects of land-use and land-cover changes and climate change on the upper Blue Nile River basin's streamflow. *Hydrol Earth Syst Sci* 22:6187–6207. <https://doi.org/10.5194/hess-22-6187-2018>

Gardiner V (1990) Drainage basin morphometry. Unwin Hyman, London

Gashaw T, Tulu T, Argaw M, Worqlul AW (2018) Modeling the hydrological impacts of land use/land cover changes in the Andassa watershed, Blue Nile Basin, Ethiopia. *Sci Total Environ* 619–620:1394–1408. <https://doi.org/10.1016/j.scitotenv.2017.11.191>

Gebremichael HB, Raba GA, Beketie KT, et al (2022) Changes in daily rainfall and temperature extremes of upper Awash Basin, Ethiopia. *Sci African* 16:e01173. <https://doi.org/10.1016/j.sciaf.2022.e01173>

Gedefaw M, Wang H, Yan D, et al (2018) Trend analysis of climatic and hydrological variables in the Awash river basin, Ethiopia. *Water (Switzerland)* 10:1–14. <https://doi.org/10.3390/w10111554>

Getahun Y, Gebre S (2015) Flood Hazard Assessment and Mapping of Flood Inundation Area of the Awash River Basin in Ethiopia using GIS and HEC-

GeoRAS/HEC-RAS Model. *J Civ Environ Eng* 05: <https://doi.org/10.4172/2165-784x.1000179>

Ghorbanian A, Kakooei M, Amani M, Mahdavi S (2020) *ISPRS Journal of Photogrammetry and Remote Sensing* Improved land cover map of Iran using Sentinel imagery within Google Earth Engine and a novel automatic workflow for land cover classification using migrated training samples. *ISPRS J Photogramm Remote Sens* 167:276–288. <https://doi.org/10.1016/j.isprsjprs.2020.07.013>

Gilleland E, Katz RW (2016) extRemes 2.0: An Extreme Value Analysis Package in R. *J Stat Softw* 72:. <https://doi.org/10.18637/jss.v072.i08>

Giusti E, Schneider W (1965) *The Distribution of Branches in River Networks* Geological Survey Professional Paper 422-g United States Geological Survey

Gu X, Zhang Q, Singh VP, et al (2017) Nonstationarity-based evaluation of flood risk in the Pearl River basin: changing patterns, causes and implications. *Hydrol Sci J* 62:246–258. <https://doi.org/10.1080/02626667.2016.1183774>

Guan S, Yang Q, Li Y, et al (2022) River flooding response to ENSO-related monsoon precipitation: Evidence from late Holocene core sediments in the Jiangnan Plain. *Palaeogeogr Palaeoclimatol Palaeoecol* 589:110834. <https://doi.org/10.1016/j.palaeo.2022.110834>

Hamed KH, Rao RA (1998) A modified Mann-Kendall trend test for autocorrelated data. *J Hydrol* 204:182–196. [https://doi.org/10.1016/S0022-1694\(97\)00125-X](https://doi.org/10.1016/S0022-1694(97)00125-X)

Hesarkazzazi S, Arabzadeh R, Hajibabaei M, et al (2021) Stationary vs non-stationary modelling of flood frequency distribution across northwest England. *Hydrol Sci J* 66:729–744. <https://doi.org/10.1080/02626667.2021.1884685>

Horton RE (1932) Drainage-basin characteristics. *Eos, Trans Am Geophys union* 13:350–361

Horton RE (1945) Erosional development of streams and their drainage basins;

- hydrophysical approach to quantitative morphology. *Bull Geol Soc Am* 56:275–370. [https://doi.org/10.1130/0016-7606\(1945\)56\[275:EDOSAT\]2.0.CO;2](https://doi.org/10.1130/0016-7606(1945)56[275:EDOSAT]2.0.CO;2)
- Houknpè J, Diekkrüger B, Afouda AA, Sintondji LOC (2019) Land use change increases flood hazard: a multi-modelling approach to assess change in flood characteristics driven by socio-economic land use change scenarios. *Nat Hazards* 98:1021–1050. <https://doi.org/10.1007/s11069-018-3557-8>
- Howe G, Slaymaker H, Harding D (1966) Flood hazard in mid-Wales. *Nature* 212:584–585
- Hu L, Nikolopoulos EI, Marra F, Anagnostou EN (2020) Sensitivity of flood frequency analysis to data record, statistical model, and parameter estimation methods: An evaluation over the contiguous United States. *J Flood Risk Manag* 13:1–13. <https://doi.org/10.1111/jfr3.12580>
- Ignacio KJ, Walling DE (1968) Time series analyses of water and sediment discharges. *Int Assoc Sci Hydrol Bull* 13:69–84. <https://doi.org/10.1080/02626666809493583>
- IPCC (2021a) In: Masson-Delmotte, V., P. Zhai, A. Pirani, S.L. Connors, C. Péan, S. Berger, N. Caud, Y. Chen, L. Goldfarb, M.I. Gomis, M. Huang, K. Leitzell, E. Lonnoy, J.B.R. Matthews, T.K. Maycock, T. Waterfield, O. Yelekçi, R. Yu, and B. Zhou (eds.). *Climate Change*
- IPCC (2021b) *Climate Change 2021: The Physical Science Basis - Summary for the Policymakers (Working Group I)*
- IPCC (2021c) *Annex IV: Modes of Variability*
- Iqbal A, Hassan SA (2018) ENSO and IOD analysis on the occurrence of floods in Pakistan. *Nat Hazards* 91:879–890. <https://doi.org/10.1007/s11069-017-3158-y>
- Jain S, Lall U (2001) Floods in a changing climate: Does the past represent the future? *Water Resour Res* 37:3193–3205. <https://doi.org/10.1029/2001WR000495>

- Jaweso D, Abate B, Bauwe A, Lennartz B (2019) Hydro-meteorological trends in the upper Omo-Ghibe river basin, Ethiopia. *Water (Switzerland)* 11:1–18. <https://doi.org/10.3390/w11091951>
- Jothimani M, Dawit Z, Mulualem W (2021) Flood Susceptibility Modeling of Megech River Catchment, Lake Tana Basin, North Western Ethiopia, Using Morphometric Analysis. *Earth Syst Environ* 5:353–364. <https://doi.org/10.1007/s41748-020-00173-7>
- Jung IW, Bae DH, Kim G (2011) Recent trends of mean and extreme precipitation in Korea. *Int J Climatol* 31:359–370. <https://doi.org/10.1002/joc.2068>
- Kabenge M, Elaru J, Wang H, Li F (2017) Characterizing flood hazard risk in data-scarce areas, using a remote sensing and GIS-based flood hazard index. *Nat Hazards* 89:1369–1387. <https://doi.org/10.1007/s11069-017-3024-y>
- Kabite G, Gessesse B (2018) Hydro-geomorphological characterization of Dhidhessa River Basin, Ethiopia. *Int Soil Water Conserv Res* 6:175–183. <https://doi.org/10.1016/j.iswcr.2018.02.003>
- Kale VS (2014) Is flooding in South Asia getting worse and more frequent? *Singap J Trop Geogr* 35:161–178. <https://doi.org/10.1111/sjtg.12060>
- Kanani-Sadat Y, Arabsheibani R, Karimipour F, Nasser M (2019) A new approach to flood susceptibility assessment in data-scarce and ungauged regions based on GIS-based hybrid multi criteria decision-making method. *J Hydrol* 572:17–31. <https://doi.org/10.1016/j.jhydrol.2019.02.034>
- Keggenhoff I, Elizbarashvili M, Amiri-Farahani A, King L (2014) Trends in daily temperature and precipitation extremes over Georgia, 1971-2010. *Weather Clim Extrem* 4:75–85. <https://doi.org/10.1016/j.wace.2014.05.001>
- Kendall M (1975) Rank correlation methods. Charles Griffin, London
- Khaliq MN, Ouarda TBMJ, Ondo JC, et al (2006) Frequency analysis of a sequence of dependent and/or non-stationary hydro-meteorological observations: A

- review. *J Hydrol* 329:534–552. <https://doi.org/10.1016/j.jhydrol.2006.03.004>
- Khorn N, Ismail MH, Nurhidayu S, et al (2022) Land use/land cover changes and its impact on runoff using SWAT model in the upper Prek Thnot watershed in Cambodia. *Environ Earth Sci* 81:. <https://doi.org/10.1007/s12665-022-10583-7>
- Khosravi K, Shahabi H, Pham BT, et al (2019) A comparative assessment of flood susceptibility modeling using Multi-Criteria Decision-Making Analysis and Machine Learning Methods. *J Hydrol* 573:311–323. <https://doi.org/10.1016/j.jhydrol.2019.03.073>
- Kisaka MO, Mucheru-Muna M, Ngetich FK, et al (2015) Rainfall Variability, Drought Characterization, and Efficacy of Rainfall Data Reconstruction: Case of Eastern Kenya. *Adv Meteorol* 2015:1–16. <https://doi.org/10.1155/2015/380404>
- Kobierska F, Engeland K, Thorarinsdottir T (2018) Evaluation of design flood estimates - a case study for Norway. *Hydrol Res* 49:450–465. <https://doi.org/10.2166/nh.2017.068>
- Koriche SA, Rientjes THM (2016) Application of satellite products and hydrological modelling for flood early warning. *Phys Chem Earth* 93:12–23. <https://doi.org/10.1016/j.pce.2016.03.007>
- Kumar R, Kumar S, Lohani AK, et al (2000) Evaluation of geomorphological characteristics of a catchment using GIS. *GIs India* 9:13–17
- Kundzewicz ZW, Graczyk D, Maurer T, et al (2005) Trend detection in river flow series: 1. Annual maximum flow. *Hydrol Sci J* 50:797–810. <https://doi.org/10.1623/hysj.2005.50.5.797>
- Kundzewicz ZW, Kanae S, Seneviratne SI, et al (2014) Flood risk and climate change : global and regional perspectives Flood risk and climate change : global and regional perspectives. *Hydrol Sci J – J des Sci Hydrol* 59:1–28. <https://doi.org/10.1080/02626667.2013.857411>
- Kundzewicz ZW, Robson AJ (2004) Change detection in hydrological records - A

review of the methodology. *Hydrol Sci J* 49:7–19.

<https://doi.org/10.1623/hysj.49.1.7.53993>

Kunkel KE, Karl TR, Squires MF, et al (2020) Precipitation extremes: Trends and relationships with average precipitation and precipitable water in the contiguous United States. *J Appl Meteorol Climatol* 59:125–142.

<https://doi.org/10.1175/JAMC-D-19-0185.1>

Lambe BT, Kundapura S (2023) Recent Changes in Hydrometeorological Extremes in the Bilate River Basin of. *J Hydrol Eng* 28:1–17.

<https://doi.org/10.1061/JHYEFF.HEENG-5853>

Lee E, Livino A, Han SC, et al (2018) Land cover change explains the increasing discharge of the Paraná River. *Reg Environ Chang* 18:1871–1881.

<https://doi.org/10.1007/s10113-018-1321-y>

Legesse D, Abiye TA, Vallet-Coulomb C, Abate H (2010) Streamflow sensitivity to climate and land cover changes: Meki River, Ethiopia. *Hydrol Earth Syst Sci*

14:2277–2287. <https://doi.org/10.5194/hess-14-2277-2010>

Legesse D, Vallet-Coulomb C, Gasse F (2003) Hydrological response of a catchment to climate and land use changes in Tropical Africa: Case study south central

Ethiopia. *J Hydrol* 275:67–85. [https://doi.org/10.1016/S0022-1694\(03\)00019-2](https://doi.org/10.1016/S0022-1694(03)00019-2)

Li J, Liu X, Chen F (2015) Evaluation of Nonstationarity in Annual Maximum Flood Series and the Associations with Large-scale Climate Patterns and Human

Activities. *Water Resour Manag* 29:1653–1668. <https://doi.org/10.1007/s11269-014-0900-z>

Li Z, Liu W zhao, Zhang X chang, Zheng F li (2009) Impacts of land use change and climate variability on hydrology in an agricultural catchment on the Loess

Plateau of China. *J Hydrol* 377:35–42.

<https://doi.org/10.1016/j.jhydrol.2009.08.007>

Liu S, Huang S, Huang Q, et al (2017) Identification of the non-stationarity of

- extreme precipitation events and correlations with large-scale ocean-atmospheric circulation patterns: A case study in the Wei River Basin, China. *J Hydrol* 548:184–195. <https://doi.org/10.1016/j.jhydrol.2017.03.012>
- Liu Z, Cuo L, Li Q, et al (2020) Impacts of climate change and land use/cover change on streamflow in beichuan river basin in Qinghai Province, China. *Water (Switzerland)* 12:. <https://doi.org/10.3390/W12041198>
- López J, Francés F (2013) Non-stationary flood frequency analysis in continental Spanish rivers, using climate and reservoir indices as external covariates. *Hydrol Earth Syst Sci* 17:3189–3203. <https://doi.org/10.5194/hess-17-3189-2013>
- Machado MJ, Botero BA, López J, et al (2015) Flood frequency analysis of historical flood data under stationary and non-stationary modelling. *Hydrol Earth Syst Sci* 19:2561–2576. <https://doi.org/10.5194/hess-19-2561-2015>
- Magesh NS, Chandrasekar N (2014) GIS model-based morphometric evaluation of Tamiraparani subbasin, Tirunelveli district, Tamil Nadu, India. *Arab J Geosci* 7:131–141. <https://doi.org/10.1007/s12517-012-0742-z>
- Maghsood FF, Moradi H, Bavani ARM, et al (2019) Climate change impact on flood frequency and source area in northern Iran under CMIP5 scenarios. *Water (Switzerland)* 11:. <https://doi.org/10.3390/w11020273>
- Mahala A (2020) The significance of morphometric analysis to understand the hydrological and morphological characteristics in two different morpho-climatic settings. *Appl Water Sci* 10:1–16. <https://doi.org/10.1007/s13201-019-1118-2>
- Mahmood S, Rahman A ur (2019) Flash flood susceptibility modeling using geomorphometric and hydrological approaches in Panjkora Basin, Eastern Hindu Kush, Pakistan. *Environ Earth Sci* 78:. <https://doi.org/10.1007/s12665-018-8041-y>
- Malede DA, Alamirew T, Andualem TG (2023) Integrated and Individual Impacts of Land Use Land Cover and Climate Changes on Hydrological Flows over Birr

- River Watershed, Abbay Basin, Ethiopia. *Water (Switzerland)* 15:.  
<https://doi.org/10.3390/w15010166>
- Mamo S, Berhanu B, Melesse AM (2019) Historical flood events and hydrological extremes in Ethiopia. Elsevier Inc.
- Mani P, Chatterjee C, Kumar R (2014) Flood hazard assessment with multiparameter approach derived from coupled 1D and 2D hydrodynamic flow model. *Nat Hazards* 70:1553–1574. <https://doi.org/10.1007/s11069-013-0891-8>
- Mann HB (1945) Nonparametric Tests Against Trend. *Econometrica* 13:245.  
<https://doi.org/10.2307/1907187>
- Manzoor S, Ahanger MA (2022) Spatio-temporal trends in precipitation and temperature means/extremes in the Himalayan states of India. *J Water Clim Chang* 13:2531–2558. <https://doi.org/10.2166/wcc.2022.395>
- Masood M, Takeuchi K (2012) Assessment of flood hazard, vulnerability and risk of mid-eastern Dhaka using DEM and 1D hydrodynamic model. *Nat Hazards* 61:757–770. <https://doi.org/10.1007/s11069-011-0060-x>
- McPhaden MJ, Zebiak SE, Glantz MH (2006) ENSO as an Integrating Concept in Earth Science. *Science (80- )* 314:1740–1745.  
<https://doi.org/10.1126/science.1132588>
- Mekonen AA, Berlie AB (2020) Spatiotemporal variability and trends of rainfall and temperature in the Northeastern Highlands of Ethiopia. *Model Earth Syst Environ* 6:285–300. <https://doi.org/10.1007/s40808-019-00678-9>
- Melkamu T, Bagyaraj M, Adimaw M, et al (2022) Detecting and mapping flood inundation areas in Fogera-Dera Floodplain, Ethiopia during an extreme wet season using Sentinel-1 data. *Phys Chem Earth* 127:103189.  
<https://doi.org/10.1016/j.pce.2022.103189>
- Memon N, Patel DP, Bhatt N, Patel SB (2020) Integrated framework for flood relief package (FRP) allocation in semiarid region: a case of Rel River flood, Gujarat,

India. Springer Netherlands

Meraj G, Romshoo SA, Yousuf AR, et al (2015) Assessing the influence of watershed characteristics on the flood vulnerability of Jhelum basin in Kashmir Himalaya. *Nat Hazards* 77:153–175. <https://doi.org/10.1007/s11069-015-1605-1>

Milly PCD, Betancourt J, Falkenmark M, et al (2008) Climate change: Stationarity is dead: Whither water management? *Science* (80- ) 319:573–574. <https://doi.org/10.1126/science.1151915>

Mishra AK, Singh VP (2010) Changes in extreme precipitation in Texas. *J Geophys Res Atmos* 115:1–29. <https://doi.org/10.1029/2009JD013398>

Mitiku AB, Meresa GA, Mulu T, Woldemichael AT (2023) Examining the impacts of climate variabilities and land use change on hydrological responses of Awash River basin, Ethiopia. *HydroResearch* 6:16–28. <https://doi.org/10.1016/j.hydres.2022.12.002>

Mo C, Zhu H, Ruan Y, et al (2022) Spatial and temporal variation characteristics and frequency analysis of extreme precipitation from 1959 to 2017: A case study of the Longtan watershed, southwest China. *J Water Clim Chang* 13:2610–2626. <https://doi.org/10.2166/wcc.2022.454>

Moore ID, Grayson RB, Ladson AR (1991) Digital terrain modelling: A review of hydrological, geomorphological, and biological applications. *Hydrol Process* 5:3–30. <https://doi.org/10.1002/hyp.3360050103>

Moriasi DN, Arnold JG, Van Liew MW, et al (2007) MODEL EVALUATION GUIDELINES FOR SYSTEMATIC QUANTIFICATION OF ACCURACY IN WATERSHED SIMULATION. *Trans Asabe* 50:885–900

Moussa R (2003) On morphometric properties of basins, scale effects and hydrological response. *Hydrol Process* 17:33–58. <https://doi.org/10.1002/hyp.1114>

Mudashiru RB, Sabtu N, Abustan I, Balogun W (2021) Flood hazard mapping

methods: A review. *J Hydrol* 603:126846.  
<https://doi.org/10.1016/j.jhydrol.2021.126846>

Mzava P, Valimba P, Nobert J (2021) Quantitative analysis of the impacts of climate and land-cover changes on urban flood runoffs: A case of dar es salaam, Tanzania. *J Water Clim Chang* 12:2835–2853.  
<https://doi.org/10.2166/wcc.2021.026>

Nag SK (1998) Morphometric Analysis Using Remote Sensing Techniques in the Chaka Sub-basin. *J Indian Soc Remote Sens* 26:70–76

Namara WG, Damisse TA, Tufa FG (2022) Application of HEC-RAS and HEC-GeoRAS model for Flood Inundation Mapping, the case of Awash Bello Flood Plain, Upper Awash River Basin, Oromiya Regional State, Ethiopia. *Model Earth Syst Environ* 8:1449–1460. <https://doi.org/10.1007/s40808-021-01166-9>

Nautiyal MD (1994) Morphometric analysis of a drainage basin using aerial photographs: A case study of Khairkuli basin, district Dehradun, U.P. *J Indian Soc Remote Sens* 22:251–261. <https://doi.org/10.1007/BF03026526>

Neitsch S., Arnold J., Kiniry J., Williams J. (2011) Soil & Water Assessment Tool Theoretical Documentation Version 2009. Texas Water Resour Inst 1–647.  
<https://doi.org/10.1016/j.scitotenv.2015.11.063>

Niehoff D, Fritsch U, Bronstert A (2002) Land-use impacts on storm-runoff generation: scenarios of land-use change and simulation of hydrological response in a meso-scale catchment in SW-Germany. *J Hydrol* 267:80–93.  
[https://doi.org/10.1016/S0022-1694\(02\)00142-7](https://doi.org/10.1016/S0022-1694(02)00142-7)

Nooka Ratnam K, Srivastava YK, Venkateswara Rao V, et al (2005) Check Dam positioning by prioritization micro-watersheds using SYI model and morphometric analysis - remote sensing and GIS perspective. *J Indian Soc Remote Sens* 33:25–38. <https://doi.org/10.1007/BF02989988>

Obeidat M, Awawdeh M, Al-Hantouli F (2021) Morphometric analysis and

- prioritisation of watersheds for flood risk management in Wadi Easal Basin (WEB), Jordan, using geospatial technologies. *J Flood Risk Manag* 14:1–19. <https://doi.org/10.1111/jfr3.12711>
- OCHA (2020) United Nations Office for the Coordination of Humanitarian Affairs, Ethiopia Humanitarian Bulletin
- Opere AO, Mkhandi S, Willems P (2006) At site flood frequency analysis for the Nile Equatorial basins. *Phys Chem Earth* 31:919–927. <https://doi.org/10.1016/j.pce.2006.08.018>
- Orke YA, Li MH (2021) Hydroclimatic variability in the bilate watershed, ethiopia. *Climate* 9:. <https://doi.org/10.3390/cli9060098>
- Ouyang R, Liu W, Fu G, et al (2014) Linkages between ENSO/PDO signals and precipitation, streamflow in China during the last 100 years. *Hydrol Earth Syst Sci* 18:3651–3661. <https://doi.org/10.5194/hess-18-3651-2014>
- Ozdemir H, Bird D (2009) Evaluation of morphometric parameters of drainage networks derived from topographic maps and DEM in point of floods. *Environ Geol* 56:1405–1415. <https://doi.org/10.1007/s00254-008-1235-y>
- Panahi A, Alijani B, Mohammadi H (2010) The Effect of the Land Use/Cover Changes on the Floods of the Madarsu Basin of Northeastern Iran. *J Water Resour Prot* 02:373–379. <https://doi.org/10.4236/jwarp.2010.24043>
- Pande CB, Moharir K (2017) GIS based quantitative morphometric analysis and its consequences: a case study from Shanur River Basin, Maharashtra India. *Appl Water Sci* 7:861–871. <https://doi.org/10.1007/s13201-015-0298-7>
- Pandya U, Patel DP, Singh SK (2021) A flood assessment of data scarce region using an open-source 2D hydrodynamic modeling and Google Earth Image: a case of Sabarmati flood, India. *Arab J Geosci* 14:1–18. <https://doi.org/10.1007/s12517-021-08504-2>
- Parker DJ (2000) *Floods*. Routledge

- Patel DP, Dholakia MB, Naresh N, Srivastava PK (2012) Water Harvesting Structure Positioning by Using Geo-Visualization Concept and Prioritization of Mini-Watersheds Through Morphometric Analysis in the Lower Tapi Basin. *J Indian Soc Remote Sens* 40:299–312. <https://doi.org/10.1007/s12524-011-0147-6>
- Patton PC, Baker VR (1976) Morphometry and floods in small drainage basins subject to diverse hydrogeomorphic controls. *Water Resour Res* 12:941–952. <https://doi.org/10.1029/WR012i005p00941>
- Perucca LP, Angilieri YE (2011) Morphometric characterization of del Molle Basin applied to the evaluation of flash floods hazard, Iglesia Department, San Juan, Argentina. *Quat Int* 233:81–86. <https://doi.org/10.1016/j.quaint.2010.08.007>
- Petrow T, Merz B (2009) Trends in flood magnitude, frequency and seasonality in Germany in the period 1951-2002. *J Hydrol* 371:129–141. <https://doi.org/10.1016/j.jhydrol.2009.03.024>
- Pettitt AN (1979) A Non-Parametric Approach to the Change-Point Problem. *Appl Stat* 28:126. <https://doi.org/10.2307/2346729>
- Pfannerstill M, Guse B, Fohrer N (2014) Smart low flow signature metrics for an improved overall performance evaluation of hydrological models. *J Hydrol* 510:447–458. <https://doi.org/10.1016/j.jhydrol.2013.12.044>
- Phan TN, Kuch V, Lehnert LW (2020) Land Cover Classification using Google Earth Engine and Random Forest Classifier—The Role of Image Composition. *Remote Sens* 12:2411. <https://doi.org/10.3390/rs12152411>
- Popa MC, Peptenatu D, Draghici CC, Diaconu DC (2019) Flood hazard mapping using the flood and Flash-Flood Potential Index in the Buzau River catchment, Romania. *Water (Switzerland)* 11:. <https://doi.org/10.3390/w11102116>
- Prosdocimi I, Kjeldsen TR, Svensson C (2014) Non-stationarity in annual and seasonal series of peak flow and precipitation in the UK. *Nat Hazards Earth Syst Sci* 14:1125–1144. <https://doi.org/10.5194/nhess-14-1125-2014>

- Rais S, Javed A (2014) Identification of Artificial Recharge Sites in Manchi Basin, Eastern Rajasthan (India) Using Remote Sensing and GIS Techniques. *J Geogr Inf Syst* 06:162–175. <https://doi.org/10.4236/jgis.2014.62017>
- Rangari VA, Umamahesh N V., Bhatt CM (2019) Assessment of inundation risk in urban floods using HEC RAS 2D. *Model Earth Syst Environ* 5:1839–1851. <https://doi.org/10.1007/s40808-019-00641-8>
- Rangari VA, Umamahesh N V., Patel AK (2021) Flood-hazard risk classification and mapping for urban catchment under different climate change scenarios: A case study of Hyderabad city. *Urban Clim* 36:100793. <https://doi.org/10.1016/j.uclim.2021.100793>
- Rientjes THM, Haile AT, Kebede E, et al (2011) Changes in land cover, rainfall and stream flow in Upper Gilgel Abbay catchment, Blue Nile basin - Ethiopia. *Hydrol Earth Syst Sci* 15:1979–1989. <https://doi.org/10.5194/hess-15-1979-2011>
- Robi MA, Abebe A, Pingale SM (2019) Flood hazard mapping under a climate change scenario in a Ribb catchment of Blue Nile River basin, Ethiopia. *Appl Geomatics* 11:147–160. <https://doi.org/10.1007/s12518-018-0249-8>
- Roy B, Khan MSM, Islam AKMS, et al (2021) Climate-induced flood inundation for the Arial Khan River of Bangladesh using open-source SWAT and HEC-RAS model for RCP8.5-SSP5 scenario. *SN Appl Sci* 3:. <https://doi.org/10.1007/s42452-021-04460-4>
- Roy S Sen, Balling RC (2004) Trends in extreme daily precipitation indices in India. *Int J Climatol* 24:457–466. <https://doi.org/10.1002/joc.995>
- Ryberg KR, Hodgkins GA, Dudley RW (2020) Change points in annual peak streamflows: Method comparisons and historical change points in the United States. *J Hydrol* 583:124307. <https://doi.org/10.1016/j.jhydrol.2019.124307>
- Saddique N, Mahmood T, Bernhofer C (2020) Quantifying the impacts of land use/land cover change on the water balance in the afforested River Basin,

Pakistan. *Environ Earth Sci* 79:1–13. <https://doi.org/10.1007/s12665-020-09206-w>

Salas JD, Obeysekera J (2014) Revisiting the concepts of return period and risk for nonstationary hydrologic extreme events. *J Hydrol Eng* 19:554–568. [https://doi.org/10.1061/\(ASCE\)HE.1943-5584.0000820](https://doi.org/10.1061/(ASCE)HE.1943-5584.0000820)

Sarkar D, Mondal P (2020) Flood vulnerability mapping using frequency ratio (FR) model: a case study on Kulik river basin, Indo-Bangladesh Barind region. *Appl Water Sci* 10:1–13. <https://doi.org/10.1007/s13201-019-1102-x>

Schumm S (1956) Evolution of drainage systems and slopes in bad-lands at Perth Amboy, New Jersey. *Geol Soc Am Bu* 67:597–646

Seleshi Y, Zanke U (2004) Recent changes in rainfall and rainy days in Ethiopia. *Int J Climatol* 24:973–983. <https://doi.org/10.1002/joc.1052>

Sen P (1968) Estimates of the regression coefficient based on Kendall's tau. *J Am Stat Assoc* 63:1379–1389

Setti S, Maheswaran R, Radha D, et al (2020) Attribution of Hydrologic Changes in a Tropical River Basin to Rainfall Variability and Land-Use Change: Case Study from India. *J Hydrol Eng* 25:5020015. [https://doi.org/10.1061/\(asce\)he.1943-5584.0001937](https://doi.org/10.1061/(asce)he.1943-5584.0001937)

Sharma PJ, Patel PL, Jothiprakash V (2020) Hydroclimatic teleconnections of large-scale oceanic-atmospheric circulations on hydrometeorological extremes of Tapi Basin, India. *Atmos Res* 235:104791. <https://doi.org/10.1016/j.atmosres.2019.104791>

Shawul AA, Chakma S (2020) Trend of extreme precipitation indices and analysis of long-term climate variability in the Upper Awash basin, Ethiopia. *Theor Appl Climatol* 140:635–652. <https://doi.org/10.1007/s00704-020-03112-8>

Shawul AA, Chakma S (2019) Spatiotemporal detection of land use/land cover change in the large basin using integrated approaches of remote sensing and GIS

- in the Upper Awash basin, Ethiopia. *Environ Earth Sci* 78:1–13.  
<https://doi.org/10.1007/s12665-019-8154-y>
- Shawul AA, Chakma S, Melesse AM (2019) The response of water balance components to land cover change based on hydrologic modeling and partial least squares regression (PLSR) analysis in the Upper Awash Basin. *J Hydrol Reg Stud* 26:100640. <https://doi.org/10.1016/j.ejrh.2019.100640>
- Sheikh MM, Manzoor N, Ashraf J, et al (2015) Trends in extreme daily rainfall and temperature indices over South Asia. *Int J Climatol* 35:1625–1637.  
<https://doi.org/10.1002/joc.4081>
- Siam MS, Eltahir EAB (2015) Explaining and forecasting interannual variability in the flow of the Nile River. *Hydrol Earth Syst Sci* 19:1181–1192.  
<https://doi.org/10.5194/hess-19-1181-2015>
- Singh O, Kumar D (2019) Evaluating the influence of watershed characteristics on flood vulnerability of Markanda River basin in north-west India. *Nat Hazards* 96:247–268. <https://doi.org/10.1007/s11069-018-3540-4>
- Singh S, Kanhaiya S, Singh A, Chaubey K (2019) Drainage network characteristics of the Ghaghghar River Basin (GRB), Son Valley, India. *Geol Ecol Landscapes* 3:159–167. <https://doi.org/10.1080/24749508.2018.1525670>
- Smith GP, Davey EK, Cox RJ (2014) Flood Hazard. *Water Res Lab Tech Rep* 7:17
- Smith K (1993) Riverine flood hazard. *Geography* 78:182–185
- Šraj M, Bezak N (2020) Comparison of time trend- and precipitation-informed models for assessing design discharges in variable climate. *J Hydrol* 589:..  
<https://doi.org/10.1016/j.jhydrol.2020.125374>
- Šraj M, Viglione A, Parajka J, Blöschl G (2016) The influence of non-stationarity in extreme hydrological events on flood frequency estimation. *J Hydrol Hydromechanics* 64:426–437. <https://doi.org/10.1515/johh-2016-0032>

- Sreedevi PD, Subrahmanyam K, Ahmed S (2005) The significance of morphometric analysis for obtaining groundwater potential zones in a structurally controlled terrain. *Environ Geol* 47:412–420. <https://doi.org/10.1007/s00254-004-1166-1>
- Strahler A (1964) Quantitative geomorphology of drainage basin and channel networks. In: Chow VT (ed) *Handbook of applied hydrology*. McGraw Hill Book Co., New York
- Strahler AN (1957) Quantitative analysis of watershed geomorphology. *Trans Am Geophys Union* 38:913. <https://doi.org/10.1029/TR038i006p00913>
- Strahler AN (1952) Hypsometric (area-altitude) analysis of erosional topography. *Geol Soc Am Bull* 63:1117–1142
- Strupczewski WG, Singh VP, Mitosek HT (2001) Non-stationary approach to at-site flood frequency modelling. III. Flood analysis of Polish rivers. *J Hydrol* 248:152–167. [https://doi.org/10.1016/S0022-1694\(01\)00399-7](https://doi.org/10.1016/S0022-1694(01)00399-7)
- Svensson C, Kundzewicz ZW, Maurer T (2005) Trend detection in river flow series: 2. Flood and low-flow index series. *Hydrol Sci J* 50:811–824. <https://doi.org/10.1623/hysj.2005.50.5.811>
- Tabari H (2020) Climate change impact on flood and extreme precipitation increases with water availability. *Sci Rep* 10:1–10. <https://doi.org/10.1038/s41598-020-70816-2>
- Tadese M, Kumar L, Koech R, Kogo BK (2020) Mapping of land-use/land-cover changes and its dynamics in Awash River Basin using remote sensing and GIS. *Remote Sens Appl Soc Environ* 19:100352. <https://doi.org/10.1016/j.rsase.2020.100352>
- Tadese MT, Kumar L, Koech R, Zemadim B (2019) Hydro-climatic variability: A characterisation and trend study of the Awash River Basin, Ethiopia. *Hydrology* 6:.. <https://doi.org/10.3390/hydrology6020035>
- Taha MMN, Elbarbary SM, Naguib DM, El-Shamy IZ (2017) Flash flood hazard

- zonation based on basin morphometry using remote sensing and GIS techniques: A case study of Wadi Qena basin, Eastern Desert, Egypt. *Remote Sens Appl Soc Environ* 8:157–167. <https://doi.org/10.1016/j.rsase.2017.08.007>
- Tamiru H, Wagari M (2022) Machine-learning and HEC-RAS integrated models for flood inundation mapping in Baro River Basin, Ethiopia. *Model Earth Syst Environ* 8:2291–2303. <https://doi.org/10.1007/s40808-021-01175-8>
- Tan ML, Gassman PW, Yang X, Haywood J (2020) A review of SWAT applications, performance and future needs for simulation of hydro-climatic extremes. *Adv Water Resour* 143:103662. <https://doi.org/10.1016/j.advwatres.2020.103662>
- Tan ML, Ibrahim AL, Yusop Z, et al (2015) Impacts de l'utilisation des sols et de la variabilité climatique sur les composantes hydrologiques dans le bassin du fleuve Johor, en Malaisie. *Hydrol Sci J* 60:873–889. <https://doi.org/10.1080/02626667.2014.967246>
- Taye MT, Dyer E, Charles KJ, Hirons LC (2021) Potential predictability of the Ethiopian summer rains: Understanding local variations and their implications for water management decisions. *Sci Total Environ* 755:142604. <https://doi.org/10.1016/j.scitotenv.2020.142604>
- Taye MT, Dyer E, Hirpa FA, Charles K (2018) Climate change impact on water resources in the Awash basin, Ethiopia. *Water (Switzerland)* 10:1–16. <https://doi.org/10.3390/w10111560>
- Taye MT, Willems P (2012) Temporal variability of hydroclimatic extremes in the Blue Nile basin. *Water Resour Res* 48:1–13. <https://doi.org/10.1029/2011WR011466>
- Tehrany MS, Jones S, Shabani F (2019) Identifying the essential flood conditioning factors for flood prone area mapping using machine learning techniques. *Catena* 175:174–192. <https://doi.org/10.1016/j.catena.2018.12.011>
- Tekleab S, Mohamed Y, Uhlenbrook S (2013) Hydro-climatic trends in the

- Abay/Upper Blue Nile basin, Ethiopia. *Phys Chem Earth* 61–62:32–42.  
<https://doi.org/10.1016/j.pce.2013.04.017>
- Teng J, Jakeman AJ, Vaze J, et al (2017) Flood inundation modelling: A review of methods, recent advances and uncertainty analysis. *Environ Model Softw* 90:201–216. <https://doi.org/10.1016/j.envsoft.2017.01.006>
- Tessema N, Kebede A, Yadeta D (2020) Modeling land use dynamics in the Kesem sub-basin, Awash River basin, Ethiopia. *Cogent Environ Sci* 6:1782006.  
<https://doi.org/10.1080/23311843.2020.1782006>
- Theil H (1950) A rank-invariant method of linear and polynomial regression analysis. *Proc K Ned Akad van Wet Series A* 5:386–392
- Tolessa T, Senbeta F, Kidane M (2017) The impact of land use/land cover change on ecosystem services in the central highlands of Ethiopia. *Ecosyst Serv* 23:47–54.  
<https://doi.org/10.1016/j.ecoser.2016.11.010>
- Torabi Haghghi A, Darabi H, Shahedi K, et al (2020) A Scenario-Based Approach for Assessing the Hydrological Impacts of Land Use and Climate Change in the Marboreh Watershed, Iran. *Environ Model Assess* 25:41–57.  
<https://doi.org/10.1007/s10666-019-09665-x>
- Ullah K, Zhang J (2020) GIS-based flood hazard mapping using relative frequency ratio method: A case study of panjkora river basin, eastern Hindu Kush, Pakistan. *PLoS One* 15:1–18. <https://doi.org/10.1371/journal.pone.0229153>
- van der Wiel K, Bintanja R (2021) Contribution of climatic changes in mean and variability to monthly temperature and precipitation extremes. *Commun Earth Environ* 2:1–11. <https://doi.org/10.1038/s43247-020-00077-4>
- Vasconcellos SM, Kobiyama M, Dagostin FS, et al (2021) Flood Hazard Mapping in Alluvial Fans with Computational Modeling. *Water Resour Manag* 35:1463–1478. <https://doi.org/10.1007/s11269-021-02794-7>
- Viste E, Korecha D, Sorteberg A (2013) Recent drought and precipitation tendencies

- in Ethiopia. *Theor Appl Climatol* 112:535–551. <https://doi.org/10.1007/s00704-012-0746-3>
- Vojtek M, Vojteková J (2016) Flood hazard and flood risk assessment at the local spatial scale: a case study. *Geomatics, Nat Hazards Risk* 7:1973–1992. <https://doi.org/10.1080/19475705.2016.1166874>
- Von Storch H, Navarra A (1995) *Analysis of Climate Variability*. Springer-Verlag, New York
- Wagesho N, Goel NK, Jain MK (2012) Investigation of non-stationarity in hydro-climatic variables at Rift Valley lakes basin of Ethiopia. *J Hydrol* 444–445:113–133. <https://doi.org/10.1016/j.jhydrol.2012.04.011>
- Wang Y, Tabari H, Xu Y, Willems P (2019) Atmospheric and human-induced impacts on temporal variability of water level extremes in the Taihu Basin, China. *J Flood Risk Manag* 12:1–14. <https://doi.org/10.1111/jfr3.12539>
- Ward PJ, Beets W, Bouwer LM, et al (2010) Sensitivity of river discharge to ENSO. *Geophys Res Lett* 37:1–6. <https://doi.org/10.1029/2010GL043215>
- Ward PJ, Eisner S, Flo Rke M, et al (2014a) Annual flood sensitivities to el nintild;O-Southern Oscillation at the global scale. *Hydrol Earth Syst Sci* 18:47–66. <https://doi.org/10.5194/hess-18-47-2014>
- Ward PJ, Jongman B, Kumm M, et al (2014b) Strong influence of El Niño Southern Oscillation on flood risk around the world. *Proc Natl Acad Sci U S A* 111:15659–15664. <https://doi.org/10.1073/pnas.1409822111>
- Wedajo GK, Muleta MK, Awoke BG (2022) Impacts of combined and separate land cover and climate changes on hydrologic responses of Dhidhessa River basin, Ethiopia. *Int J River Basin Manag* 1–14. <https://doi.org/10.1080/15715124.2022.2101464>
- Weiss A (2001) Topographic position and landforms analysis. In: Poster presentation, ESRI user conference, San Diego, CA

- Welde K, Gebremariam B (2017) Effect of land use land cover dynamics on hydrological response of watershed: Case study of Tekeze Dam watershed, northern Ethiopia. *Int Soil Water Conserv Res* 5:1–16. <https://doi.org/10.1016/j.iswcr.2017.03.002>
- WMO (2021) WMO atlas of mortality and economic losses from weather , climate and water extremes. World Meteorological Organization (WMO), Geneva 2, Switzerland
- WMO (2008) Guide to meteorological instruments and methods of observation. Guide to Meteorol Instruments Methods Obs WMO-No. 8:I.14–7
- Woldegebrael SM, Kidanewold BB, Zaitchik B, Melesse AM (2020) Rainfall and Flood Event Interrelationship - A Case Study of Awash and Omo-Gibe Basins, Ethiopia. *Int J Sci Eng Res* 11:
- Woldesenbet TA, Elagib NA, Ribbe L, Heinrich J (2017) Hydrological responses to land use/cover changes in the source region of the Upper Blue Nile Basin, Ethiopia. *Sci Total Environ* 575:724–741. <https://doi.org/10.1016/j.scitotenv.2016.09.124>
- Woltemade CJ, Hawkins TW, Jantz C, Drzyzga S (2020) Impact of Changing Climate and Land Cover on Flood Magnitudes in the Delaware River Basin, USA. *J Am Water Resour Assoc* 56:507–527. <https://doi.org/10.1111/1752-1688.12835>
- Worako AW, Haile AT, Taye MT (2021) Streamflow variability and its linkage to ENSO events in the Ethiopian Rift Valley Lakes Basin. *J Hydrol Reg Stud* 35:100817. <https://doi.org/10.1016/j.ejrh.2021.100817>
- Worku T, Khare D, Tripathi SK (2017) Modeling runoff–sediment response to land use/land cover changes using integrated GIS and SWAT model in the Beressa watershed. *Environ Earth Sci* 76:1–14. <https://doi.org/10.1007/s12665-017-6883-3>
- Wu H, Li X, Qian H (2021) Temporal variability in extremes of daily precipitation,

- daily maximum and minimum temperature in Shaanxi, China. *J Atmos Solar-Terrestrial Phys* 215:105585. <https://doi.org/10.1016/j.jastp.2021.105585>
- Wudineh FA, Moges SA, Kidanewold BB (2022) Detecting Hydrological Variability in Precipitation Extremes: Application of Reanalysis Climate Product in Data-Scarce Wabi Shebele Basin of Ethiopia. *J Hydrol Eng* 27:.  
[https://doi.org/10.1061/\(asce\)he.1943-5584.0002156](https://doi.org/10.1061/(asce)he.1943-5584.0002156)
- Wudineh FA, Moges SA, Kidanewold BB (2021) Flood Change Detection and Attribution Using Simulation Approach in Data-Scarce Watersheds: A Case of Wabi Shebele River Basin, Ethiopia. *J Water Resour Prot* 13:362–393.  
<https://doi.org/10.4236/jwarp.2021.135023>
- Yan Y, Wu H, Gu G, et al (2020) Exploring the ENSO Impact on Basin-Scale Floods Using Hydrological Simulations and TRMM Precipitation. *Geophys Res Lett* 47:.  
<https://doi.org/10.1029/2020GL089476>
- Youssef AM, Pradhan B, Hassan AM (2011) Flash flood risk estimation along the St. Katherine road, southern Sinai, Egypt using GIS based morphometry and satellite imagery. *Environ Earth Sci* 62:611–623. <https://doi.org/10.1007/s12665-010-0551-1>
- Zaroug MAH, Eltahir EAB, Giorgi F (2014) Droughts and floods over the upper catchment of the Blue Nile and their connections to the timing of El Niño and la Niña events. *Hydrol Earth Syst Sci* 18:1239–1249. <https://doi.org/10.5194/hess-18-1239-2014>
- Zhang X, Xiao Y, Wang K, Wang T (2023) A study on the spatial and temporal evolution of multi-year extreme precipitation in the Huaihe River Basin. *Theor Appl Climatol* 397–405. <https://doi.org/10.1007/s00704-023-04416-1>
- Zhang Y, Moges S, Block P (2016) Optimal cluster analysis for objective regionalization of seasonal precipitation in regions of high spatial-temporal variability: Application to Western Ethiopia. *J Clim* 29:3697–3717.  
<https://doi.org/10.1175/JCLI-D-15-0582.1>

Zuo Q, Song Y, Wang H, et al (2021) Spatial variations of extreme precipitation events and attribution analysis in the main water resource area of the Belt and Road Initiative. *Theor Appl Climatol* 144:535–554.  
<https://doi.org/10.1007/s00704-021-03556-6>

## LIST OF PUBLICATIONS

1. Tola, S.Y., Shetty, A. Extreme hydroclimatic variability and impact of local and global climate system anomalies on extreme flow in the Upper Awash River basin. *Theor Appl Climatol* (2023). <https://doi.org/10.1007/s00704-023-04510-4>
2. Tola, S.Y., Shetty, A. Quantification of change in land cover and rainfall variability impact on flood hydrology using a hydrological model in the Ethiopian river basin. *Environ Earth Sci* **82**, 254 (2023). <https://doi.org/10.1007/s12665-023-10929-9>
3. Tola, S.Y., Shetty, A. Flood hazard map of the Becho floodplain, Ethiopia, using nonstationary frequency model. *Acta Geophys.* (2023). <https://doi.org/10.1007/s11600-023-01074-9>
4. Tola, S.Y., Shetty, A. Flood susceptibility modeling based on morphometric parameters in Upper Awash River basin, Ethiopia using geospatial techniques. *Sustain. Water Resour. Manag.* **8**, 49 (2022). <https://doi.org/10.1007/s40899-022-00642-z>
5. Tola, S.Y., Shetty, A. Land cover change and its implication to hydrological regimes and soil erosion in Awash River basin, Ethiopia: a systematic review. *Environ Monit Assess* **193**, 836 (2021). <https://doi.org/10.1007/s10661-021-09599-6>

## ***Curriculum Vitae***

### **Sintayehu Yadete Tola (Ph.D)**

Faculty of Water Supply and Environmental Engineering

Arba Minch University, PO Box-21

Arba Minch, Ethiopia

Mobile: +251 938 986 908

E-Mail:

[sintayadete5@gmail.com](mailto:sintayadete5@gmail.com)/[sintayehu.yadete@amu.edu.et](mailto:sintayehu.yadete@amu.edu.et)



---

### **Research Topics**

- Analysis of extreme hydroclimatic variables
- Hydrological modeling with SWAT/SWAT+
- Flood modeling and mapping with the HEC-RAS model
- Nonstationary flood frequency modeling and uncertainty analysis
- Impact of land cover change and climate variability on extreme flow

### **Education**

- Ph.D. degree in Water Resources Engineering and Management (2024)  
National Institute of Technology Karnataka, Surathkal, India.
- M.Sc. degree in Hydraulic Engineering (2016)  
Arba Minch University, Ethiopia
- B.Sc. degree in Water Supply and Environmental Engineering (2011)  
Arba Minch University, Ethiopia

### **Scientific Employment**

- Chair head of Environmental Engineering, Faculty of Water Supply and Environmental Engineering, Arba Minch University, Water Technology Institute, Ethiopia (July 2018 to July 2019)
- Lecturer, Arba Minch University, Water Technology Institute, Ethiopia (2016 to present)  
Teaching and final-year project supervision
- Assistant Lecturer, Arba Minch University, Water Technology Institute, Ethiopia (2012 to 2016)  
Teaching and examining student
- Graduate Assistant II, Arba Minch University, Water Technology Institute, Ethiopia (2011 to 2012)  
Teaching and examining student

### **Research Grant**

- Title: Analysis of dam overtopping risk based on univariate and bivariate flood frequency Analysis (parametric and non-

parametric approach), Gidabo Earth Fill Dam, Rift Valley Lake River Basin, Ethiopia (Arba Minch University, Water Resources Research Center, 2019)

### Peer-review Publications

6. **Tola, S.Y.**, Shetty, A. Extreme hydroclimatic variability and impact of local and global climate system anomalies on extreme flow in the Upper Awash River basin. *Theor Appl Climatol* **153**, 1117–1137(2023). <https://doi.org/10.1007/s00704-023-04510-4>
7. **Tola, S.Y.**, Shetty, A. Quantification of change in land cover and rainfall variability impact on flood hydrology using a hydrological model in the Ethiopian river basin. *Environ Earth Sci* **82**, 254 (2023). <https://doi.org/10.1007/s12665-023-10929-9>
8. **Tola, S.Y.**, Shetty, A. Flood hazard map of the Becho floodplain, Ethiopia, using nonstationary frequency model. *Acta Geophys.* (2023). <https://doi.org/10.1007/s11600-023-01074-9>
9. **Tola, S.Y.**, Shetty, A. Flood susceptibility modeling based on morphometric parameters in Upper Awash River basin, Ethiopia using geospatial techniques. *Sustain. Water Resour. Manag.* **8**, 49 (2022). <https://doi.org/10.1007/s40899-022-00642-z>
10. **Tola, S.Y.**, Shetty, A. Land cover change and its implication to hydrological regimes and soil erosion in Awash River basin, Ethiopia: a systematic review. *Environ Monit Assess* **193**, 836 (2021). <https://doi.org/10.1007/s10661-021-09599-6>

### Publications Under review

1. Characterization of the surface lake and evaluation of lake benefits on unconfined aquifers- A study on coastal Karnataka Lake, India (Under review, Water Conservation Science and Engineering)

### Ph.D. Thesis

- Thesis title: Flood modeling and mapping in the Upper Awash River basin, Ethiopia.

### Research Profile

- [Google Scholar](#)
- [Research Gate](#)